Thesis :- Conduction of heat within a body subjected to aerodynamic heating at hypersonic speeds .

List of errata

Page	Line	Errata	Corrected to
5	23	T_o	$T_{o\infty}$
9	5	$\left(\frac{p}{p_{sl}}\right)^{\frac{1}{2}}$	$\left(\frac{p_\infty}{p_{sl}}\right)^{\frac{1}{2}}$
I4	I0	emissity	emissivity
22	I2	$\frac{d\xi}{d\varphi}\left(\phi^4 - \xi^{-\frac{1}{2}}\right)$	$\frac{d\xi}{d\varphi}\int_0^{\xi}\left(\phi^4 - \xi^{-\frac{1}{2}}\right) d\xi$
58	2I	dervied	derived
66	7	(4.2.I0)	(4.2.8.)
72	5	cross	crossed
86	I5	4.2.I0	(4.2.8)
I56	last line	x=0.75	x = - 0.75
200	I5	(4.2.I0)	(4.2.8)

SUMMARY

Rockets, Satellites and other space-craft moving at supersonic and hypersonic speeds through the atmosphere present a formidable problem of high temperature heat transfer from the boundary layer. The boundary layer temperature becomes very high and at a flight speed of Mach number 10 or more, it is of the order of 4000°C or higher. The forward tip, nose or leading edges of the moving body experience maximum heating and efforts are being made first to reduce aerodynamically the amount of heating by suitable design and second to effect cooling by suitable means.

In the present work, efforts have been made to find by how much the heat conductivity of the material can help to reduce the temperature at the leading edge of the body subjected to the aerodynamic heating. Theoretical analysis of the heat balance equations indicates that the heat conductivity of material can play an important role in transferring the heat from the nose region to the downstream part of the body. The effects of the different geometry of the conducting skin on the nose temperature have also been discussed briefly.

A short review of the works of many investigators indicates that the aerodynamic heating is a function of Reynolds number, Mach number, Pradtl number, ratio of specific heats of air and the ratio of the surface temperature of the body to the ambient temperature. Hence during level flight at a constant speed, the laminar boundary layer aerodynamic heating at any point on the body would be inversely proportional to the square root of its distance from the nose. With this as a guiding factor, a reflector was designed to provide a pattern of heat distribution on a plane similar to that of aerodynamic heating. It was thought that the use of a reflector

with a single heating element as a heat source, would give the most convenient method of providing the required pattern of heat distribution. Necessary basic differential equations for the design of a reflector were derived. An analytical test method was also developed to find the actual heat distribution given by a reflector using a heating element of finite size.

Work was carried on to find a suitable heating element to provide maximum heat energy in a high vacuum with the minimum size to suit the reflector. Materials like tungsten, pure nickel, graphite and lampblack were tested in high vacuo.

In order to obtain high accuracy in the reflector profile, a suitable method of construction was developed. Since none of the conventional heat radiation measuring instruments was suitable for measuring heat flux $\propto \quad x^{-\frac{1}{2}}$, a suitable radiometer was designed and constructed for this purpose. A water calorimeter was designed and constructed to calibrate the radiometer. Other necessary equipments such as vacuum chamber, model support tray, etc. were also designed and made.

Since only a limited amount of radiant heat was available from the heating element, high thermal conductivity materials could not be used for the conducting skin models. Models of Staybrite stainless steel ($k = 3.90$ ft.lb/ft/sec/°K) and Frequentite ($k = 0.65$ ft.lb/ft/sec/°K) were made and tested under different rates of heating in a high vacuum of the order of 10^{-5} torr. Test results were plotted, and compared with the theoretical predictions of Nonweiler and the radiation equilibrium temperature, and the conclusions were drawn from them.

CONDUCTION OF HEAT WITHIN A BODY SUBJECTED TO AERODYNAMIC HEATING AT HYPERSONIC SPEEDS

by

Birendra Prasad Sinha , B. Tech. (Hons.)

Thesis submitted for the degree of Ph.D.
to the Faculty of Engineering,
The University of Glasgow.

September, 1966.

ACKNOWLEDGMENTS

The auther wishes to acknowledge his indebtedness to Professor T.R.F. Nonweiler and Mr. H.H.Y. Wong for their guidance , advice and encouragement in pursuing the work embodied in this thesis and he very sincerely thanks them. He is also thankful to Dr. A.S. Thom and other members of the staff at the University of Glasgow for their useful advice and help in carrying out this investigation.

Thanks are also due to the Patna University (India),for granting him the necessary leave to pursue this work.

CONTENTS

APPENDICES :

LIST OF FIGURES

LIST OF TABLES

NOMENCLATURE

a	speed of sound.
a_0	constant , (section 4.2.)
A	surface area.
c	characteristic temperature, defined by equation (2.2.2)
C	Sutherland's constant (i.e, $\mu \propto \frac{T^{3/2}}{T + C}$)
C_f	coefficient of skin friction ($= \frac{f_s}{\frac{1}{2}\rho u^2}$)
C_i	concentration by weight of the i th species.
C_p	specific heat of gas at constant pressure.
$\bar{C}_p$	$\Sigma C_i C_{pi}$
C_v	specific heat of gas at constant volume.
D_{12}	coefficient of diffusion of atoms into molecules.
f_s	shear stress.
g	acceleration due to gravity.
G_r	Grashof number ,
h	coefficient of heat transfer , ($= \frac{q}{T_{aw} - T_w}$)
H	enthalpy.
H_i	dissociation enthalpy per unit mass.
J	mechanical equivalent of heat
k	thermal conductivity
K_h	$\frac{1}{2} \rho_\infty u_\infty^3$
ℓ	characteristic length ,defined by equation (2.2.2)
L_1	defined by equation (4.2.4)
L	length of the body surface.
L_e	Lewis number ($= \frac{\rho D_{12} \bar{C}_p}{k}$)

m molecular weight of gas.

M Mach number.

n viscosity-conductivity exponent.

i.e. $\frac{\mu}{\mu_o} = \frac{k}{k_o} = \left(\frac{T}{T_o}\right)^n$

N_u Nusselt number $\left(= \frac{h L}{k} \right)$

p gas pressure.

P_r Prandtl number, $\frac{C_p \mu}{k}$

Q constant, $q_x . x^{\frac{1}{2}}$

Q' heat intensity of the heating element per unit length.

q heat flux into the surface $\left\{ = k_w . \left(\frac{\delta T}{\delta y}\right)_w \right.$

r radius of thevature of the reflector.

r_o value of r at the starting point of the reflector profile.

r_f recovery factor $\left(= \frac{T_{aw} - T_w}{u^2 / 2gJC_p} \right)$

r_h radius of the heating element.

r_m minimum radius of the reflector profile.

R gas constant.

R_e Reynolds number $\left(= \frac{\rho u L}{\mu} \right)$

S defined by equation (4.2.11)

S_o value of S at θ_o.

t thickness of the conducting skin

T static temperature.

T_{aw} adiabatic wall temperature of the gas.

T_r temperature of the conducting skin at the rear end.

u component of the gas velocity parallel to the x-axis.

v component of the gas velocity parallel to the y-axis.

x_o constant, defined by equation 4.2.2.

ρ gas density.

α slope of the reflector.

γ ratio of specific heats of gas at constant pressure to that at constant volume.

δ defined by equation (A-1).

ε emissivity.

θ angle between the radius vector of the reflector profile and y-axis. (fig. 4.2.1).

θ_o value of θ at the starting point of the reflector profile.

θ_h value of θ for which hot end of the plane of irradiation receives the reflected ray.

λ fineness ratio $\frac{x}{t}$

Λ value of ξ at $x = L$.

μ coefficient of viscosity of gas.

ν non-dimensional area of the conducting skin ,(eqn. 2.2.5)

ξ non-dimensional length of the conducting skin ,(eqn. 2.2.5).

ϕ non-dimensional temperature of the conducting skin (eqn.2.2.5.)

σ Stefan-Boltzmann constant.

τ non-dimensional thickness of the conducting skin ,(eqn. 2.2.5.).

ϕ_o value of ϕ at the nose of the conducting skin.

ϕ_r value of ϕ at the rear end of the conducting skin.

ω angle subtended by the reflected ray with y-axis.

Subscripts :

δ condition at the edge of the boundary layer.

∞ free stream condition.

o stagnation condition or nose condition.

w condition at the surface of the body.

aw adiabatic wall condition.

sl value at the sea-level.

SUMMARY

Rockets, Satellites and other space-craft moving at supersonic and hypersonic speeds through the atmosphere present a formidable problem of high temperature heat transfer from the boundary layer. The boundary layer temperature becomes very high and at a flight speed of Mach number 10 or more, it is of the order of 4000°C or higher. The forward tip, nose or leading edges of the moving body experience maximum heating and efforts are being made first to reduce aerodynamically the amount of heating by suitable design and second to effect cooling by suitable means.

In the present work, efforts have been made to find by how much the heat conductivity of the material can help to reduce the temperature at the leading edge of the body subjected to the aerodynamic heating. Theoretical analysis of the heat balance equations indicates that the heat conductivity of material can play an important role in transferring the heat from the nose region to the downstream part of the body. The effects of the different geometry of the conducting skin on the nose temperature have also been discussed briefly.

A short review of the works of many investigators indicates that the aerodynamic heating is a function of Reynolds number, Mach number, Prndtl number, ratio of specific heats of air and the ratio of the surface temperature of the body to the ambient temperature. Hence during level flight at a constant speed, the laminar boundary layer aerodynamic heating at any point on the body would be inversely proportional to the square root of its distance from the nose. With this as a guiding factor, a reflector was designed to provide a pattern of heat distribution on a plane similar to that of aerodynamic heating. It was thought that the use of a reflector

with a single heating element as a heat source, would give the most convenient method of providing the required pattern of heat distribution. Necessary basic differential equations for the design of a reflector were derived. An analytical test method was also developed to find the actual heat distribution given by a reflector using a heating element of finite size.

Work was carried on to find a suitable heating element to provide maximum heat energy in a high vacuum with the minimum size to suit the reflector. Materials like tungsten, pure nickel, graphite and lampblack were tested in high vacuo.

In order to obtain high accuracy in the reflector profile, a suitable method of construction was developed. Since none of the conventional heat radiation measuring instruments was suitable for measuring heat flux $\propto x^{-\frac{1}{2}}$, a suitable radiometer was designed and constructed for this purpose. A water calorimeter was designed and constructed to calibrate the radiometer. Other necessary equipments such as vacuum chamber, model support tray, etc. were also designed and made.

Since only a limited amount of radiant heat was available from the heating element, high thermal conductivity materials could not be used for the conducting skin models. Models of Staybrite stainless steel ($k = 3.90$ ft.lb/ft/sec/°K) and Froquentite ($k = 0.65$ ft.lb/ft/sec/°K) were made and tested under different rates of heating in a high vacuum of the order of 10^{-5} torr. Test results were plotted, and compared with the theoretical predictions of Nonweiler and the radiation equilibrium temperature, and the conclusions were drawn from them.

CHAPTER 1

HYPERSONIC FLOW

1.1 Introduction

Retardation of a high speed fluid stream flowing over a body, generates a boundary layer. This process of retardation also brings about a conversion of high kinetic energy of the free-stream into thermal energy in the boundary layer which is further increased by frictional heating at the surface of the body. As long as the speed of the fluid stream or the flight speed of the body is not high enough to generate heat to cause such a high temperature in the boundary layer as to produce any chemical or electronic reaction, the heat transfer at the body surface from the boundary layer to the body is governed purely by thermal conduction. Under this condition, the rate of aerodynamic heating is estimated by assessing the enthalpy-gradient at the surface. Efforts have also been made by many investigators to assess the heat transfer to the body by considering the temperature gradient at the surface, with some modifications. These approaches are valid for boundary layer temperatures below $3000^{\circ}K$.

Above a temperature of $3000^{\circ}K$, chemical reaction sets in and at still higher temperatures electronic reaction begins and therefore, change of phase of the gas occurs. In such cases, the heat of reaction has also to be taken into account to assess the rate of heat transfer to the body.

During the last ten to fifteen years, many investigators have suggested different theories to assess the rate of aerodynamic heating, but only a few of them will be discussed briefly in the following sections.

Basically two solutions of this problem are essential:- one for the undissociated air, and the other for the dissociated air which is the state of the boundary layer air, if the flight Mach number is very high.

1.2 Boundary Layer at Supersonic and Hypersonic Speeds

From the general point of view of having laminar flow and small drag, a sharp leading edge is desirable. At high supersonic speeds, however, the attached shock wave at the leading edge causes a high rate of heat transfer and the maintenance of a sharp leading edge becomes an intricate problem. In order to avoid this, and also to allow for internal heat conduction, all bodies at such high speeds must be blunt nosed or radiused to some extent.

A distinct layer is most likely to exist, independent of the detached bow-shock wave of a radiused leading edge, if the boundary layer thickness is much less than the shock-detachment distance. Since the boundary layer thickness varies inversely as the square root of the Reynolds number, and the detachment distance is independent of Reynolds number, there is a minimum Reynolds number, below which the bow shock wave and boundary layer merge. It is not likely that such a low Reynolds number would be attained at high supersonic or hypersonic flight before free-molecule flow starts.[10]

The radiused nose or leading-edge would have a large falling pressure gradient and also there would be a large heat transfer to the surface at hypersonic speeds. These two factors are expected to contribute toward maintaining a laminar boundary layer in that region[8]. Transition to the turbulent layer somewhere downstream is expected, but not enough work either analytical or experimental has been done to find the point of transition and the relative importance of factors influencing the transition.

In general, pressure gradients in the boundary layer both parallel and normal to the surface of the hypersonic body are expected to be negligible, and the temperature gradient along the surface would be negligible compared to that across the boundary layer, except near the nose or the leading edge.

The high temperature boundary layer near the leading edge makes its analysis very difficult. Variations of the gas properties such as viscosity, specific heat, thermal conductivity and so on are so much that they can no longer be treated as constant in the solution of the boundary layer equations of continuity, momentum and energy.

The flow field near the leading edge of the body flying at hypersonic speed has three distinct regions. The strong bow shock wave, the inviscid flow region and the entropy layer. Interactions between these regions influence greatly the amount of heat transfer to the body. The temperature behind the shock wave may or may not be high enough, depending on the flight conditions, to cause the dissociation and ionisation of the air molecules. If these phenomena are absent, the problem is comparatively less difficult and the analysis to assess the heat-transfer

has to take into account only the variations of gas properties with temperature[3,4].

At temperatures above 3000°K, dissociation of oxygen molecules would start and above 7000°K that of nitrogen. Dissociation being an endothermic reaction, the temperature behind the shock wave would tend to drop as the flow proceeds further. Chemical equilibrium would be maintained if the recombination rates of atoms are fast enough at the local temperature and pressure[10]. But it is unlikely that complete thermo-chemical equilibrium would be maintained. The atoms having higher kinetic energy than the molecules would move faster and some of them, at least, would diffuse across the stream-lines to the surface of the body, where recombination may result, depending on the surface conditions. This condition of flow known as 'frozen boundary layer' does not attain thermo-chemical equilibrium.

Besides the higher temperature required for the dissociation of nitrogen molecules than that for oxygen molecules, the former needs greater dissociation energy also, which is 225100 cal per mole. compared to 117960 of the latter[18]. Moreover the dissociation of nitrogen molecule is very slow and appreciable dissociation occurs only at small densities; and hence dissociation of oxygen molecules will predominate over that of nitrogen in flight at hypersonic speeds. In fact Wood[18] found that a significant dissociation of nitrogen molecules would not occur in flight at any altitude at Mach numbers less than 14.

The rates of heat-transfer under these two conditions would be much different, if atoms recombine anywhere in the boundary layer or at the

surface[10]. However, if the wall is non-catalytic to recombination, causing accumulation of atoms of gas, the rate of heat transfer to the body would be much reduced. Efforts have been made to study the catalycity of different materials to the recombination of gas atoms. The degree of catalicity would depend on the nature of surface, local temperature, local pressure and the nature of species. Varying degrees of recombination would give different rates of heat transfer.

The frozen boundary layer has much more influence on the down stream flow field than the equilibrium boundary layer. The large amount of energy locked up with the frozen degree of freedom is likely to change the flow-field downstream substantially.

1.3 Aerodynamic Heat Transfer

In order to assess the magnitude of problem involved in finding the amount of aerodynamic heat transfer, works of many investigators can be quoted, reference of some of which are given in the bibliography[1-18]. They have considered two very distinct aspects of this problem:-

(a) Aerodynamic heat transfer involving no chemical or electronic reactions, such as, dissociation, recombindation, ionisation etc., and

(b) aerodynamic heat transfer in dissociated air flow.

The free stream stagnation temperature in a boundary layer can be expressed as

$$To = T_\infty \left(1 + \frac{\gamma - 1}{2} M_\infty^2\right)$$

This equation shows that temperature in a boundary layer is a function of square of free air stream velocity and hence it rises very

rapidly with increasing speed to very high values. This renders the problem of study of boundary layer characteristics to find the aerodynamic heat transfer at hypersonic speeds difficult in two ways. Firstly, the changes in the physical properties of boundary layer air are so much that they can no longer be treated as constants in the solution of boundary layer equations of conservation of mass, momentum and energy. Secondly, the amount of heat transfer from the boundary layer to the body becomes very large, causing over-heating of the body. This is because the aerodynamic heating is proportional to the difference of wall temperature Tw and the adiabatic wall temperature Taw which is related to the stagnation temperature through a recovery factor r_f, i.e.

$$q = h \quad (Taw - Tw)$$

where

$$Taw = T_\infty \left(1 + r_f \frac{\gamma - 1}{2} M_\infty^2\right) \qquad \ldots (1.3.1)$$

The value of recovery factor r_f, is affected by the Mach number, Reynolds number and the Prandtl number. Though the whole process of compression through the shock wave up to the stagnation point is adiabatic, but non-reversible due to certain losses and hence the stagnant air at the surface of the body never reaches the value of free-stream stagnation temperature. The coefficient of heat transfer h, also is not constant. Thus it can be seen that any attempt to seek a solution of the problem of assessing the magnitude of aerodynamic heat transfer encounters considerable complications of having to treat the physical properties of air, as well as the recovery factor and the film coefficient of heat transfer as variables. This is the reason why there is no straight forward simple expression available to calculate exactly the amount of aerodynamic heat transfer at

different speeds of flight.

The problem, however, has been tackled by different workers by making certain assumptions to render the variables behave as constants under certain specific conditions of flight. For example, based on the results of Von Karman and Tsien[14] and Drainerd and Emmons[12], Eckert and Weise[11] concluded that for a limited variation of Prandtl number from 0.72 to 1.2, Mach number 0 to 10 and temperature exponent of viscosity and thermal conductivity of 0.5 to 1.25 the recovery factor r_f in a laminar flow can be represented approximately by

$$r_f = (Pr)^{\frac{1}{2}}$$

This has also been supported by Kaye[6] for Mach number less than 8. In dissociated air at very high Mach numbers for highly cooled surfaces of a hypersonic body, Kemp, Rose and Detra[16] found that $(Pr)^{\frac{1}{2}}$ represented satisfactorily the recovery factor.

Similar approximation has also been made about the film coefficient of heat transfer, h. For example, after comparing the analytical results of different investigators, including that of Crocco-Conforto and Von Karman and Tsien, Johnson and Rubesin[2] concluded that heat transfer to a flat plate in a laminar flow can be given as

$$Nux = \tfrac{1}{2}\left\{\left(C_{fx} \ (Rex)^{\frac{1}{2}}\right)\right\} (Rex)^{\frac{1}{2}} \ (Pr)^{1/3} \qquad \ldots(1.3.2)$$

where,

$$Nux = \frac{h.x}{k}$$

The subscript x refers to a characteristic length x measured along the length of the plate from the leading edge as well as to the local values of all quantities represented in the equation. The term $\left\{C_{fx} \ (Rex)^{\frac{1}{2}}\right\}$ is important and is amenable to further simplification.

It is found to depend upon Mach number, wall temperature and viscosity temperature exponent n. However, Johnson and Rubesin[2] found that effects of these parameters could be eliminated if all properties were evaluated at a fluid temperature T^1 defined by

$$\frac{T^1}{T_\infty} = 1 + 0.032\,M^2 + 0.58\left(\frac{T_w}{T_\infty} - 1\right)$$

under this condition, quantity $\{C_{fx}\,(Rex)^{\frac{1}{2}}\}$ in equation (1.3.2) takes almost a constant value of 0.664. Equation (1.3.2), therefore becomes,

$$Nux = 0.332\,(Rex)^{\frac{1}{2}}\,(Pr)^{1/3}$$

or

$$q_x = 0.332\,(Taw-Tw)\,(K\,P_r^{1/3})\,\left(\frac{\rho_x u_x}{\mu_x}\right)^{\frac{1}{2}}\left(\frac{1}{x}\right)^{\frac{1}{2}} \quad \ldots(1.3.3)$$

A turbulent flow is more complicated than a laminar flow, yet some attempt has been made to find a suitable relation to assess the aerodynamic heat transfer. For instance, Colburn established a simple expression to find the local heat transfer coefficient without frictional heating. However, his expression,

$$Nux = 0.0296\,(Rex)^{0.8}\,(Pr)^{1/3} \quad \ldots(1.3.4)$$

was found by Crocco and others to be valid also for the frictional heating[2].

Apart from these simplified expressions for the aerodynamic heat transfer, some direct solutions of the problem obtained by solving numerically the boundary layer equations of conservation of mass, momentum and energy are also available. Of course, these solutions also involve one or another assumptions regarding the variation of physical properties, pressure distribution etc., and thereby restricting their use to specific conditions of flight. For example, Nonweiler[3] assumed that variation of specific heats of diatomic gas at high temperature follows the Fowler and Guggenheim

(Statistical Thermodynamics) formula, given by

$$\frac{mc_p}{(mc_p)_\infty} = \frac{9}{7}$$

and treated the body as isothermal with no pressure gradient. He obtained the expression for heat transfer as,

$$q_x = 0.43 \left(\frac{p_\infty}{p_{sl}}\right)^{\frac{1}{2}} U_\infty^2 \left\{ \left(\frac{T_{sl} + C}{T_{sl}}\right) \frac{\rho_{sl}\ \mu_{sl}\ a_{sl}}{x} \right\}^{\frac{1}{2}} \quad (1.3.5)$$

In this expression, a mean Prandtl number equal to 0.782 was used. Now it is well known that the average value of Prandtl number of air at high temperature is about 0.71. If this value of Prandtl number is used, then equation (1.3.5) reduces to

$$q_x = 0.486 \left(\frac{p_\infty}{p_{sl}}\right)^{\frac{1}{2}} U_\infty^2 \left\{ \left(\frac{T_{sl} + C}{T_{sl}}\right) \frac{\rho_{sl} \cdot \mu_{sl} \cdot a_{sl}}{x} \right\}^{\frac{1}{2}} \quad (1.3.6)$$

Theories predicting the aerodynamic heat transfer at speeds causing dissociation of air molecules in the boundary layer, have also been advanced recently by some authors, such as, Lees[8] and Fay and Riddell[10]. Since dissociation of air molecules is an endothermic reaction, it tends to reduce the temperature of the boundary layer air and consequently the amount of heat transfer should reduce. However, since the flow encounters lower temperature and lower pressure as it moves downstream, dissociated air molecules tend to recombine. The recombination is an exothermic reaction and hence the amount of heat transfer increases with the degree of recombination.

Dissociation and recombination further complicate the problem of heat transfer. Hence in order to simplify the problem, Lees[8] as well as Fay and Riddell[10] had to make a number of assumptions about Prandtl number, Lewis number, variation of viscosity etc. Though the validity of their assumptions have no experimental verification, prediction of heat transfer

by their theories have been found to be quite compatible within reasonable limits with the experimental results of Kemp, Rose and Detra[16] and Rose and Stark[17].

Since, these theories of Lees[8] and Fay and Riddell[10] seem to be reasonably accurately predicting the aerodynamic heat transfer in dissociated air, it would be quite justified here to examine, what difference these chemical reactions actually make to the amount of heat transfer. For example, if the stagnation point heat transfer is considered, Fay and Riddell found that effect of dissociation at the stagnation point is to increase the heat transfer by a factor of

$$\left\{ 1 + \left(Le^{0.52} - 1 \right) \left(\frac{Hi}{H} \right)_o \right\} \quad \text{for the equilibrium flow.}$$

and

$$\left\{ 1 + \left(Le^{0.63} - 1 \right) \left(\frac{Hi}{H} \right)_o \right\} \quad \text{for the frozen flow.}$$

These factors show that, the chemical reactions have just a very moderate effect on the rates of heat transfer, because the Lewis number of air is close to unity. If the upper limit of Lewis number Le = 1.4 is taken, these factors give increases of 21 and 25 per cent respectively.

On the other hand if the surface is non-catalytic to atom recombination, dissociation of air molecules would reduce the heat transfer quite considerably, depending upon the degree of dissociation.

In order to bring out more clearly the problem of aerodynamic heating and subsequent rise of temperature of a body, some numerical example will be quite helpful at this stage. All these theories and simplified expressions including others not discussed here, which predict aerodynamic heat transfer differ to a certain extent among themselves, and there has not been enough experimental work to ascertain most exclusively the most

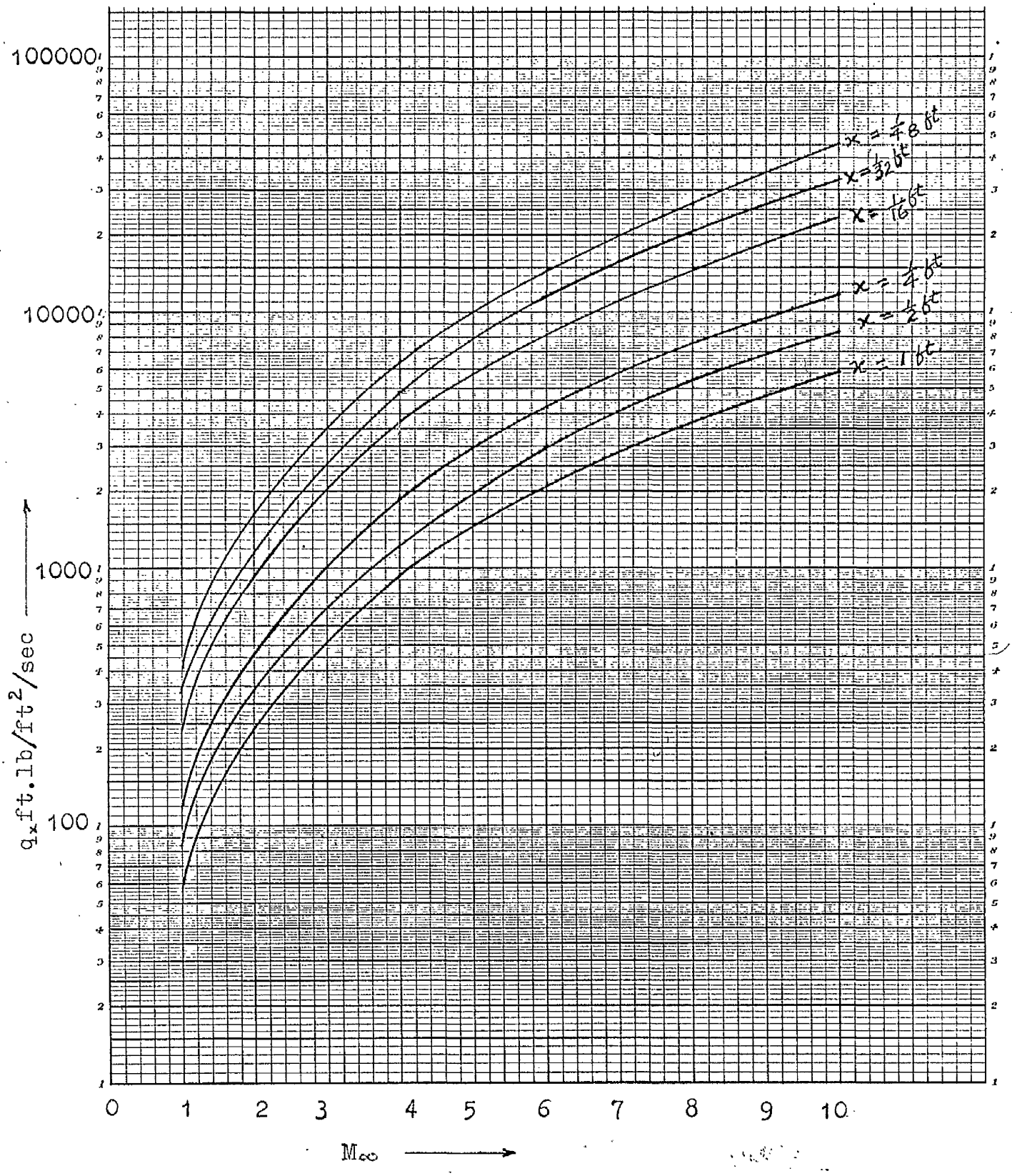

DATA SHEET No. 52 LOGARITHMIC (5 CYCLE) × 60 DIVISION

FIG.1.3.1. Aerodynamic heating rates at a distance x from the nose on a flat plate at different Mach numbers of flight.

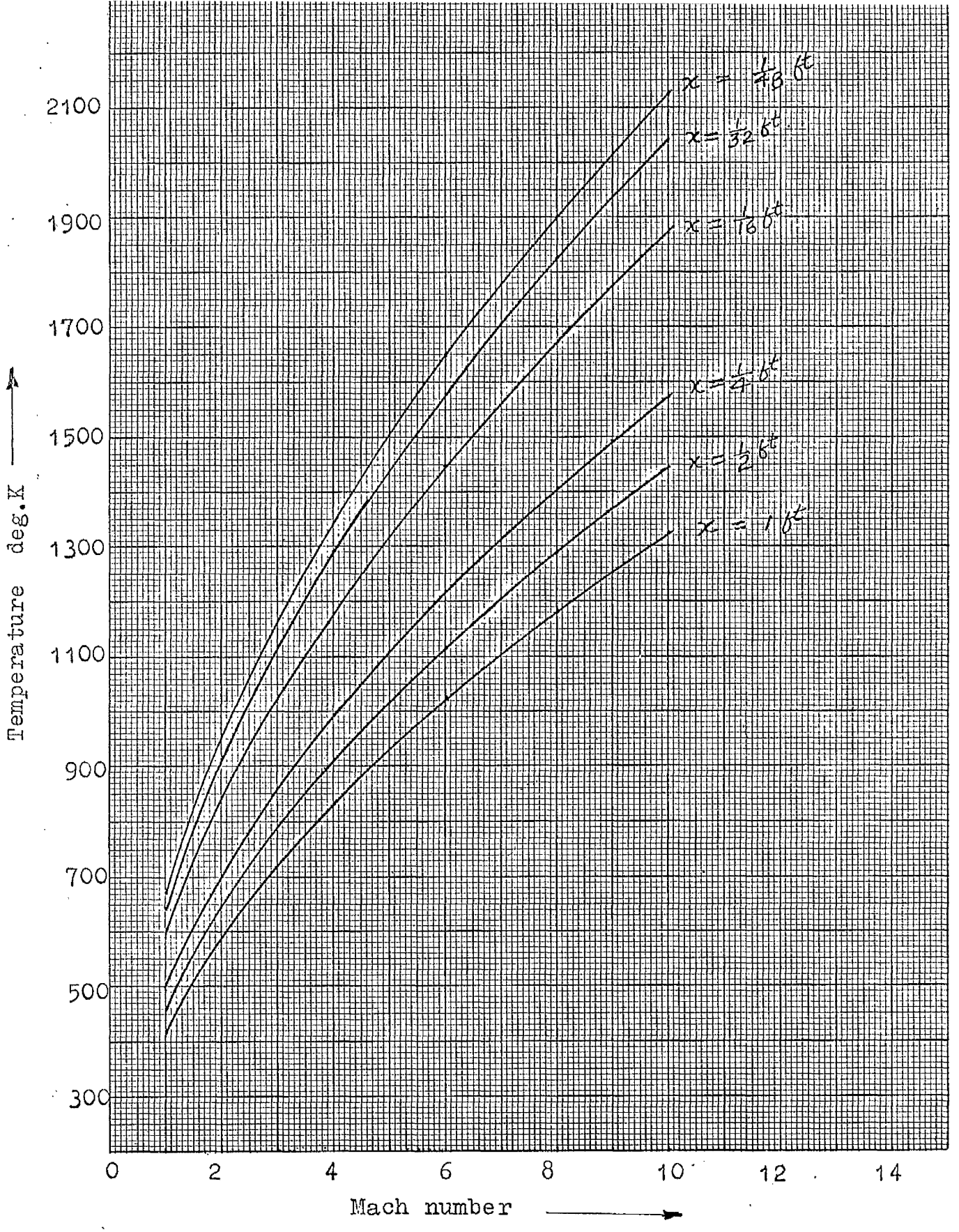

FIG.1.3.2. Radiation equilibrium temperature at a distance x from the nose in a non-cnducting flat plate at different Mach number of flight.

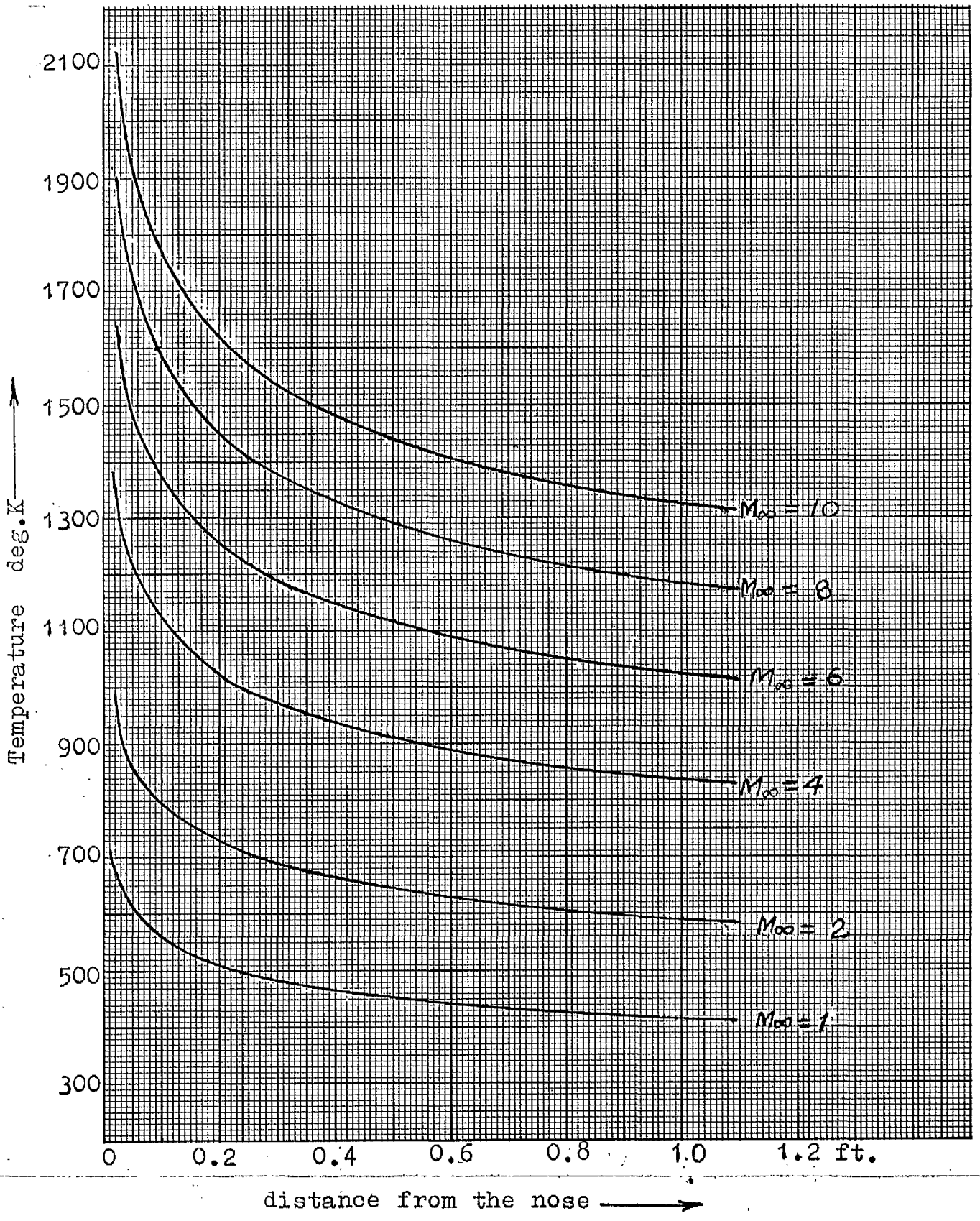

FIG.1.3.3. Radiation equilibrium temperature distribution in a non-conducting flat plate at different Mach number of flight.

accurate one. However, the interest of the present work of finding the order of magnitude of aerodynamic heating can easily be served by any one of them.

Laminar heat transfer data to a flat body fig. (1.3.1) have been calculated by using equation (1.3.6) and "U.S. Standard Atmosphere 1962". A flight at a height of 100,000 ft. has been assumed. Local heat transfer to a point as close as 1/48 ft. from the leading edge has been included.

In order to find out the temperature of the body, the usual procedure of equating the aerodynamic heat input to the radiation cooling has been adopted. An emissity of 0.5 was assumed for the flat plate. The results are plotted in figures (1.3.2) and (1.3.3).

From equation (1.3.1) it is evident that the boundary layer air at the stagnation point will attain a temperature of about $3000^{0}C$ at a flight Mach number of 8 at a height of 100,000 ft. Since the dissociation of oxygen molecules starts at this temperature, prediction of aerodynamic heating above $M_{\infty} = 8$ must include the effects of dissociation and subsequent recombination. But as the data on the degree of dissociation and recombination are not available, their effects have not been included in the graph of figure (1.3.1).

1.4 Discussion

All these theories predict that in a sustained flight at any height at any Mach number, the aerodynamic heating is proportional to $\frac{1}{\sqrt{x}}$ in a laminar flow. This, in turn, implies that heating at the leading edge or nose is infinite. However, this can be proved to be physically impossible due to various reasons. Firstly, the originating boundary layer near the nose is thin due to rarefaction and hence the inhomogeneous

air molecules in that region are capable of transferring only a finite amount of heat energy to the surface[21]. Secondly, interactions between the nose shock wave and the boundary layer and even the minute presence of slip velocity and temperature jump at the surface in the nose region, would tend to reduce the amount of aerodynamic heat transfer[19]. Lastly, for the reasons outlined in section 1.2, the leading edge of all hypersonic bodies has to be radiused to a certain extent. This will lead to a further reduction of aerodynamic heating at the leading edge. In fact, Nonweiler[22] found that for a round nose, the heating becomes inversely proportional to the square root of the nose radius.

There are other considerations as well which adversely affect the validity of these theories to be applied to the nose. For example, the assumption of an isothermal body with no pressure gradient in the boundary layer in all these theories is approximately correct in the down stream region of the body, but not in the nose region, where both the pressure and temperature gradients are expected to be quite considerable. The influence of pressure gradient on the heat transfer coefficient is found to be small, and is negligible, if the flight Mach number is high, but the influence of temperature gradient is not small. In certain cases with temperature gradient considered[13] the increase in the value of heat transfer is sufficient to upset the basis of isothermal surface heat transfer.

Thus it can be seen that theories predicting aerodynamic heat transfer break down at the nose due to its singular behaviour, and hence a precise calculation of amount of aerodynamic heating at the nose can not be made at this stage. However, the fact that nose suffers the maximum heating is beyond dispute and unless, in the absence of any cooling

arrangement, the conductivity of material of the body plays an important role in transferring the heat from the leading edge to the down stream region, radiation equilibrium temperature (fig 1.3.2) in the nose region reaches the working limit of the present day material considerably at a low Mach number of flight.

At this stage, it is evident that the usual assumption of zero heat conductivity (or negligible heat conductivity) gives rise to two serious problems of hypersonic flow :-

(a) The body under such assumption attains considerably a high temperature in the nose region, whereas it remains quite at a low temperature everywhere away from the nose; and

(b) in the nose regions the body maintains a very steep temperature gradient (fig. 1.3.3) and yet, according to the usual assumption, it is not conducting any reckonable amount of heat away from the nose. This appears to be very much unnatural and hence it is quite important to investigate

(i) the role of heat conductivity of material in transferring aerodynamic heat from the nose region to the down stream of the body.

(ii) the subsequent nose temperature, and

(iii) the actual temperature distribution in the body.

The interests of the present work, therefore would be concentrated to the study of the nose region mainly. For reasons, outlined in section 1.2, the nose region is expected to maintain the laminar flow and hence

laminar aerodynamic heating would be assumed in the further analysis of the temperature distribution.

CHAPTER II

ONE-DIMENSIONAL THEORY OF HEAT CONDUCTION IN A BODY UNDER AERODYNAMIC HEATING

2.1 Introduction

The study of the effect of heat conduction along the skin of a body subjected to aerodynamic heating has not attracted much attention. This is mainly because at subsonic and supersonic speeds of flight the problem of over-heating of the nose does not arise and hence the aircraft designers did not bother to look to this problem. But this is becoming more important with the hypersonic flight of more recent origin.

Nonweiler[21], first time, in 1952, envisaged that conductivity of material is very important in providing an effective means of cooling the leading edge. After making some analysis[19], he found that the maximum temperature attained by the leading edge is given by,

$$To = 1.15 \left(\frac{Q^4}{\epsilon^3 \sigma^3 kt} \right)^{1/13}$$

Later on, after making more precise approach [22] he found that for a uniform thickness conducting skin, leading edge temperature can be represented by

$$To = 1.306 \left(\frac{Q^4}{\epsilon^3 \sigma^3 kt} \right)^{1/13} \qquad \ldots(2.1.1)$$

Using equation (2.1.1) and the heating data of the example considered in section 1.3 and assuming a conducting skin of thickness 0.1 ft. and conductivity 10 ft.lb/ft/sec/$^\circ$R the maximum leading edge temperature comes to about 1600°C at $M_\infty = 10$, even for a most severe aerodynamic heating

rate due to such a low altitude of flight as 100,000 ft. for hypersonic flight. The adiabatic wall temperature of the air at this condition of flight is about 7000°C. Thus, one can see that provided equation (2.1.1) holds good, the leading edge temperature of the hypersonic body is much lower compared to the adiabatic wall temperature of the air. Under the same condition of flight, a point at a distance of 1/48 ft. from the leading edge of a non-conducting hypersonic body was shown in figure 1.3.3 to reach a temperature of 1850°C and hence the leading edge temperature of that body would be certainly much higher.

From the numerical example considered in this section, it appears that though heat conductivity of the skin reduces the leading edge temperature yet it is so high that it does not have much practical importance. But, it should be remembered that an altitude of 100,000 ft. for a hypersonic flight at $M_\infty = 10$ is too low from the point of view of aerodynamic heating. In fact, if the altitude of flight is increased to 200,000 ft. the aerodynamic heating would be reduced to 1/9th and consequently the leading edge temperature would come down to about 800°C which will be quite well within the temperature limit of many alloys.

In the following sections of this chapter, details of Nonweiler's analytical results of the leading edge temperature and temperature distributions in a conducting skin will be considered. Different geometry of the conducting skin and their effects on the leading edge temperature will also be discussed.

2.2 Basic Equations of Heat Balance.

Even though, no hypersonic body should have a sharp leading edge, yet it has to be tapered down to a small thickness near the leading edge. The conducting skin in that region, therefore, would be thin compared to its conducting length. Under this condition, temperature across the thickness of the skin can be taken as uniform, and hence the heat can be assumed to be conducting only in a longitudinal direction, provided that span of the hypersonic body is big enough so as not to interfere with the heat conduction in that direction.

The aerodynamic heating would be identical on either surface of a body, symmetrical to the longitudinal axis. Though, as discussed in Chapter I strictly neither the body in hypersonic flow remains isothermal nor pressure remains constant on the surface, nor any of the physical properties of air remains constant, yet for all practical purposes of finding the aerodynamic heating, variation in the temperature of the body, pressure and the physical properties of air along the length of the body can be assumed to be negligible. Under this condition, local aerodynamic heating (equations 1.3.3 or 1.3.6) in a sustained flight at any altitude can be given as

$$q_x = \frac{Q}{(x)^{\frac{1}{2}}} \qquad \ldots(2.2.1a)$$

where Q is a constant.

If the solar heat radiation is neglected, a steady state heat balance equation of a body in hypersonic flow, can be written down as

$$\frac{d}{dx}\left[\left(kt\,(x)\,\frac{dT}{dx}\right)\right] = \varepsilon\,\sigma\,T^4 - \frac{Q}{(x)^{\frac{1}{2}}} \qquad \ldots(2.2.1)$$

Where the term on the left side of the equation, represents the heat conducted away along the skin, and the first term on the right is the heat radiated away from the surface of the body.

Nonweiler[22] has considered different aspects of this equation in detail and solved it for different geometry of the conducting skin. Very briefly, some aspects of his solution will be described here.

In order to understand the effects of variation of one quantity in equation (2.2.1) over the other, it would be preferable to render them non-dimensional.

To do this, Nonweiler defined basic units of length ℓ and absolute temperature c as

$$\ell = \left(\frac{K^4}{\varepsilon \sigma Q^3}\right)^{2/5}$$

$$c = \left(\frac{Q^2}{\varepsilon \sigma k}\right)^{1/5} \qquad \ldots\ldots(2.2.2)$$

Using the asterisked signs to denote the quantities, measured in these basic units, the conduction equation (2.2.1) becomes

$$\frac{d}{dx^*}\left(t^* \frac{dT^*}{dx^*}\right) = (T^*)^4 - (x^*)^{-\frac{1}{5}} \qquad \ldots (2.2.3)$$

The cross sectional area of the conducting material between the plane x = constant and x = o may be given as,

$$A(x) = \int_o^x t(x)\, dx \qquad \ldots (2.2.4)$$

If x_r, T_r denote the reference values of length and temperature and t_r and A_r the reference values of thickness and area in case of the geometrically similar shapes, then using Greek symbols, quantities can be made non-dimensional as follows

$$\xi = \frac{x}{x_r} \quad , \quad \tau = \frac{t}{t_r}$$
$$\nu = \frac{A}{A_r} \quad , \quad \phi = \frac{T}{T_r} \qquad \ldots(2.2.5)$$

provided that the reference quantities obey the relations

$$A_r^{*} T_r^{*} (x_r^{*})^{-3} = t_r^{*} T_r^{*} (x_r^{*})^{-2} = (T_r^{*})^{4} = (x_r^{*})^{-\frac{1}{2}} \qquad \ldots(2.2.6)$$

Using equation (2.2.5), equations (2.2.3) and (2.2.4) can be deduced to

$$\frac{d}{d\xi}\left\{ \tau \frac{d\phi}{d\xi} \right\} = \phi^{4} \xi^{-\frac{1}{2}} \qquad \ldots (2.2.7a)$$

$$\frac{d\nu}{d\xi} = \tau \, , \quad \nu(o) = o \qquad \ldots (2.2.7b)$$

Equation (2.2.7a) is the non-dimensional form of the heat balance equation. On integration, equation (2.2.7a) gives the non-dimensional thickness as

$$\tau(\xi) = \frac{d\xi}{d\phi} (\phi^{4} \xi^{-\frac{1}{2}}) \qquad \ldots (2.2.8)$$

The relations given in equation (2.2.6) is further extended to relate one reference quantity with others as follows :-

$$\lambda_r = (x_r^{*})^{-\frac{5}{8}} = (t_r^{*})^{-5/13} = (A_r^{*})^{-5/21} = (T_r^{*})^{5}$$
$$(x_r^{*}) = (\lambda_r)^{-8/5} = (t_r^{*})^{8/13} = (A_r^{*})^{8/21} = (T_r^{*})^{-8}$$
$$(t_r^{*}) = (\lambda_r)^{-13/5} = (x_r^{*})^{13/8} = (A_r^{*})^{13/21} = (T_r^{*})^{-13}$$
$$(A_r^{*}) = (\lambda_r)^{-21/5} = (x_r^{*})^{21/8} = (t_r^{*})^{21/13} = (T_r^{*})^{-21}$$
$$(T_r^{*}) = (\lambda_r)^{1/5} = (x_r^{*})^{-\frac{1}{8}} = (t_r^{*})^{-1/13} = (A_r^{*})^{-1/21}$$

$\ldots(2.2.9)$

where $\lambda_r = \frac{x_r}{t_r}$, a fineness ratio.

Equation (2.2.9) gives a wide range of solutions and shows precisely how variation of one quantity effects the others. For example, the temperature of a uniform thickness skin is affected by the twenty-first root of the area, thirteenth root of the thickness and eighth root of length. Thus one can see that variation of conducting skin length, effects the temperature much more than that of area.

All the reference quantities in equation (2.2.9) are measured in terms of the basic units of length ℓ and temperature c, which in turn depend on values of ε, k and Q. With the flight conditions known, ε, k, and Q will be known and so will be ℓ and c. Then any solution of equation (2.2.5) can be applied to give one of the reference quantity and then with the help of equation (2.2.9) other quantities can be found out.

2.3 Temperature Distribition in a Conducting Skin of Uniform Thickness.

When the conducting skin has uniform thickness, i.e. $\tau = 1$, the non-dimensional heat balance equation (2.2.7a) reduces to

$$\frac{d^2\phi}{d\xi^2} = \phi^4 - \xi^{-\frac{1}{8}} \qquad \ldots(2.3.1a)$$

and equation (2.2.7b) to

$$\frac{d\nu}{d\xi} = 1 \quad , \quad \nu(o) = o \qquad \ldots(2.3.1b)$$

The boundary conditions are

$$\frac{d\phi}{d\xi} = o \text{ at } \xi = o \text{ and } \xi = \Lambda \qquad \ldots(2.3.2)$$

Equation (2.3.1a) is a non-linear second order differential equation for which there is no known analytical solution. Using the boundary conditions equation (2.3.2) Nonweiler[22] solved equation (2.3.1a) numerically by assuming various values of ϕ_o at $\xi = o$ and proceeding in the direction of increasing ξ, until $\frac{d\phi}{d\xi}$ reversed in sign. A graph of some typical solutions is reproduced in figure (2.3.1) from his work[22]. In figure (2.3.2) ϕ_o is shown as a function of Λ from which it is evident that for $\Lambda \rightarrow \infty$, ϕ_o reaches the asymptotic value of 1.306, a figure which it approaches with a reasonable accuracy for all practical purposes for values of $\Lambda \geq 2$. In figure (2.3.3) reproduced from Nonweiler's work[22], the cross-sectional area A of the conducting skin has been plotted against the nose temperature To for various selected values of fineness ratio $\frac{L}{t}$ and for fixed values of the thickness.

In order to find a relation between the minimum nose temperature To and the cross-sectional area A, first, an expression for the non-dimensional area ν can be derived as follows:-

Using equations (2.2.5) and (2.2.9),

$$\nu = \frac{A}{A_r} = \left(\frac{A}{\ell^2}\right)\left(\frac{To}{c}\right)^{21} = \Lambda\left(\phi_o\right)^{21} \qquad \ldots(2.3.3)$$

or $$\frac{To}{c} = \phi_o \Lambda^{1/21} \left(\frac{\ell^2}{A}\right)^{1/21}$$

Nose temperature, To will be minimum when $\phi_o \cdot \Lambda^{1/21}$ is minimum. Nonweiler[22] found that for $\Lambda = 0.65$, $\phi_o \cdot \Lambda^{1/21}$ was minimum and equal to 1.308. Hence,

$$\frac{To}{c} = 1.308 \left(\frac{\ell^2}{A}\right)^{1/21} \qquad \ldots(2.3.4)$$

gives the minimum nose temperature corresponding to a conducting skin Area A.

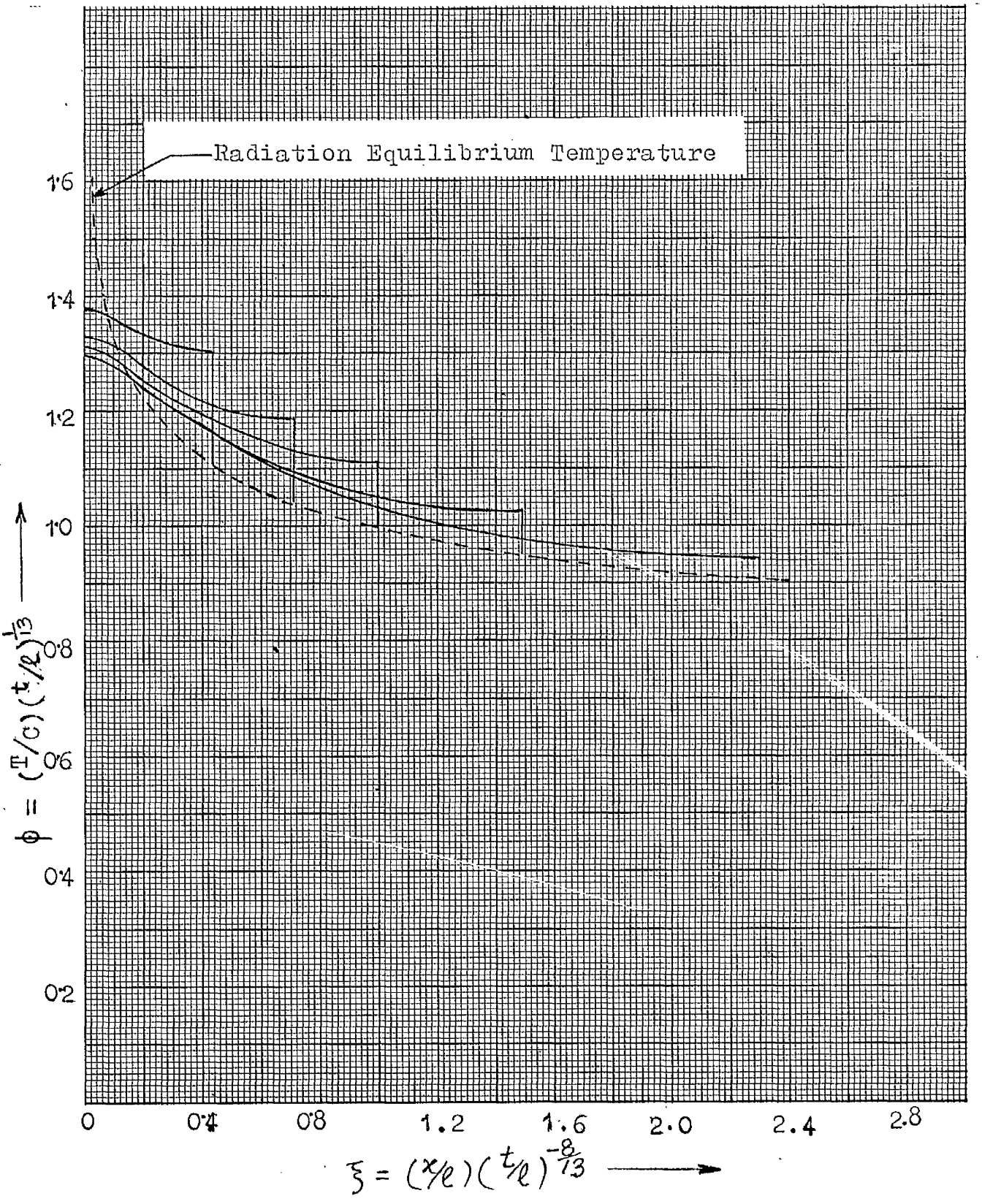

FIG. 2.3.1

Some typical temperature distributions over shapes of Uniform thickness.

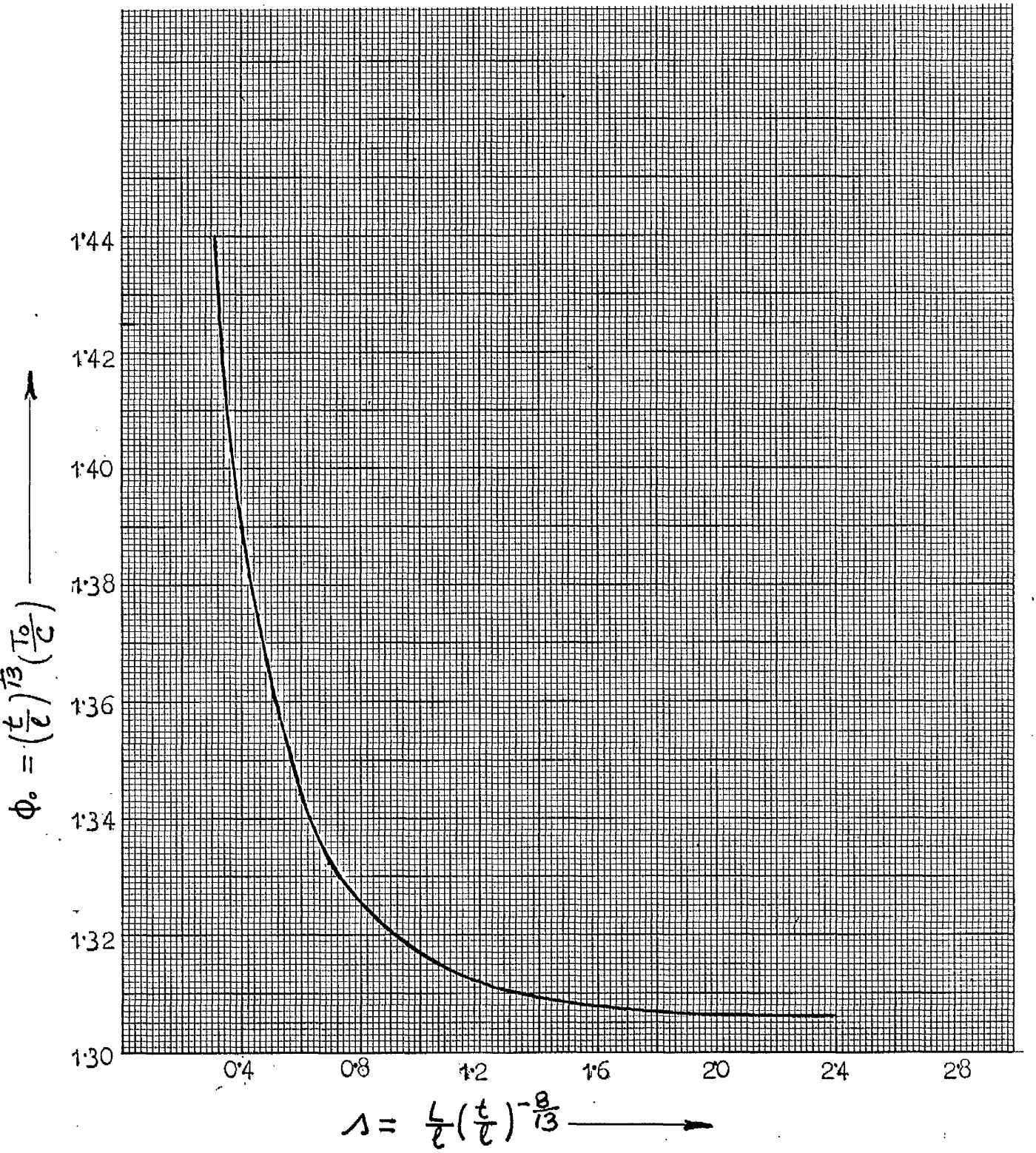

FIG.2.3.2.

Variations of nose temperature with length of surface having uniform thickness.

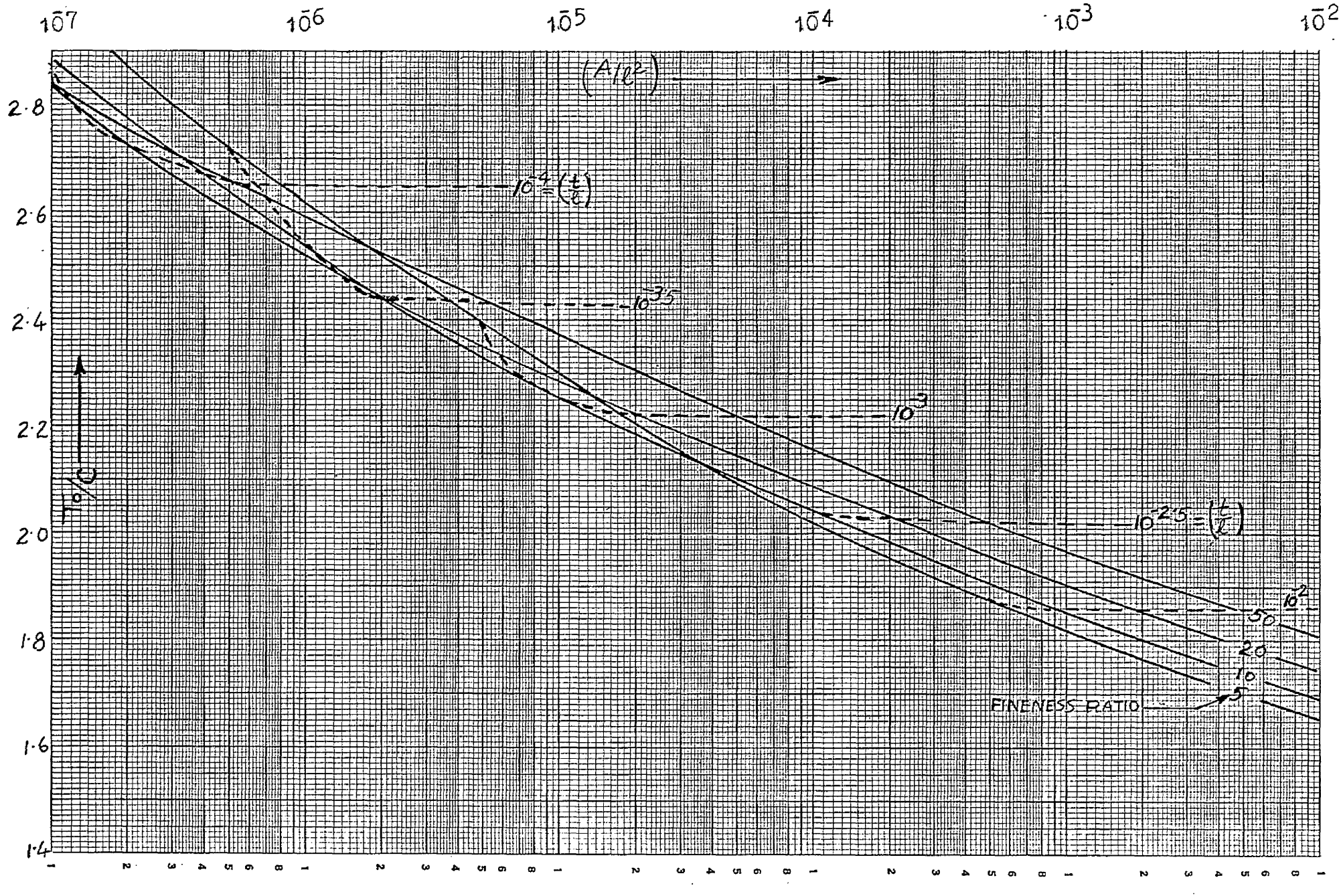

FIG. 2.3.3. Nose temperature of surfaces having uniform thickness.

An useful relation between the length of the conducting skin L and nose temperature To can also be obtained as

$$\lambda = \frac{L^2}{A} = \left(\frac{\lambda^2}{\nu}\right)\left(\frac{To}{c}\right)^5 \qquad \ldots(2.3.5)$$

Using equations (2.3.3), equation (2.3.5), is further deduced to

$$L = \ell . \lambda . \left(\frac{c}{To}\right)^8$$

$$\text{or} \quad L = \lambda \left(\frac{Q}{\varepsilon \sigma To^4}\right)^2 \qquad \ldots (2.3.6)$$

Since φ_o becomes asymptotic to a value of 1.306 for $\lambda \geq 2$ (vide figure 2.3.2), a relation for minimum nose temperature independent of cross-sectional area A, but still involving the conducting skin thickness t can be derived as follows:-

Using equation 2.2.9

$$\Phi_o = 1.306 = \left(\frac{t}{\ell}\right)^{1/13}\left(\frac{To}{c}\right)$$

or

$$To = 1.306 \left\{\frac{Q^4}{(\varepsilon\sigma)^3 kt}\right\}^{1/13} \qquad \ldots(2.3.7)$$

which is valid for $\lambda \geq 2$.

Under this condition, equation (2.3.6) reduces to

$$L_{min} = 2\left(\frac{Q}{\varepsilon \sigma To^4}\right)^2 \qquad \ldots(2.3.8)$$

where L_{min} is the minimum length of the conducting skin required to give a minimum nose temperature To given by equation (2.3.7). Any decrease in the length given by equation (2.3.8) will raise the nose temperature but length greater than L_{min} will have no appreciable effect on the nose temperature.

In order to get a picture of numerical magnitudes of nose temperature, conducting skin length and area, involved in a hypersonic flight, a numerical example of a flight at an altitude of 200,000 ft. can be considered. An average conductivity of 10 ft.lb./ft./Sec/°K can be taken as representative of the conductivities of many alloys. In general, the metals and their alloys do not have high radiant heat emissivity, but a value of 0.9 can be taken on the assumption that leading edges are coated black with some suitable paint. Using equation (1.3.6), the value of Q at M_∞ = 10 comes to 875 ft.lb./ft.$^{3/2}$/Sec. This gives a minimum nose temperature To = 938°K, if a conducting skin of thickness 0.1 ft. is assumed. From equation (2.3.8), a minimum length of 2.5 inch of the conducting skin is obtained, thus, yielding a conducting skin cross-sectional area of 3.00 sq.inch. in all.

If, however, the emissivity is reduced to 0.45 i.e. half of what has been taken in the example above, the nose temperature becomes 1100°K, an increase of about 17% only. The effect of the thermal conductivity on the nose temperature is even smaller. For instance, if the thermal conductivity of the conducting skin is reduced to half i.e.5 ft.lb/ft./sec/°K, the nose temperature increases to 989°K, an increase of about 5.4 per cent only.

The quantity which maximum influences the nose temperature is the aerodynamic heating itself, which will depend both on the speed as well as other conditions of flight, such as altitude etc. If the speed of flight is increased by 50 per cent at the same altitude i.e. M_∞ = 15 in the example under consideration, the new value of Q becomes 1968 ft.lb/ft.$^{3/2}$/Sec. This will raise the nose temperature to 1204°K, an increase of 28.3 per cent.

2.4 Discussion

One might argue that in the beginning of a hypersonic flight, the steady state condition of heat transfer will not be reached to allow the equation (2.2.1) to hold good, and there will be a tendency to 'shoot' up the nose temperature very quickly due to severe aerodynamic heating. True, but during the transient state, though, there will be a tendency to raise the nose temperature to a high value, yet the value of this transient nose temperature will not go beyond the one for the steady state, because, as soon as the temperature gradient builds up in the nose region the skin would start conducting heat away from the nose region to the downstream part of the hypersonic body.

There is another very relevant question as to how the geometry of the conducting skin would effect the nose temperature of a hypersonic body. This question can easily be examined in the light of Nonweiler's[22] solutions for different shapes of conducting skins. He considered three more different cases :-

(a) linear temperature gradient in a conducting skin,

(b) temperature distribution in a wedge-shaped nose,

and

(c) optimum shape of a conducting skin with a minimum cross-sectional area for a stipulated nose temperature, and found the solutions for the minimum nose temperature as

$$\frac{To}{c} = 1.292 \left(\frac{\ell^2}{A} \right)^{1/21} \qquad \ldots(2.4.1)$$

$$\frac{To}{c} = 1.341 \left(\frac{\ell^2}{A} \right)^{1/21} \qquad \ldots(2.4.2)$$

and

$$\frac{To}{c} = 1.286 \left(\frac{\ell^2}{A} \right)^{1/21} \qquad \ldots(2.4.3)$$

respectively. Comparing equations (2.4.1) to (2.4.3) with equation (2.3.4), one finds that the optimum shape gives the minimum nose temperature for a given area of the conducting skin. The uniform thickness skin gives about 1.7% higher nose temperature than the optimum shape. The highest nose temperature is obtained in wedge shaped nose which is 4.2% higher than that of optimum shape.

So small difference in nose temperatures predicted by the different shapes of the conducting skin has great importance from the point of view of design of the aircraft. Because it leaves the aircraft designer much scope to manoeuvre for designing the shape of the leading edge to suit other requirements. From the numerical example considered in section 2.3, it can also be seen that the required length and area of the conducting skin are so small that they create no difficulty to the designer.

EXPERIMENTAL PLANNING AND LAYOUT

3.1 Introduction:- A hypersonic flow tunnel equipped to provide a continuous, constant, hypersonic flow at different Mach numbers for a sufficient period of time to establish a steady state of temperature in a hypersonic body placed inside it, would have been the best way to study the resultant temperature distribution. This type of apparatus not being available in the department, some means have to be found to simulate the aerodynamic heating according to the $\frac{Q_1}{x^{\frac{1}{2}}}$ distribution. Among a number of possibilities, radiant heating is by far the simplest. In order to eliminate convection, the testing body is best to be placed in an evacuated chamber. This leaves whether it will be better for the heat source to be outside or inside the same chamber. In either case, the walls of the chamber must be kept cool in order to reduce the background radiation.

3.2 Heating the Model.

The conducting skin model can not be provided with a contact heating, as it will not allow the model to emit its own heat radiation which constitutes a means of its cooling (vide the theory in section 2.2). The radiant heating, however, offers a simple means to heat the model.

A simple way to provide the radiant heat energy from the heat source will be to hold the model parallel to the source, a little apart, so that it receives mostly the normal heat radiation. In order to emit the radiant heat energy similar to $\frac{Q_1}{x^{\frac{1}{2}}}$, the source should be able to generate the heat energy in the same pattern. This can be done conveniently by arranging a number of electrical conductors, parallel to each other, in such a way that their electrical resistance follows $\frac{Q_1}{x^{\frac{1}{2}}}$. The ends of these conductors can be

joined to form a continuous circuit so that the same current passes through them. A plain reflector arranged above the conductors will reflect back heat to the model placed below the conductors and thus will tend to even up the heat distributed by the direct radiation from the conductors. However this will not produce a very even curve of heat distribution, conforming to $\frac{Q}{x^2}$, because the portions of the model lying between two consecutive conductors will not receive sufficient heating.

In order to avoid the uneven-ness in the heat distribution pattern, a still better method would be to use a curved reflector with a single heating element. Analytical design side of this type of reflector will be discussed in detail in the next chapter.

3.3 Arrangement of the Model and Heat Source.

The model has to be kept inside a vacuum chamber to eliminate the interference by convection. But the heat source with reflector can be arranged outside the chamber, with a provision on its top surface of a sealed window of some such material which allows the maximum transmission of the infra red radiation to the model. However, this arrangement will have two difficulties to overcome:-

i. Refractivity of the material of the window will cause a change in the direction of the heat rays, and this will effect the heat distribution pattern to a certain extent, and,

ii. unless cooled by some suitable means, the window pane will tend to get heated up, which, in turn, will interfere with the heat distribution.

The thinner window plate will have higher transmission of heat rays than the thicker one, but for strength to stand the atmospheric load due to

the chamber being evacuated, a certain thickness of the plate depending on the overall size of the window, will be necessary. If the reflector with the heat source is mounted inside the chamber, there will be no difficulties although, this requires a bigger vacuum chamber and a bigger set of vacuum pump to evacuate it.

3.4 The Model

3.4.1 Size of the Model:- The theory in section 2.2 assumed that there is no variation of temperature across the thickness of the conducting skin. This necessarily means that the conducting skin has to be thin. In other words, theory will be valid for the large fineness ratios, which implies a large size of the model for a given thickness. But a larger size of the model would need a larger vacuum chamber and a larger set of vacuum pump, and hence higher costs. On the other hand for the convenience of fixing the thermocouples, at least $\frac{1}{8}$inch thick skin would be preferable. Taking these points into consideration, it was decided to use a 6 inch long conducting skin model. By varying the thickness from 1 to $\frac{1}{8}$ inch, this would give fineness ratios of 6 to 48.

The theory in section 2.2 also assumes that span of the conducting skin in transverse direction is large enough, so as not to interfere with the one dimensional heat conduction in a longitudinal direction. In order to achieve this objective, the model with at least 12 inch width will be required for a 6 inch long conducting skin model, so that along the central section, where temperature distribution is to be measured, any interference from the free ends will be negligibly small.

3.4.2 Properties of the Model Materials.

The conducting skin models have to be made from such materials which can maintain their shapes at the temperature of their applications of about 800°K (vide section 3.4.3) in a high vacuum of about 10^{-4} torr (vide section 3.6) without suffering any deformation. They should also have a suitable low vapour pressure, since the evaporation of material at the temperature of application in high vacuum may alter the surface properties as well as increase the chamber pressure. It is essential that they have suitable thermal conductivities appropriate to the theory for a stipulated range of temperatures in the models, subject to the available heat from the heating element (vide section 3.4.3).

Besides, the material should be isotropic. A less degassing materials will be preferable from the point of view of vacuum.

3.4.3 Estimation of the Heat Conductivity of the Model Material:-

The theory in section 2.3, predicts useful solutions of the heat balance equation (2.3.1a) in the range of $\Im = 0.42$ to $\Im = 2.3$, the corresponding values of Φ being 1.3 and 0.94 respectively. Since the stipulated length of the conducting skin model is 6 inches, its uniform thickness can be taken anything between 1 and $\frac{1}{8}$ inch, giving fineness ratios of 6 to 48. For the preliminary selection of the model materials, a value of 0.8 can be taken for the emissivity. In the theory, ambient heating has been ignored on the assumption that it is negligible compared to the aerodynamic heating at hypersonic speeds. Hence, if the effects of environment on the test is not to be appreciable, the tests should aim at high temperatures of the model, which also implies high rates of heating. But the higher is the model temperature, the smaller will be the range of

materials, suitable for the model. A simple calculation shows that effect of the environment is not more than 2% if the mean temperature of the model is about 500°C. Hence a temperature of 800°K at the leading edge of the model can be assumed in the preliminary calculation to estimate the heat conductivity of the material.

Using equation (2.2.2) the relations for ξ and ϕ can be expressed in terms of physical quantities themselves, i.e.

$$\xi = \left(\frac{x}{\ell}\right)\left(\frac{t}{\ell}\right)^{-8/13} = x\left(\frac{\varepsilon\sigma Q^3}{k^4 t^4}\right)^{2/13} \qquad \ldots(3.4.1)$$

and

$$\phi = \left(\frac{T}{c}\right)\left(\frac{t}{\ell}\right)^{1/13} = T\left\{\frac{(\varepsilon\sigma)^3 kt}{Q^4}\right\}^{1/13} \qquad \ldots(3.4.2)$$

Equations (3.4.1) and (3.4.2) yield the following expressions for k and Q :-

$$k = \frac{1}{\xi^2 \phi^3}\left\{\left(\frac{\varepsilon\sigma}{t} x^2 T^3\right)\right\} \qquad \ldots(3.4.3)$$

and

$$Q = \left(\frac{T}{\phi}\right)^{13/4}\left\{(\varepsilon\sigma)^3 kt\right\}^{1/4} \qquad \ldots(3.4.4)$$

Using equations (3.4.3) and (3.4.4) and figures (2.3.1) and (2.3.2) values of k and Q have been calculated for the lower and upper useful limits of ξ = 0.42 and 2.3 respectively and the model thicknesses of $\frac{1}{8}$ and 1 inch. They are given in table 3.4.1

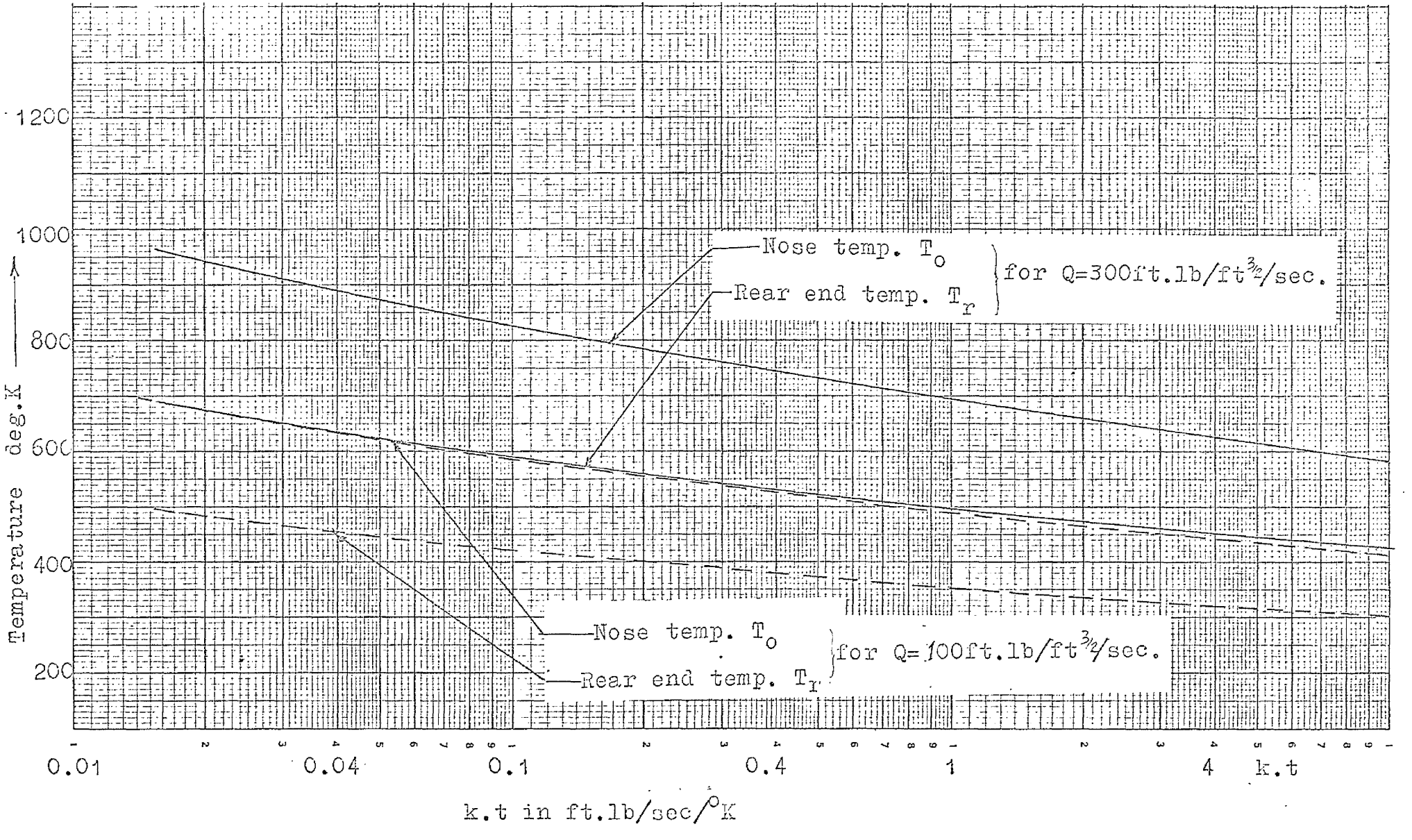

FIG.3.4.1. The minimum nose and rear end temperatures vs. the product k.t.

TABLE 3.4.1

Thermal conductivity of model materials.

$\xi = \lambda$	$\phi = \phi_o$	L (inch)	t (inch)	To (°K)	Q ft.lb/ft$^{3/2}$/sec	k ft.lb/ft/sec/ok
0.42	1.382	6	$\frac{1}{8}$	800	382.35	82.4
0.42	1.382	6	1	800	382.35	10.3
2.3	1.306	6	$\frac{1}{8}$	800	262.2	3.26
2.3	1.306	6	1	800	262.2	0.41

From table 3.4.1 it can be observed that the range of heat conductivity of model materials is so large that from the point of view of conductivity, almost all metals qualify for the conducting skin models, provided the required amount of heat is available. The choice of a particular metal will depend on the thickness of the model and the value of ξ at which experiment is to be carried on.

However, comparatively lower heat conductivity of the model material will be necessary, if the experiment is to be carried on to test the validity of the theory for the larger value of ξ . This can be seen from table 3.4.1 as well as from figure 3.4.1 in which the temperatures at the leading edge and the rear end of the skin have been plotted against the product k.t. The values in this figure refer to the minimum value of ϕ_o (equation 2.3.7)

and the corresponding value of ϕ at the rear end taken from figure 2.3.1. Figure 3.4.1 also shows that as the product kt and hence the thermal conductivity k for a given thickness t increases, the difference between the nose temperature and the rear end temperature decreases, rendering the experimental verification of the theory more vulnerable to the experimental error. Later on, (section 5.5) it has also been found that only a limited amount of heat is available from the heating elements due to temperature limits of their materials, thus restricting the use of only a low conductivity materials for the model.

All pure metals have high heat conductivity. For the low range of conductivities, one has to look to alloys and ceramics. Amongst the alloys, especially 18/8 stainless steel, nichrome and monel metal have low values of 4.0, 2.8 and 4.7 ft.lb/ft./sec/^{o}k respectively.

Though from the point of view of the thermal conductivity, ceramics offer a good prospect for conducting skin models, but for accurate manufacturing. The conductivities of different types of ceramics vary almost from 0.3 to 1.5 ft.lb/ft./sec/^{o}k. Besides, the ceramic bodies having the same ingredients, will have different heat conductivities, depending on the structure. The glassy matrix has lower conductivity than that of crystalline phase. The structure of the fired body will vary with the sizes of the particles, degree of packing, mixing and firing conditions. Thus to maintain a particular thermal conductivity, all these variables have to be controlled.

During the process of drying and firing; ceramic bodies undergo a lot of shrinkage, creating problems of maintaining the size accurately and danger of cracks. To machine ceramic bodies, after they are fired at high temperatures, is not as easy as to machine a metallic body.

3.5 Estimation of the Heating Power Required from the Heat Source.

Roughly speaking, Q equal to 400 ft.lb/ft.$^{3/2}$/sec (vide table 3.4.1) would be required to get a nose temperature of 800^{o}k on the model. From this, the total heat input to the 6 inch long model can be estimated as follows:-

$$\text{Total heat} = \int_0^L \frac{Q}{x^{\frac{1}{2}}}\, dx$$

$$= 2\, Q\, L^{\frac{1}{2}}$$

$$\simeq 565 \text{ ft.lb/ft.span/sec.}$$

If the reflector covers about 2/3 surface of the heating element, its heat output should be 850 (= 565 x 3/2) ft.lb/ft.length/sec. which is about 1140 watts in electrical units.

Some heat would be absorbed by the reflector and some would be wasted outside the model. Thus the actual heat utilized by the model can be assumed to 30 to 40 per cent of that emitted by the element. Hence the net power of the heating element per ft.length can be estimated to the order of 3 to 3.5 k. watts.

3.6 Order of Magnitude of Vacuum Required.

The convective heat loss from the conducting skin has not been considered in the theory in sections 2.2 and 2.3. Hence, if this loss is allowed to occur in the test models, it will interfere with the heat balance of the skin, in which the loss of heat by radiation only has been considered. The convective heat loss in air is not negligible as well, because, depending on the difference of temperatures of the model and its surrounding, it may be as high as its radiation heat loss itself.

The results plotted in figure 25-3 of "Heat Transfer[27]" shows that free convection becomes insignificant if the product of Grashof number and

Prandtl number is less than 100. With the stipulated temperatures of 800°K of the model, this requires that the air density be reduced to the order of 10^{-5} to 10^{-6} lb/ft.^{3} which in turn implies a vacuum of the order of 10^{-2} to 10^{-3} torr. A still higher vacuum of the order of 10^{-4} to 10^{-5} torr will be advantageous as it will further reduce the free molecular heat transfer.

CHAPTER IV

DESIGN OF THE REFLECTOR

4.1 Introduction:-

In order to provide a heating on a conducting skin model, similar to the aerodynamic heating, it was decided (vide section 3.2) to design a reflector. To do it, the basic equations of the reflector were derived in section 4.2 and a preliminary study of the effects of variations of parameters of the reflector was made and conclusions drawn in section 4.3. It was found that, though the basic equations of the reflector in section 4.2 were same, different combinations of signs of parameters yielded three different types of reflectors:-

(a) Single and direct ray reflector:- The reflected rays do not cross each other before they are incident on the plane of irradiation and the point of incidence of reflected rays starts at one end of the irradiated plane for the initial value of θ and moves on in one direction only, as the reflector profile is traced over by varying the value of θ .

(b) Single and crossed ray reflector:- This is the same as above, but the reflected rays cross each other before they are incident on the plane of irradiation, and,

(c) Composite reflector:- Up to a certain value of θ the point of incidence of the reflected ray moves in one direction only on the irradiated plane and then it reverses its direction for further variation in θ . This in effect, results in allowing any one point of the irradiated plane to receive reflected rays from two completely separate portions of the reflector profile.

Effect of finite size of the heating element was also taken up. Some of the reflectors were designed with the help of computer and tested both analytically and experimentally to assess their performances. When the performances of these reflectors were not found as good as desirable, a multi-curve reflector was designed with the help of a computor. It was then constructed, and tested.

4.2 The Reflector Profile :-

As discussed in Chapter I, the coefficient of heat transfer at a point on a body with laminar boundary layer is inversely proportional to the square root of its distance from the nose, i.e.

$$h \propto x^{-\frac{1}{2}}$$

$$\text{or} \quad h = \frac{Q}{x^{\frac{1}{2}}} \qquad \ldots(4.2.1)$$

Where Q is some constant whose value depends on the flight conditions.

Since all hypersonic bodies have to be rather blunt nosed and because the originating boundary layer at the nose is thin (vide Chapter I) the heating rate at the nose is not infinite. Equation (4.2.1) is modified, therefore, to give a finite rate of heat input at the nose, i.e.

$$h = \frac{Q}{(x-x_0)^{\frac{1}{2}}} \qquad \ldots(4.2.2)$$

Where x_0 is a constant.

In figure (4.2.1) if XP is the plane irradiated by the reflector ARB giving the heat distribution $\frac{Q}{(x-x_0)^{\frac{1}{2}}}$

$$XP = x$$

$$OX = \text{constant } a_0$$

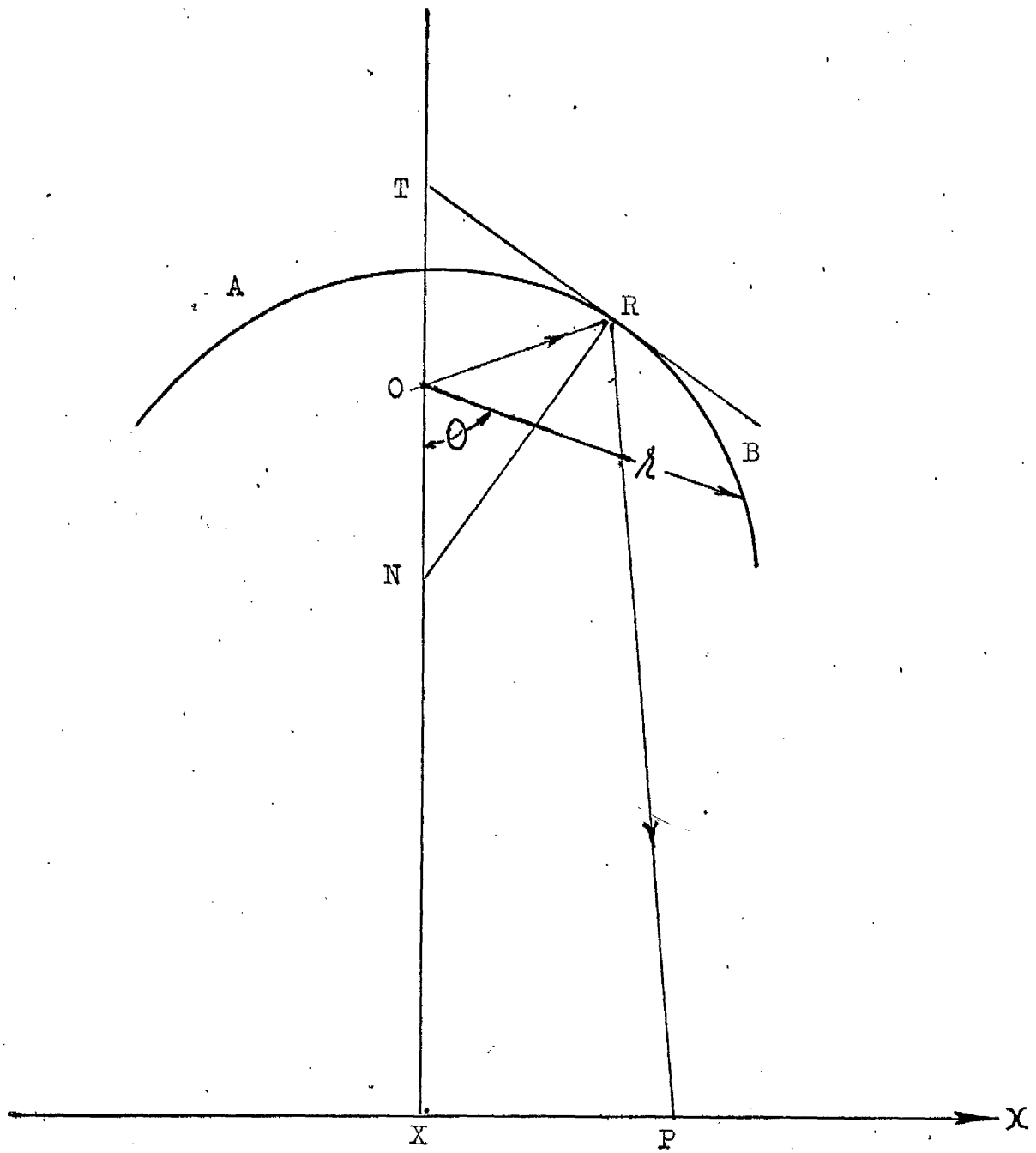

FIG. 4.2.1.

REFLECTOR PROFILE

$\angle XOR = \theta$

RN = Normal at R on the reflector profile.

Q' = heat intensity of the heat source at O (assumed a line source) then the total heat energy from an infinitesimal arc $d\theta$ of the heat source would be $Q' d\theta$. If this amount of heat falls on a length dx of XP about P, then the heat distribution on the plane XP would be given by -

$$\frac{Q' d\theta}{dx} = \frac{Q'}{x'(\theta)}$$

For the reflector to give the required heating on XP, this should be equal to the aerodynamic heating i.e.

$$\frac{Q'}{x'(\theta)} = \frac{Q}{(x-x_o)^{\frac{1}{2}}} \qquad \ldots(4.2.3)$$

Let $Q' = 2QL_1^{\frac{1}{2}}$ $\qquad \ldots(4.2.4)$

Then equation (4.2.3) reduces to

$$2L_1^{\frac{1}{2}} (x-x_o)^{\frac{1}{2}} = \frac{dx}{d\theta}$$

or $$(x-x_o) = L_1 (\theta - \theta_o)^2 \qquad \ldots(4.2.5)$$

Where it is assumed that the ray of radiation from O making an angle θ_o with OX impingos on the "edge" of irradiated plane at $x = x_o$.

In order to get all the incident radiation on XP nearly parallel, it is necessary to have $(x-x_o)$ small compared with OX and so L_1 should be small compared with OX.

In polar co-ordinates r and θ , with 0 as origin and $r = r(\theta)$, OX as y - axis (i.e. $\theta = 0$), the angle RNX is given by

$$\angle RNX = \theta - \tan^{-1}\left(\frac{r'}{r}\right) \qquad \ldots(4.2.6)$$

where

$$r' = \frac{dr}{d\theta}$$

From geometry $\angle ORN = -\tan^{-1}\left(\frac{r'}{r}\right)$ and by the laws of spectral reflection, RP makes an angle of $\left\{\theta - \pi - 2\tan^{-1}\left(\frac{r'}{r}\right)\right\}$ with OX. In cartisian co-ordinates with 0 as origin, the inclination of RP can be given as

$$\tan\left[\theta - \pi - 2\tan^{-1}\left(\frac{r'}{r}\right)\right] = \frac{x - r\sin\theta}{y - r\cos\theta}$$

$$= \frac{x - r\sin\theta}{a_o - r\cos\theta} \qquad \ldots(4.2.7)$$

With r and so r' known as a function of θ , this determines x as a function of θ .

Equation (4.2.7) can be expressed in a more convenient form as

$$\frac{r'}{r} = \tan\left[\left(\frac{\theta - \pi}{2}\right) - \tfrac{1}{2}\tan^{-1}\left(\frac{x - r\sin\theta}{a_o - r\cos\theta}\right)\right] \qquad \ldots(4.2.8)$$

If the direct irradiation of plane XP by the heat source, which will be of the order of $Q'\left(\frac{a_o}{a_o^2 + x^2}\right)$ is taken into account, equation (4.2.3) becomes

$$\frac{Q'}{x'(\theta)} + \frac{Q' a_o}{a_o^2 + x^2} = \frac{Q}{(x - x_o)^{\frac{1}{2}}}$$

After a little calculation, this leads to

$$\frac{dx}{d\theta} = \frac{1}{\left[\frac{1}{2L_1^{\frac{1}{2}}(x - x_o)^{\frac{1}{2}}} - \frac{a_o}{a_o^2 + x^2}\right]} \qquad \ldots(4.2.9)$$

Equations (4.2.8) and (4.2.9) determine the profile of the required reflector.

Since at $x = x_o$, the term $\frac{1}{2L_1^{\frac{1}{2}}(x-x_o)^{\frac{1}{2}}}$ becomes infinite, equation (4.2.9) is further modified to suit the computer as

$$\frac{dS}{d\theta} = \frac{1}{\left(1 - \frac{2a_o L_1 S}{a_o^2 + x^2}\right)} \qquad \ldots(4.2.10)$$

where

$$S = \left(\frac{x-x_o}{L_1}\right)^{\frac{1}{2}} \qquad \ldots(4.2.11)$$

Equations (4.2.8), (4.2.10) and (4.2.11) were used on the Deuce computer to find the most suitable shape of the reflector with radiant energy emitted from a point source.

In determining the shape of the reflector, the following limitations were observed:

1. The total solid angle subtended by the reflector at any point on the irradiated plane was not to exceed 10 per cent of 2π, so that the amount of incident rays on that point, caused by the reflected rays coming from the irradiated plane did not exceed one per cent of the total irradiation.
2. The ratio of the minimum radius of the reflector to that of the heating filament was not to be less than 10.

4.3 Preliminary Study of the Parameters of the Reflector

The main objects of the preliminary study of the parameters were to find their effects on the shape of the reflector and on the plane of

Design Parameters:-

$\theta_0 = 45^\circ$, $r_0 = 0.30$, $x_0 = -0.10$, $S_0 = -2.25$, $L_1 = 0.06$.

Results:- $\theta_h = 195^\circ$, $r_m = 0.04785$ at $\theta = 180^\circ$,

x varies from 0.20375 to -0.10 to 0.54811.

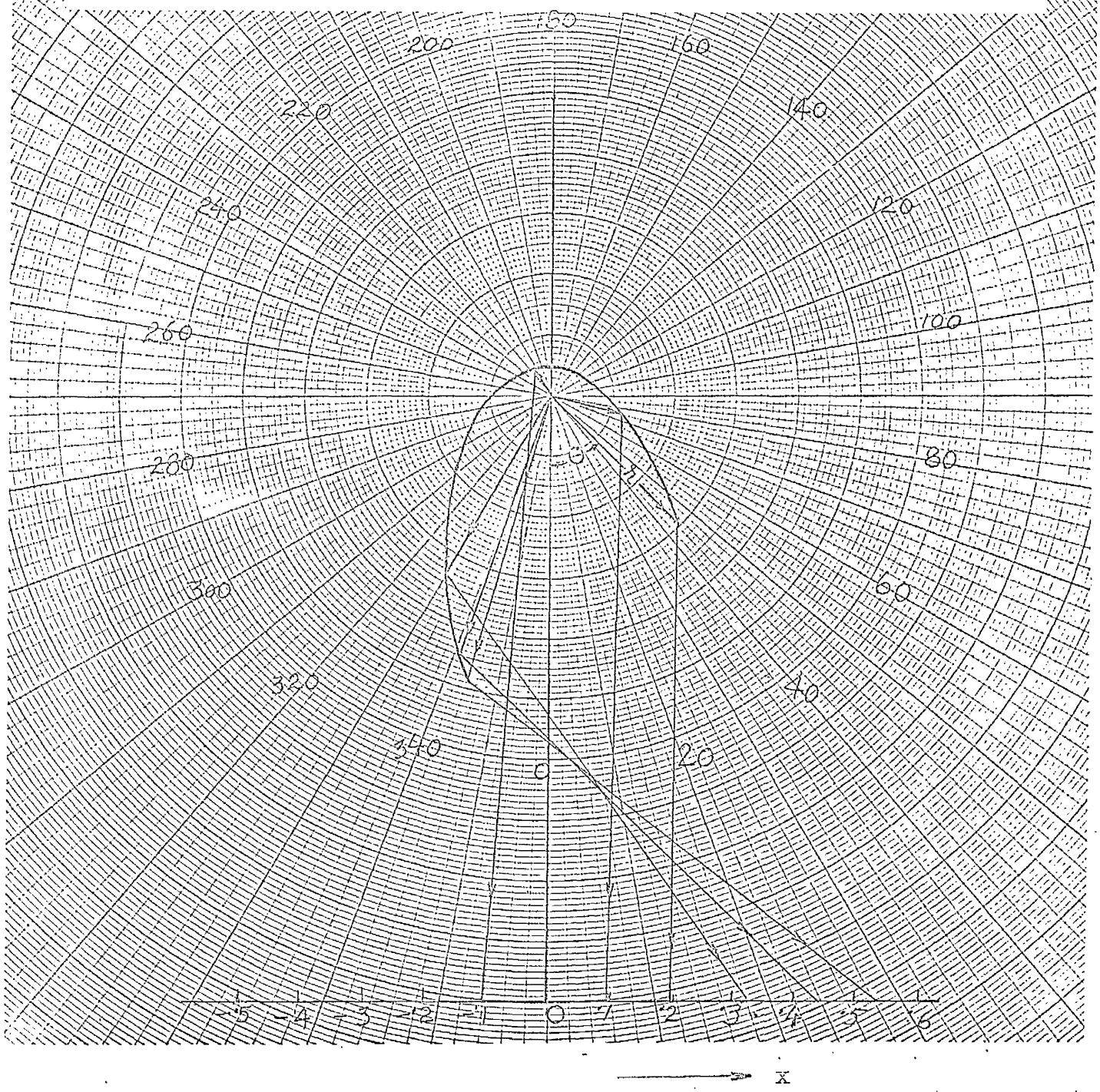

FIG.4.3.1. Variation of θ_0. $\theta_0 = 45^\circ$.

Design Parameters:-

$\theta_o = 75^\circ$, $r_o = 0.30$, $x_o = -0.10$, $S_o = -2.25$, $L_1 = 0.06$

Results:- $\theta_h = 225^\circ$, $r_m = 0.12249$ at $\theta = 180^\circ$,

x varies from 0.20375 to -0.10 to 0.28756.

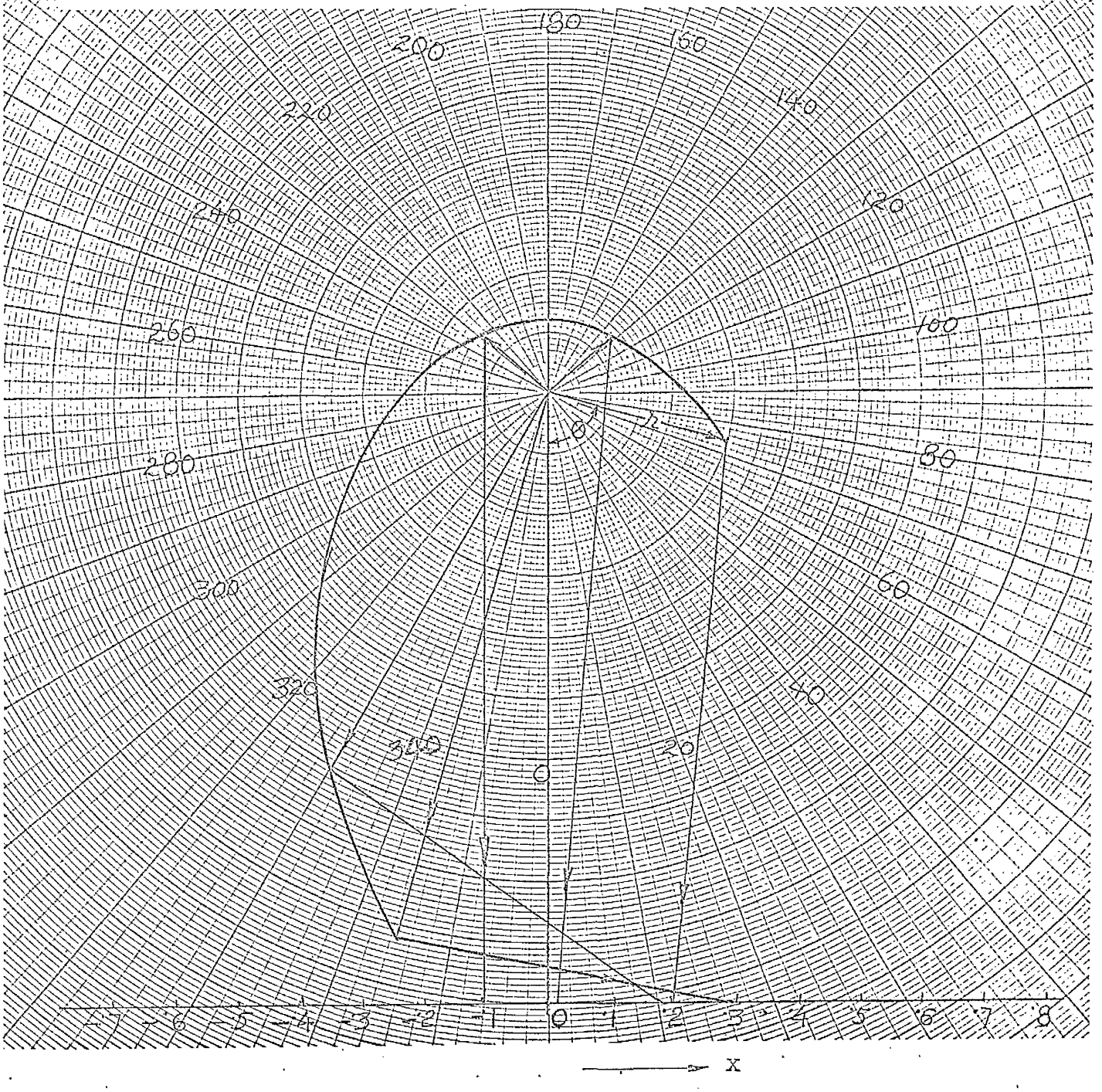

FIG.4.3.2. Variation of θ_o. $\theta_o = 75^\circ$

irradiation so that ultimately a reflector most suitable to serve the purpose in the further experiments, could be designed. This was also important to find the value of the θ_h i.e. the value of θ for which the hottest point on the plane of irradiation, received the reflected rays. In deriving the equations of the reflector (section 4.2) no account was taken of the position of the heating element in intercepting some of the reflected rays. Whatever is done, at least some of the reflected rays would be intercepted, but it is important to see that reflected rays due to be incident in the region of hottest point, do not get intercepted by the filament.

In order to reduce the bulk of work, first parameters x, x_o and r were divided by a_o to render them non-dimensional and then the numerical value of a_o was taken as unity. This eliminated the need to study a_o seperately.

The reflector profile could be started in the first quadrant and traced up to the fourth quadrant or vice versa. Both these methods were adopted and a large number of results taken and studied. Just only a few of them to help to explain certain conclusions drawn from these results are given in figures 4.3.1 to 4.3.12. A line as a source of radiant heat was assumed in the preliminary study.

4.3.1 Reflector Profile starting in the First Quadrant.

Variation of θ_o :- Keeping other parameters constant, the value of θ_o was varied in the design of the reflectors of figures 4.3.1 and 4.3.2. From these two figures, it can be seen that:-

(i) the greater value of θ_o, yields more even reflector profile and the value of r_m is larger, making easier to observe the second limitation started in section 4.2. In fact the value of r_m has almost increased threefold when the value of θ_o has changed from 45^o to 75^o. However, if the value of r_m is compared with the value of r at $\theta = 75^o$ in figure 4.3.1, then $\frac{r_m}{r_{(\theta = 75^o)}}$ of figure 4.3.1 is practically the same as $\frac{r_m}{r_{(\theta = \theta_o = 75^o)}}$ of figure 4.3.2. Thus, the gain shown in the value of r_m by increasing θ_o from 45^o to 75^o is nullified. But the larger value of θ_o will have the adverse effect of decreasing the efficiency in terms of utilization of heat available from the heat source.

(ii) The value of θ_o neither controls the point of the incidence of reflected ray corresponding to $\theta = \theta_o$, nor the position of the hottest point on the plane of irradiation. However, the extent of the plane of irradiation seems to depend on the value of θ_o, larger value gives smaller length of the plane. This is important from the point of view of controlling the length of the plane of irradiation, because only 6 inch long models of the conducting skin have to be used (vide section 3.4)

(iii) The greater value of θ_o results in greater value of θ_h as well, and,

(iv) Tracing the reflector profile with a negative value of So and a positive increment $d\theta$, yields a composite reflector.

Variation of x_o

Keeping other parameters of reflector of figure 4.3.1 constant, two more results with $x_o = 0.00$ and $x_o = 0.10$ were taken and are plotted in figures 4.3.3 and 4.3.4 respectively. From the comparison of these three figures, the following observations can be made:-

Design Parameters:-

$\theta_o = 45^\circ$, $r_o = 0.3$, $x_o = 0.0$, $S_o = -2.25$, $L_1 = 0.06$

Results:- $\theta_h = 195^\circ$, $r_m = 0.0356$ at $\theta = 180^\circ$

x varies from 0.30375 to 0.00 to 0.63701

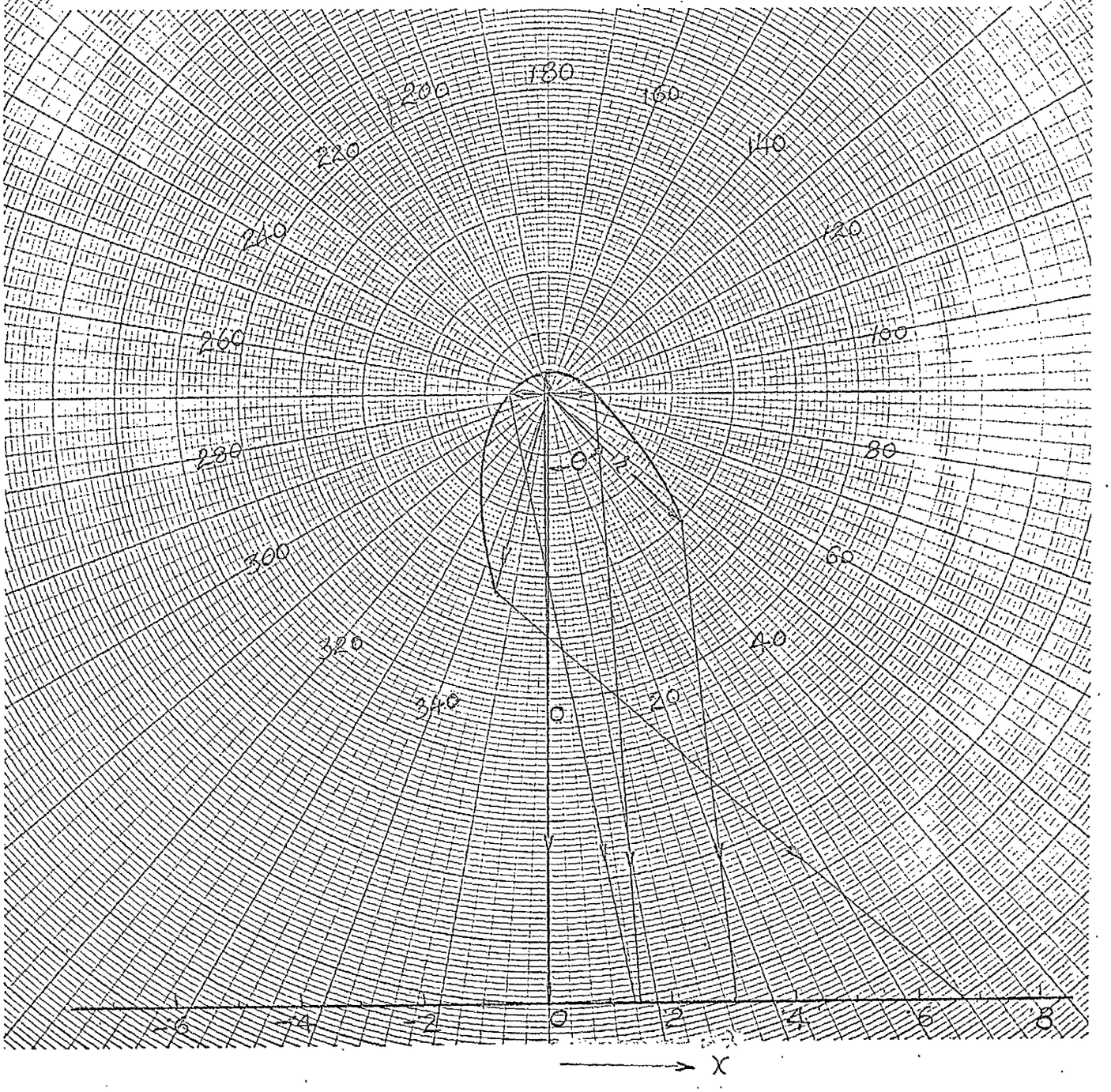

FIG. 4.3.3. Variation of X_o . $X_o = 0.00$

Design Parameters:-

$\theta_o = 45^\circ$, $r_o = 0.3$, $x_o = 0.10$, $S_o = -2.25$, $L_1 = 0.06$

Results.- $\theta_h = 195^\circ$, $r_m = 0.0215$ at $\theta = 180^\circ$

x varies from 0.40375 to 0.10 to 0.72615

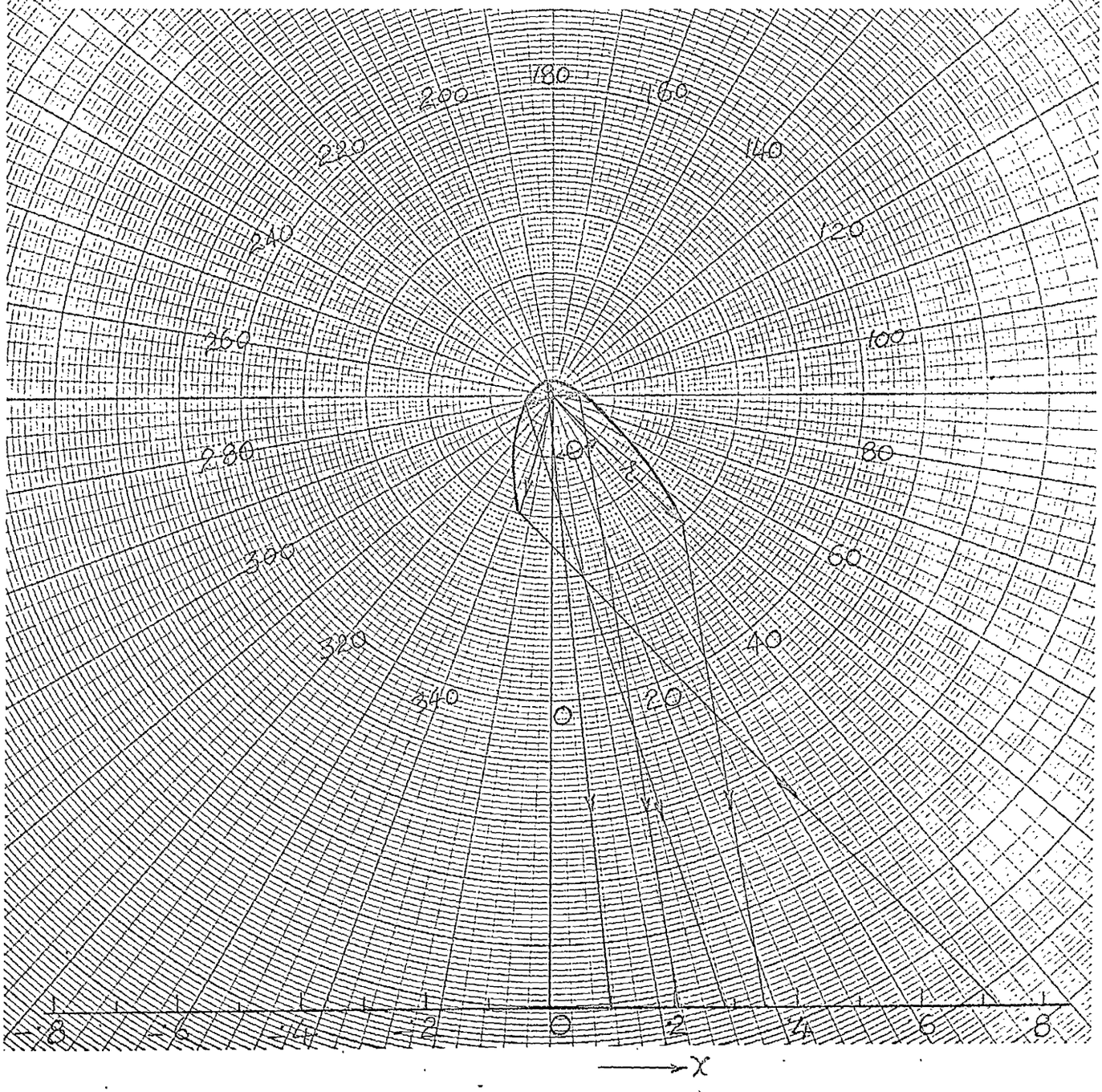

FIG.4.3.4. Variation of x_o. $x_o = 0.10$

Design Parameters:-

$\theta_o = 45°$, $r_o = 0.30$. $x_o = 0.0$, $S_o = -1.00$, $L_1 = 0.06$

Results.- $\theta_h = 105°$, $r_m = 0.0466$ at $\theta = 195°$

x varies from 0.06 to 0.0 to 0.89301

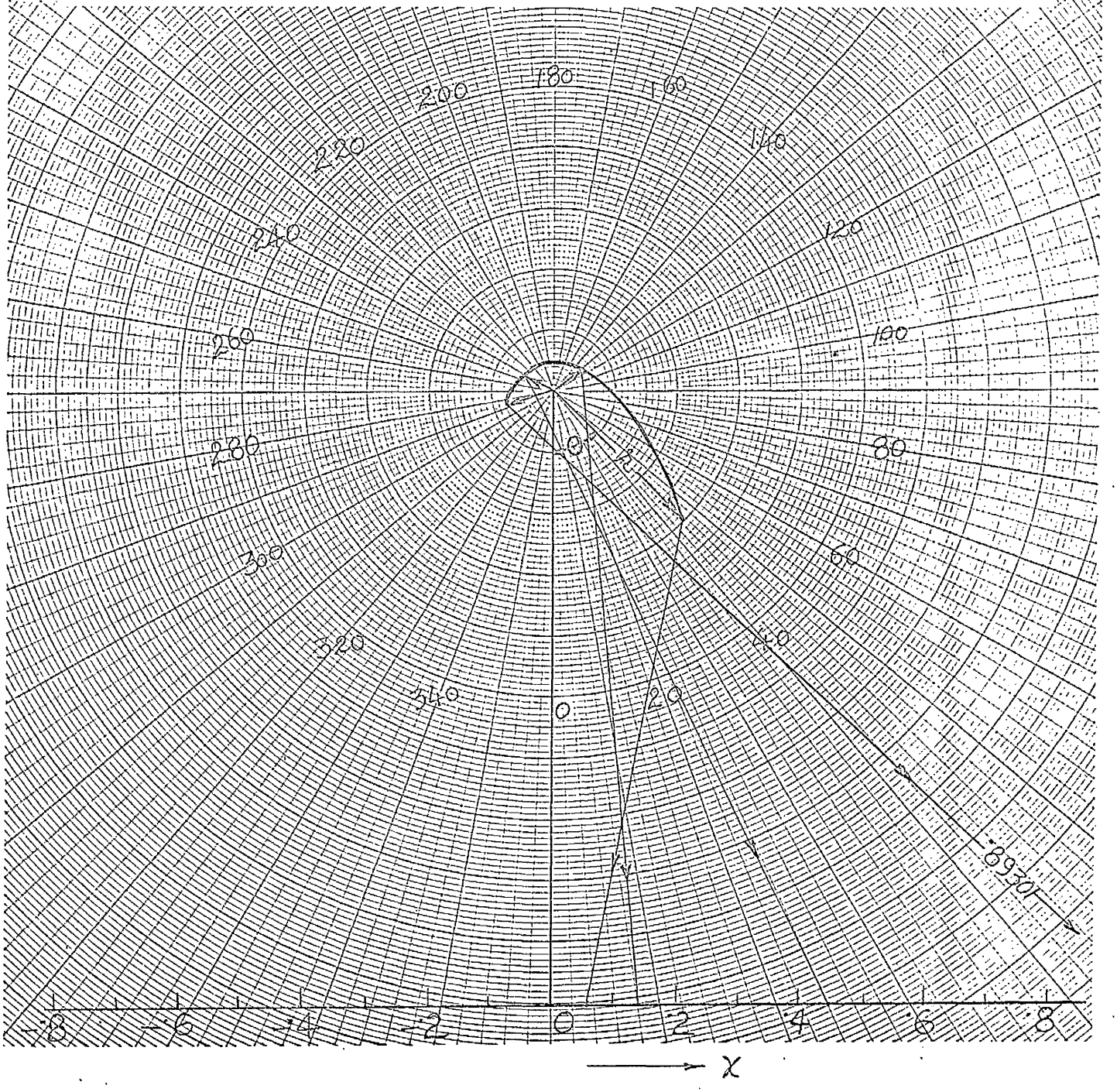

FIG.4.3.5. Variation of S_o. $S_o = -1.00$

Design Parameters:-

$\theta_o = 45°$, $r_o = 0.30$, $x_o = 0.00$, $S_o = 1.00$ $L_1 = 0.06$

Results.- $\theta_h = 45°$, $r_m = 0202$ at $\theta = 240°$.

x varies from 0.06 to 2.38317

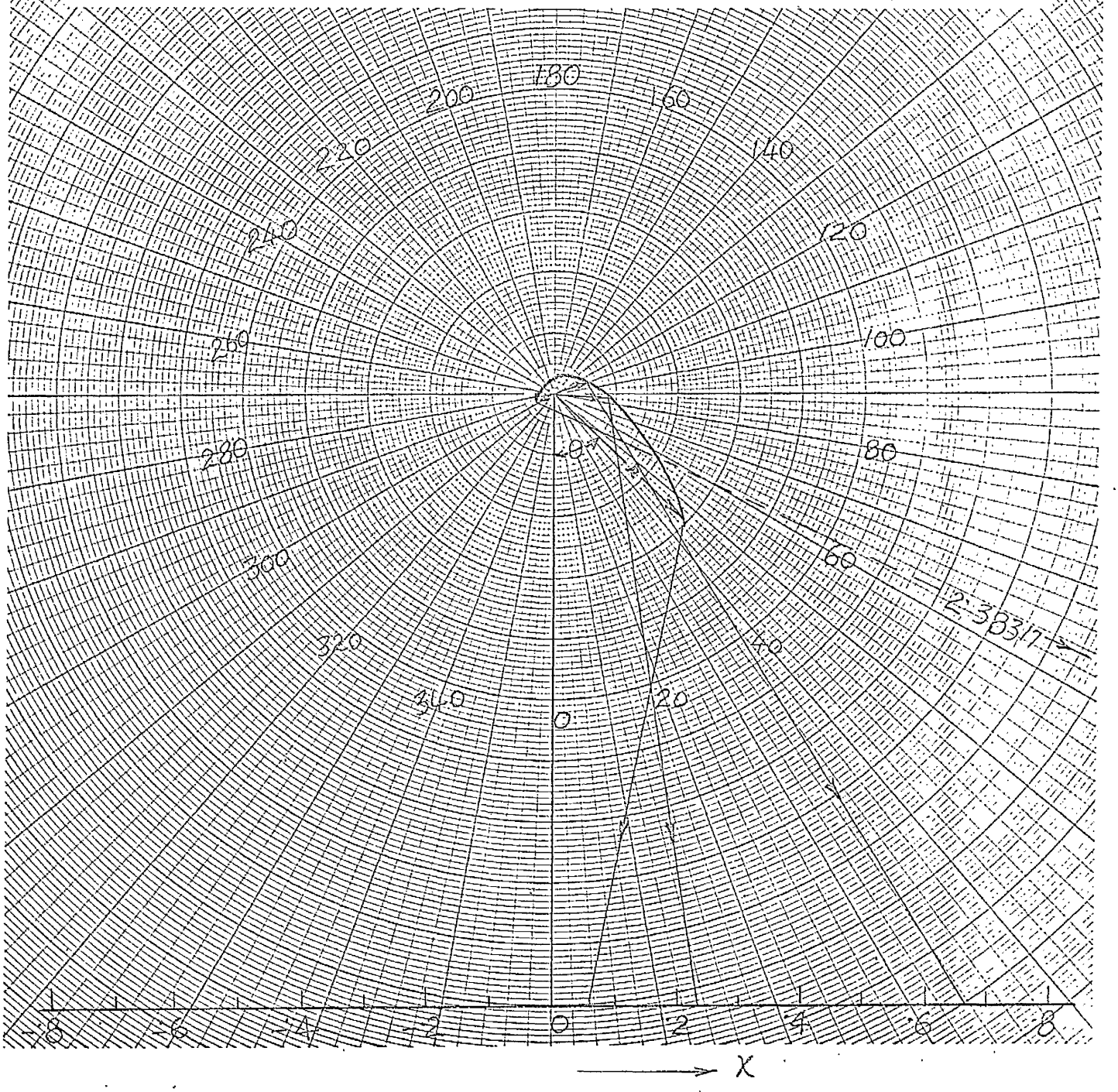

FIG.4.3.6. Variation of S_o. $S_o = 1.00$

(i) The negative value of x_o results in more even reflector profile than the positive value.

(ii) The larger negative value of x_o yields a greater length of the plane of irradiation, but the length does not increase in the same proportion as the value of x_o, but some what less.

(iii) There is no effect of the value of x_o on the value of θ_h.

(iv) The hottest point on the plane of irradiation corresponds to the value of x_o itself. This, of course, is evident, from the equations of the reflectors also; and

(v) Any value of x_o, positive or negative, does not effect the type of the reflector.

Variation of S_o :- To study the effects of variation of S_o, the results plotted in figures 4.3.3, 4.3.5 and 4.3.6 for S_o = -2.25, - 1.00, and 1.00 respectively, can be compared and the following conclusions drawn:-

(i) The positive value of S_o yields a single and crossed ray reflector whereas a negative value gives a composite reflector.

(ii) Effect on the curvature of the reflector profile is also very large. The negative value of S_o gives the value of r_m more than twice to that obtained from the numerically equal positive value of S_o.

(iii) The values of θ_h are different for identical values of S_o but of opposite sign.

(iv) Single and crossed ray reflector obtained with positive value of S_o gives more than twice the length of the plane of irradiation of the composite reflector designed with numerically equal negative value of S_o, and

(v) The larger the negative value of S_o, the smaller is the length of the plane of irradiation.

Design Parameters:-

$\theta = 45^{\circ}$, $r_o = 0.30$, $x_o = 0.00$, $S_o = -2.25$, $L_1 = 0.09$.

Results.- $\theta_h = 195^{\circ}$, $r_m = 0.0207$ at 180°.

x varies from 0.455625 to 0.00 to 0.5956

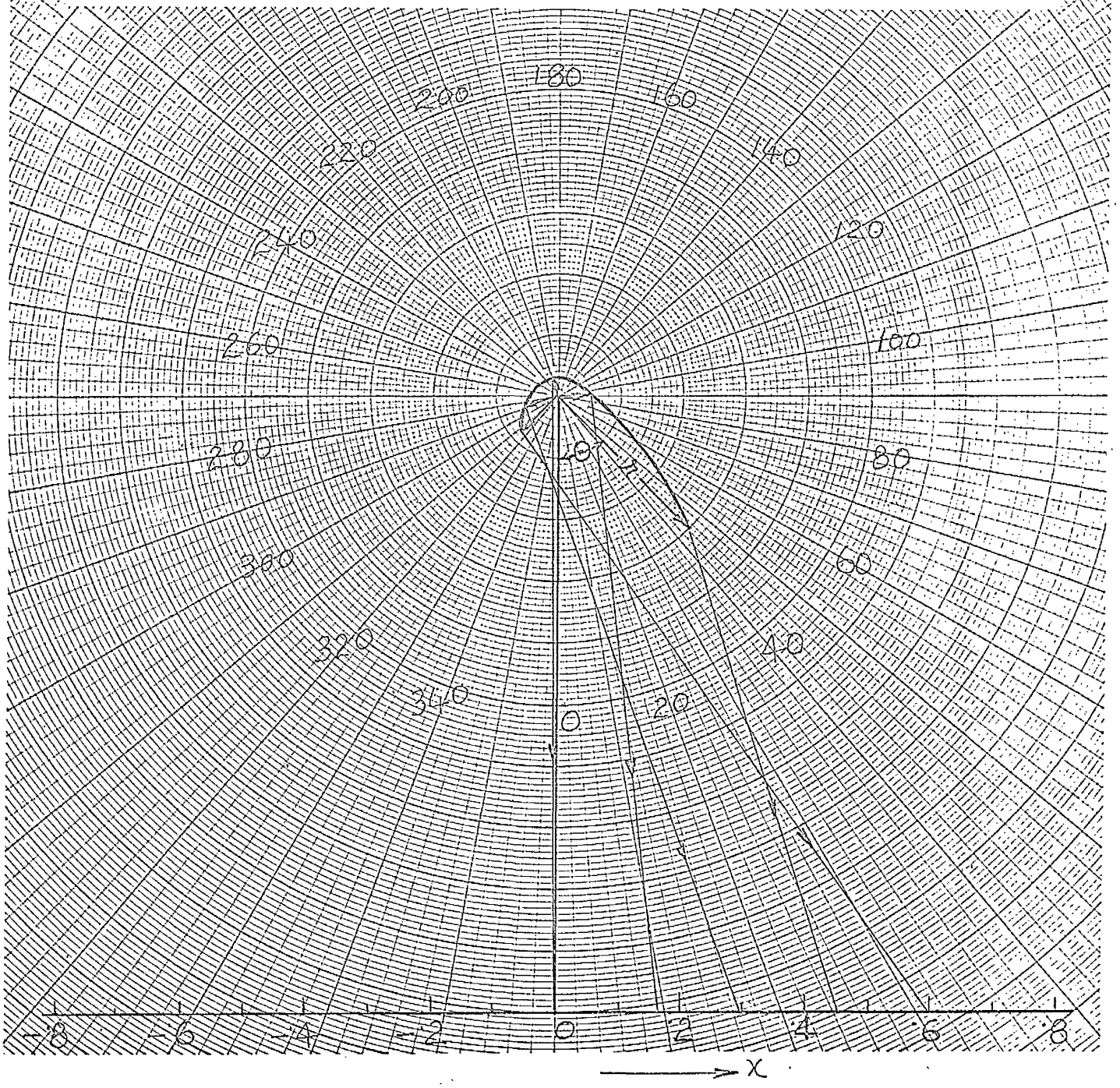

FIG.4.3.7. Variation of L_1. $L_1 = 0.09$.

Variation of L_1

From equation (4.2.4) it is evident that L_1 can not be negative, if it has to be of any physical significance. Therefore, results with positive values of L_1 only were taken, one of which is plotted in figure (4.3.7) for $L_1 = 0.09$ to compare it with the results of figure 4.3.4 in which $L_1 = 0.06$ was taken. The following conclusions can be derived from them:-

(i) The smaller value of L_1 yields larger value of r_m and hence a more even reflector profile.

(ii) Larger value of L_1 results in a greater length of the plane of irradiation. Incidentally, the increase in the length of the plane proportional to the increase in the value of L_1 in these two examples cited is a bit misleading because the value of x_o in both cases was taken zero.

(iii) The value of θ_h is not effected by the value of L_1, and

(iv) The value of L_1 does not determine the type of the reflector.

Variation of r_o :- Results obtained by varying r_o showed that it had practically no effects either on the reflector profile or on the plane of irradiation, except that the radius of the profile everywhere was approximately proportionally increased or decreased as the value of r_o.

4.3.2. Reflector Profile Starting in the Fourth Quadrant

The conclusions dervied from the bigger value of θ_o in section 4.3.1 are true for the smaller value of θ_o if the reflector profile is started in the fourth quadrant and traced back to the first quadrant by assigning a negative value of $d\theta$. This can be easily seen from figures 4.3.8 and 4.3.9.

The same is true for the conclusions drawn with respect to L_1, the bigger value of L_1 in this case has the same effects as the smaller value of

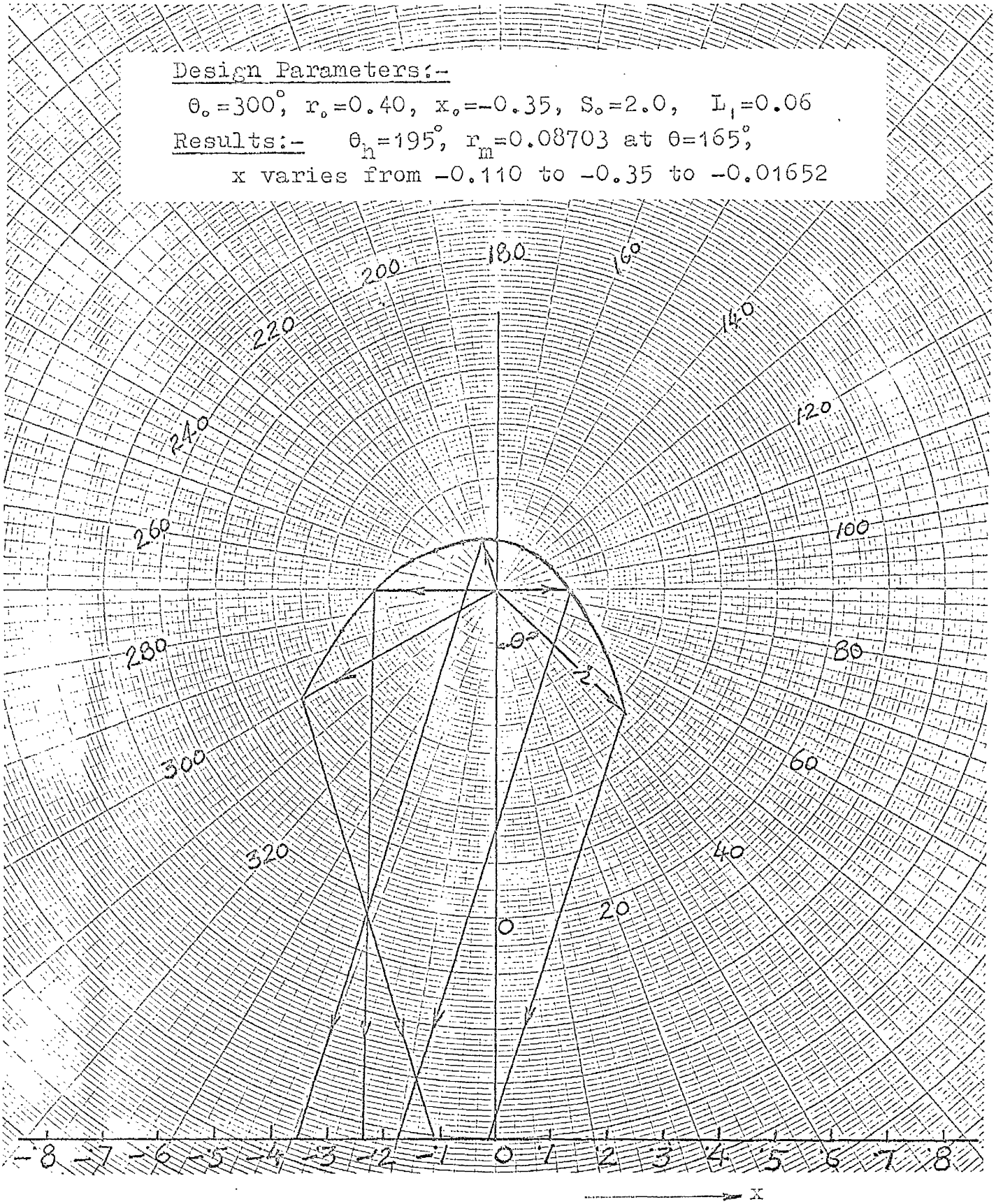

FIG. 4.3.8. Variation of θ_0. $\theta_0 = 300^\circ$.

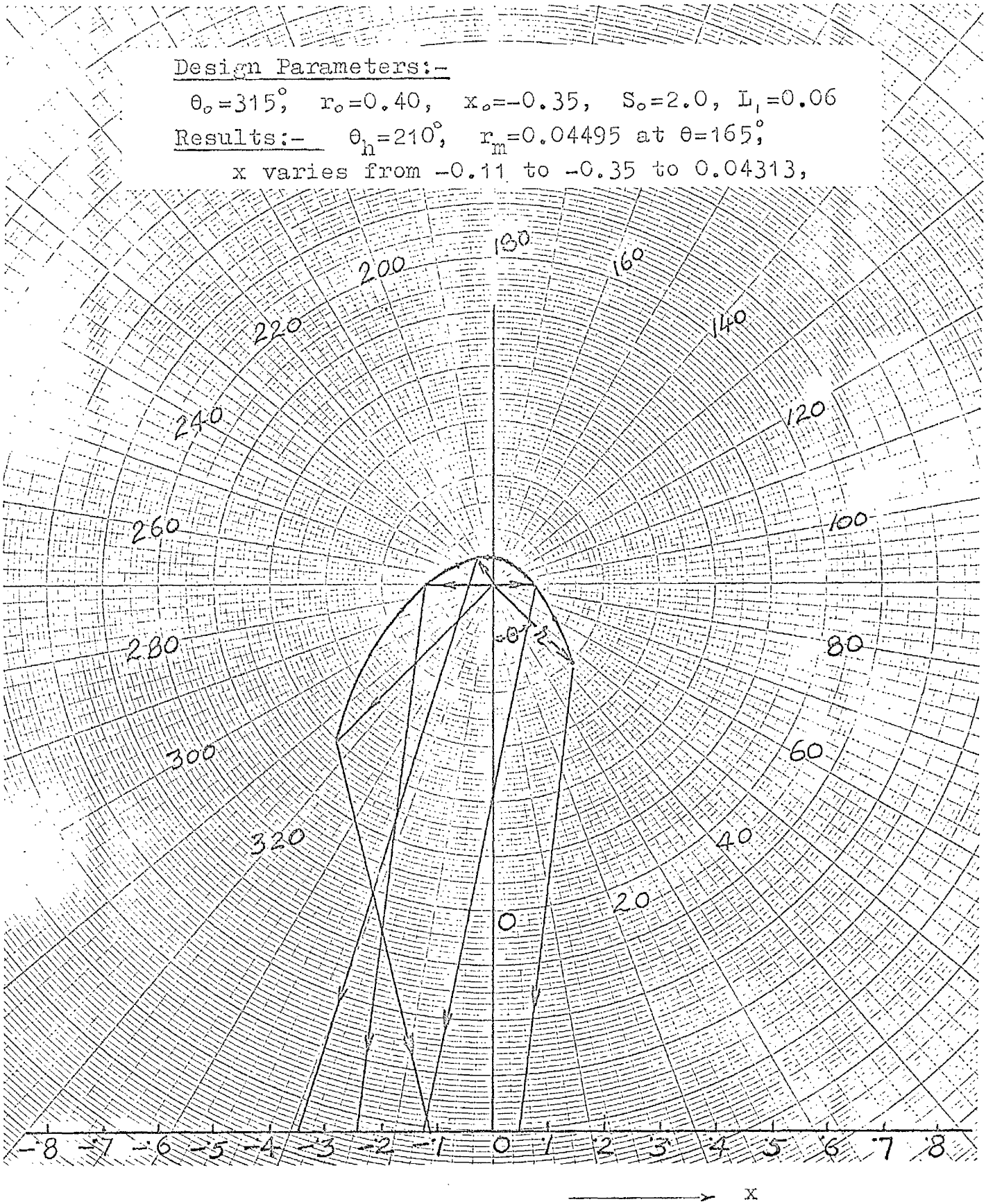

FIG. 4.3.9. Variation of θ_o. θ_o=315°.

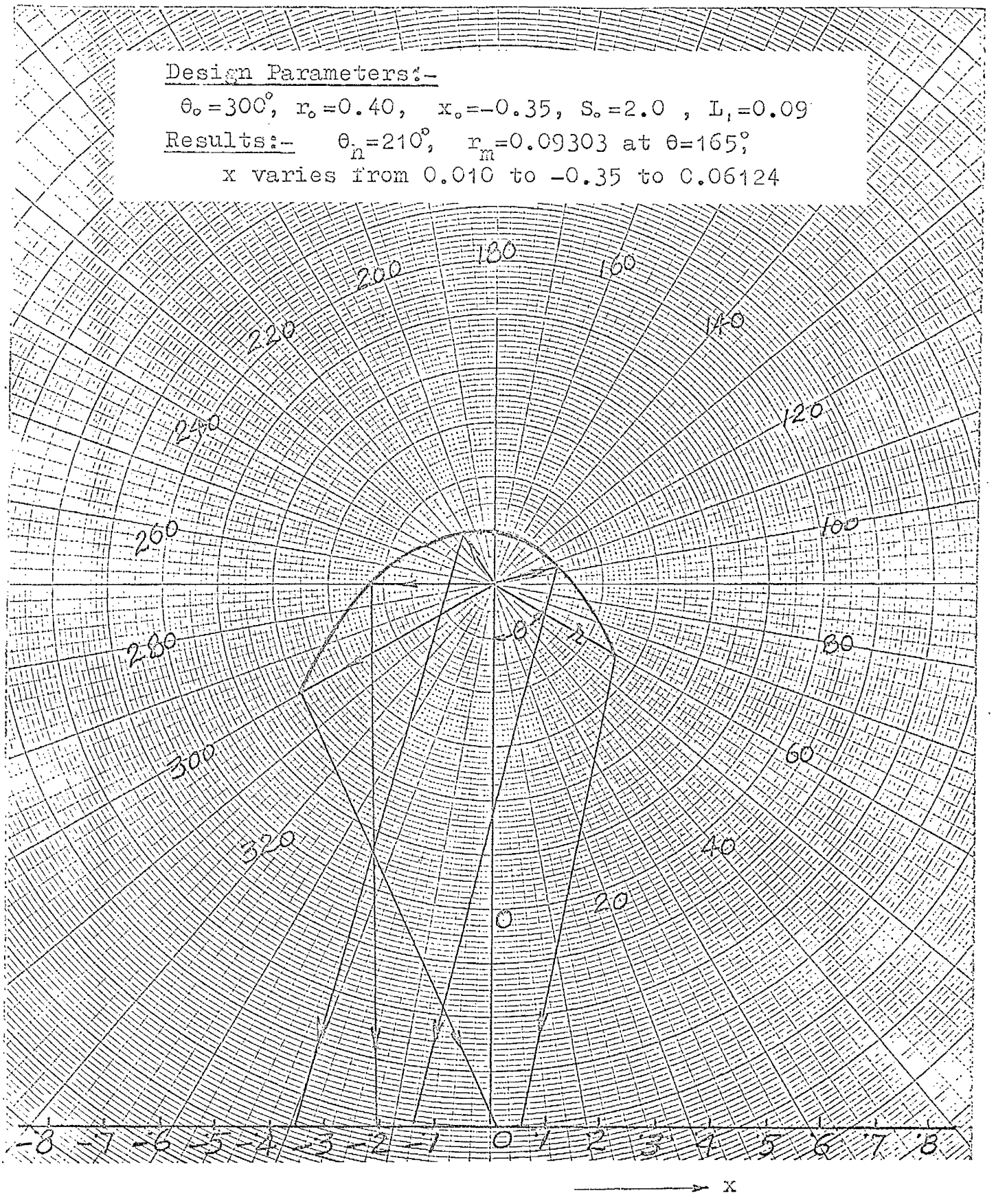

FIG. 4.3.10. Variation of L_1. L_1=0.09.

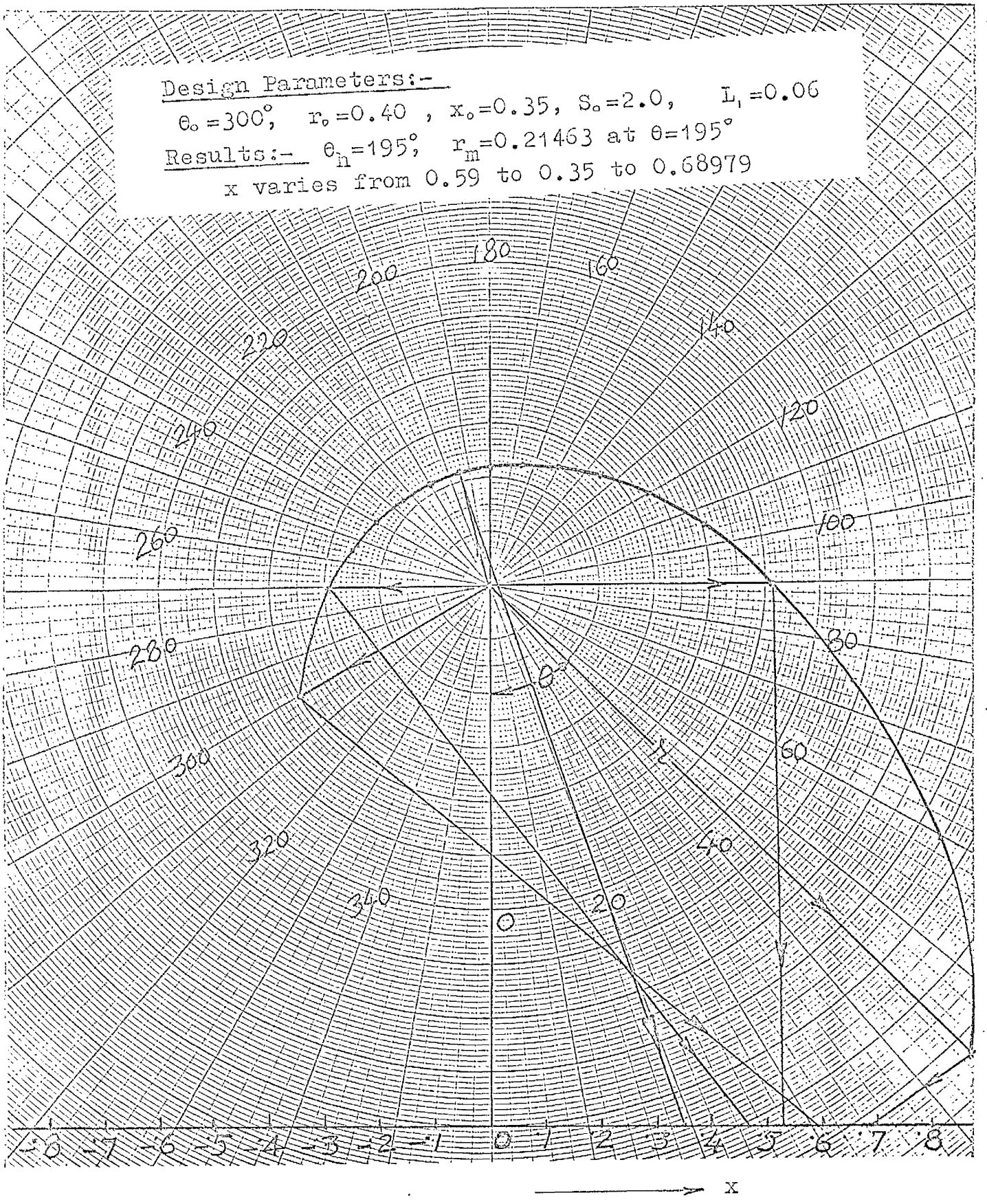

FIG. 4.3.11. Variation of x_o. $x_o = 0.35$.

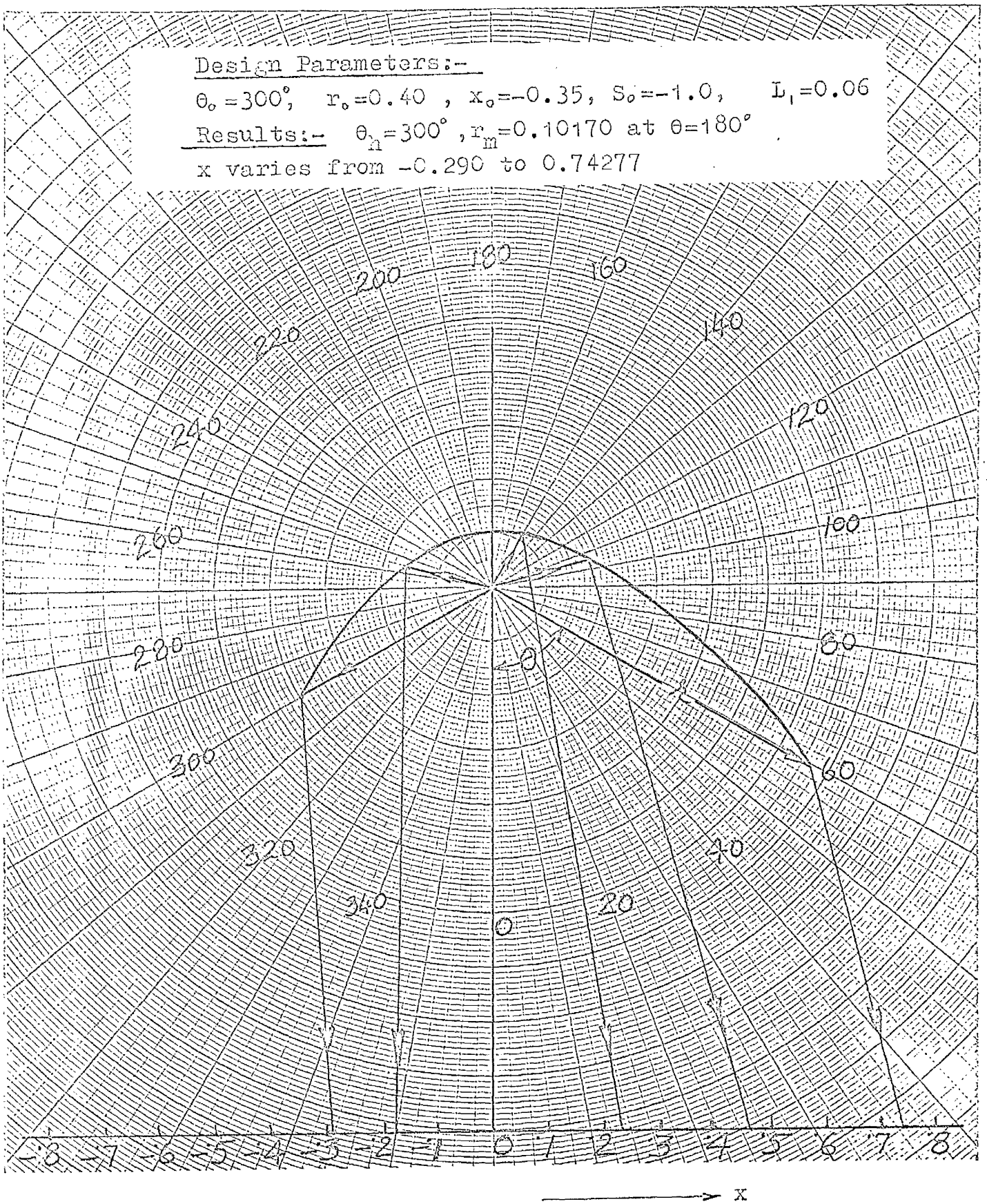

FIG. 4.3.12. Variation of S_o. $S_o = -1.00$.

L_1 for the reflector profile started in the first quadrant (comparisons of figures 4.3.8 and 4.3.10).

In case of x_o and S_o, it is just the question of change of sign i.e. conclusions drawn for the negative values of x_o or S_o in section 3.4.1 are exactly true for their positive values and vice-versa for the reflector starting in the fourth quadrant (figures 4.3.8, 4.3.11 and 4.3.12). But this should not be overlooked that whereas positive value of S_o in section (4.3.1) resulted in a single and crossed ray reflector, the negative value of S_o in figure 4.3.12 produces a direct ray reflector. Besides, the position of the hottest point on the plane of irradiation does not coincide with the value of x_o which happened in the case of the other two types of the reflector.

4.3.3 Types of the reflectors.

From the results discussed in sections 4.3.1 and 4.3.2 it can be observed that basically three different types of reflectors can be obtained by assigning different signs to their parameters. These are (i) single and crossed ray reflector (ii) single and direct ray reflector and (iii) composite reflector. The signs of their parameters can be tabulated as follows:-

Position of θ_o	$d\theta$	x_o	L_1	S_o	Types of reflectors
First quadrant	+ ve	+ ve or - ve	+ ve	+ ve	Single and crossed ray
Fourth quadrant	- ve	+ ve or - ve	+ ve	- ve	Single and direct ray
First quadrant	+ ve	+ ve or - ve	+ ve	- ve	Composite
Fourth quadrant	- ve	+ ve or - ve	+ ve	+ ve	Composite

4.4. Effects of Finite Size of Heating Element

A finite size of the heating element (section 5.6) is inevitable to get sufficient amount of heat energy. But so far, heat was assumed to radiate from a point source, and therefore, the error involved in the heat distribution due to use of a finite size of the heating element is unknown. This, however, would undoubtedly increase with the increasing size of the filament. Since the power requirements has to be of the order of 3 to 3.5 kilowatts; a simple calculation shows that the minimum diameter of the filament can not be less than $\frac{1}{4}$ inch, if the working temperature of the filament is not to exceed $2000^{o}k$ for an assumed value of $\varepsilon = 0.8$. This would certainly upset the heat

distribution, unless the size of the heating element is given due consideration in the design of the reflector itself.

A completely new set of differential equations, of the reflector was derived, which are given in appendix A. The new approach includes the consideration of reflection of total radiant energy emitting from all parts of the filament, visible to a point of the reflector at which they are incident. Equations (4.2.10), (4.2.11) and (A-10) were further used to find the most suitable profile of the reflector.

Results taken with and without consideration of the size of the heating element, having identical other parameters, showed that there was no appreciable difference in the shape of the reflectors, if the radius of the heating element was not more than about 15 per cent of the radius of the reflector at $_{0}$. But even an infinitesimally small change in the curvature at any point of the reflector profile would greatly shift the points of incidence of reflected rays on the plane of irradiation. From this point of view, therefore, consideration of the size of heating element in the design of the reflector was necessary.

4.5 Single Reflectors

4.5.1 Design and Development:- Preliminary study of the effects of variation of parameters gave an adequate idea of how to predict the type of reflector, but not enough knowledge to estimate precisely the shape of its profile and its performance. Therefore, the design development and experimental testing of the performance of any type of the reflector was absolutely necessary.

To develop any type of reflector, the process of reiteration was followed. Results with some values of parameters were taken on the computer, graphs of reflector profile and the plane of irradiation plotted and then values of parameters modified to bring about the desired change in the curvature and/or size of the reflector and/or in the plane of irradiation in the next computer run. The process was repeated again and again until a most suitable profile of the reflector was obtained. At this stage, an idea of the size of heating element and that of scale was necessary to assign numerical values to the diameter of the filament and the other parameters.

Finally two sets of results, one for the direct ray single reflector and the other for the crossed ray single reflector, were accepted for construction and testing. The results are given in tables 4.5.1 for crossed ray reflector and 4.5.2 for the direct ray at an interval of 10 degrees. Originally results were taken at an interval of 2 degrees for the sake of good accuracy in the profile and to save space, they are given here at an interval of 10 degrees.

4.5.2 Construction:- Two half inch thick pieces of Sindanyo were marked and cut accurately into the shape of the reflector profile. The position of the filament was also marked accurately on the Sindanyo pieces and half inch diameter holes were drilled through them to fit Sindanyo plugs with $\frac{5}{32}$ inch diameter holes to take up the filament support rod of alumina. Alumina was used to support the coiled filament for its electrical insulating property and its high working temperature. A 24 gauge, well polished copper sheet was then bent over the Sindanyo pieces, which were held rigid

TABLE 4.5.1

CROSSED RAY REFLECTOR: DESIGN DATA

Parameter:-

$\theta_o = 40^o$, $r_o = 0.175$, $S_\theta = 0.00$
$d\theta = 1^o$, $x_o = -0.160$, $L_1 = 0.0094$

$r_\lambda = 0.003456333$ scale = 33 inches

θ (degrees)	r	x
40^o	0.17500	-0.16000
50	0.13052	-0.15973
60	0.10177	-0.15893
70	0.08236	-0.15762
80	0.06876	-0.15580
90	0.058971	-0.15349
100	0.051777	-0.15070
110	0.04642	-0.14746
120	0.042415	-0.14375
130	0.03934	-0.13960
140	0.03726	-0.13501
150	0.03576	-0.12997
160	0.03483	-0.12447
170	0.03442	-0.11852
180	0.03450	-0.11208
190	0.03508	-0.10515
200	0.03618	-0.09770
210	0.03787	-0.08971
220	0.04025	-0.08114
230	0.04348	-0.07196
240	0.04777	-0.06215
250	0.05346	-0.05166
260	0.06106	-0.04047
270	0.07130	-0.02854
280	0.08539	-0.01584
290	0.10523	-0.00236
300	0.13400	+0.01194
310	0.17718	0.02706
314	0.20045	0.03334

TABLE 4.5.2

SINGLE DIRECT RAY REFLECTOR: DESIGN DATA

Parameter:-

$\theta o = 270^o$ ro = 0.300 δo = 0.00
$d\theta = 2^o$ xo = 0.300 L_1 = 0.065

r_h = .007608333 Scale = 15 inches

θ (degrees)	r	x	Slope (radians)
270^o	0.30000	0.30000	2.6045
260	0.27380	0.30180	2.5292
250	0.25360	0.30704	2.4142
240	0.23831	0.31550	2.3226
230	0.22715	0.32699	2.2230
220	0.21958	0.34136	2.1157
210	0.21527	0.35846	2.0293
200	0.21392	0.37820	1.9345
190	0.21563	0.40049	1.8314
180	0.22049	0.42527	1.7477
170	0.22879	0.45249	1.6552
160	0.24107	0.48213	1.5538
150	0.25813	0.51419	1.4707
140	0.28117	0.54868	1.3780
130	0.31195	0.58563	1.2750
120	0.35307	0.62506	1.1894
110	0.40839	0.66704	1.0917
100	0.48365	0.71159	0.9795
90	0.58734	0.75879	0.8818

TABLE 4.5.3.

SINGLE CROSSED RAY REFLECTOR

Experimental test for the heat distribution

Theoretical x - co-ordinate of the hottest point
= -0.16 (non-dimensional)
or - 5.28 inches.

Experimentally found x co-ordinate of the hottest point
= -5.45 inches.

Distance from the hottest point		Relative heat intensity for the best fit of data	Remarks
Non-dimensional	Inches		
-0.053	-1.75	0.42	
-0.0227	-0.75	1.11	
-0.0076	-0.25	1.182	
0.00	0.0	1.23	The hottest point
0.0076	0.25	1.18	
0.0379	1.25	0.955	
0.0682	2.25	0.727	
0.0985	3.25	0.50	
0.1288	4.25	0.833	
0.1591	5.25	0.773	
0.1894	6.25	0.652	

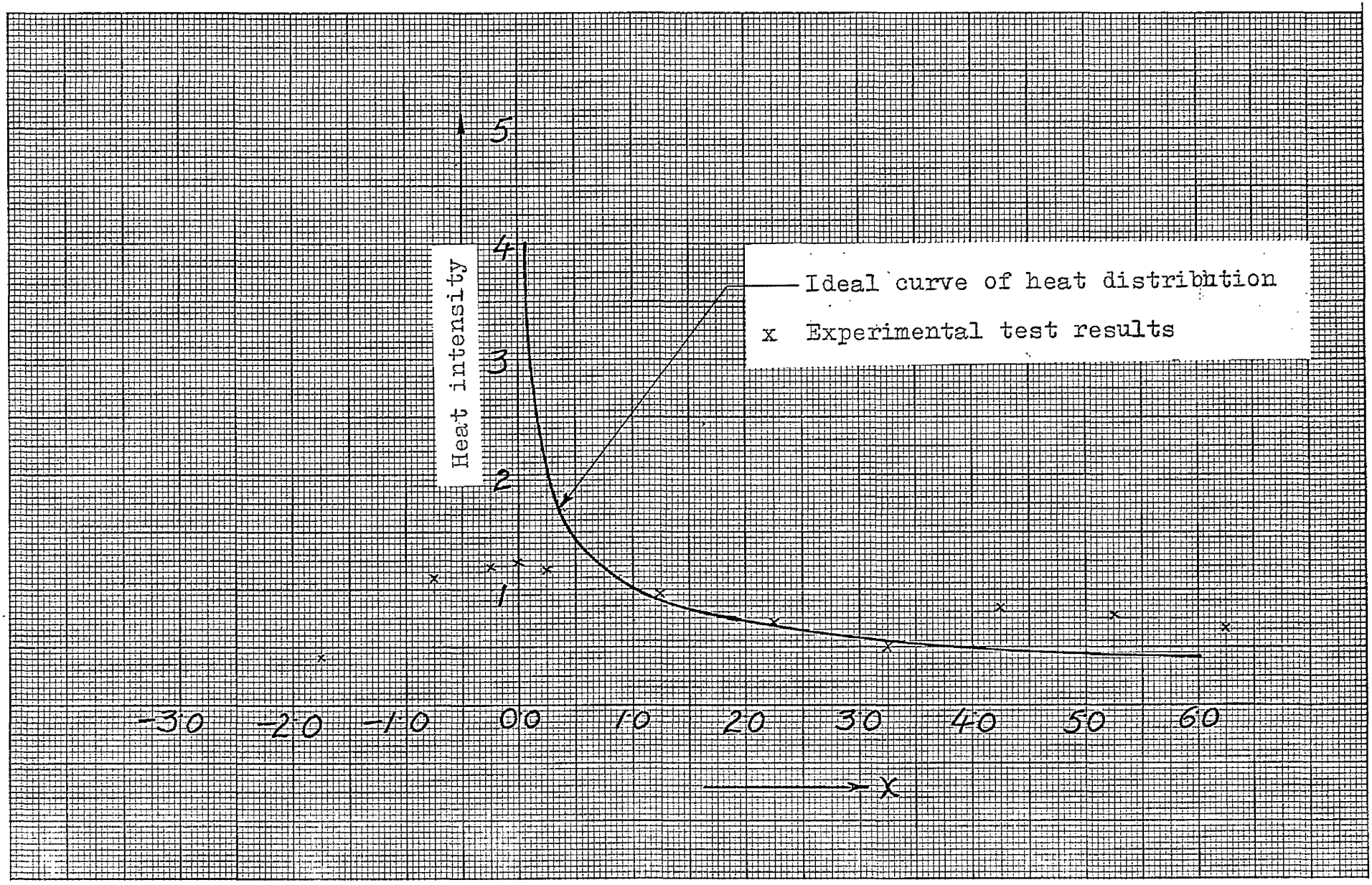

FIG.4.5.1. Heat distribution given by the Single Crossed Ray reflector of table 4.5.1.

and parallel to each other on a wooden frame, sitting square on a surface table. The copper was used for thereflector for its high reflectivity of infra-red radiation, and the Sindanyo for its low coefficient of thermal expansion and easy workability.

The first reflector made was the cross ray single reflector.

4.5.3 Experimental Test of the Single Crossed Ray Reflector:- A circular foil Gordon's type radiometer[41] was especially made for the measurement of the intensity of radiation impinging on the model (vide section 6.4). Since the vacuum chamber and the vacuum pumps were not available by that time, tests of the reflector were carried out in the atmosphere. Care was taken to minimise all draughts of air. To support the reflector rigidly in position and to allow a controlled movement of the radiometer in the plane of irradiation, a test rig was designed and constructed. A nichrome wire filament, wound around an alumina rod, was used as a heating element. The e.m.f. signals of the radiometer were recorded by a Vernier potentiometer with the help of a null-point galvanometer, using the balanced circuit. The experimental test results of the reflector are given in table 4.5.3 and they are plotted in figure 4.5.1.

4.5.4 Discussion of Results:- Results of the test are very disappointing, as the intensity of heating at the hot end of the plane of irradiation is not as high as expected. There might be several reasons. Some of the small terms dropped to simplify equation (A-6) in the design of the reflector profile might have affected the results slightly. Secondly,

since the hot end of the plane of irradiation receives reflected rays from an end portion of the reflector profile, it is likely to lose some of the heat rays. This is because any point on the plane of irradiation receives reflected rays from a large portion of the reflector profile (vide appendix-B), on account of the heating element not being a point source. And, if that point happens to receive the reflected rays from an end portion of the reflector, the reflector profile must be continued further, enough to complete the reflection of all heat rays due to that point from the heating element. The second effect, however, is eliminated in composite reflectors, which will be discussed later and their test results should show how important is this effect of the size of the heating element. These results completely cancel out any idea of using the single direct ray reflector. However, later on, when an analytical method of testing a reflector was developed (appendix-B), the single direct ray reflector of design data given in table 4.5.2 was also tested. Results of the test, along with that of others, are given in section 4.7.

Convection loss in air during the preliminary tests, manufacturing error in reflector profile, and reflection in improper directions due to undulated reflector surface must also have contributed toward the failure of this reflector to produce high intensity of heating at the hot end of the plane of irradiation.

4.6 COMPOSITE REFLECTORS

4.6.1 Design and Development :- In the development of a composite reflector, an important point to be considered is that the hot end of the plane of irradiation does not receive rays from that region of the reflector whose reflected rays are intercepted by the heating element. The differential equations governing the shape of the reflector do not take into account the interception of the reflected rays by the filament and hence this could only be done by drawing the reflector profile with heating element in position, after it has been designed and then tracing the reflected rays to check the interception.

Whether the reflector profile is started in the first quadrant or in the fourth quadrant, generally the value of θ_h comes to about 180° and because the radius of the reflector in that region is small, the reflected rays bound for the hot end region are usually intercepted.

To shift the value of θ_h to the desired direction, a careful study was made of the effects of variation of x_o, S_o, and L_1 on θ_h. Results after results of design data were taken on computer, reflector profiles were drawn with the heating element in position and the reflected rays were traced. The process was repeated again and again, each time after modifying the values of x_o, S_o and L_1 to improve the results in the next run.

Since it was decided to use 6 inch long model of the conducting skin, care was taken to see that six inch long plane of irradiation was obtained.

TABLE 4.6.1

COMPOSITE REFLECTOR (1) DESIGN DATA

Parameters:-

$\theta_o = 90^o$, $r_o = 0.21$, $\delta_o = -1.75$
$d\theta = 3^o$, $x_o = -0.80$, $L_1 = 0.180$
$r_4 = 0.0074$, scale = 15 inches

θ (degrees)	r	x	slope
90	0.2100	-0.24875	0.58214
96	0.19907	-0.28183	0.6133
102	0.18830	-0.32017	0.6594
108	0.17948	-0.35771	0.7056
114	0.17232	-0.39431	0.7519
120	0.16658	-0.43018	0.7985
126	0.16210	-0.46500	0.8455
132	0.15874	-0.49877	0.8927
138	0.15642	-0.53141	0.9404
144	0.15506	-0.56281	0.9644
150	0.15462	-0.59287	1.0372
156	0.15510	-0.62148	1.0864
162	0.15647	-0.64853	1.1362
168	0.15878	-0.67387	1.1867
174	0.16206	-0.69737	1.2379
180	0.16638	-0.71889	1.2898
186	0.17182	-0.73827	1.3426
192	0.17852	-0.75535	1.3963
198	0.18661	-0.76997	1.4511
204	0.19628	-0.78192	1.5070
210	0.20778	-0.79104	1.5642
216	0.22139	-0.79708	1.6229
222	0.23747	-0.79985	1.6833
228	0.25644	-0.79907	1.7455
234	0.27885	-0.79447	1.8102
240	0.30530	-0.78572	1.8775
246	0.33653	-0.77244	1.9482
252	0.37335	-0.75419	2.0230
258	0.41665	-0.73042	2.1028
264	0.46724	-0.70041	2.1451
270	0.52575	-0.66322	2.2838
276	0.59226	-0.61751	2.3894
282	0.66599	-0.56129	2.5090
288	0.74486	-0.49132	2.6465
294	0.82544	-0.40168	2.8048

TABLE 4.6.2.

COMPOSITE REFLECTOR (1)

Experimental Test for Heat Distribution

x - co-ordinate	Distance from the hottest point (inch)	Relative heat intensity for the best fit	Remarks
-3.5	8.20	0.304	
-4.0	7.70	0.320	
-4.5	7.20	0.344	
-5.0	6.70	0.369	
-5.5	6.20	0.389	
-6.0	5.70	0.495	
-6.5	5.20	0.489	
-7.0	4.70	0.481	
-7.5	4.20	0.686	
-8.0	3.70	0.505	
-8.5	3.20	0.529	
-9.0	2.70	0.529	
-9.5	2.20	0.539	
-10.0	1.70	0.812	
-10.5	1.20	1.070	
-11.00	0.70	1.034	
-11.25	0.45	1.189	
-11.50	0.20	1.396	
-11.60	0.10	1.412	
-11.70	0.0	1.452	The hottest point
-11.80	-0.10	1.432	
-11.90	-0.20	1.373	
-12.00	-0.30	1.280	
-12.25	-0.55	1.017	
-12.50	-0.80	0.760	
-13.00	-1.30	0.409	

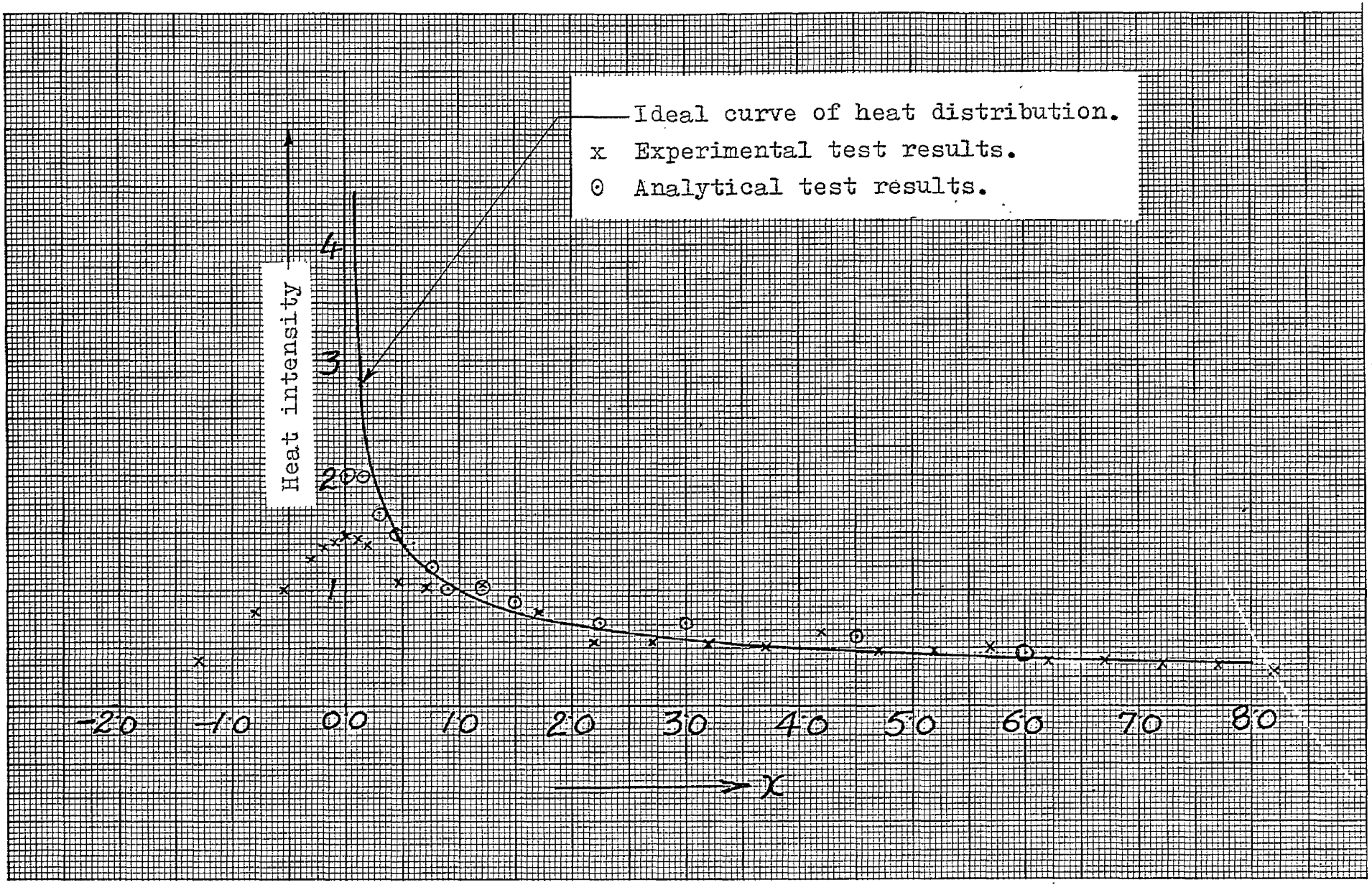

FIG. 4.6.1. Heat distribution given by the Composite reflector of table 4.6.1.

4.6.2 Construction and test:- The reflector with the design data given in table 4.6.1 was made and tested. To make the reflector, the process of construction outlined in section 4.6.2 was followed. Using the Gordon's type radiometer (section 6.4) and following the same procedure as for single reflectors (section 4.5.3), it was then tested. The results are given in table 4.6.2 and plotted in figure 4.6.1.

As expected, the composite reflector gave much higher intensity of heating at the hot end of the irradiated plane than the single reflectors. However, it still did not provide high enough intensity of heating at the hot end to meet the requirement of the present problem.

In order to improve the heating at the hot end further, it was thought to manipulate the values of x_o, S_o, L_1 in such a way that the point of incidence of reflected ray corresponding to θ_o fell in the region of hot end and moved towards the hottest point first as the reflector profile was traced with the positive value of $\Delta\theta$ and then traced back up to the full range of the plane of irradiation. Based on this idea, a reflector was designed, made and tested. The design data are given in table 4.6.3. The experimental test results are given in table 4.6.4 and plotted in figure 4.6.2. From the figure, it is evident that heat intensity at the hot end has improved further, but still it is not enough to serve the purpose of this problem.

4.7 ANALYTICAL TEST OF HEAT DISTRIBUTION GIVEN BY A REFLECTOR

In the preliminary tests of the reflectors designed with the help of computer and made with an average accuracy in the workshop, many

TABLE 4.6.3

COMPOSITE REFLECTOR (2) DESIGN DATA

Parameters:-

$\theta_o = 90^o$ $r_s = 0.300$ $S_o = -0.7500$
$d\theta = 2^o$ $x_o = -0.500$ $L_1 = 0.06$

$= 0.009510416$ Scale = 12 inches

θ (degrees)	r	x	slope
90	0.3000	-0.4663	0.4585
100	0.2773	-0.4788	0.5615
110	0.2602	-0.4886	0.6637
120	0.2475	-0.4954	0.7655
130	0.2387	-0.4992	0.8675
140	0.2331	-0.4999	0.9698
150	0.2306	-0.4972	1.0730
160	0.2310	-0.4911	1.1772
170	0.2342	-0.4813	1.2830
180	0.2404	-0.4676	1.3905
190	0.2496	-0.4498	1.4782
200	0.2623	-0.4276	1.6130
210	0.2788	-0.4005	1.7289
220	0.2997	-0.3682	1.8490
230	0.3258	-0.3300	1.9739
240	0.3577	-0.2853	2.1048
250	0.3964	-0.2331	2.2427
260	0.4428	-0.1725	2.3889
270	0.4975	-0.1023	2.5444
280	0.5610	-0.0209	2.7096
290	0.6333	+0.0790	2.8838
300	0.7144	0.1799	3.0645

TABLE 4.6.4

COMPOSITE REFLECTOR (2)

Experimental Test for Heat Distribution

x-co-ordinate	Distance from the hottest point	Relative heat intensity for best fit	Remarks
2.00	7.80	0.022	
1.50	7.30	0.231	
1.00	6.80	0.262	
0.50	6.30	0.634	
0.0	5.80	0.491	
-0.5	5.30	0.464	
-1.0	4.80	0.467	
-1.5	4.30	0.489	
-2.0	3.80	0.521	
-2.5	3.30	0.621	
-3.0	2.80	0.756	
-3.5	2.30	0.617	
-4.0	1.80	0.600	
-4.5	1.30	0.692	
-5.0	0.80	1.247	
-5.25	0.55	1.455	
-5.40	0.40	1.507	
-5.50	0.30	1.518	
-5.60	0.20	1.546	
-5.70	0.10	1.586	
-5.80	0.0	1.595	Hottest point
-5.90	-0.10	1.585	
-6.00	-0.20	1.495	
-6.25	-0.45	1.183	
-6.50	-0.70	0.714	
-7.00	-1.20	0.314	

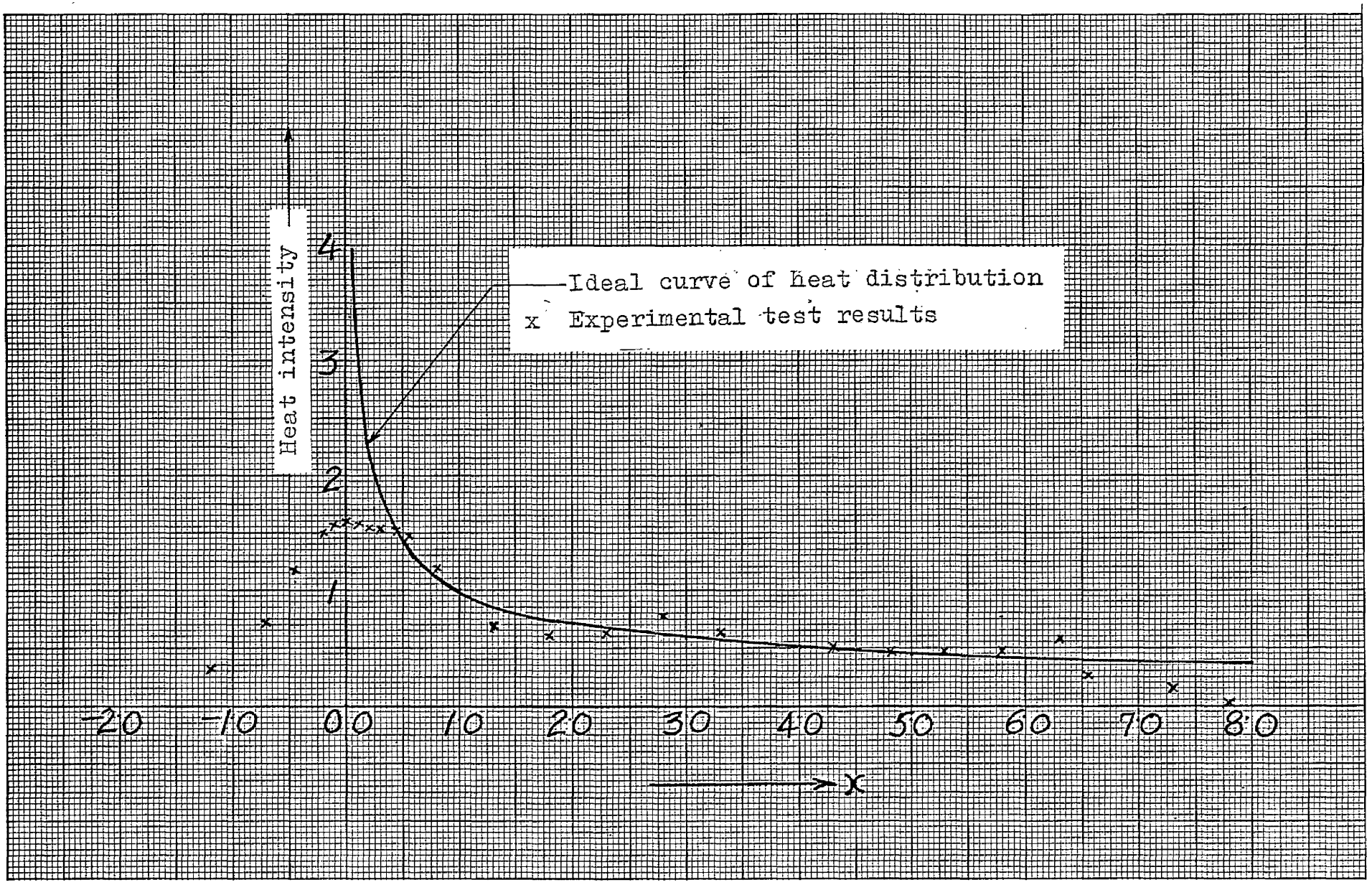

FIG.4.6.2. Heat distribution given by the Composite reflector of table 4.6.3.

factors cropped up, which rendered it difficult to assess the true performance of reflectors. These factors were:-

(1) Manufacturing error in the reflector

(2) Reflection in an improper direction due to the undulated surface of the reflector

(3) Interference by the convection of air, and

(4) Inadequacy of the radiometer to measure the heat intensity at different points on the plane of irradiation.

In order to eliminate the influence of these factors, an analytical method to find the heat intensity at a point on a plane of irradiation of a reflector was developed (appendix B) using this method; the heat intensity at various points from one end to another on the plane of irradiation can be determined and plotted. A curve passing through them, then, represents the heat distribution given by that reflector. This method, of course, assumes hundred per cent accuracy in the reflector profile and the reflectivity in the right direction.

Using equations (B-7) and (B-9), the single reflector of design data given in table 4.5.2 and the composite reflector of design data given in table 4.6.1 were tested on the computer. Test results are given in tables 4.7.1 and 4.7.2 and plotted in figures 4.7.1 and 4.6.1 respectively.

4.8 MULTI-CURVE REFLECTORS

4.8.1 Design, Development and Test of Multi-curve Reflectors:- Analytical tests given in tables 4.7.1 to 4.7.2 have left no doubt that practically little can be done to improve further the intensity of heating at the hot

TABLE 4.7.1.

SINGLE DIRECT RAY REFLECTOR

Analytical Test Results

x = co-ordinate of the hottest point on the plane of irradiation
= 0.20 (non-dimensional)
or 4.35 inches.

Distance from the hottest point		Arcs of filament irradiating the point (degrees) from - to	Total arcs of filament irradiating the point (degrees)	Relative heat intensity to give the best fit
Non-dimensional	Inches			
-0.09	-1.35	00 - 00	00.00	0.0
-0.05	-0.75	270 - 251 245 - 239	25	0.625
-0.04	-0.60	270 - 233 223 - 221	38	0.95
-0.02	-0.30	270 - 219 217 - 216	52	1.30
-0.01	-0.15	269 - 213 211 - 210	57	1.425
0.0	0.0	269 - 265 263 - 207 205 - 203	62	1.55
0.01	0.15	265 - 261 257 - 247 245 - 201	58	1.45
0.02	0.30	257 - 253 251 - 247 245 - 241 239 - 197	54	1.35
0.03	0.45	250 - 247 245 - 241 239 - 235 233 - 195	49	1.225
0.04	0.60	239 - 236 230 - 189 187 - 185	46	1.15

TABLE 4.7.1. Continued

Distance from the hottest point		Arcs of filament irradiating the point (degrees) from - to	Total arcs of filament irradiating the point (degrees)	Relative heat intensity to give the best fit
Non-dimensional	Inches			
0.06	0.90	226 - 225 215 - 179 177 - 174	40	1
0.11	1.65	200 - 199 195 - 193 190 - 162	31	0.78
0.20	3.00	163 - 157 154 - 138	20	0.5
0.31	4.65	125 - 113 111 - 110	13	0.325
0.35	5.25	117 - 116 113 - 108	6	0.15

TABLE 4.7.2.

COMPOSITE REFLECTOR (1)

Analytical Test Results

x - cordinate of the hottest point on the plane of irradiation = - 0.78 (non-dimensional) or -11.70 inches

Distance from the hottest point		Arcs of the filament irradiating the point (degrees) from - to	Total arcs of filament irradiating the point (degrees)	Relative heat intensity for the best fit	Remarks
non-dimensional	Inches				
-0.08	-1.20	205 - 225	20	0.50	
-0.06	-0.90	191 - 237	46	1.150	
-0.04	-0.60	185 - 244	59	1.475	
-0.02	-0.30	178 - 250	72	1.80	
-0.01	-0.15	176 - 252	76	1.90	
0.00	-0.0	171 - 254	83	2.075	The hottest point
0.01	0.15	169 - 227 232 - 256	82	2.05	
0.02	0.30	165 - 216 243 - 259	67	1.675	
0.03	0.45	164 - 210 248 - 262	60	1.50	
0.04	0.60	162 - 209 252 - 262	57	1.425	
0.05	0.75	160 - 202 256 - 262	48	1.20	
0.06	0.90	158 - 196 258 - 265	45	1.125	
0.08	1.20	154 - 190 263 - 268	41	1.025	
0.10	1.50	149 - 184 266 - 268	37	0.925	
0.15	2.25	143 - 172 275 - 276	30	0.750	
0.20	3.00	131 - 160 281 - 282	30	0.75	
0.30	4.50	116 - 139 289 - 290	24	0.600	
0.40	6.00	101 - 119	18	0.450	

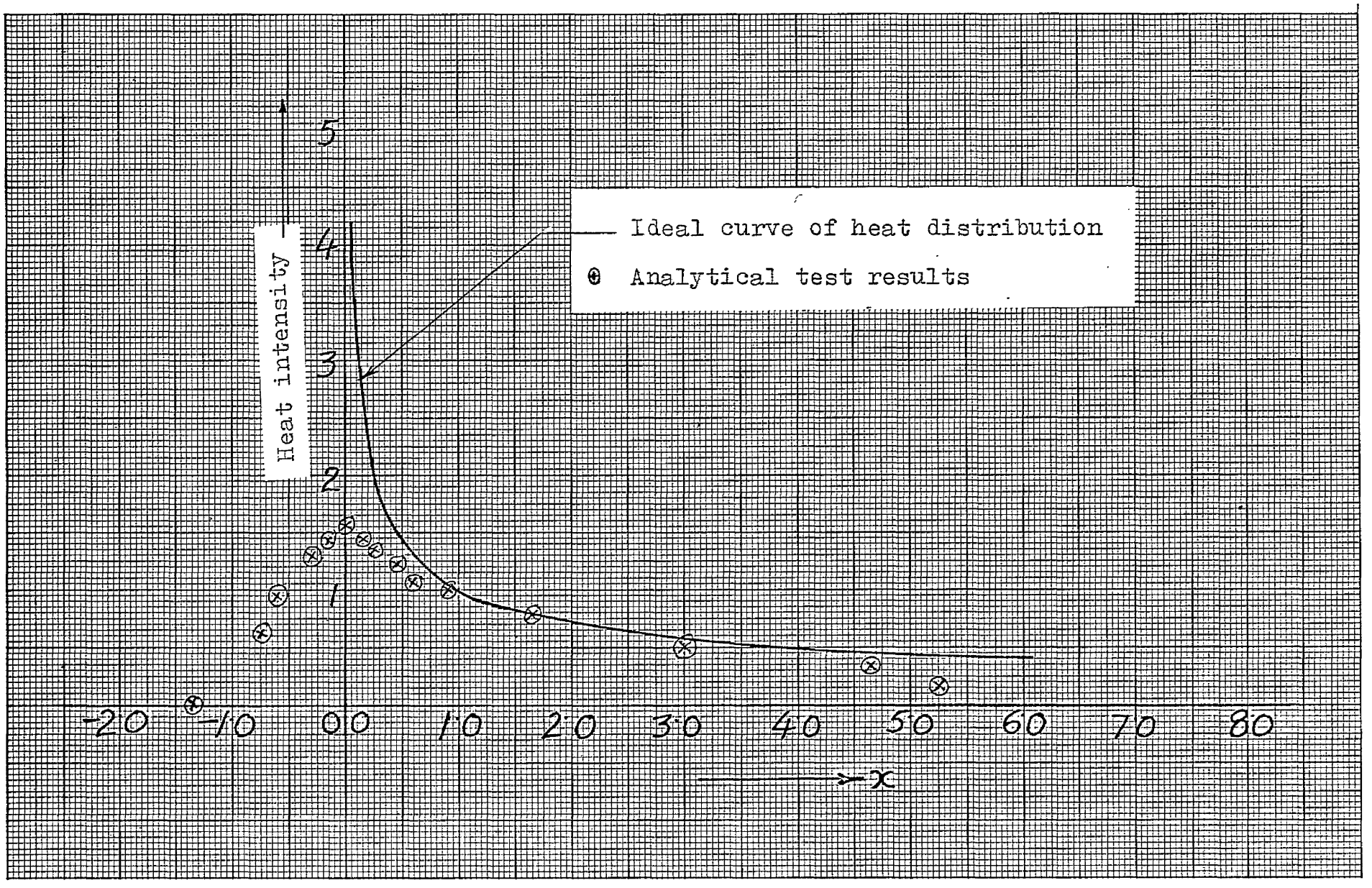

FIG. 4.7.1. Heat distribution given by the Single Direct Ray reflector of table 4.5.2.

end of the plane of irradiation. On one hand, a line source of heating was ideal to give a desired heat distribution curve, incorporating a high intensity of heating at the hot end of the plane; on the other hand a finite size of the heating element was necessary to obtain a sufficient heat energy. The latter deviated a great deal from the ideal case and produced a much reduced heat intensity at the hot end. This is due to the fact that any beam of rays, say $O_1 R_1 O_2$ (figure B-1) from a finite size heating element, after being reflected by a point on the reflector, strikes a region $P_1 P_2$ (figure B-1) on the plane of irradiation (and not a point), thus causing the heat of the beam to spread over a certain region. For a single curve reflector, therefore, it becomes impossible to build up a very high heat intensity, which is required at the hot end of the plane of irradiation.

In order to improve the situation, a further step of designing a multi-curve reflector was taken up. To do it, the value of parameters in equations (4.2.10), (4.2.11) and (A-10) at the different stages of the reflector profile had to be controlled precisely so that the major part of the reflector profile reflected the heat rays, to the hot end region. Reflector thus designed had to be subjected to the analytical test on the computer, using equations (B-7) and (B-9), and the heat distribution plotted on a graph. The heat distribution curve when drawn, may not look very even and so it has to be improved by repeating the procedure of designing the reflector again on computer with improved values of the parameters. The procedure has to be reiterated a number of times, till a desired smooth curve of heat distribution is obtained. Following this procedure, and after designing and analytically testing more than a dozen of reflectors, the final

reflector with as many as seven constituent curves was accepted. The design parameters and data are given in table 4.8.1 and the reflector is shown in figure 6.2.4. The analytical test results are given in table 4.8.2 and plotted in figure 4.8.1.

The reflector made following the procedure outlined in section 4.5.2, was tested experimentally using a rectangular foil radiometer (section 6.4). The test results are given in table 4.8.3 and plotted in figure 4.8.1.

4.8.2 Discussion of Results:- Figure 4.8.1 shows that the multi-curve reflector produced a much higher intensity of heating at the hot end of the plane of irradiation and hence has considerably improved the heating requirement. The analytical test of this reflector shows that heat distribution curve follows the ideal heat distribution curve up to as near as $\frac{1}{25}$ inch from the leading edge. This can be assumed to be quite satisfactory to represent the actual heating at the nose, in view of the comments made in section 1.4, especially of Nonweiler[22] that the aerodynamic heating becomes inversely proportional to the square root of the nose radius.

The experimental test value of the heat intensity at the hot end of the plane of irradiation is much lower than the analytical test value. This is due to the manufacturing error in the reflector, interference by convection of air, and unsuitability of the radiometer used. Besides, in the analytical test on the computer, the term involving the direct radiation was neglected and hence the test gave a bit higher heat intensity everywhere.

A considerable amount of heat lost beyond the plane of irradiation occupied by the model is a drawback of this type of reflector, but it should not be overlooked that this sort of heat loss is incurred in the single as well as in the composite reflectors; also, may be a bit less.

TABLE 4.8.1.

MULTI-CURVE REFLECTOR: DESIGN DATA

Parameters:- Scale 16" inches

Curve I			
$\theta_0 = 45^0$	$\lambda_0 = 0.30000$	$S_0 = -0.100$	
$d\theta = 1^0$	$x_0 = -0.5271$	$L_1 = 0.250$	
$r_k = 0.007$			
Curve II			
$\theta_0 = 60^0$	$\lambda_0 = 0.234667726$	$S_0 = -0.0010$	
$d\theta = 1^0$	$x_0 = -0.5699$	$L_1 = 0.0001$	
$r_k = 0.007$			
Curve III			
$\theta_0 = 70^0$	$\lambda_0 = 0.205368279$	$S_0 = -0.001$	
$d\theta = 1^0$	$x_0 = -0.6000$	$L_1 = 0.0001$	
$r_k = 0.007$			
Curve IV			
$\theta_0 = 95^0$	$\lambda_0 = 0.160344118$	$S_0 = -0.001$	
$d\theta = 1^0$	$x_0 = -0.6180$	$L_1 = 0.0001$	
$r_k = 0.007$			
Curve V			
$\theta_0 = 120^0$	$\lambda_0 = 0.138795756$	$S_0 = -0.001$	
$d\theta = 1^0$	$x_0 = -0.6250$	$L_1 = 0.0001$	
$r_k = 0.007$			
Curve VI			
$\theta_0 = 145^0$	$\lambda_0 = 0.131570929$	$S_0 = -0.001$	
$d\theta = 1^0$	$x_0 = -0.6240$	$L_1 = 0.0001$	
$r_k = 0.007$			
Curve VII			
$\theta_0 = 160^0$	$\lambda_0 = 0.132785322$	$S_0 = -1.15$	
$d\theta = 1^0$	$x_0 = -0.575$	$L_1 = 0.42$	
$r_k = 0.007$			

TABLE 4.8.1. Continued

θ (degrees)	r	x	Slope
45	0.3000	-0.5261	0.0168
46	0.2947	-0.5254	0.0276
48	0.2845	-0.5265	0.0435
50	0.2749	-0.5270	0.0711
52	0.2659	-0.5270	0.0928
54	0.2574	-0.5265	0.11447
56	0.2494	-0.5253	0.13624
58	0.2418	-0.5235	0.15808
60	0.2347	-0.5699	0.16393
62	0.2282	-0.5699	0.18481
64	0.2219	-0.5699	0.20558
66	0.2161	-0.5699	0.22626
68	0.2106	-0.5699	0.2468
70	0.2054	-0.6000	0.2578
72	0.2005	-0.6000	0.2781
74	0.1959	-0.6000	0.2984
76	0.1916	-0.6000	0.3186
78	0.1875	-0.6000	0.3387
80	0.1836	-0.6000	0.3588
82	0.1799	-0.6000	0.3788
84	0.1764	-0.6000	0.3987
86	0.1731	-0.6000	0.4186
88	0.1700	-0.6000	0.4384
90	0.1671	-0.6000	0.4582
92	0.1643	-0.6000	0.4780
94	0.1616	-0.6000	0.4977
95	0.1603	-0.6180	0.5019
96	0.1591	-0.6180	0.5117
98	0.1568	-0.6180	0.5313
100	0.1546	-0.6180	0.5509
102	0.1525	-0.6180	0.5704
104	0.1506	-0.6180	0.5900
106	0.1488	-0.6180	0.6094
108	0.1470	-0.6180	0.6289
110	0.1454	-0.6180	0.6483
112	0.1439	-0.6180	0.6677
114	0.1425	00.6180	0.6871
116	0.1412	-0.6180	0.7064
118	0.1399	-0.6180	0.7258

θ (degrees)	r	x	Slope
120	0.1388	-0.6250	0.7429
122	0.1378	-0.6250	0.7622
124	0.1368	-0.6250	0.7815
126	0.1359	-0.6250	0.8008
128	0.1352	-0.6250	0.8200
130	0.1344	-0.6250	0.8393
132	0.1338	-0.6250	0.8585
134	0.1333	-0.6250	0.8778
136	0.1328	-0.6250	0.8970
138	0.1324	-0.6250	0.9162
140	0.1321	-0.6250	0.9354
142	0.1318	-0.6250	0.9546
144	0.1316	-0.6250	0.9738
145	0.1316	-0.6240	0.9838
146	0.1315	-0.6240	0.9934
148	0.1315	-0.6240	1.0126
150	0.1315	-0.6240	1.0318
152	0.1316	-0.6240	1.0510
154	0.1318	-0.6240	1.0710
156	0.1321	-0.6240	1.0024
158	0.1324	-0.6240	1.1086
160	0.1328	-0.01955	1.1278
162	0.1322	-0.0354	1.3799
164	0.1316	-0.0511	1.3925
166	0.1312	-0.0667	1.4051
168	0.1309	-0.0822	1.4177
170	0.1307	-0.0976	1.4304
172	0.1306	-0.1129	1.4432
174	0.1306	-0.1281	1.4560
176	0.1307	-0.1431	1.4690
178	0.1309	-0.1581	1.4819
180	0.1312	-0.1729	1.4950
182	0.1316	-0.1876	1.5081
184	0.1321	-0.2022	1.5212
186	0.1327	-0.2167	1.5345
188	0.1334	-0.2311	1.5478
190	0.1342	-0.2453	1.5613
192	0.1352	-0.2594	1.5748
194	0.1362	-0.2733	1.5884
196	0.1373	-0.2871	1.6021
198	0.1386	-0.3008	1.6158
200	0.1400	-0.3143	1.6297
202	0.1415	-0.3276	1.6437
204	0.1432	-0.3408	1.6578
206	0.1450	-0.3537	1.6720
208	0.1469	-0.3665	1.6864

θ (degrees)	r	x	Slope
210	0.1490	-0.3791	1.7008
212	0.1512	-0.3914	1.7154
214	0.1537	-0.4036	1.7302
216	0.1562	-0.4154	1.7451
218	0.1590	-0.4271	1.7601
220	0.1619	-0.4384	1.7753
222	0.1651	-0.4495	1.7907
224	0.1684	-0.4602	1.8062
226	0.1720	-0.4707	1.8220
228	0.1758	-0.4808	1.8379
230	0.1799	-0.4905	1.8540
232	0.1842	-0.4998	1.8704
234	0.1888	-0.5088	1.8870
236	0.1938	-0.5173	1.9038
238	0.1990	-0.5253	1.9209
240	0.2046	-0.5329	1.9383
242	0.2106	-0.5400	1.9550
244	0.2169	-0.5465	1.9740
246	0.2237	-0.5524	1.9923
248	0.2309	-0.5578	2.0110
250	0.2386	-0.5625	2.0301
252	0.2468	-0.5665	2.0496
254	0.2556	-0.5698	2.0696
256	0.2649	-0.5724	2.0900
258	0.2749	-0.5741	2.1110
260	0.2856	-0.5749	2.1325
262	0.2969	-0.5748	2.1547
264	0.3091	-0.5738	2.1776
266	0.3220	-0.5716	2.2012
268	0.3358	-0.5683	2.2257
270	0.3504	-0.5638	2.2511
272	0.3660	-0.5579	2.2776
274	0.3825	-0.5505	2.3052
276	0.4001	-0.5415	2.3342
278	0.4186	-0.5306	2.3647
280	0.4382	-0.5177	2.3969
282	0.4587	-0.5025	2.4312
284	0.4802	-0.4846	2.4678
286	0.5026	-0.4634	2.5073
288	0.5256	-0.4382	2.5500
290	0.5493	-0.4080	2.5969
292	0.5732	-0.3709	2.6490
294	0.5972	-0.3231	2.7082
296	0.6208	-0.2588	2.7780

TABLE 4.8.2.

MULTI-CURVE REFLECTOR

Analytical Test for Heat Distribution

x - co-ordinate of the hottest point on the plane of irradiation = -0.55 or -8.80 inches

Distance from the hottest point		Arcs of filament irradiating the point (degrees)	Total arcs of filament irradiating the point (degrees)	Relative heat intensity for the best fit
Absolute	Inches	from - to		
-0.17	2.72	0 - 0	0	0.0
-0.15	-2.40	120 - 160	40	1.33
-0.10	-1.6	70 - 160	90	3.00
-0.05	-0.80	60 - 160 252 - 263	111	3.7
-0.02	-0.32	60 - 160 238 - 274	136	4.53
-0.01	-0.16	46 - 160 236 - 276	154	5.13
0.00	0.0	45 - 160 233 - 277	159	5.30
0.01	0.16	45 - 70 89 - 94 112 - 119 132 - 143 231 - 254 271 - 278	78	2.6
0.02	0.32	45 - 70 228 - 251 274 - 281	57	1.9
0.03	0.48	45 - 60 67 - 70 226 - 247 277 - 281	43	1.433
0.04	0.64	45 - 60 223 - 244 280 - 283	39	1.3
0.05	0.80	45 - 60 221 - 242 281 - 283.5	38.5	1.283
0.06	0.96	50 - 60 219 - 239 282 - 284.5	32.5	1.083
0.10	1.60	212 - 231 286 - 288	21	0.70

TABLE 4.8.2. Continued

Distance from the hottest point		Arcs of filament irradiating the point (degrees)	Total arcs of filament irradiating the point (degrees)	Relative heat intensity for the best fit
Absolute	Inches	from - to		
0.15	2.40	204 - 222 299 - 300	19	0.633
0.25	4.00	189 - 205	16	0.53
0.35	5.60	176 - 192	16	0.53
0.40	6.40	170 - 185	15	0.5

TABLE 4.8.3.

MULTI-CURVE REFLECTOR

Experimental results of the heat distribution

x - co-ordinate (inch)	Distance from the hottest point (inch)	Relative heat intensity for the best fit	Remarks
-1.00	7.80	0.375	
-2.00	6.80	0.585	
-3.00	5.80	0.533	
-4.00	4.80	0.487	
-5.00	3.80	0.555	
-6.00	2.80	0.573	
-6.50	2.30	0.737	
-7.00	1.80	0.759	
-7.50	1.30	0.851	
-8.00	0.80	1.064	
-8.25	0.55	1.509	
-8.50	0.30	2.287	
-8.60	0.20	2.440	
-8.70	0.10	2.675	
-8.80	0.0	2.815	The hottest point
-8.90	-0.10	2.747	
-9.00	-0.20	2.633	
-9.25	-0.45	2.283	
-9.50	-0.70	1.798	
-10.00	-1.20	1.387	
-10.50	-1.70	1.211	
11.00	-2.20	0.574	

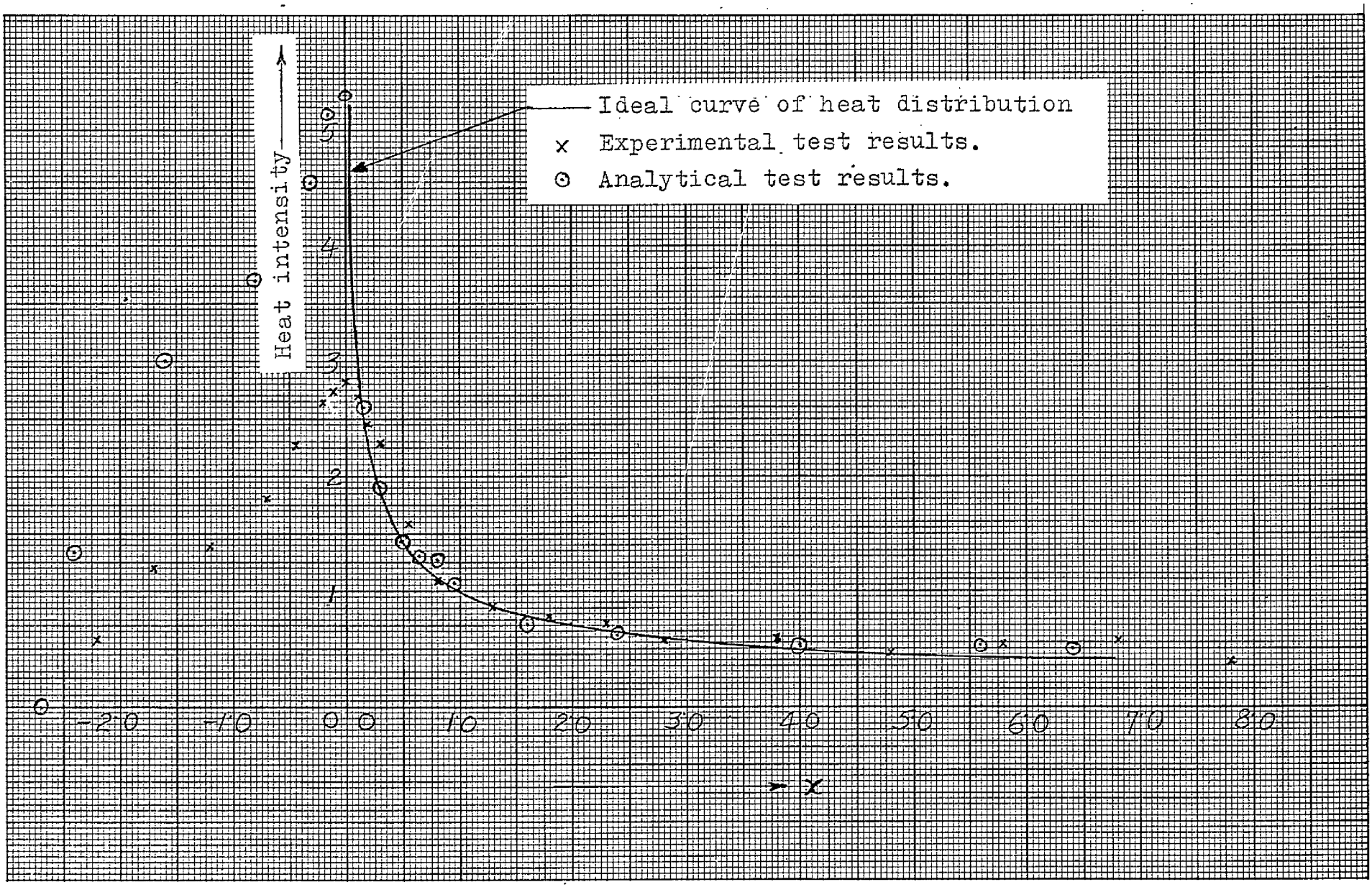

FIG. 4.8.1. Heat distribution given by the Multi-Curve reflector of table 4.8.1.

CHAPTER V

THE HEATING ELEMENT

5.1 Introduction

Different power outputs from the heating element will be required so that models of the conducting skins of materials of different thermal conductivities can be tested. A rough estimate of the heating rates on the models in section 3.5 showed that power output from a 12 inch long heating element should be up to 3.5 k.watts for a stipulated nose temperature of 800°K (vide section 3.4.3).

The heat output from a heating element can be obtained from the Stefan-Boltzman law of heat radiation, namely,

$$P = \varepsilon\sigma(T_1^4 - T_2^4)\,A \qquad \ldots(5.1.1)$$

where,

P = heat output (Watts)

ε = Emissivity of the element

σ = Stefan constant

(5.67×10^{-12} Watts per cm^2 per $(^\circ K)^4$

A = Surface area of the element (sq.cm.)

T_1 = Temperature of the element ($^\circ K$)

T_2 = Temperature of the environment ($^\circ K$)

In the present case, the contribution by T_2^4 is very small compared to that of T_1^4 and may be ignored. For a working temperature of 1800°K and $\varepsilon = 0.7$ of the heating element, its minimum diameter for a 12 inch length comes to about $\frac{1}{4}$ inch in order to produce the estimated 3 k.w. heat energy. This renders it unsuitable to use any solid rod or a tube of any

metal or alloy as heating element since the electrical resistance will be very small. A helically wound fine wire filament supported on a rod of a suitable material is a probable choice.

5.2 SUPPORT ROD

5.2.1 Necessary characteristics of the support rod material

The following are the physical, chemical and electronic characteristics required of the material of the support rod:-

(a) A bad conductor of electricity, unless insulated from the heating filament by some other means.

(b) very low vapour pressures at high temperatures.

(c) a high creep strength at a temperature of application of about $1500^{o}C$.

(d) a high melting point.

(e) a low electron emission at the high temperature of application.

and (f) no chemical reaction with the material of the heating filament.

5.2.2 A detailed survey of the high temperature materials

A detailed study of the properties of high temperature materials was undertaken. The collected data on these properties are given in table 5.2.1. Metallic rods could not be used directly to support the heating filament because of their good electrical conductivity. Ceramics are the obvious choice.

Amongst the refractory oxides, except Alumina and oxides of Beryllium, Calcium, Chromium, Magnesium, Thorium, Uranium and Zirconium-

TABLE 5.2.1

High Temperature Materials and their Physical Characteristics.

Material, and Melting point	Ultimate tensile strength p s i	creep property	total normal emissivity	Vapour pressure torr	Electrical resistivity x 10^6 ohm-cm	Electron emission amp/cm^2	Remarks
Nickel 1450	55000 to 85000 (24)	-	25°C - .045) unoxi- 1000°C - .19) dised (32) 200°C - .37) oxidised 1200°C - .85) (32)	1140°C - 10^{-5} 1250°C - 10^{-4} (34)	20°C - 6.85 600°C - 37.2 1000°C - 48.3 (24)	-	oxidises quickly in air above 700°C.
Nichrome 1395	-	100 hrs. life at 500 psi at 1250°C (25)	1000°C - 0.87) oxi- 1300°C - 0.89) dised (32)	-	20°C - 150.0 (32)	-	oxidises quickly in air above 700°C
Chromium 1890	-	100 hrs. life at 7000 psi at 1095°C (25)	-	907°C - 10^{-5} 992°C - 10^{-4}	20°C - 13.0 (32)	-	oxidises quickly in air above 700°C
Platinum 1773	20,000-24,000 (24)	-	1000°C - .15 (unoxidised) (24)	1285°C - 10^{-5} 1480°C - 10^{-4} 1740°C - 10^{-3} (24)	20°C - 10.6 (24)	-	does not oxidise in air up to 1400°C (24)
Columbium or Niobium (2500)	40,000-55000 at 20°C (25)	100 hrs. life at 7000 psi at 982°C (25)	1500°C - .19) unoxi- 2000°C - .24) dised (24)	2000°C - 1.39×10^{-6} 2210°C - 4.4×10^{-5} (24)	0°C - 15.24 600°C - 38.96 (24)	1800°K - 6.95×10^{-5} 2000°K - 1.16×10^{-2} (35)	oxidises very quickly in air above 350°C
Molybdenum 2620	20°C - 60,000 1000°C - 25000 (25)	100 hrs. life at 12000 psi at 1093°C (25)	1500°C - .19) unoxi- 2000°C - .24) dised (24)	1923°C - 10^{-5} 2095°C - 10^{-4} (24)	20°C - 5.0 1000°C - 27.0 1500°C - 43.0 (26)	1800°K - 1.05×10^{-4} 2000°K - 2.15×10^{-3} (35)	oxide volatilises above 720°C
Tantalum 2996	20°C - 60000 1000 °C - 20000 (25)	100 hrs. life at 7000 psi at 1200°C (25)	1500°C - .21) unoxi- 2000°C - .25) dised (24)	2400°C - 10^{-5} 2590°C - 10^{-4} (24)	20°C - 12.5 1000°C - 54.0 1500°C - 72.0 (26)	1800°K - 3.32×10^{-4} 2000°K - 6.21×10^{-3} (35)	Non-adherent oxide formed above 500°C.

TABLE 5.2.1 contd.

Material, and Melting point	Ultimate tensile strength p s i	creep property	total normal emissivity	Vapour pressure torr	Electrical resistivity x 10^6 ohm-cm	Electron emission amp/cm	Remarks
Tungsten 3400	1390°C - 50000 1670°C - 18000 1940°C - 10000 (25)	100 hrs. life at 8000 psi at 1500°C (25, 30)	1525°C - .236)smooth- 1825°C - .269)dised (32)	2067°C - 10^{-8} 2550°C - 10^{-5} (32)	20°C - 5.51 1500°C - 50.05 1700°C - 56.6 (32)	1800°K - 4.47×10^{-5} 2000°K - 1.00×10^{-3} 2200°K - 1.33×10^{-2} (35)	-
1% Thoria-tungsten alloy	1370°C - 50000 1650°C - 40000 1925°C - 28000 (25)	-	-	Above 1700°C the metal Thoria evaporates out (28)	-	1600°K - 4.06×10^{-2} 1800°K - 0.428 2000°K - 2.864 (35)	Thoria is not stable in surface to surface contact with W above 2200°C (32)
2% Thoria-tungsten alloy	1370°C - 35000 1650°C - 31000 1925°C - 26000 (25)	100 hrs. life at 13000 psi at 1500°C (25, 30)	-	Above 1700°C the metal Thoria evaporates out (28)	-	1600°K - 4.06×10^{-2} 1800°K - 0.428 2000°K - 2.864 (35)	Thoria is not stable in surface to surface contact with W above 2200°C (32)
Alumina 2030	25°C - 37000 1000°C - 28000 1500°C - 3500 (29)	-	1060°C - 0.21 (29)	Up to 2200°C resists high vacuum (25)	500°C - 1.5×10^{17} 1000°C - 5×10^{12} 1500°C - 10^{10} (29)	-	No reaction with W or Mo up to 1900°C (26)
Magnesium oxide 2800	-	-	1060°C - 0.31 (29)	Up to 1600°C resists high vacuum (25)	1500°C - 1.5×10^{9} (29)	-	No reaction with W up to 2000°C and Mo up to 1600°C (31)
Zirconium oxide 2500	25°C - 15000 (29)	-	1060°C - 0.24 (29)	-	500°C - 10^{11} 2000°C - 40×10^{6} 1500°C - 5×10^{6}	-	No reaction with W up to 1600°C and with Mo up to 2200°C (31)

Note:- Quantity in bracket gives reference number.

others have melting points lower than 2000°C and hence they are not suitable for this application. Beryllium oxide is not used generally because of its health hazards. Calcium and chromium oxides have not been developed to be used alone as ceramics, but they constitute certain percentages in different ceramic bodies. Uranium oxide also is not used for general purpose. Prohibitively high cost of some of these oxides stands in the way of their general application.

Aluminium, Magnesium and Zirconium oxides form the most general purpose ceramics. Magnesium and Zirconium oxides have higher working temperatures of 2300°C compared to 1900°C of Alumina, but they have less mechanical strength at high temperatures, much lower electrical resistance and lower thermal conductivity. Their behaviour in high vacuum in surface to surface contact with refractory metals which might have to be used for heating filament, is not very well known. Johnson[31] found that Zirconium oxide becomes unstable in vacuum in contact with tungsten at 1600°C.

Alumina does not react with any of the refractory or platimum group metals up to a temperature of 1750°C. Its tensile strength goes on improving with percentage of purity.[29] But the purity of most of the commercial alumina products does not go beyond 99%. The Degussit Alumina ($AL_2O_3 > 99.5\%$) supplied by Messrs. Bush Beach and Segner Bayley Ltd., was found to be the purest and hence it was used.

In order to reduce the sagging of the heating element to a minimum, the filament support rod must have a high mechanical strength and creep property at the high temperature of application. The figure 5.2.1 shows the ultimate tensile strength of Alumina, Molybdenum, Tantalum, Tungsten; one percent thoriated

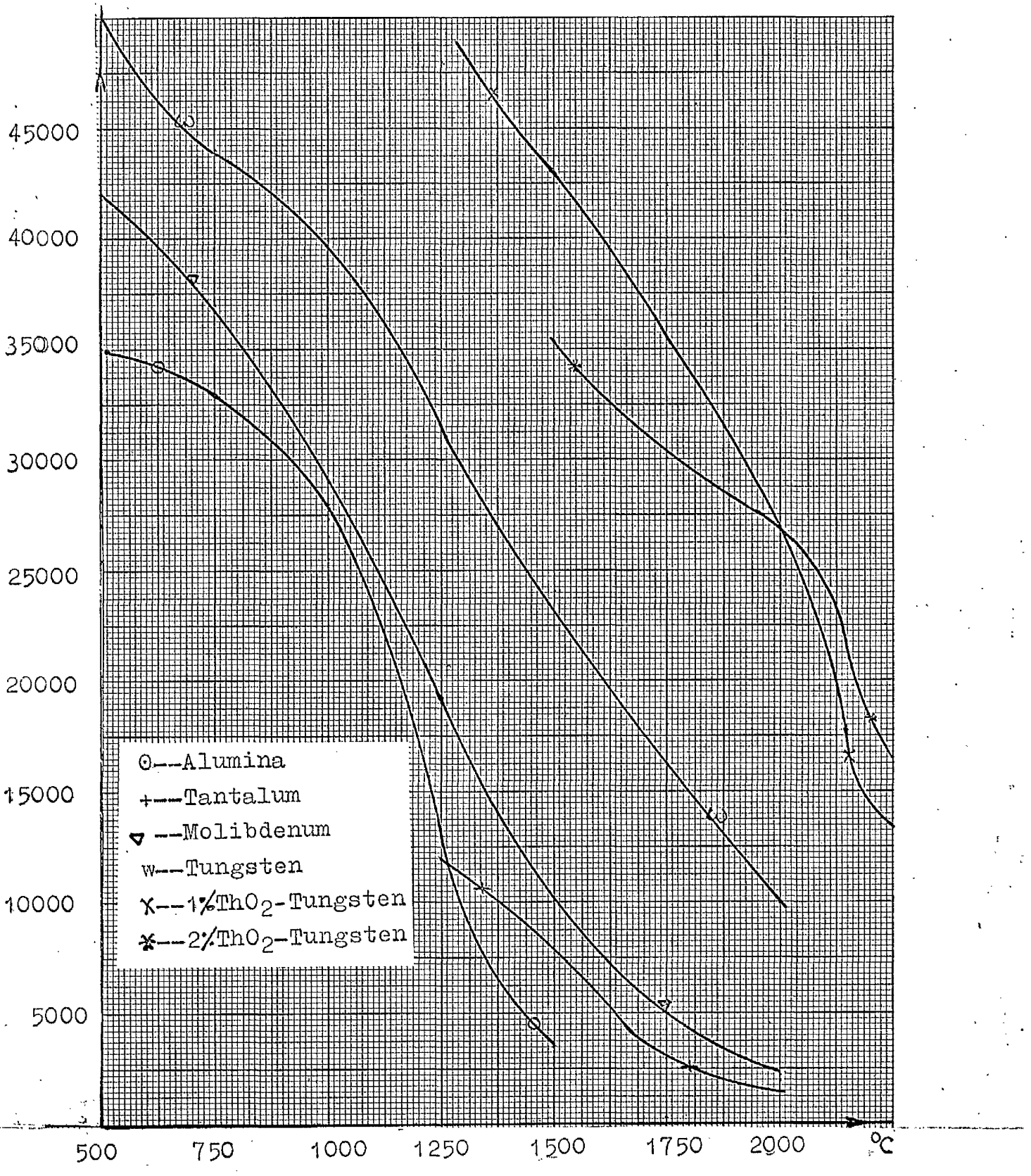

FIG. 5.21. Ultimate tensile strength of high temperature materials, p.s.i. (alumina-ref. 29, 2%ThO_2-W--ref. 30 and others ref. 33)

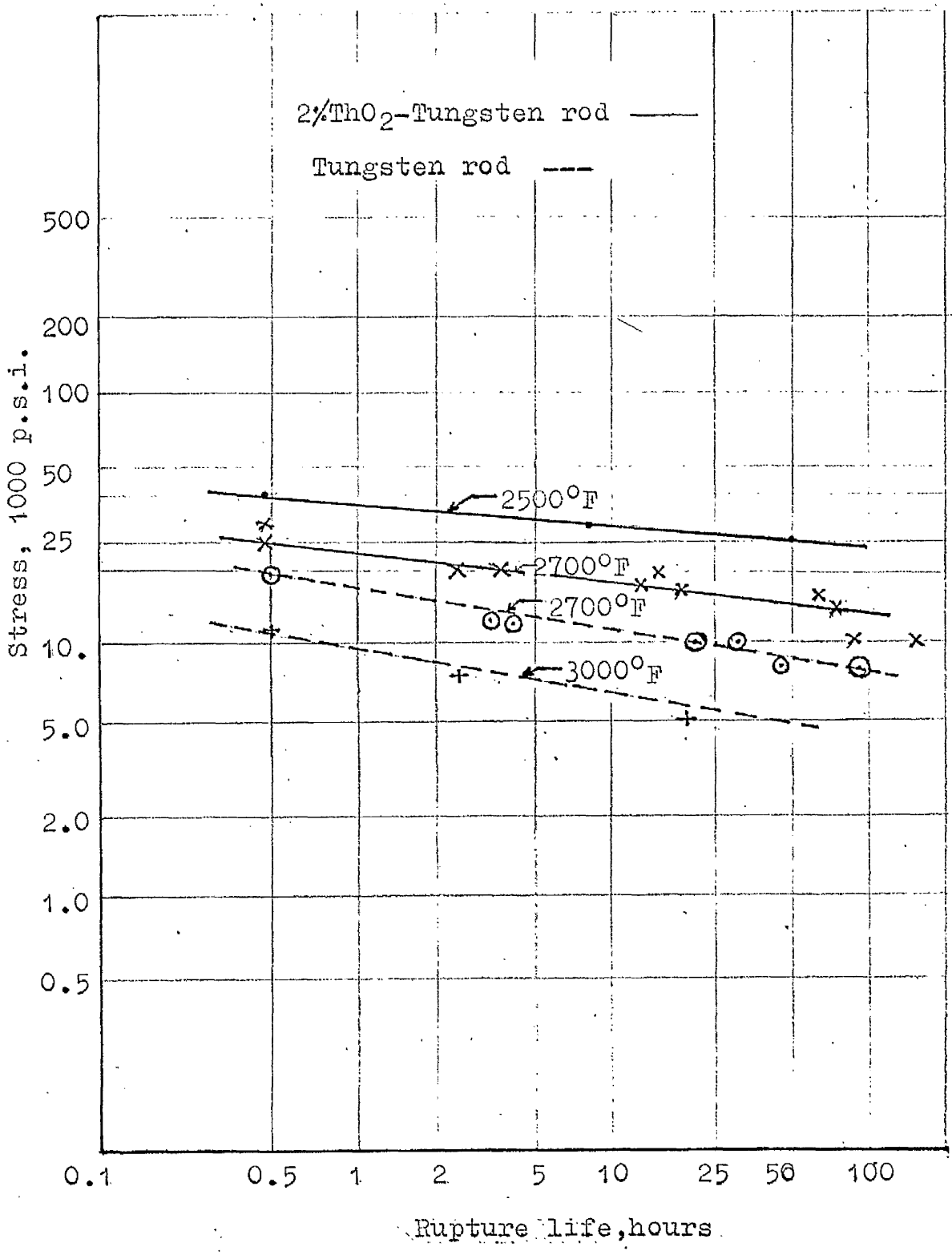

FIG.5.2.2. Stress-Rupture properties of Tungsten and 2%ThO2-Tungsten rods (ref.30)

Tungsten and two percent thoriated Tungsten, at different temperatures. As shown in this figure, Alumina maintains a good strength up to 1000°C, but above that, there is a rapid drop of its strength. This renders it unsuitable for its application to support the heating filament. Thoriated tungstens have higher strengths at high temperatures than any of the unalloyed refractory metals. Figure 5.2.2 reproduced from Sell's[30] physical metallurgy of Tungsten and Tungsten base alloys shows the creep properties of thoriated Tungsten against that of the pure Tungsten.

Finally, Degussit Alumina tube ($Al_2O_3 > 99.5\%$) 4 mm. outside dia. x 3 mm. inside dia. threaded with a ground 2.8 mm. diameter, 2% thoriated Tungsten rod was used to support the filament. There was no danger of the alumina tube breaking at high temperatures due to different thermal expansions of rod and the tube. The coefficient of thermal expansions are 5.2×10^{-6} per °C and 7.7×10^{-6} per °C of Tungsten and Alumina respectively up to 1000°C.

5.3 HEATING FILAMENT MATERIALS

High working temperature, high total radiant emissivity and low vapour pressure are the main physical properties required for the material of the heating filament. A good ductility for easy coiling and an average electrical conductivity are also necessary. It is absolutely essential to have no chemical reaction with the alumina tube at high temperatures in high vacuo. Absence of, or at least a minimum of electronic phenomena, such as electron-emission etc. are also desirable.

From table 5.2.1 it is evident that almost all unoxidised metals or their unoxidised alloys have poor emissivity and hence to produce the required amount of heat, the filament has to work at a much higher temperature. But the temperature can not be allowed to go above 1500°C because of liability of sagging of the filament support-rod. Even for working at this level of temperatures only a few metals are available, viz. Platinum, Rhenium, Molybdenum, Niobium, Tantalum and Tungsten.

Besides the high cost, Platinum and Rhenium have the disadvantage of lower emissivity and higher vapour pressure at high temperatures than that of refractory metals. Their volatile oxide formation is another disadvantage.

Molybdenum is cheapest in the refractory metal group and is more ductile than Tungsten. Moreover, Molybdenum oxides evaporate out in high vacuum at about 1000°C. Its evaporation rates at high temperatures are much higher than that of Tungsten and Tantalum.

Tantalum compares with Tungsten in emissivity and vapour pressure but its very high cost is a disadvantage. The oxides of tantalum are more stable. They decompose or volatilize at a temperature level of 1700 to 1800°C compared to 1300°C of tungsten[24]. Even after long heating, and in spite of recrystallization, no brittleness occurs with tantalum as with molybdenum and tungsten[26]. But in hydrogen, oxygen, nitrogen or carbon-containing atmospheres, gas absorption and chemical reactions begin with formation of hydride, oxide, nitride or carbide, causing immediate brittleness which can not be removed - or at least only partially. Only hydride formation is reversible so that tantalum rendered brittle by hydrogen, can be softened again by heating in high vacuum[26].

Tungsten, with its very high melting point of about 3400°C, low vapour pressures and good mechanical strengths at high temperatures, appears suitable for its application at high temperatures in high vacuo. The high temperature emissivity of unoxidised tungsten also is higher than that of any other refractory metals or other high temperature materials such as Nickel, Chromium or Platinum. But tungsten is much more difficult to work than molybdenum or tantalum.

So far as electrical resistance is concerned, all refractory metals have poor resistance compared to the conventional heating-element materials such as nickel, chromium and their alloys. Expressed in microhm-cm, the specific resistance of tungsten, molybdenum and tantalum range from 5 to 12.5 at room temperature, whereas nickel and chromium alloys range from 110 to 145.

5.4 TUNGSTEN AND PURE NICKEL FILAMENTS

5.4.1 Experimental tests on tungsten filaments

From the various properties considered in section 5.3 it is obvious that the tungsten is the best amongst the refractory metals for the present application as heating filament. Hence a number of tests were carried out to examine its suitability in the condition of the present problem. To test it, the tungsten filament, coiled and supported on an alumina rod, was sealed in a pyrex glass tube of about 50 mm. diameter, which was subsequently evacuated to a vacuum of 10^{-3} torr. Metal-(tungsten)in-glass seal, one at either end of the glass tube, provided the electrical terminals to the tungsten filament. When the electrical power was put on, the filament heated up and started oxidising. It had

already been slightly oxidised during its sealing in the glass tube, which could not be avoided easily. On further heating, the oxides evaporated out at about 1250°C leaving the tungsten surface smooth and shining. The evaporated, dark blue tungsten oxide got deposited on the glass tube wall, rendering it almost opaque. It was, therefore, necessary to prevent oxidation of the tungsten filament in order to avoid the reflector's surface getting coated with oxides due to their subsequent evaporation. All efforts to prevent oxidation in the further test of tungsten failed.

To prevent the oxidation of tungsten in a large vacuum chamber, even in a high vacuum of 10^{-4} to 10^{-5} torr, was going to be exceedingly difficult. Slow diffusion of air molecules through the walls of the chamber and degassing of models, reflector and other equipment inside it, would be enough to provide a stream of oxygen molecules for a continuous oxidation of tungsten filament. Besides, unoxidised tungsten has very low emissivity compared to that of oxidised nickel or nickel alloy, and hence in order to produce the heat generated by an oxidised nickel filament at 1200°C, tungsten has to work at 1600° to 1700°C. This swings the decision in favour of a nickel or a nickel alloy heating filament.

Though chromium has a higher melting point than nickel and equally good emissivity, it can not be used alone or alloyed with nickel at high temperatures in high vacuo because of its high vapour pressures. Both nickel and nickel oxide have very low vapour pressures at high temperatures[34] and the oxide's emissivity[36] of the order of 0.8 to 0.85 at temperatures of 1000 to 1200°C. Since nickel filament working at a lower temperature of 1100 to 1200°C produces the same heat output as tungsten filament at higher temperatures of 1500 to 1600°C, use of nickel filament renders the filament

support tube of alumina, reinforced with the thoriated tungsten rod, more rigid against sagging.

All commercial nickels are not more than 99 per cent pure; which in a high vacuum do not stand a temperature higher than about 900°C. Pure nickel (99.92%) was obtained from the British Driver-Harris Co. to be used for the filament. Their special alloy "Therlo" (29% Ni, 17% Co and the balance iron) did not give better results than high purity nickel. Besides, it is not as much ductile as pure nickel and hence it is more difficult to work.

5.42 Experimental tests on Pure Nickel Filaments

Heat radiated by an oxidised high purity nickel wire, freely suspended in a high vacuum, was determined by Wong[23]. His results are plotted in figure 5.5.1.

However, in order to estimate precisely the heat output from a nickel filament, helically wound on a ceramic support tube, an experiment under similar conditions was necessary. To do it, a 0.028 inch diameter pure nickel wire was helically wound (26.T.P.I) on a ceramic rod of 0.156 inch diam. x 4 inch length. The surface area of the helically wound portion of this heating element was 15.89 sq.cm. This was oxidised at 850°C for 30 minutes andthen tested in high vacuo of 10^{-5} to 16^{-6} torr at different temperatures. The results aregiven in table 5.4.1 and plotted in figure 5.5.1. The temperature of the filament was measured by an optical pyrometer.

On prolonged testing above 1000°C Wong[23] found that emissivity of the oxidised nickel gradually reduced after a service of about 6 hours. This might have been mainly due to the evaporation of the oxide film. However, this will have the effect of reducing the heating capacity of the bare oxidised nickel wire, and thereby curtailing its suitability above 1000°C in the present application.

TABLE 5.4.1

HEAT OUTPUT OF OXIDISED NICKEL FILAMENT

Temperature OC	Vacuum Torr	Heat output Watts	Watts per sq. cm.	Remarks
750	6×10^{-6}	55.50	3.49	Olive green oxide film adhered well up to the end of the expirement.
790	6×10^{-6}	66.20	4.17	
815	6×10^{-6}	77.99	4.91	
840	6×10^{-6}	91.30	5.75	
865	6×10^{-6}	104.30	6.56	
888	6×10^{-6}	118.72	7.47	At 1070^{0}C, one of the brighter glowing ends of the filament at the junction with the power terminals burned out.
905	6×10^{-6}	134.30	8.45	
930	6×10^{-6}	150.30	9.46	
955	6×10^{-6}	168.00	10.57	
985	5×10^{-6}	185.00	11.64	
1012	5×10^{-6}	202.70	12.75	
1035	5×10^{-6}	222.00	13.97	
1055	5×10^{-6}	239.80	15.09	
1070	5×10^{-6}	256.60	16.36	

5.5 GRAPHITE AND LAMPBLACK PLASTERED FILAMENTS

From the tests on oxidised Nickel filaments (section 5.4) it is evident that maximum heat power available from the oxidised nickel filament was about 800 to 900 watts per ft. length of the filament of diameter 0.224 inch. This falls short of requirement (section 3.5). In order to increase power output, it was necessary to test materials of higher emissivity and of higher working temperature. With this idea, oxidised nickel filaments plastered with pastes of lampblack and Fibreflex cement (a high vacuum cement, which can withstand a temperature up to 1260°C - supplied by Messrs. Carborundum Co.) and graphite and Fibreflex cement were tested in the similar conditions as the oxidised nickel filaments (section 5.4.2). The mixing of the cement with the lampblack is likely to reduce its emissivity and hence care was taken to keep the proportion of cement just sufficient to form a 'workable' paste. The test results are given in tables 5.5.1 and 5.5.2, and are plotted in figure 5.5.1. For the sake of comparison, graphs of heat output of unoxidised nickel and tungsten are also shown in the same figure.

A test run of lampblack paste, plastered over the tungsten filament, did not show any advantage over the nickel filament plastered with the same paste.

On prolonged testing at high temperature it was found that graphite burned out more quickly than lampblack. A test run at 1100°C for 15 hours in a vacuum of 10^{-6} torr was carried out to ascertain the life of the lampblack-pasted filament. At the end of the test, lampblack was found to have burned out in small patches at different parts of the filament,

but the filament was still working well. Even in this high vacuum there are molecules of oxygen available to cause a slow burning of the lampblack, which can only be reduced further by using a suitable "getter" like titanium to absorb the oxygen molecules or by flushing the vacuum chamber with inert gases.

In the tests, temperature of the filament was measured by an optical pyrometer and heat output in watts in terms of current and voltage by an ammeter and a voltmeter respectively. A large 18 inch diameter pyrex glass bell jar formed the part of the vacuum chamber. The surface area of each filament was 15.89 sq.cm.

TABLE 5.5.1

HEAT OUTPUT FROM THE LAMPBLACK PLASTERED NICKEL FILAMENT

Temperature ^{o}C	Vacuum Torr	Heat output Watts	Watts per sq. cm.	Remarks
770	7×10^{-6}	94.80	5.97	
790	7×10^{-6}	108.40	6.82	
810	7×10^{-6}	123.60	7.78	
833	7×10^{-6}	138.45	8.71	
862	6×10^{-6}	155.20	9.77	
892	6×10^{-6}	171.36	10.78	
923	5×10^{-6}	189.00	11.89	
964	5×10^{-6}	208.05	13.09	At about 1155°C some cracks on the lampblack plaster appeared.
985	4×10^{-6}	226.00	14.22	
1010	4×10^{-6}	244.40	15.38	
1035	5×10^{-6}	264.00	16.61	
1060	5×10^{-6}	285.66	17.98	
1082	6×10^{-6}	306.72	19.30	
1107	7×10^{-6}	331.00	20.83	
1132	7×10^{-6}	354.12	22.29	
1155	7×10^{-6}	378.54	23.82	
1185	7×10^{-6}	404.88	25.48	

TABLE 5.5.2

HEAT OUTPUT FROM THE GRAPHITE PASTED NICKEL FILAMENT

Temperature °C	Vacuum Torr	Heat output Watts	Watts per sq. cm.	Remarks
720	6×10^{-6}	71.00	4.47	
740	6×10^{-6}	81.60	5.14	
760	6×10^{-6}	94.80	5.97	
782	6×10^{-6}	107.60	6.77	
812	6×10^{-6}	123.60	7.78	
840	6×10^{-6}	138.80	8.74	
865	5×10^{-6}	155.20	9.77	
890	5×10^{-6}	172.00	10.82	
920	5×10^{-6}	189.00	11.89	
955	5×10^{-6}	208.05	13.09	
980	5×10^{-6}	226.40	14.25	
1000	5×10^{-6}	241.5	15.20	
1015	5×10^{-6}	261.8	16.48	A few cracks developed at the filament at about 1152°C, but it was still working well.
1035	5×10^{-6}	282.9	17.80	
1065	5×10^{-6}	302.88	19.06	
1095	5×10^{-6}	327.50	20.61	
1125	5×10^{-6}	352.3	22.17	
1152	5×10^{-6}	376.65	23.70	
1180	5×10^{-6}	402.08	25.30	

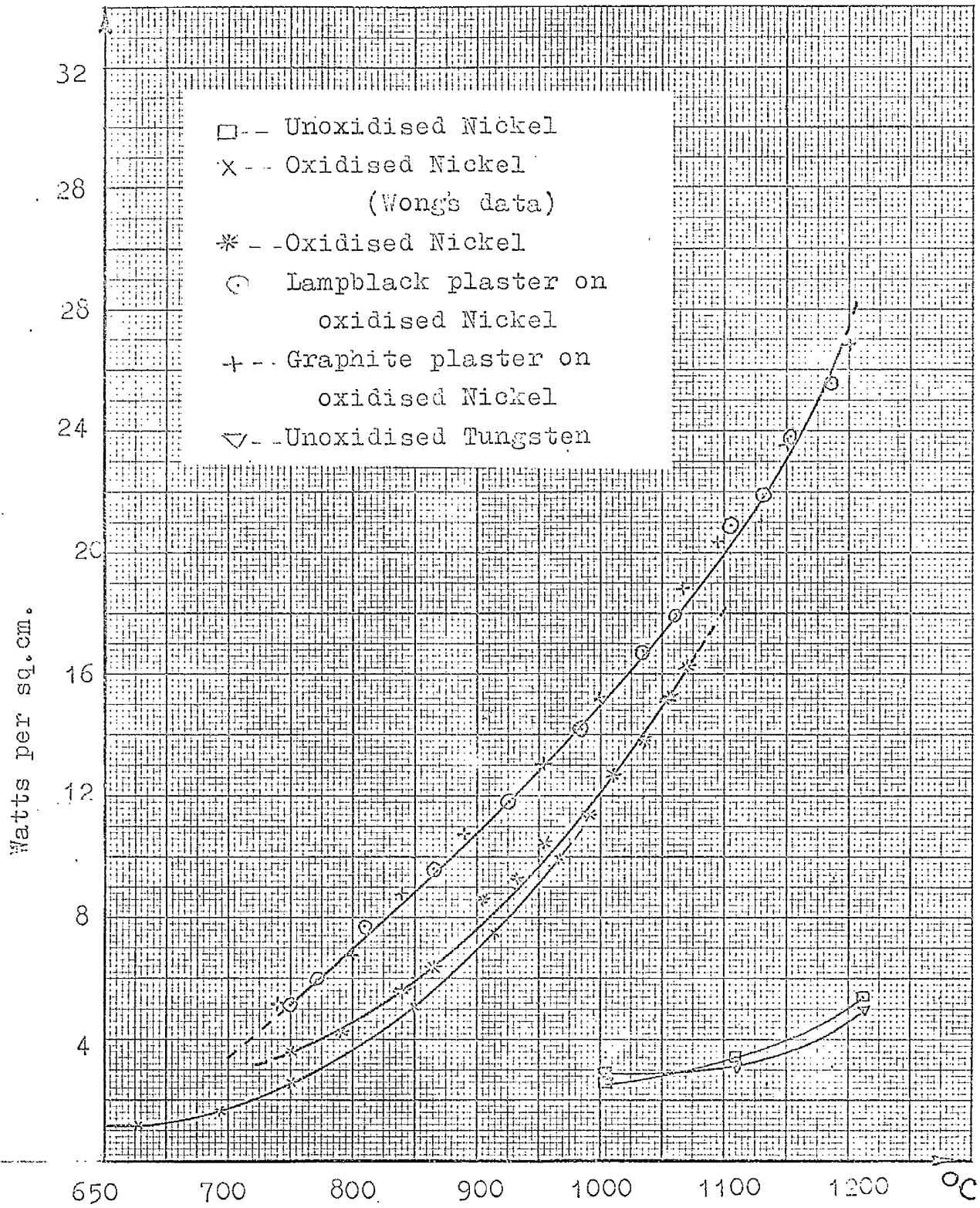

FIG.5.5.1.

Heating Capacity of different materials at high temperatures.

5.6. Discussion of results and the final design of the heating elements.

The discrepancy in the results of the present work and that of Wong[23] for the radiant heat capacity of high purity nickel-wire is due to two different conditions of tests. The alumina rod supporting the nickel coil in the present work was a little longer than the coil and hence it provided an extra surface for the heat radiation. This has not been accounted for in calculating the heat output per unit area from the filament, since the object was to find the material of the filament giving maximum heat output under the conditions in which the filament was to be used later in the experiment.

The figure 5.5.1 clearly shows that there is a substantial gain of 30 to 40 per cent in heat output by use of lampblack and graphite over the bare oxidised nickel filament. Therefore, a nickel filament oxidised at 850°C for 30 minutes and supported on 4mm. outside diam. x 3 mm. inside diam. Degussit alumina tube ($Al_2O_3 > 99.5\%$) and plastered with a paste of lampblack and Fibreflex cement, was finally selected to be used. The alumina tube was reinforced with a ground, 2.8 mm. diam., 2% thoriated tungsten rod to strengthen it against sagging at nigh temperatures. Over all diameter of the filament including the plaster comes to about 0.219 to 0.220 inch. This leaves the filament undersize by about 0.004 to 0.005 inch, because the designed diameter is 0.224 inch (vide section 4.8); which will be made up at high temperatures due to thermal expansion. Working at 1100°C, this filament would produce about 1.2 K-watts per ft. length.

This should be remembered, however, that lampblack filament also suffers the drawback of a slow evaporation and burning at the high temperature

of application of about 1100°C. This, not only reduces the life of the filament, but also the deposition of evaporated lampblack and its oxide on the highly polished reflector surface interferes with the working of the reflector. Therefore, it is desirable to start the heating of the filament only when a desired high vacuum is obtained, and then to carry on the test as quickly as possible.

CHAPTER VI

FABRICATION OF EQUIPMENT AND INSTRUMENTS

6.1 Introduction

A method was developed to obtain a high accuracy in the construction of the reflector. Since the experiments had to be carried on in high vacuo (vide section 3.6), a large vacuum chamber to house the reflector and the test-model, was designed and constructed. The pumping system consisted of a 6 inch diffusion pump and a single stage rotary pump.

To measure the heat distribution accurately, radiometers were developed and calibrated using a water calorimeter and a uniform source of heat. The water calorimeter and the heater were designed and constructed especially for this purpose. To support the conducting skin model in position and also to facilitate the handling of the thermocouple wires, a model support tray was designed and constructed.

6.2 Fabrication and test of a multi-curve reflector

6.2.1 Essential characteristics of the material of the reflector

High reflectivity of infra-red radiation and capacity to take up and maintain a mirror-like surface finish were the most essential features required from the material of the reflector. A high thermal conductivity was also desirable, to reduce the temperature gradient across the thickness of the reflector and between one portion and another. Gold and silver range high for the reflectivity of radiation of 0.6 micron to 10 micron wave lengths. Copper and Aluminium come next, and both work very well in high vacuo. Copper, because of higher thermal conductivity than that of aluminium and unlike

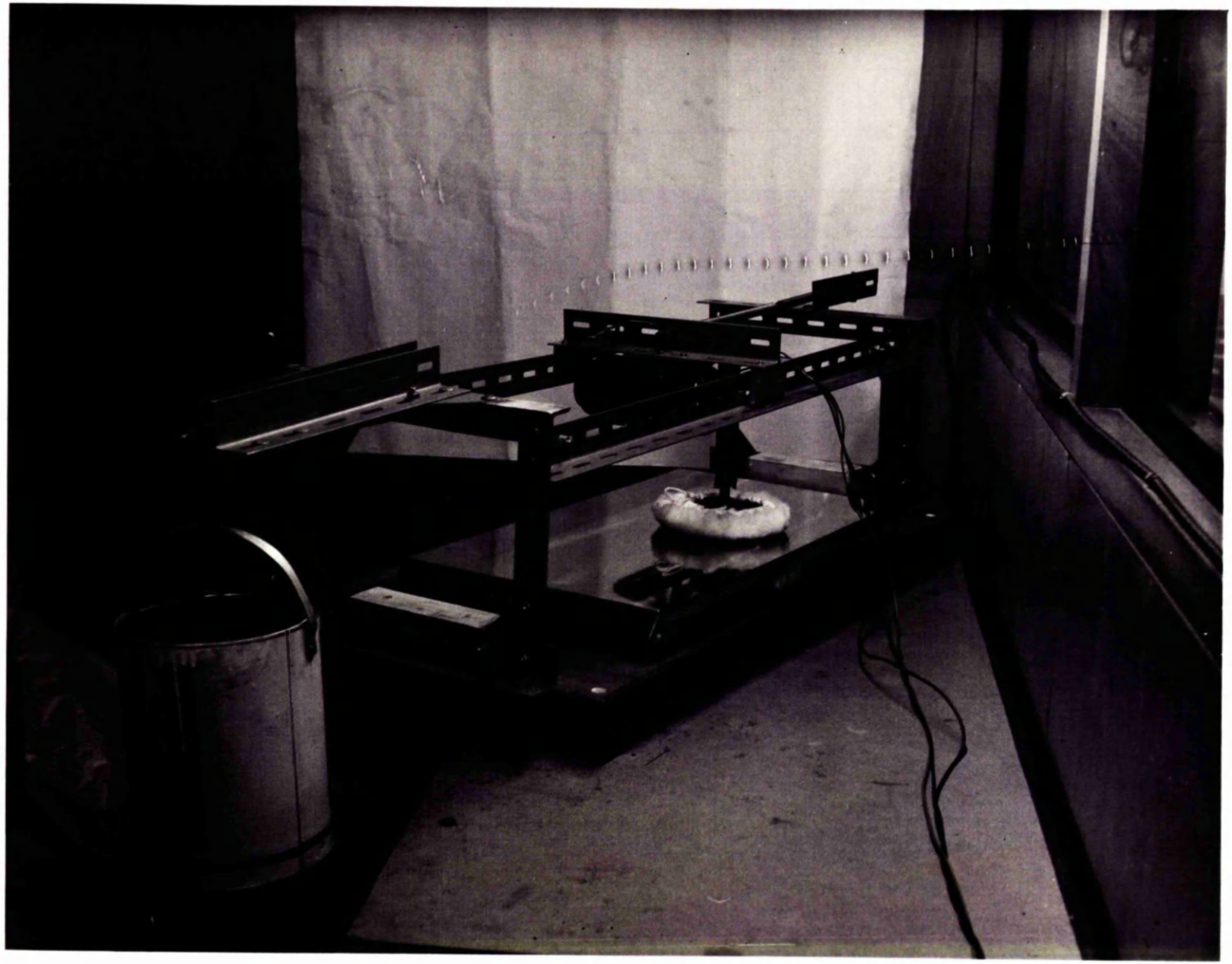

FIG. 6.2.1. Polishing the copper sheet.

aluminium having no difficulty with the process of soldering, was selected for the reflector.

6.2.2. Reflector's sensitivity to the manufacturing error

Sample calculations using equations (C-3) and (C-4) of appendix- C clearly indicate the reflector's sensitivity to manufacturing error. An error of $\pm$ 0.001 inch in the radius of the reflector profile at any point amounts to an error of the order of $\pm$ 0.10 inch and more in the points of incidence of the reflected rays. Therefore, the idea of machining the reflector out of a copper block is not attractive, because the cutting tools are most likely to leave marks on the surface, and any polishing of the curved surface of the reflector would not easily remove these marks. Hence it was decided to make a copper sheet reflector, bent to proper shape with the help of a block jig conforming to the inner shape of the reflector.

6.2.3 To polish the copper sheet

A scratch-free, highly polished copper sheet was specially obtained, but it was found that the surface-finish was not good enough. Firstly, an attempt was made to stick a thin metallised melinex sheet (supplied by Vacuum Research Ltd.) to the inside surface of the copper reflector, by means of some silicone or other adhesives. The sheet had a very high surface finish giving a very high reflectivity and it needed no further surface treatment. Another very great advantage was that it could be peeled off the copper reflector-frame and replaced easily by another piece of the sheet whenever necessary. In the limited time available, however, no way could be found to get rid of the air bubbles which had the tendency to be trapped between the melinex and the copper sheets during the process of adhering

together. Besides, the melinex sheet gives a flat surface only under tension. The air bubble and the adhesive, however small, tend to spoil the smoothness of the surface. From the point of view of cooling, a rather thin melinex sheet of the order of one or two thousandths of an inch was preferable, but such thin sheets yielded more easily to the trapped air bubbles and adhesive, producing a kinked surface, than the thick sheet. Too thick a melinex sheet could not be used because of the cooling problem. The method, therefore, was dropped forthwith in preference to the known but tedious process of polishing the copper sheet to a mirror-like finish.

In order to polish the copper sheet, a rig was constructed to support a variable speed electric motor mounted on ball bearings to facilitate its motion on rails and to house the copper sheet mounted on a wooden board (figure 6.2.1). A very soft, 5 inch diameter lamb's wool pad attached to the motor-spindle polished the copper sheet, using diamond pastes of three different grades of 3 micron, 1 micron and $\frac{1}{4}$ micron with hyprez fluid. Working against the spring-tension attached to the motor, water flowing in or out of the can (figure 6.2.1) gave movement to the lamb's wool pad. Though the motor could run up to 300 r.p.m., the tendency of the hyprez fluid to fly off the pad due to centrifugal force did not allow the speed to go beyond about 150 r.p.m. Up to this speed range, faster speed of pad was found to produce better finish of the surface.

6.24 Method of fabrication

First, a master template conforming to the shape of the multi-

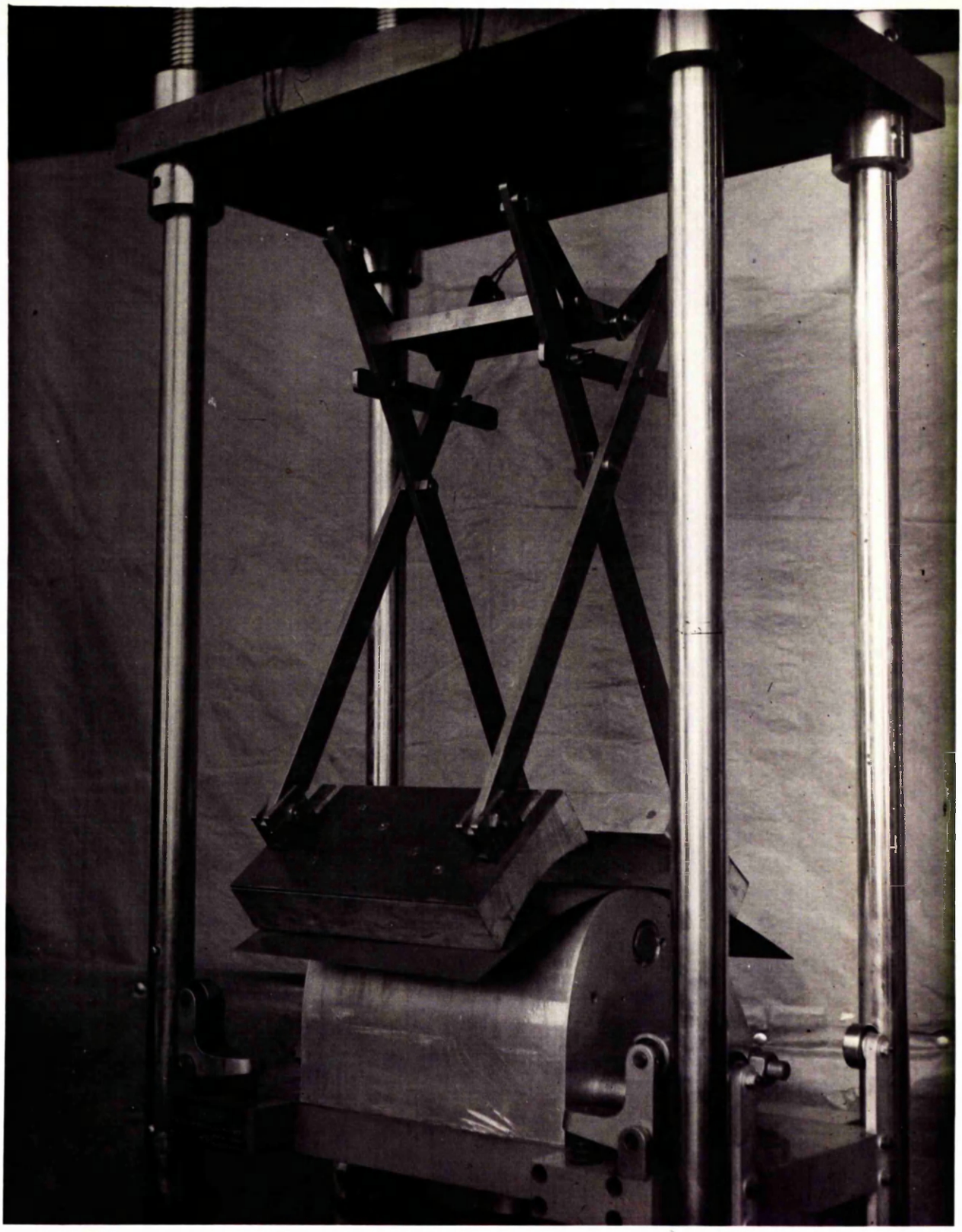

FIG. 6.2.2. Reflector forming mechanism.

curve reflector of table 4.8.1 was made from a $\frac{1}{4}$ inch thick stub steel plate. The co-ordinates of the reflector profile were marked on the plate and then machined out very accurately. Later it was checked on a milling machine using a dial gauge, and errors removed by filing the curved surface carefully. On final check, the master jig was found to be accurate within $\pm$ 0.002 inch.

A female template was also produced from a $\frac{1}{4}$ inch thick stub steel plate and was checked with the help of the master template, using a light-box. Twelve one-inch thick aluminium alloy plates were roughly cut in the shape of the reflector profile and assembled together, using three one-inch diameter steel bolts, passing through the jig-bored holes in them. Then this rigid block of plates was further machined accurately on a profile shaping machine using the master jig as template. To improve further the accuracy, the aluminium laminar block was carefully rubbed with a swiss file and emery paper using hi-spots blue and the female template. Over-all accuracy of the aluminium block template was brought to within $\pm$0.003 inch. These inaccuracies were distributed in a very irregular way and were mostly negative. The copper sheet, due to its own strength and stiffness, was not expected to follow these irregular negative errors and hence was expected to conform more accurately to the shape of the reflector.

It was necessary to exercise great care in handling and working with the thin copper sheet whose one surface had a mirror-like finish. Besides, it was necessary to ensure that the forming process allowed no gap, however small, to exist between the copper sheet and the block

FORMING OF REFLECTOR

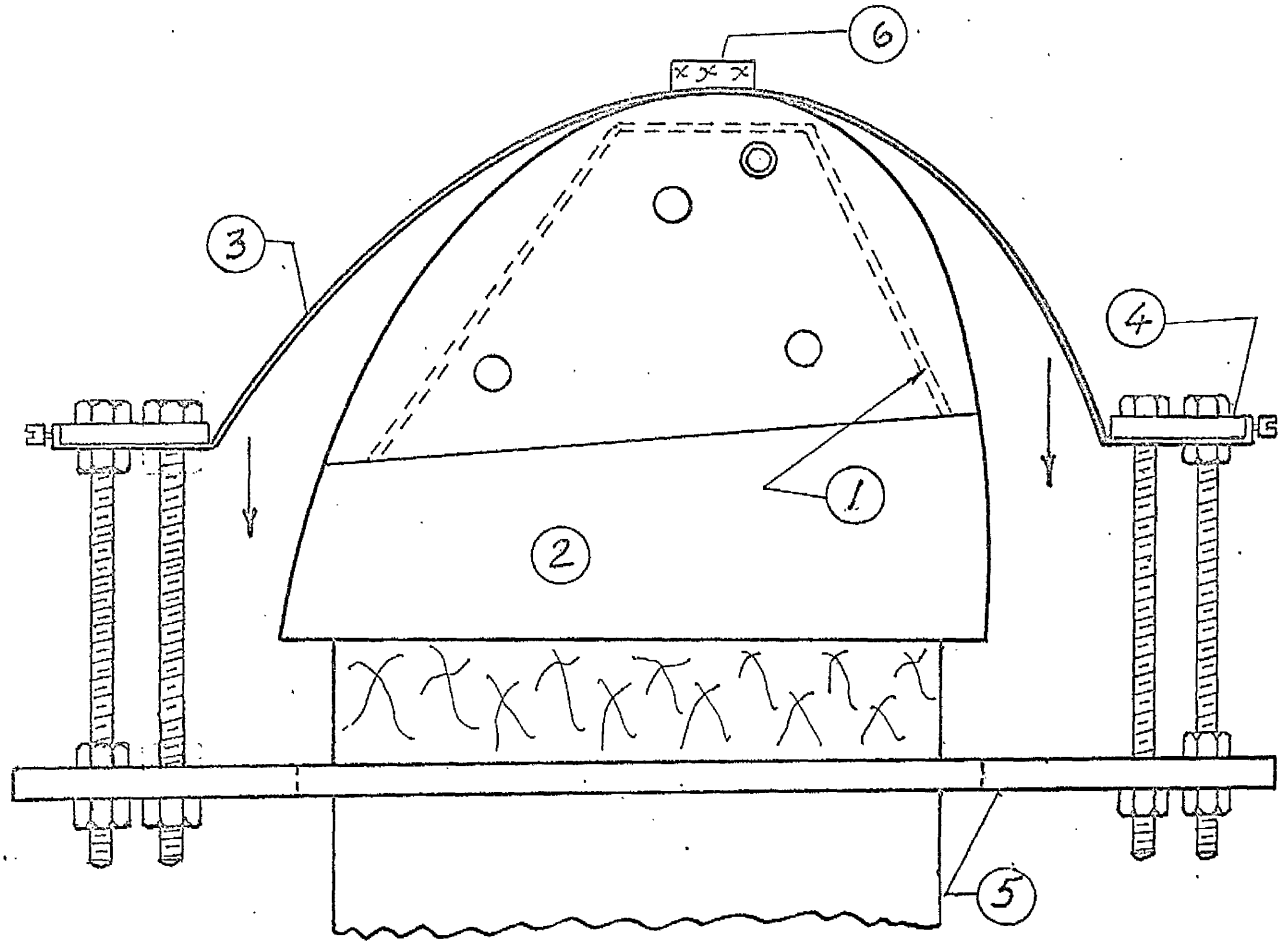

FIG. 6.2.3.

1. Cooling water passage in the aluminium side plate
2. Block jig.
3. Copper sheet.
4. Steel bar.
5. Base plate.
6. Wood clamp.

template once the former was bent over the latter. A sudden large change in curvature at 160° in the reflector profile produced a ridge which caused difficulty in smooth bending of the sheet. A link mechanism (fig. 6.2.2) designed to perform the process of forming the reflector, was not successful, because it allowed gaps of a few thousandths of an inch here and there between reflector and block template.

The process shown in figure 6.2.3, however, succeeded very well. In order to eliminate the interference by the ridge in the reflector profile in bending, and to prevent movement of the copper sheet during the process of forming, it was first clamped at the top of the aluminium block. Both sides of the copper sheet were then pulled down simultaneously by means of the inner rows of screws, while screws in the outer rows kept the steel bars level and ensured tight contact of the copper sheet against the aluminium block at the corners. A 0.0005 inch thick melinex sheet placed between the copper sheet and the aluminium block safeguarded the polished surface of the copper sheet against any damage.

To provide rigidity as well as support to the reflector, the copper sheet was screwed over two aluminium side plates, $\frac{1}{8}$ inch thick, one at each end. These two plates were marked, machined and brought to conform accurately with the aluminium block to which they were fixed, one on either side, by means of three $\frac{5}{8}$ inch diameter screws and a pair of locating pins. A 0.0005 inch thick melinex sheet was placed in between the aluminium block and the plates so that the reflector could slip out easily from the block jig after it was fabricated. $\frac{1}{4}$ inch diameter holes were drilled inside the aluminium plates to allow cooling water to pass through them. Cooling

of the plates was absolutely necessary to eliminate distortion and expansion of the plates due to heating, causing error in the reflector profile, as well as in the position of the filament which they support. This was also necessary to eliminate interference in the heat distribution on the model, if the plates were hot.

6.2.5 Cooling of the reflector

It was difficult to provide an effective means of cooling the reflector. An attempt to soft solder any cooling device on the top surface of the reflector could cause damage to its reflecting polished surface. The only solution, therefore, was to use cold setting bonding materials, such as 'araldite' or 'metallux'. An idea to build a cooling box of copper sheet on the top surface of the reflector, with a number of intermediate ribs to provide rigidity to the reflector as well as to the cooling box, was abandoned, because of comparatively poor strength of the bonding materials against excessively high water pressure acting on the reflector's large surface area in the vacuum.

In order to eliminate the effect on the reflector of the cooling water pressure acting against the vacuum, a completely different device was used. Wade's couplings were silver soldered, one at either end of $\frac{3}{16}$ inch outside diameter x $\frac{1}{8}$ inch inside diameter x $13\frac{3}{4}$ inch length copper tubes. The tubes were soft soldered to 0.012 inch x $\frac{5}{16}$ inch x $12\frac{3}{4}$ inch copper strips, and these copper strips were bonded on the top surface of the reflector at a pitch of one inch by means of araldite AY111. In a 1:1 proportion, araldite was mixed with aluminium powder to increase its thermal conductivity. Tubes were not bonded directly on to the reflector, because contact area would have

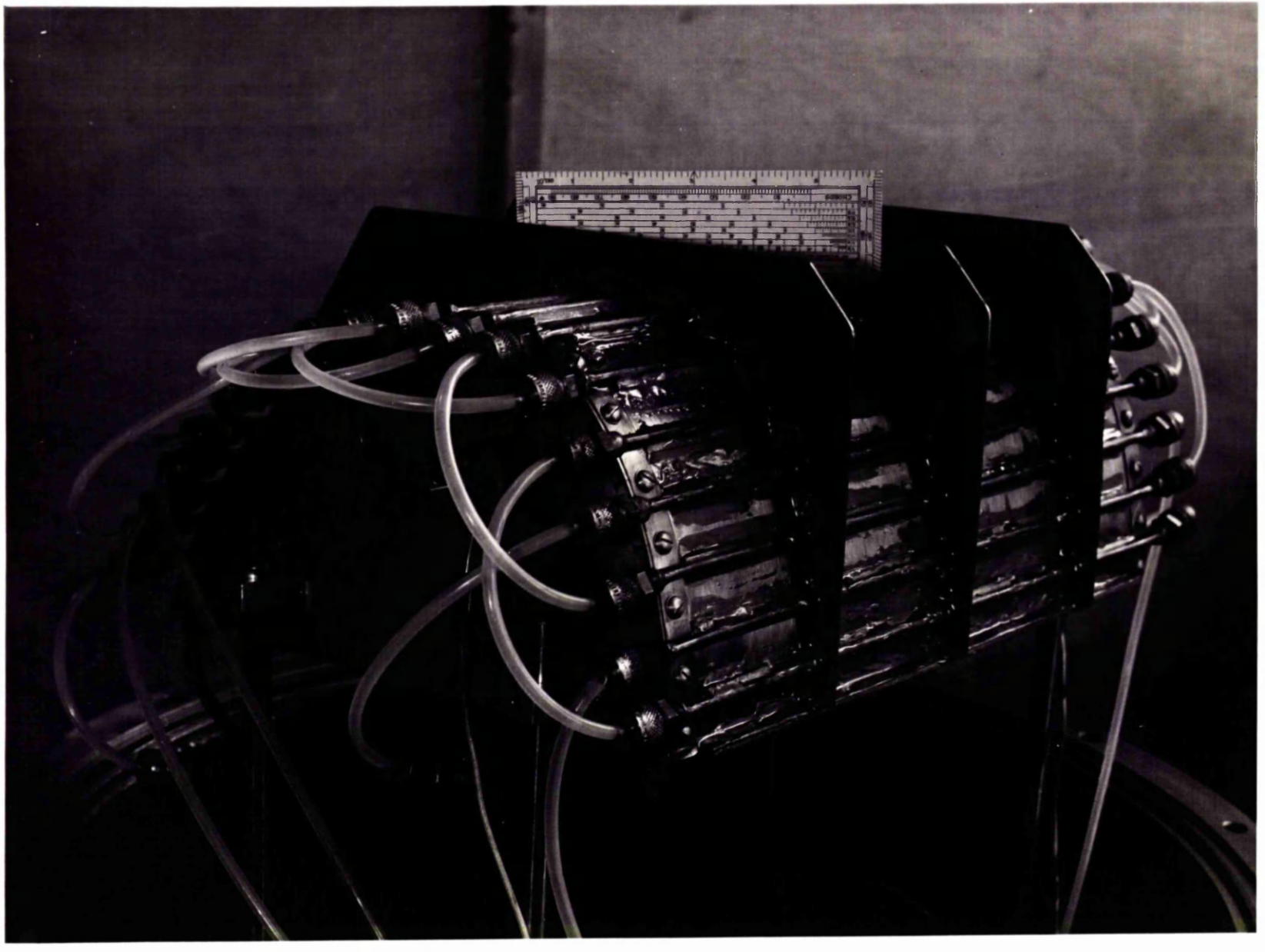

FIG. 6.2.4. The multi-curve reflector.

been smaller and consequently cooling loss effective. Using silicon O-rings and P.T.F.E. tubings, Wade's couplings were joined to form two water cooling circuits.

In order to provide further rigidity to the reflector, three more copper ribs, spaced as shown in figure 6.2.4, were bonded to it, using the same araldite AY 111.

6.2.6 Test and Discussion of Results:- In all, two reflectors were made, one with 0.017 and another with 0.035 inch thick copper sheets. They were tested experimentally in a high vacuum of about 10^{-5} torr, to find their performance, using the radiometer described in section 6.4.4. Their test results are given in tables 6.2.1 and 6.2.2 and are plotted in figures 6.2.5 and 6.2.6 respectively.

Comparison of figures 6.2.5 and 6.2.6 with figure 4.8.1 shows that the experimental results obtained on the reflector in section 4.8 have been approximately repeated by these two reflectors also. This is quite contrary to one's expectation to get higher heat intensity at the hot end of the plane of irradiation by using these two reflectors, because of the elaborate method followed to make them more accurately. However, this can be explained by considering the effects of the shape and size of the heating elements on the performance of a reflector. In these two reflectors lampblack plastered filaments were used, whose shape and size could not be maintained as accurately as the bare wire filament which was used in the reflector of section 4.8. Since the reflector is sensitive, not only to its manufacturing errors but also to the shape and size of the filaments, these must have affected, to a certain extent, the performance of these two reflectors.

A little difference in the results of figures 6.2.5 and 6.2.6 can also be ascribed to this reason, since two different filaments were used in the two reflectors.

TABLE 6.2.1.

MULTI-CURVE REFLECTOR

(0.017 inch thick copper sheet)

Experimental Test results for the heat distribution

x - co-ordinate (inch)	Distance from the hottest point (inch)	Relative heat intensity for the best fit	Remarks
-2.8	6.00	0.52	
-3.3	5.50	0.51	
-3.8	5.00	0.49	
-4.3	4.50	0.46	
-4.8	4.00	0.49	
-5.3	3.50	0.61	
-5.8	3.00	0.60	
-6.3	2.50	0.67	
-6.8	2.00	0.718	
-7.3	1.50	0.78	
-7.8	1.00	1.12	
-8.0	0.80	1.18	
-8.20	0.60	1.425	
-8.40	0.40	1.79	
-8.60	0.20	2.36	
-8.70	0.10	2.56	
-8.75	0.05	2.66	
-8.80	0.00	2.71	— — — The hottest point
-8.85	-0.05	2.67	
-8.90	-0.10	2.52	
-9.00	-0.20	2.24	
-9.20	-0.40	2.01	
-9.40	-0.60	1.48	
-9.50	-0.70	1.25	
-9.55	-0.75	1.15	

TABLE 6.2.2.

MULTI-CURVE REFLECTOR

(0.035 inch thick copper sheet)

Experimental Test results for the heat distribution

x - co-ordinate (inch)	Distance from the hottest point (inch)	Relative heat intensity for the best fit	Remarks
2.55	6.25	0.51	
2.80	6.00	0.54	
3.05	5.75	0.53	
3.30	5.50	0.53	
3.55	5.25	0.52	
3.80	5.00	0.50	
4.05	4.75	0.49	
-4.30	4.50	0.48	
-4.55	4.25	0.47	
-4.80	4.00	0.47	
-5.05	3.75	0.48	
-5.30	3.50	0.49	
-5.55	3.25	0.50	
-5.80	3.00	0.57	
-6.05	2.75	0.78	
-6.30	2.50	0.79	
-6.55	2.25	0.78	
-6.80	2.00	0.76	
-7.05	1.75	0.76	
-7.30	1.50	0.79	
-7.55	1.25	0.83	
-7.80	1.00	1.09	
-8.00	0.80	1.20	
-8.20	0.60	1.45	
-8.30	0.50	1.625	
-8.40	0.40	1.86	
-8.50	0.30	2.09	
-8.60	0.20	2.27	
-8.70	0.10	2.32	
-8.75	0.05	2.48	
-8.80	0.00	2.59	The Hottest Point

TABLE 6.2.2. Continued

x - co-ordinate (inch)	Distance from the hottest point (inch)	Relative heat intensity for the best fit	Remarks
-8.85	-0.05	2.47	
-8.90	-0.10	2.37	
-9.00	-0.20	2.29	
-9.20	-0.40	2.09	
-9.30	-0.50	1.97	
-9.40	-0.60	1.62	
-9.50	-0.70	1.29	
-9.55	-0.75	1.16	

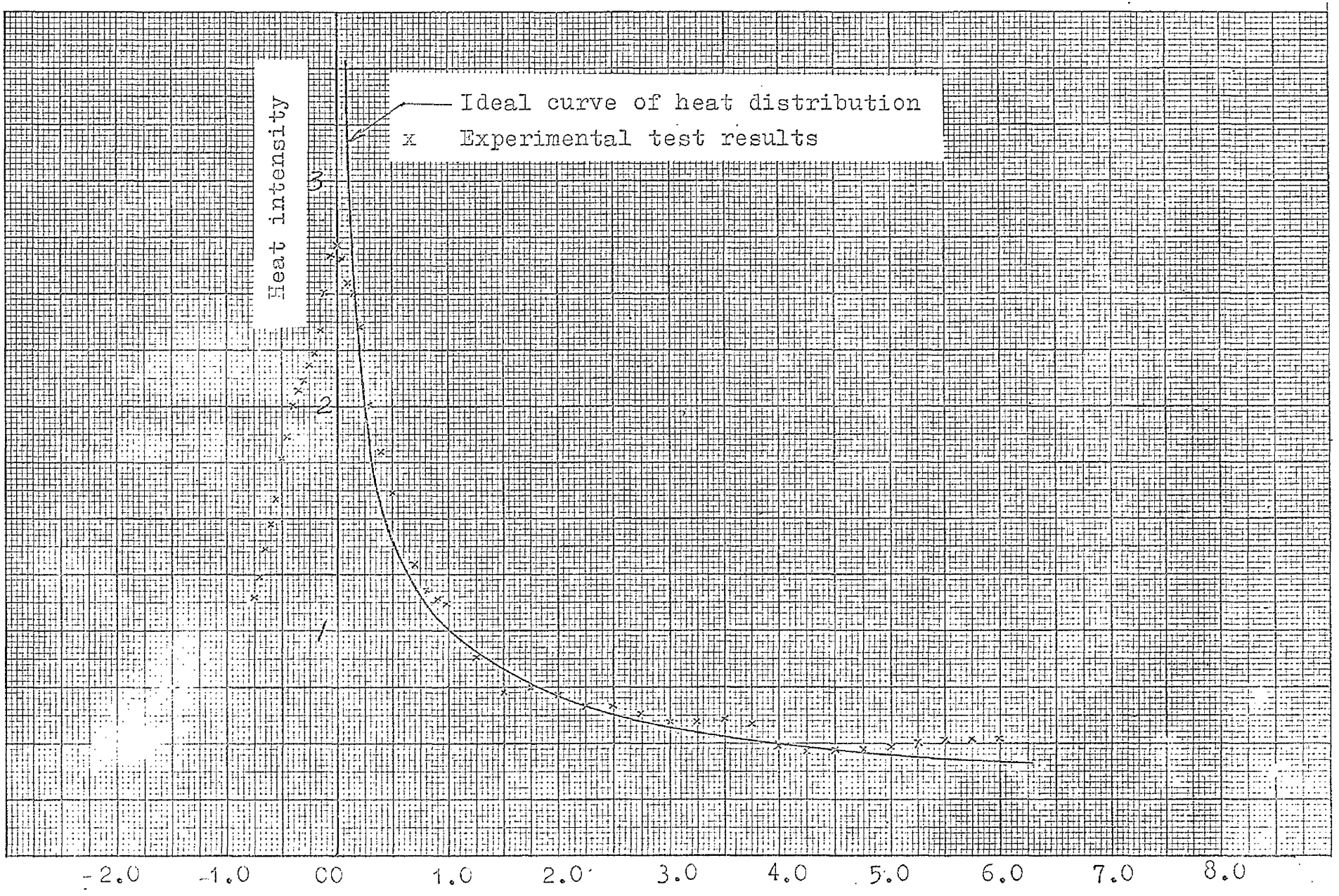

FIG. 6.2.5 Calibration of the Multi-Curve Reflector

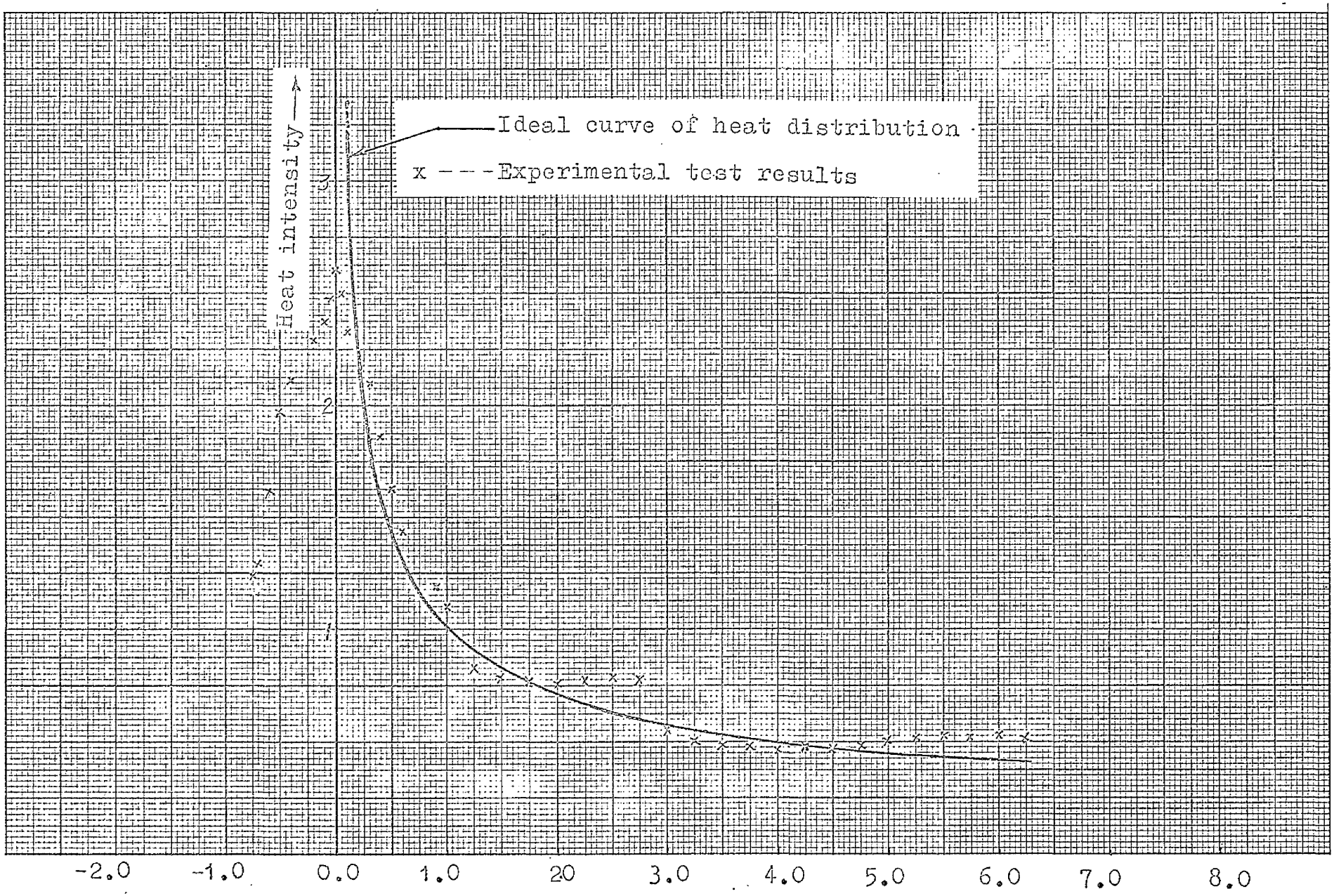

FIG. 6.2.6. Calibration of the Multi-Curve Reflector

6.3 Vacuum Chamber

A vacuum chamber with the inside dimensions of 22 inch diameter and 30 inch height (figure 6.3.1) was designed and constructed to accommodate the reflector and the model. It consists of 4 pieces: bottom plate, bottom chamber, top chamber and the top plate. The $\frac{5}{8}$ inch thick bottom plate has a 9 inch diameter clear bore in the centre to fit the baffle valve. Four $\frac{1}{2}$ inch diameter stainless steel rods screwed into the bottom plate, support the reflector. Electric power leads are also housed in the bottom plate. They consist of copper rods in glass seals which are further sealed vacuum tight by means of O-rings.

The bottom chamber is provided with a Wilson seal and three flanged ports, having 2 inch nominal bore. The Wilson seal takes up the radiometer rod and the thermocouple elements pass through one of the three flanged ports. Through another flanged port two water cooling circuits were arranged for the reflector. The remaining one port is spare for any future eventual needs. The $\frac{1}{4}$ inch diameter copper tubes soldered to the chamber walls provide the water cooling circuits. Besides, there are four more copper tubes, $\frac{3}{16}$ inch diameter, brazed to the bottom chamber to provide water cooling circuits, two of which were used for the radiometer. The nickel plated inside surface of the chamber was further painted black with Britannia-D to increase the absorption of heat radiation incident on it. The Britannia-D has an emissivity of 0.90 and it was further tested for its workability in high vacuum before applying it to the vacuum chamber.

VACUUM CHAMBER

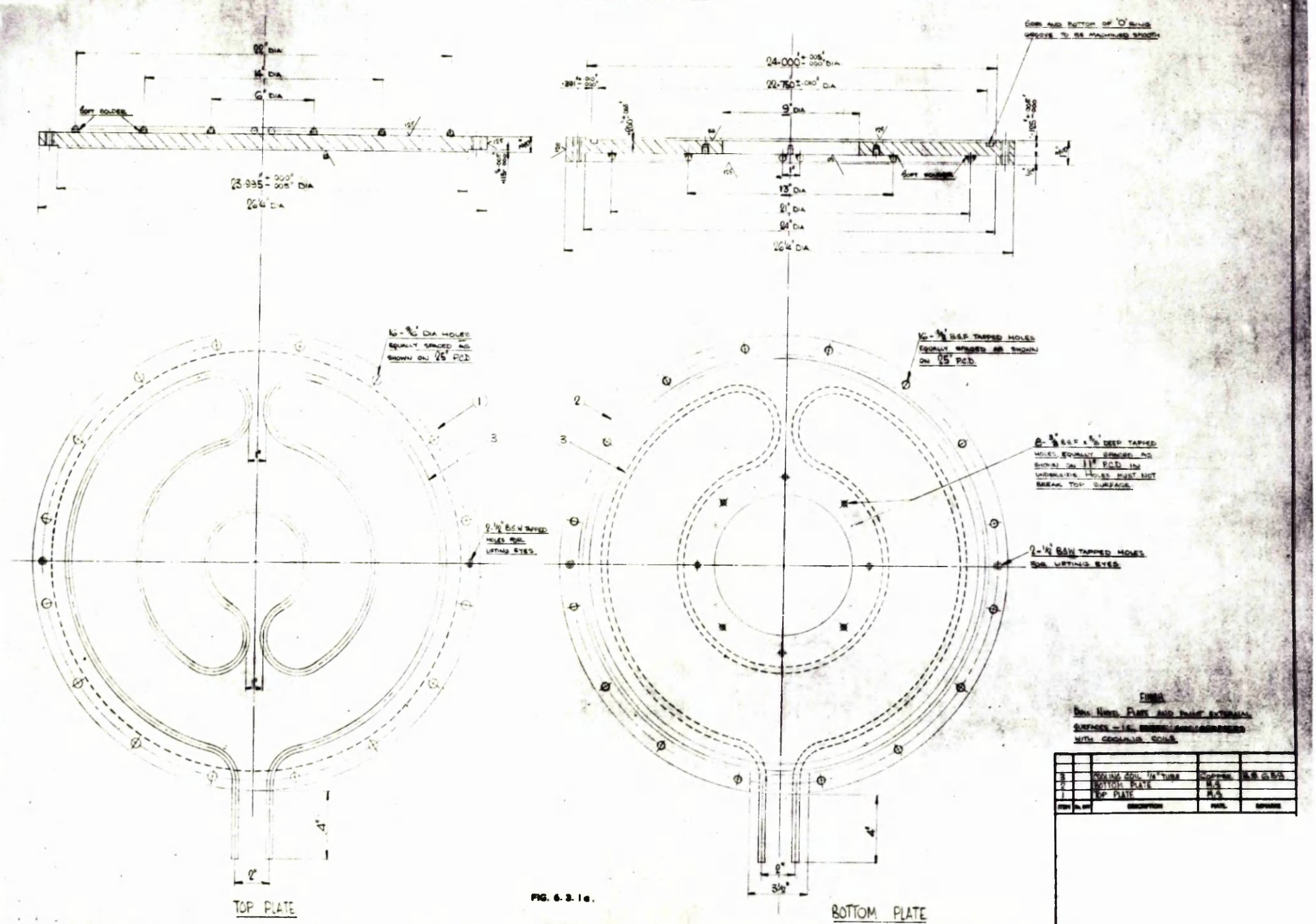

FIG. 6.3.1a.

FINISH

ALL METAL PARTS AND PAINT EXTERNAL SURFACES — I.C. ENAMEL AS SUPPLIED WITH COOLING COILS.

ITEM	NO. OFF	DESCRIPTION	MATL.	REMARKS
3		ROLLING COIL ¼" TUBE	COPPER	B.S. 659
2		BOTTOM PLATE	M.S.	
1		TOP PLATE	M.S.	

VACUUM CHAMBER

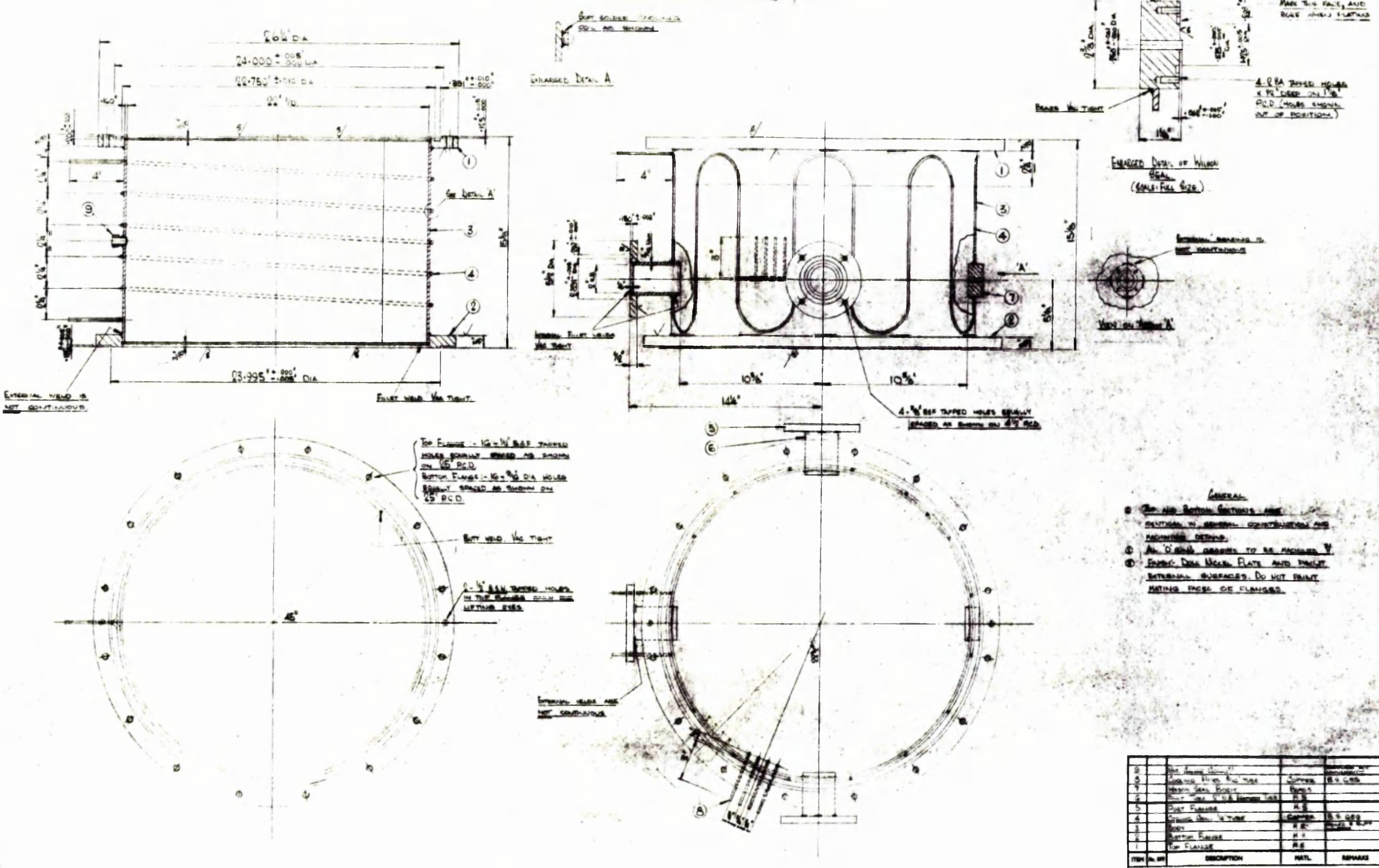

FIG. 6.3.1b.

6.4 Radiometers

6.4.1 Introduction:- An acute variation of heat intensity across the length of the planeof irradiation necessitated the development of a special type of radiometer to measure the heat distribution accurately. Most of the conventional types of radiometer can only be used if the heat radiation is uniform on certain areas, not less than the exposed surface of the sensing element, i.e. Gardon's radiometer,[41] Adhav's and Kemp's radiometer.[40]

Since for cooling the passive junctions, Mole's thermopile[37] depends on the mass of the metal block whose heat capacity is limited, its measurement of heat radiation can not remain constant in continuous use. The Houghton and Brewer[38] radiometer is only suitable for radiation measurement in the upper atmosphere. Ward's radiometer[39] is too complicated and big to be used in the present problem.

Adhav's and Kemp's radiometer[40] uses a gold foil as sensing element and hence is very costly. Besides, the hemispherical receiver is too large to be suitable for measuring the heat radiation in the present problem. Gardon's radiometer[41] is quite sensitive and simple to make and it also has a small time constant. The original Gardon's radiometer relied for cooling the passive junction of Constantan circular foil on the heavy mass of copper block to which it was soldered. This would certainly cause at least some small fluctuation of the temperature of the passive junction.

Sinn's, Pickard's and Hinkley's thermopile[42] is sufficiently improved and not too complicated to make. The annular brass ring holding the copper posts which form the cold junctions, is different from the brass water-

CIRCULAR FOIL RADIOMETER

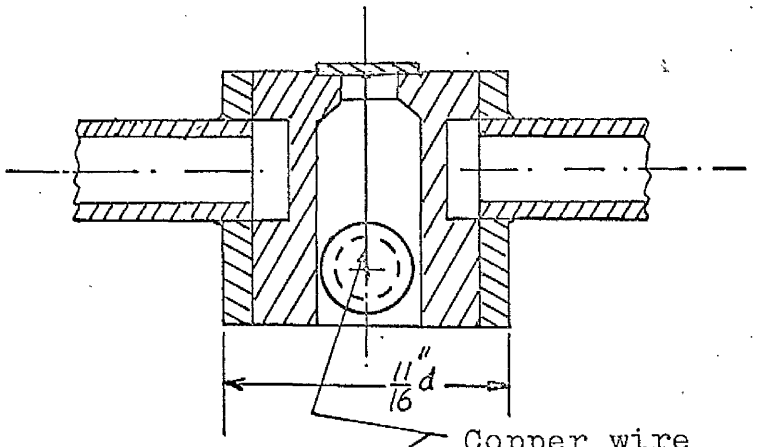

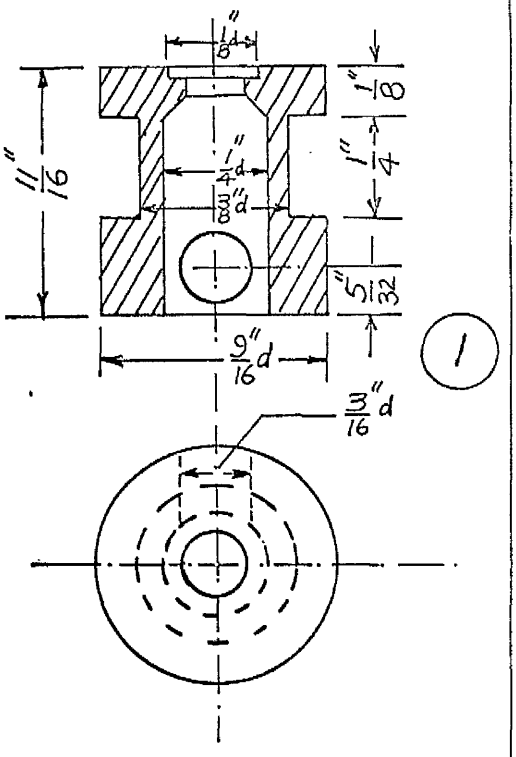

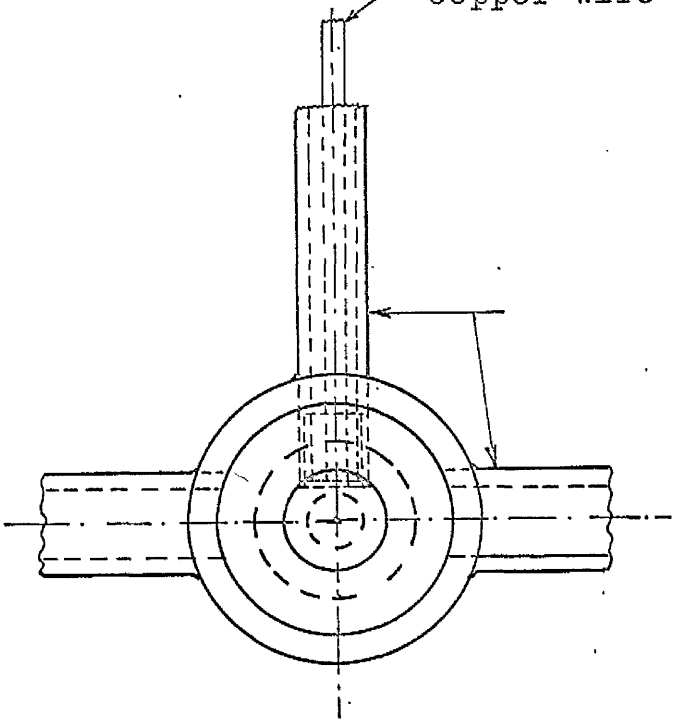

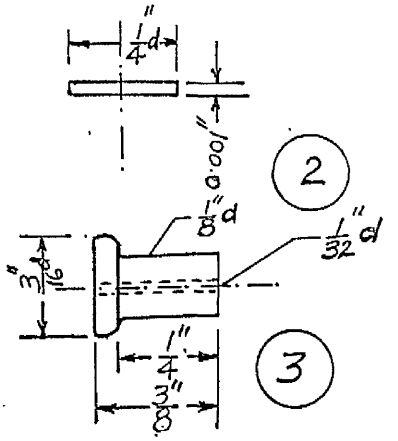

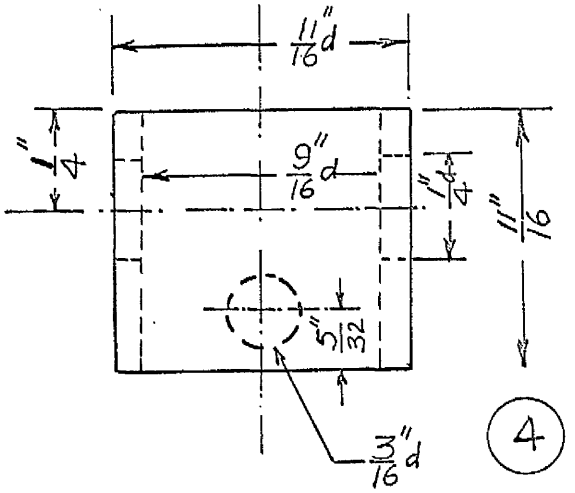

1. Body:- Copper.
2. Foil:- Constantan.
3. Plug:- P.T.F.E.
4. Jacket:- Copper.

FIG. 6.4.1.

jacket and to that extent, the cooling of the passive junction might not be highly effective, especially when it is measuring a high intensity of heat radiation.

6.4.2 Design and Construction of a Gardon's type radiometer:- First, a Gardon's type radiometer[41] was designed and constructed (fig. 6.4.1) with a principal modification of incorporating a water jacket to cool the passive junction. Since the sensitivity of such radiometers is inversely proportional to the thickness of the sensing circular foil, 0.001 inch thick constantan foil was used. In order to reduce the heat loss along the copper wire, a very small diameter wire, as small as 0.003 inch, was spot-welded at the centre of the foil. An attempt to weld 0.0015 inch diameter wire was unsuccessful.

6.4.3 Rectangular foil radiometer:- In the further development of this type of radiometer, the circular foil used as sensing element was changed to a rectangular foil (fig. 6.4.2). This was necessary to account for the acute variation of radiant heat along the length of the plane of irradiation. Moreover, it had the advantage of allowing the longer length of the foil for getting higher sensitivity. The width of the foil was $\frac{1}{16}$ inch but it could be further reduced if necessary. Constantan with its low thermal conductivity ensures high sensitivity.

The sensitivity of a radiometer can be increased, either by increasing the diameter of the sensing foil (the length in the case of rectangular foil) or by increasing the number of pairs of active and passive junctions. The former method increases the difference of temperatures between the hot and cold junctions, and thereby increases the radiation heat loss (and also the

RECTANGULAR FOIL RADIOMETER

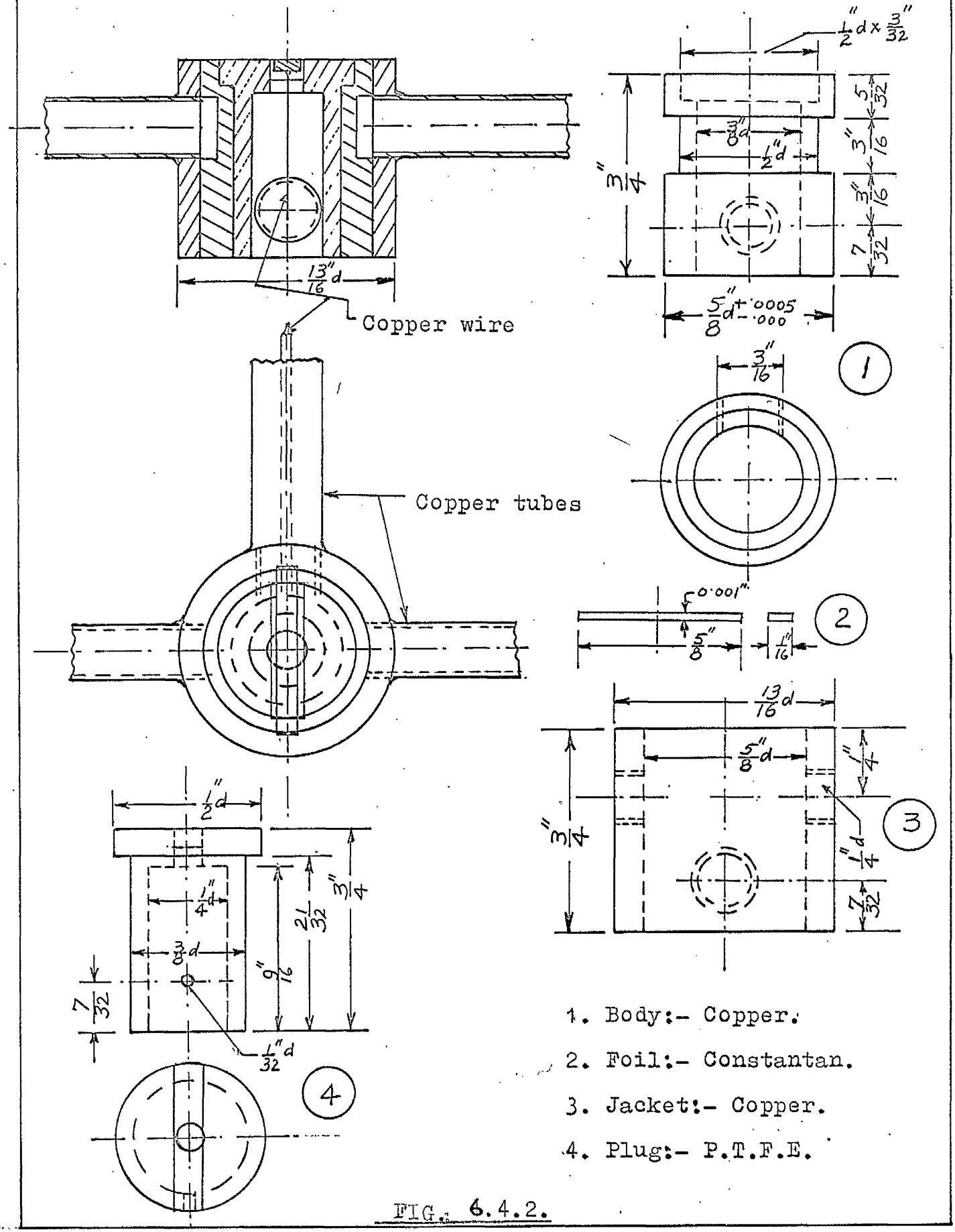

FIG. 6.4.2.

WATER CALORIMETER

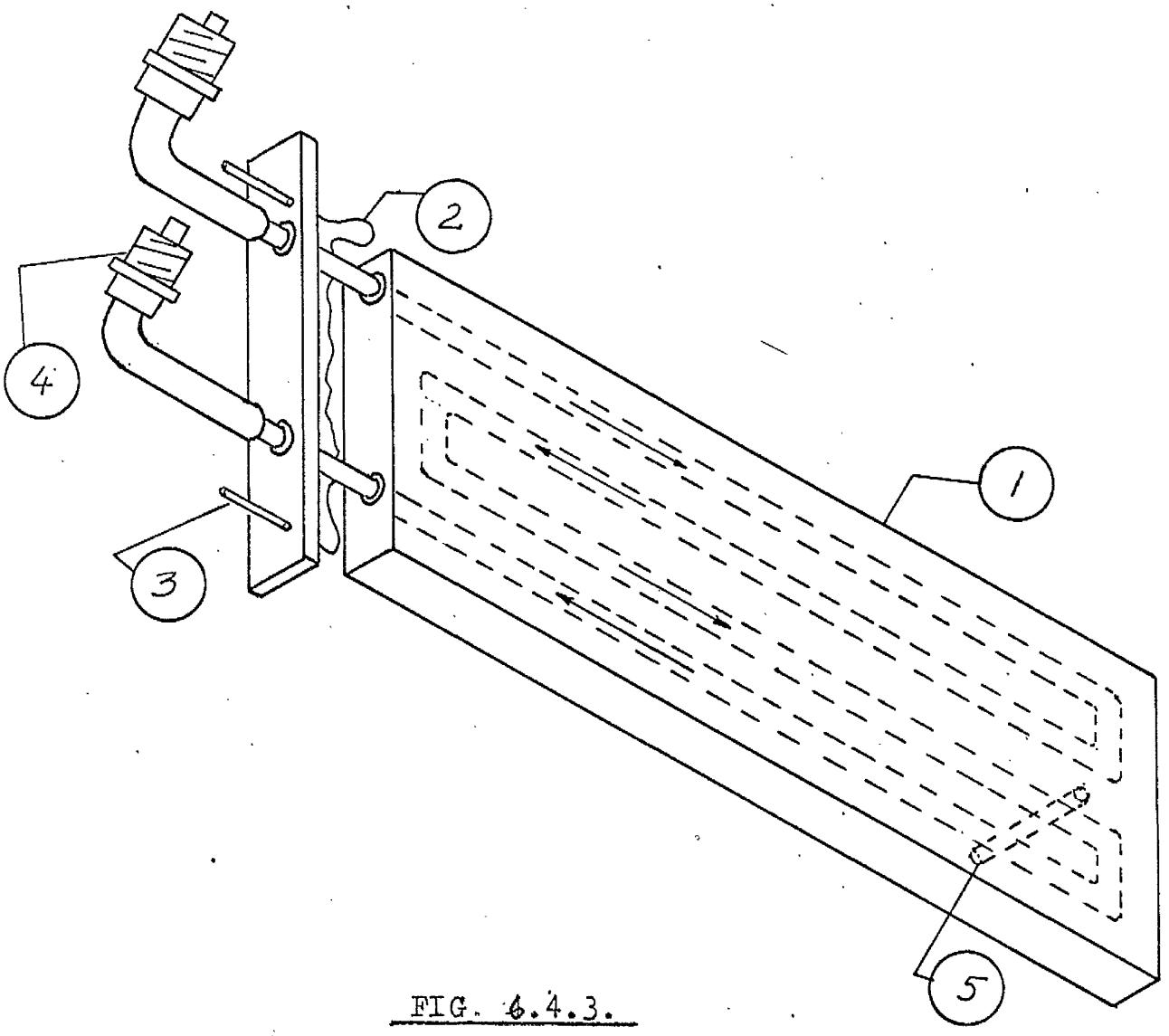

FIG. 6.4.3.

1. Body :-Copper 4×13/16×1/4 inches;
   1/16 inch diam. passage for water.
2. Thermocouples:- 0.004 inch diam. Eureka and Vacrom wires.
3. Thermocouple Terminals:- Copper.
4. Wades Couplings.
5. Alumina support rod.

convective heat loss, if used in atmosphere) from the foil. The latter method, though more complicated, is more accurate and therefore was adopted for further development of the radiometer.

6.4.4 Further development and calibration of radiometers:- To test the radiometer, a water calorimeter was designed and constructed (fig. 6.4.3). Since a hole smaller than $\frac{1}{16}$ inch diameter of 4 inch length could not be drilled through the body of the calorimeter, a 24 s.w.g. copper wire was inserted into the holes before soldering the water inlet and outlet tubes to it, in order to reduce the water flow through them. The temperature difference of water flowing in and out of the calorimeter is registered by the copper constantan thermocouple. The top surface of the calorimeter is painted black, to absorb maximum heat radiation, with Britannia-D, a heat and vacuum resistant paint, of known emissivity of 0.90. The other surfaces are smooth and lightly polished. In order to minimise the heat loss by conduction from the lower surface of the calorimeter, a $\frac{1}{16}$ inch diameter small alumina rod, stuck to it by means of araldite, supports it above any base on which it might have to be placed during the experiment.

Preliminary tests of a few more different types of radiometers made, were done to find their performance. Test results of some wire thermopiles were also very encouraging. S.R. Aggrawah (Department of Aeronautics and Fluid Mechanics) took up the further development, based on the principle of the thermopile, and designed a radiometer (fig. 6.4.4) consisting of 10 pairs of hot and cold junctions. This radiometer was used in the further work of the project and hence its calibration chart is reproduced from his work in table 6.4.1. The thermocouple elements were Eureka and Vacrom of

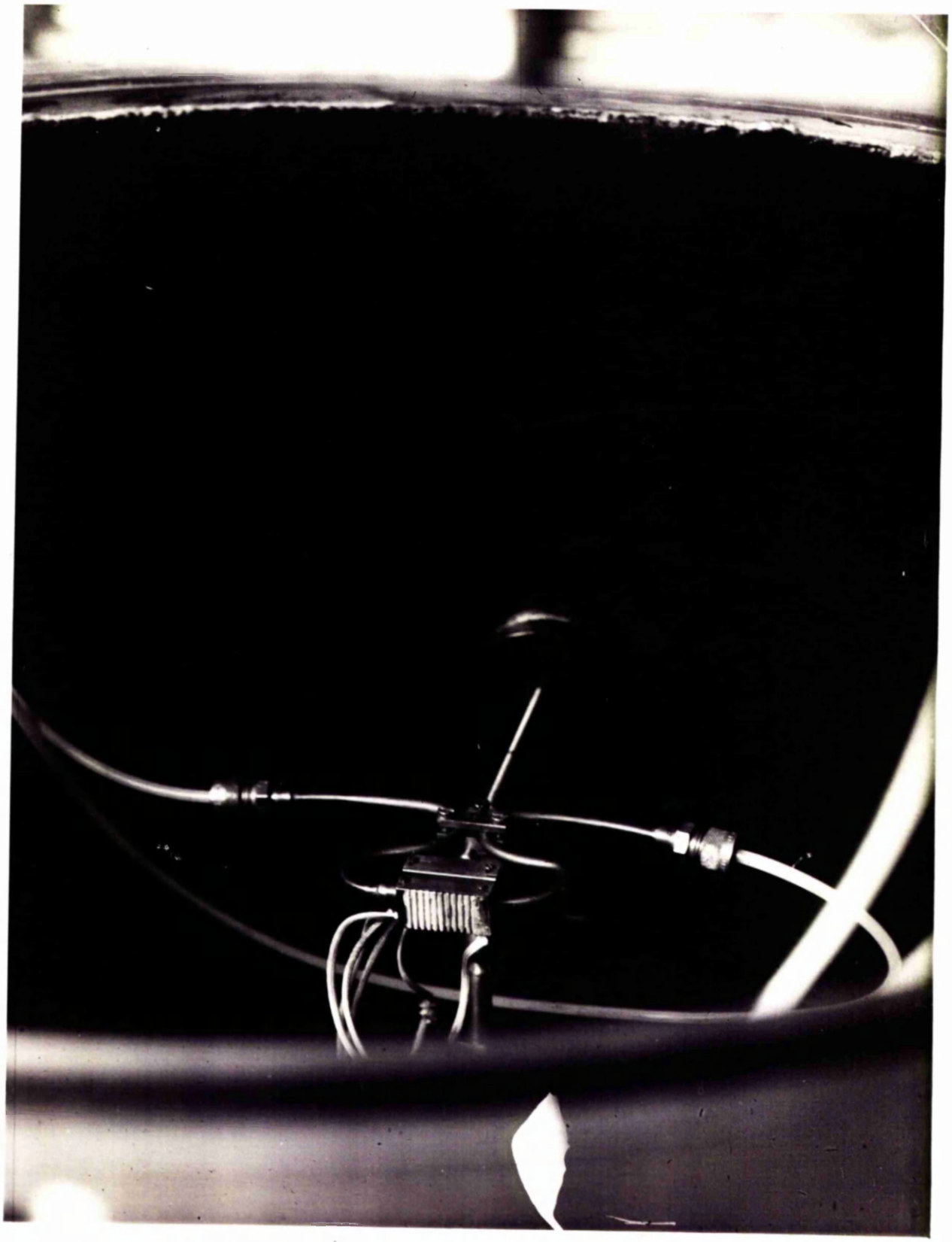

FIG. 6.4.4. The radiometer

RADIOMETER

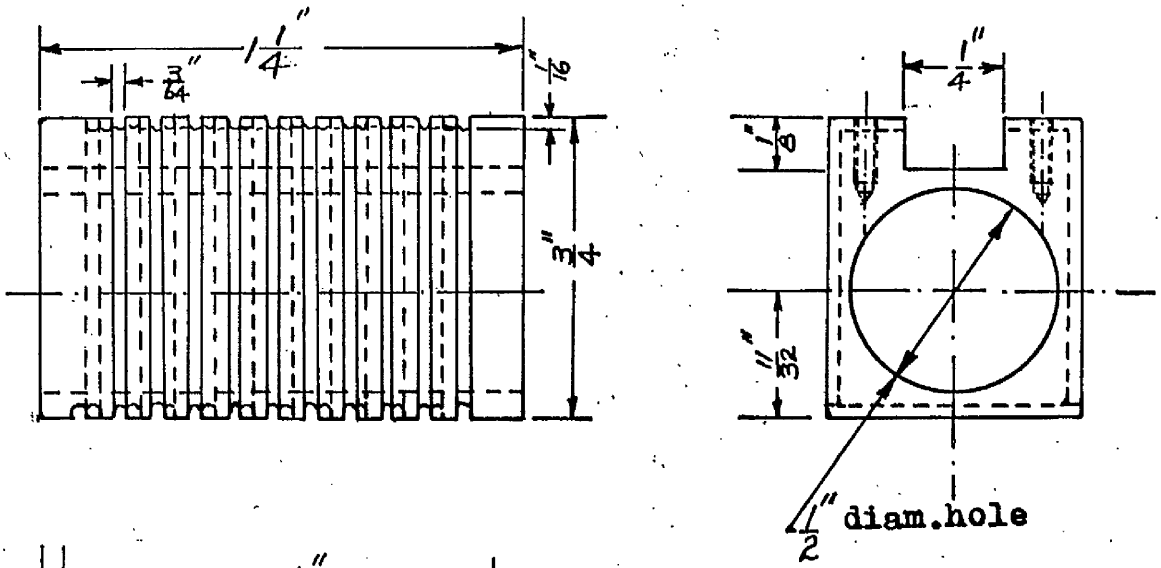

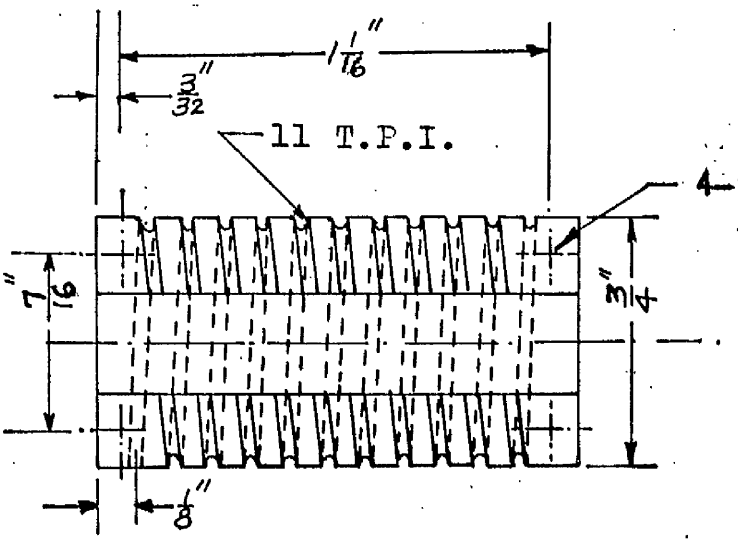

RADIOMETER BODY — COPPER

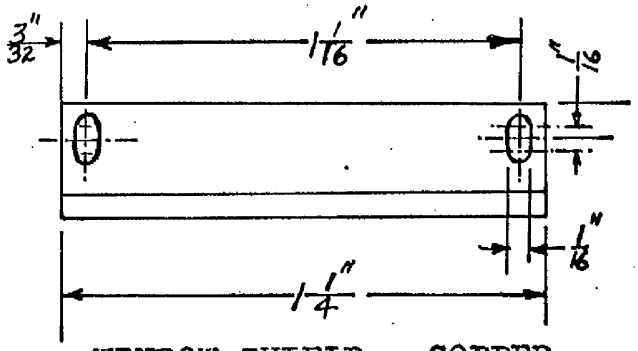

WINDOW SHIELD — COPPER

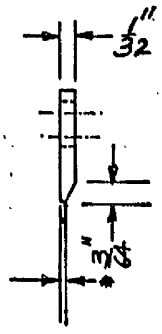

* to be left thick enough to provide a straight edge.

FIG. 6.4.4.

0.004 inch diameter wires. Figure 6.4.5 shows the arrangement of the apparatus, except the glass bell jar, for the calibration of the radiometer.

Table 6.4.1

CALIBRATION OF RADIOMETER

Radiometer reading (uv)	Heat intensity $Cal/cm^2/Sec.$
0	0
1515	0.02425
4287	0.075
6133	0.109
8493	0.1582
11457	0.193
14713	0.2475
17972	0.329
21690	0.398
25387	0.477
29293	0.568
32127	0.671
37785	0.802
41689	0.951
46716	1.142
48407	1.185
54949	1.391
60944	1.530
66491	1.85

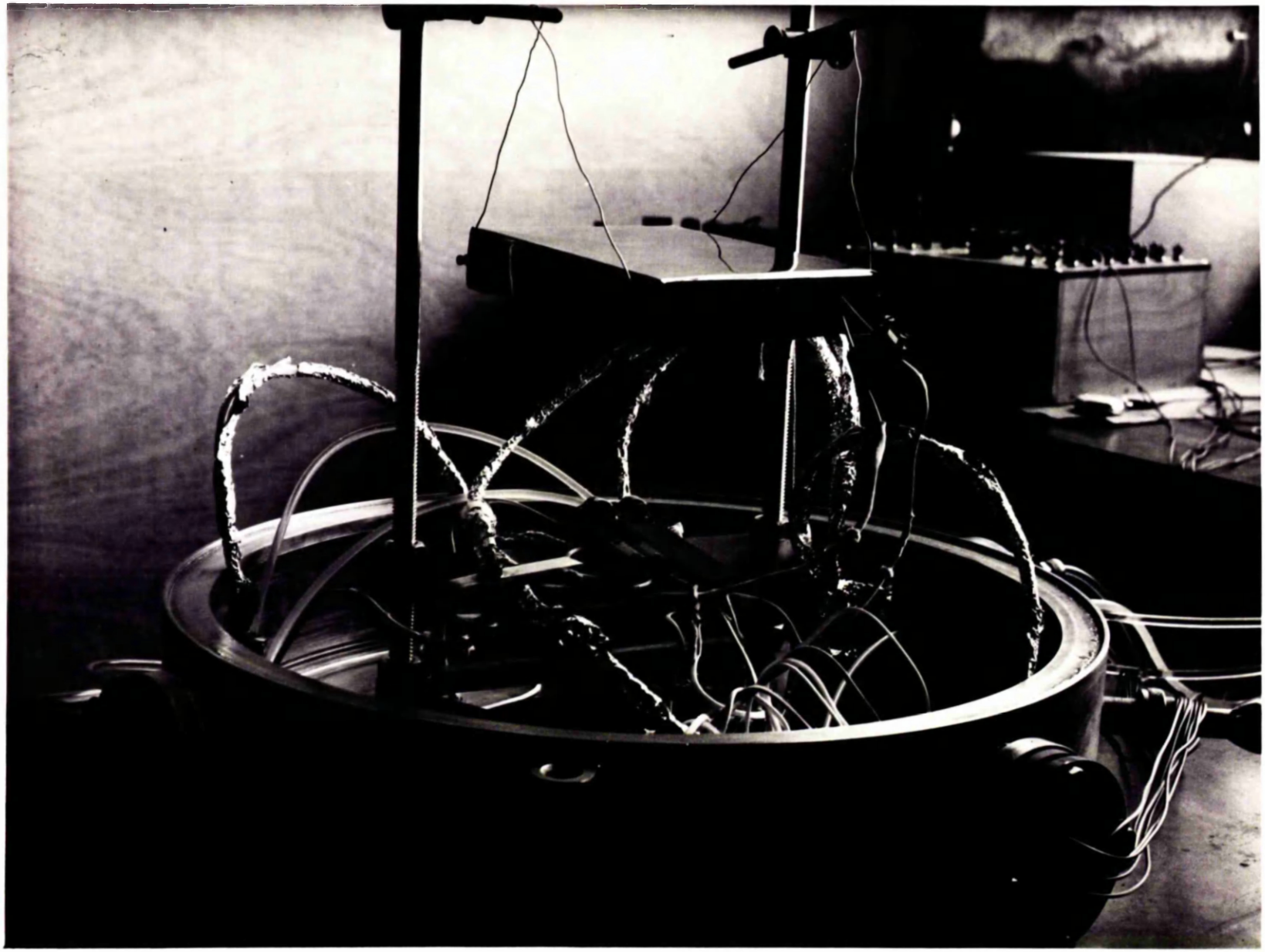

FIG. 6.4.5. Calibration of the radiometer.

6.5 MODEL SUPPORT TRAY

The model support tray (fig. 6.5.1) was designed to support the model of conducting skin, and to provide facility for its accurate location with respect to the reflector and the heating element. This also provides facility for holding in position the thermocouple elements fixed to the model. To minimise outgassing in vacuum, the tray was made of stainless steel. Four screw legs, one at each corner of the tray, help in its levelling and adjusting the distance from the heating element.

Models do not sit directly on the model support tray. They are supported on four corners by means of $\frac{5}{32}$ inch diameter alumina rods which are fixed to the four aluminium adjusting screws. These adjusting screws rest on the model support tray. Because of low thermal conductivity of alumina and with the point contact between the model and alumina rod, the heat loss from the model by conduction is reduced to a minimum.

MODEL SUPPORT TRAY

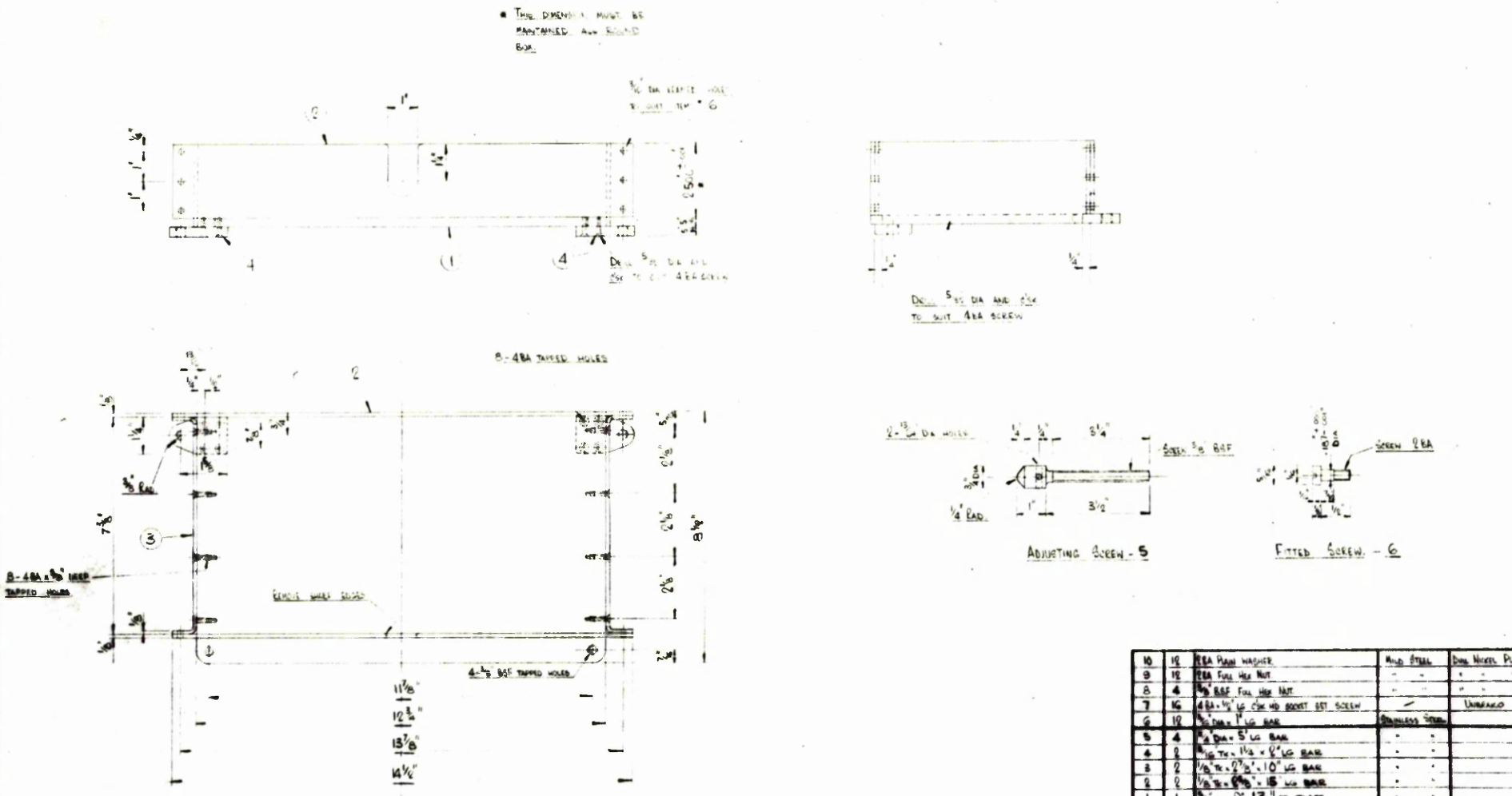

ITEM	No. OFF	DESCRIPTION	MATL.	REMARKS
10	12	4BA Plain washer	Mild Steel	Zinc Nickel Plate
9	12	4BA Full Hex Nut	" "	" " "
8	4	5/16 BSF Full Hex Nut	" "	" " "
7	16	4BA x 1/2" LG CSK HD BOOST SET SCREW	/	Unplated
6	12	5/16 DIA x 1" LG BAR	Stainless Steel	
5	4	1/4 DIA x 5" LG BAR	" "	
4	2	1/16 TK x 1 1/2 x 8" LG BAR	" "	
3	2	1/8 TK x 2 3/8 x 10" LG BAR	" "	
2	2	1/8 TK x 5/8 x 15" LG BAR	" "	
1	1	1/8 TK x 9" x 13" LG PLATE	" "	

FIG. 6.5.1

6.6 OTHER EQUIPMENTS AND ASSEMBLY OF THE APPARATUS

A simple line diagram of the assembly of the apparatus is shown in figure 6.6.1. In order to reduce the length of the air passage from the vacuum chamber to the diffusion pump, the baffle valve was directly fixed to the bottom plate of the chamber; as shown in the diagram. Care was also taken to arrange the connection of the rotary and diffusion pumps with a minimum of tubing. The Edwards oil vapour fractionating diffusion pump F 603, working in conjunction with Edwards 1 SC 450 rotary pump was capable of producing an ultimate vacuum of 5×10^{-7} torr.

To measure vacuum, Pirani and Penning gauges were provided. Pirani gauge head was connected to the roughing line and the Penning gauge head directly to the top chamber.

The reflector was supported on four $\frac{1}{2}$ inch diameter stainless steel rods fixed to the bottom plate of the chamber. Positions of the holes to take up these stainless steel rods were decided such that the plane containing the radiometer rod was normal to the plane of the heating filament. These holes were accurately marked, drilled amd tapped.

To facilitate the handling and connection of more than a dozen of thermocouples fixed to the model, a thermocouple junction box was constructed. To record the e.m.f. signals of the thermocouples and the radiometer, Tinsley Vernier Potentiometer and Tinsley Galvanometer were provided.

The radiometer was fixed on a $\frac{1}{4}$ inch diameter stainless steel rod which passed through the Wilson seal in the lower vacuum chamber. The controlled movement to this rod was given by means of another threaded screw,

nut of which had a perspex pointer fixed on its top surface. The pointer moved on a scale when the threaded screw moved the radiometer rod, thus indicating the position of the radiometer on the scale.

Power supply to the heating element was provided through single phase voltage transformers, two of which worked in series to give a fine control of the voltage. In order to get an idea of power input to the heating element, provisions were made to measure the current and voltage across the heating element.

Cooling water to the reflector, vacuum chamber, radiometer, and the diffusion pump was supplied through different circuits. To supply enough water to the reflector, two different circuits were used, and the head of water had to be raised to about 110 ft., using a water pump in the line.

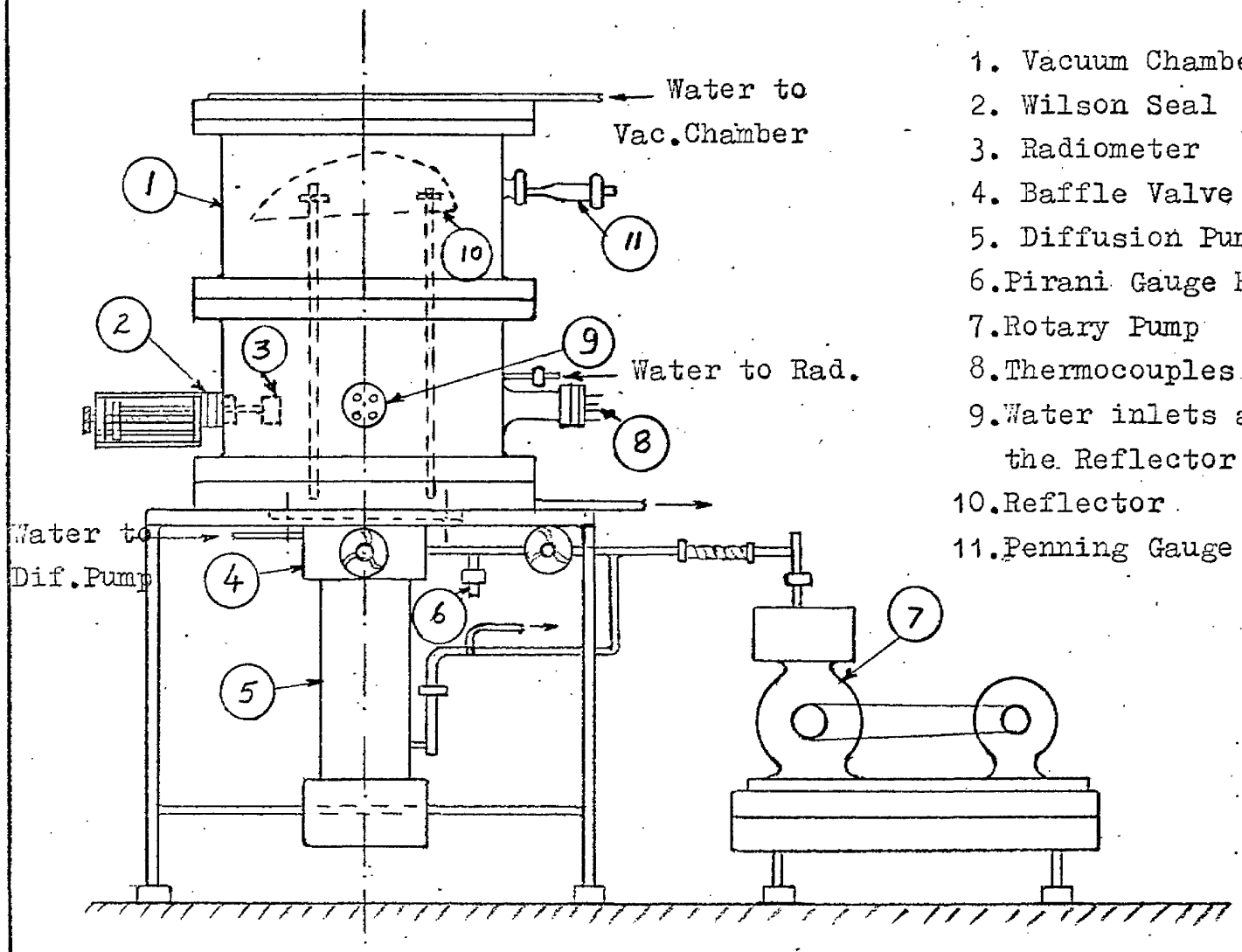

1. Vacuum Chamber
2. Wilson Seal
3. Radiometer
4. Baffle Valve
5. Diffusion Pump
6. Pirani Gauge Head
7. Rotary Pump
8. Thermocouples
9. Water inlets and outlets for the Reflector
10. Reflector
11. Penning Gauge Head

FIG.6.6.1. Assembly of the Apparatus

CHAPTER VII

EXPERIMENTS ON THE HEAT CONDUCTING SKIN MODELS

7.1. Introduction:-

The estimated heat power of 3 to 3.5 K.watts (section 3.5) could not be obtained from the heating element. The nickel filament plastered with lampblack and Fibreflex cement (section 5.6) could give at most of 1.25 K.watts per ft. length. Besides, by using a multi-curve reflector, almost 30 to 35 per cent heat is wasted beyond the leading edge of the model. Thus, the available heat to the model falls far short of the estimated requirement and consequently only low thermal conductivity materials could be used for the conducting skin models, in order to get its temperature as high as possible. Staybrite stainless steel, supplied by Messrs. Firth—Vickers, having thermal conductivity of 3.57 at 20°C and 4.51 ft. lb /ft./sec./°K at 700°C, was used for $\frac{1}{8}$ inch, $\frac{1}{4}$ inch and $\frac{1}{2}$ inch thick models. Another $\frac{1}{2}$ inch thick model was made of Frequentite ceramic, supplied by Messrs. Steatite and Porcelain Products Ltd.

7.2. Stainless Steel Models

7.21. Preparation of the Models:-

Three 6 inch long x 12 inch wide models of Staybrite stainless steel having thickness of $\frac{1}{2}$ inch, $\frac{1}{4}$ inch and $\frac{1}{8}$ inch were prepared. Both surfaces of each model were first machined and ground accurately. Two rows of thermocouple holes, six in each of them and $\frac{1}{4}$ inch off centre

line were drilled through one surface. The details of the size and location of holes are given in table 7.2.1. Holes with different depth were drilled to find a temperature across the thickness of the model if it existed. The surface of the steel plate was sand blasted uniformly. Later, this surface was oxidised in an electric oven at 650°C for one hour in order to increase its emissivity. With the sand blasted surface facing upwards, the stainless steel plate rested on the furnace bed with a heat resistant soft paper in between to reduce the oxidation of this surface. The furnace was raised slowly to 650°C and then it was maintained for one hour at this temperature before power to the furnace was cut off. The steel plate model was left inside the furnace to cool down.

In order to reduce the radiation heat loss from the bottom and side faces, they were polished with carborundum paste and then with the 3 micron diamond paste. The emissivity of the stainless steel is itself low and after such polishing, it could have been reduced to almost 0.05 or less.

TABLE 7.2.1.

Size and location of thermocouple holes in steel models

Thickness t of the model (inch)	depth of the hole (inch)	diameter of the hole (inch)	Distance of the thermocouple from the leading edge (inch)					
			1	2	3	4	5	6
$\frac{1}{2}$	$\frac{1}{8}$	0.032	$\frac{1}{8}$	$\frac{5}{8}$	$1\frac{3}{8}$	$2\frac{3}{8}$	$3\frac{7}{8}$	$5\frac{3}{4}$
	$\frac{3}{8}$	0.039	$\frac{1}{8}$	$\frac{5}{8}$	$1\frac{3}{8}$	$2\frac{3}{8}$	$3\frac{7}{8}$	$5\frac{3}{4}$
$\frac{1}{4}$	$\frac{1}{16}$	0.032	$\frac{1}{8}$	$\frac{5}{8}$	$1\frac{3}{8}$	$2\frac{3}{8}$	$3\frac{7}{8}$	$5\frac{3}{4}$
	$\frac{3}{16}$	0.036	$\frac{1}{8}$	$\frac{5}{8}$	$1\frac{3}{8}$	$2\frac{3}{8}$	$3\frac{7}{8}$	$5\frac{3}{4}$
$\frac{1}{8}$	$\frac{1}{16}$	0.032	$\frac{1}{8}$	$\frac{5}{8}$	$1\frac{3}{8}$	$2\frac{3}{8}$	$3\frac{7}{8}$	$5\frac{3}{4}$
	$\frac{1}{16}$	0.032	$\frac{1}{8}$	$\frac{5}{8}$	$1\frac{3}{8}$	$2\frac{3}{8}$	$3\frac{7}{8}$	$5\frac{3}{4}$

7.2.2. Fixing of the Thermocouples:- Using an electric spark in a reducing atmosphere, thermocouples of Eureka and Vacrom wires of diameter 0.004 inch were made. Except in the $\frac{3}{8}$ inch deep holes in the $\frac{1}{8}$ inch thick model, thermocouples in all other holes in the models were fixed by means of a very soft lead pencil (Venus 5B). To do it, the elements forming the bead were separated out and then the pointed end of the soft pencil on the bead with elements on either side, pushed the bead inside the hole. While doing so, the end of the pencil breaks off and thus jams the hole to secure the thermocouple wires in position. Just outside the hole, a piece of twin bore ceramic sleeve, 0.062 inch diameter and about $\frac{1}{8}$ inch long was used to

keep the elements apart; thereafter, the elements were covered separately by Refrasil sleevings.

In order to fix the thermocouple junction at the bottom of the $\frac{5}{8}$ inch deep holes in the half inch thick model and to insulate the thermocouple wires from the walls of the holes, a twin bore ceramic sleeve of 0.035 inch diameter was pushed up to the bead. A drop of silver emulsion (supplied by Messrs Acheson Colloids Ltd.) on the thermocouple bead before insertion was used to improve the thermal contact at the bottom of the hole. The silver emulsion should be applied a little liberally, so that the part of the ceramic sleeving also gets attached to the side of the hole, rendering the bond stronger. Thermocouple elements, outside the twin bore ceramic sleeving were kept separated first by a single bore ceramic tubing and then by a Refrasil sleeving.

In case of the $\frac{1}{4}$ inch thick steel model, all thermocouples, fixed by means of lead pencil, were used in the main test. Later on, however, one of the thermocouples in the leading edge hole ($x = \frac{1}{8}$ inch) was replaced by one with the twin bore ceramic sleeve to find if a temperature gradient existed across the thickness of the model. But this could not detect any temperature gradient in that model.

7.2.3 Insulation of the bottom surface of the model

The model in the model support tray (vide section 6.5) did not rest on its bed, but in order to avoid the heat loss due to conduction, it was supported on four pointed alumina rods, one at each corner. Thus the actual support was reduced to four points only. The alumina rods were fixed in the aluminium adjusting screws which sat on the bed of the model support box.

The heat loss through conduction was, thus, minimised to a negligible quantity. But still the heat loss through radiation from the bottom surface could take place, which, of course, because of surface being polished, would be small. Aluminium foil supported on a fine copper wire mesh, was slipped below the model; taking care that it did not touch the surface of the model. In fact, it was kept about $\frac{1}{8}$ to $\frac{3}{16}$ inch below the lower surface of the model. The aluminium foil with its high reflectivity would reflect most of the heat radiation back to the model. Thus, for all practical purposes, the lower surface of the model could be assumed perfectly insulated, while the oxidised top surface received heating from the heating element.

By virtue of the low emissivity of the stainless steel, there is reason to believe that any heat loss through radiation from the polished side faces would be negligible. The model in its working position is shown in figure 7.2.1. Figure 7.2.2 shows the general arrangement of the model on the support tray with the reflector in position.

7.2.4 Tests on the Stainless Steel Models

The experiments were carried on in a high vacuum of about 10^{-5} torr. The heating was applied gradually. On each model three sets of readings were taken for three different rates of heating of 800 watts, 1000 watts and 1200 watts of the heating element. Sufficient time was allowed for each reading to achieve a steady state of temperature. Final readings were recorded only when thermocouple readings were steady for at least a quarter of an hour. The experimental results are given in tables 7.2.2 to 7.2.4.

In order to find the value of Q, the radiometer reading was taken at X = 0.75 inch and then with the help of graph of figure 6.2.5, this reading

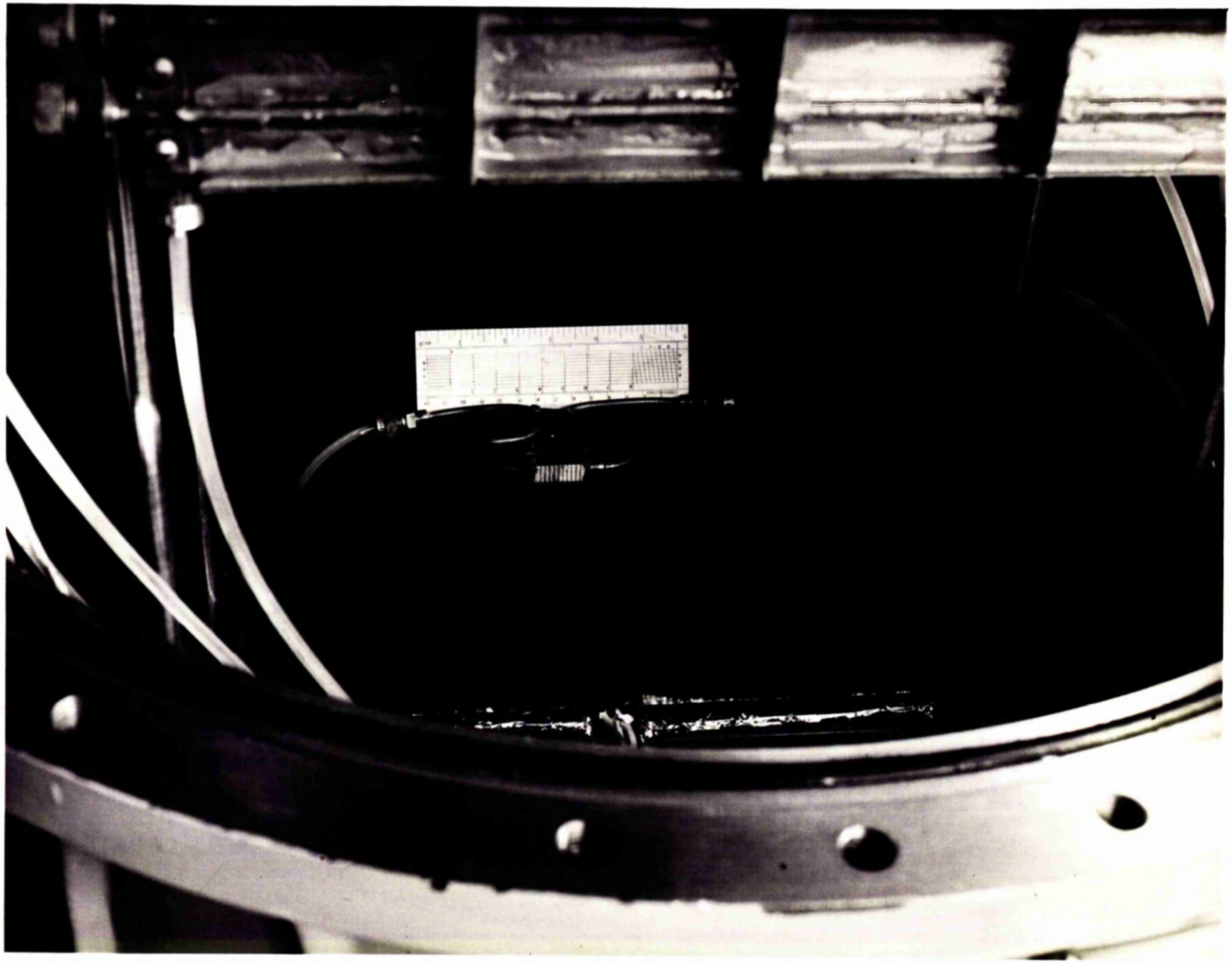

FIG. 7.2.1. The model in the working position.

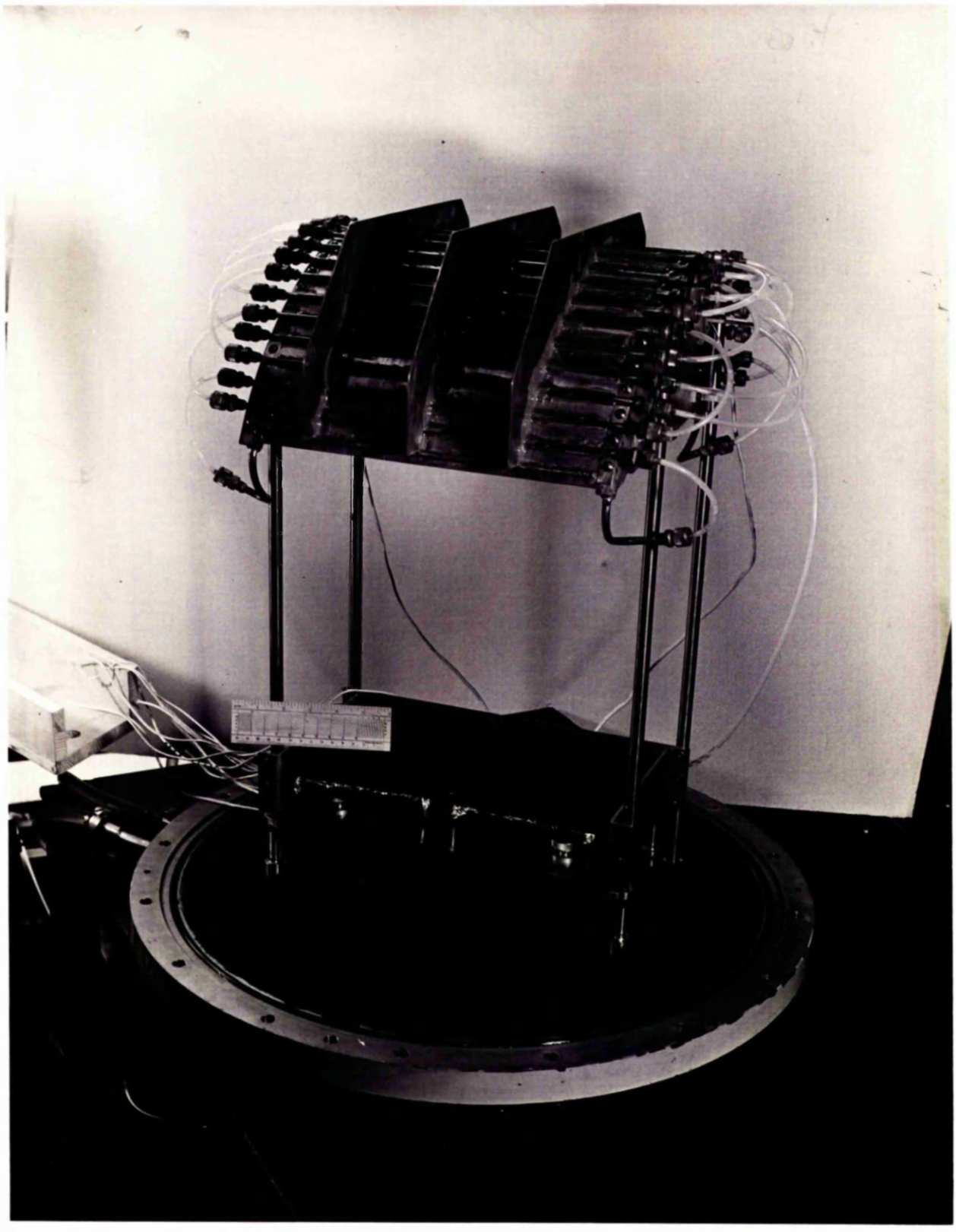

FIG. 7.2.2. The general arrange-ment of the model and the reflector.

was transferred to any point on the model. The heat intensity at that point was determined from the radiometer calibration chart given in table 6.4.1. From the heat intensity, the value of Q was calculated, using Q = heat intensity $\times \sqrt{x}$. Care was taken to supply enough water to the reflector, vacuum chamber, and the radiometer to keep them cool.

TABLE 7.2.2

Test values of temperatures in a $\frac{1}{8}$ inch thick stainless steel model.

Distance from the leading edge	Depth of thermocouple hole	Heating=800 watts Radiometer value of = 50.35 ft.lb./$ft^{3/2}$/sec	Heating=1000 watts Radiometer value of = 66.14 ft.lb/$ft^{3/2}$/sec.	Heating= 1200 watts Radiometer value of = 79.22 ft.lb/$ft^{3/2}$/sec.
inch	inch	deg. k	deg. k	deg. k
$\frac{1}{8}$	$\frac{1}{8}$	483.85	506.33	531.42
	$\frac{3}{8}$	483.68	506.23	531.14
$\frac{5}{8}$	$\frac{1}{8}$	482.76	504.91	529.75
	$\frac{3}{8}$	483.64	506.06	531.0
$1\frac{3}{8}$	$\frac{1}{8}$	-	-	-
	$\frac{3}{8}$	477.56	499.53	523.17
$2\frac{3}{8}$	$\frac{1}{8}$	475.69	496.2	519.66
	$\frac{3}{8}$	476.22	496.78	520.32
$3\frac{7}{8}$	$\frac{1}{8}$	469.88	489.36	511.34
	$\frac{3}{8}$	469.94	489.56	511.54
$5\frac{3}{4}$	$\frac{1}{8}$	-	-	-
	$\frac{3}{8}$	464.74	484.13	504.58

TABLE 7.2.3

Test values of temperatures in a $\frac{1}{4}$ inch thick stainless steel model.

Distance from the leading edge	Depth of thermocouple hole	Heating=800 watts Radiometer value of = 50.35 ft.lb/ft$^{3/2}$/sec.	Heating=1000 watts Radiometer value of = 66.14 ft.lb/ft$^{3/2}$/sec.	Heating=1200 watts Radiometer value of = 79.22 ft.lb/ft$^{3/2}$/sec.
inch	inch	deg. k	deg. k	deg. k
$\frac{1}{8}$	1/16	498.31	529.82	552.62
	3/16	498.34	529.85	552.68
$\frac{5}{8}$	1/16	496.60	527.68	550.24
	3/16	496.50	527.56	550.15
$1\frac{3}{8}$	1/16	490.08	519.64	541.0
	3/16	-	-	-
$2\frac{3}{8}$	1/16	481.69	509.08	529.54
	3/16	481.44	508.82	529.38
$3\frac{7}{8}$	1/16	471.96	497.04	576.11
	3/16	471.70	496.88	516.00
$5\frac{3}{8}$	1/16	466.07	490.08	508.41
	3/16	465.95	489.93	508.29

TABLE 7.2.4

Test values of temperatures in a $\frac{1}{8}$ inch thick stainless steel model.

Distance from the leading edge	Depth of Thermocouples	Heating=800 watts Radiometer value of = 49.6 ft.lb/ft$^{3/2}$/sec.	Heating=1000 watts Radiometer value of = 64 ft.lb/ft$^{3/2}$/sec.	Heating=1200 watts Radiometer value of = 77.12 ft.lb/ft$^{3/2}$/sec.
inch	No.	deg. k	deg. k	deg. k
$\frac{1}{8}$	1	506.24	538.84	563.52
	2	505.86	538.60	563.33
$\frac{5}{8}$	1	501.33	533.20	556.60
	2	501.67	533.27	557.24
$1\frac{3}{8}$	1	491.26	521.11	542.75
	2	491.24	521.10	542.74
$2\frac{3}{8}$	1	478.83	505.45	526.05
	2	478.34	505.20	525.61
$3\frac{7}{8}$	1	461.90	486.10	503.68
	2	461.51	485.65	503.40
$5\frac{3}{8}$	1	454.61	477.73	494.60
	2	454.22	477.37	494.26

7.2.5. Theoretical Temperature Distribution in the Stainless Steel Models:-

In the calculation to find the temperature distribution in the models, according to the theory in section 2.3, an effective value of Q was necessary. In order, to get the effective value of Q, the value of Q obtained from the radiometer reading was multiplied by the emissivity of the oxidised surface of the steel models, average value [43] of which can be taken as 0.7.

The average heat conductivity of 3.95 ft lb/ ft/sec/^{o}K was taken for the range of temperatures of 200 to 300^{o}C in the models. The calculated values of temperatures are given in tables 7.2.5 to 7.2.7. Both the experimental and the theoretical results are plotted in figures 7.2.3 to 7.2.11. By ignoring the heat conducting of the skin, the radiation equilibrium temperatures were also calculated and plotted in the same figures for comparison.

TABLE 7.2.5.

Theoretical Values of Temperatures in $\frac{1}{8}$ inch Thick Stainless Steel models

Distance from the leading edge	Heating = 800 Watts Effective value of Q=35.25 ft. lb./ ft^{3}/2/ sec	Heating = 1000 Watts Effective value of Q=46.30 ft. lb./ ft^{3}/2/ sec	Heating = 1200 Watts Effective value Q=55.45 ft. lb./ ft^{3}/2/ sec
inch	degree K	degree K	degree K
0	454.8	488.0	515.6
$\frac{1}{8}$	454.4	487.8	515.4
$\frac{5}{8}$	452.5	486.9	514.3
$1\frac{3}{8}$	451.5	482.0	508.3
$2\frac{3}{8}$	447.3	474.7	500.0
$3\frac{7}{8}$	440.8	466.4	491.8
$5\frac{3}{4}$	437.9	464.00	486.9
6	437.6	463.2	486.1

TABLE 7.2.6.

Theoretical Values of temperatures in a $\frac{3}{4}$ inch thick Stainless Steel Model

Distance from the leading edge	Heating = 800 Watts Effective value of Q = 35.35 ft. lb./ ft^3/2/ sec.	Heating= 1000 Watts Effective value of Q = 46.30 ft. lb./ ft^3/2/ sec.	Heating = 1200 Watts Effective value of Q = 55.45 ft. lb./ ft^3/2/ sec.
inch	degree K	degree K	degree K
0	463.25	500.00	527.85
$\frac{1}{8}$	463.00	499.50	527.30
$\frac{5}{8}$	462.20	496.38	522.97
$1\frac{3}{8}$	455.32	488.14	510.87
$2\frac{5}{8}$	444.37	472.16	492.22
$3\frac{7}{8}$	433.63	458.80	477.14
$5\frac{5}{4}$	424.33	449.44	469.20
6	424.00	448.70	468.60

TABLE 7.2.7.

Theoretical values of Temperatures in a $\frac{1}{8}$ inch thick stainless steel model

Distance from the leading edge	Heating = 800 Watts Effective value of Q = 34.72 ft. lb./ $ft^{3}/2$ /sec.	Heating = 1000 Watts Effective value of Q = 44.8 ft. lb./ $ft^{3}/2$ / sec.	Heating = 1200 Watts Effective value of Q = 54 ft. lb. / $ft^{3}/2$ / sec.
inch	Degree K	Degree K	DegreeK
0	477.25	515.0	544.0
$\frac{1}{8}$	476.00	514.4	543.1
$\frac{2}{8}$	467.42	505.0	532.0
$1\frac{3}{8}$	452.01	490.8	513.2
$2\frac{3}{8}$	436.00	468.1	489.6
$3\frac{2}{8}$	419.8	447.05	464.
$5\frac{3}{4}$	409.27	435.17	450.33
6	408.40	434.28	450.05

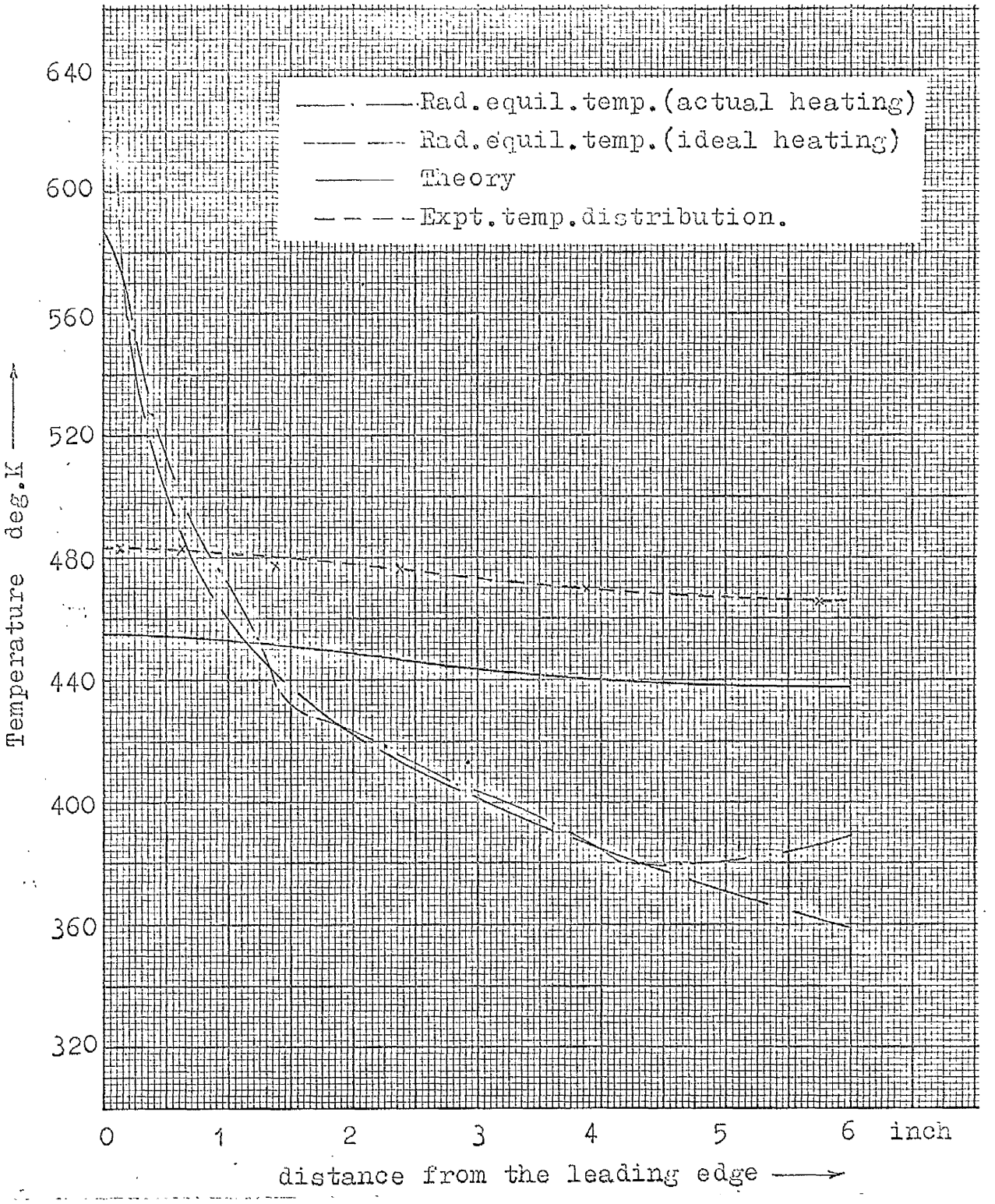

FIG. 7.2.3 Temperature distribution in a stainless steel model, t=0.5 inch, Q=35.25ft.lb/ft$^{3/2}$/sec.

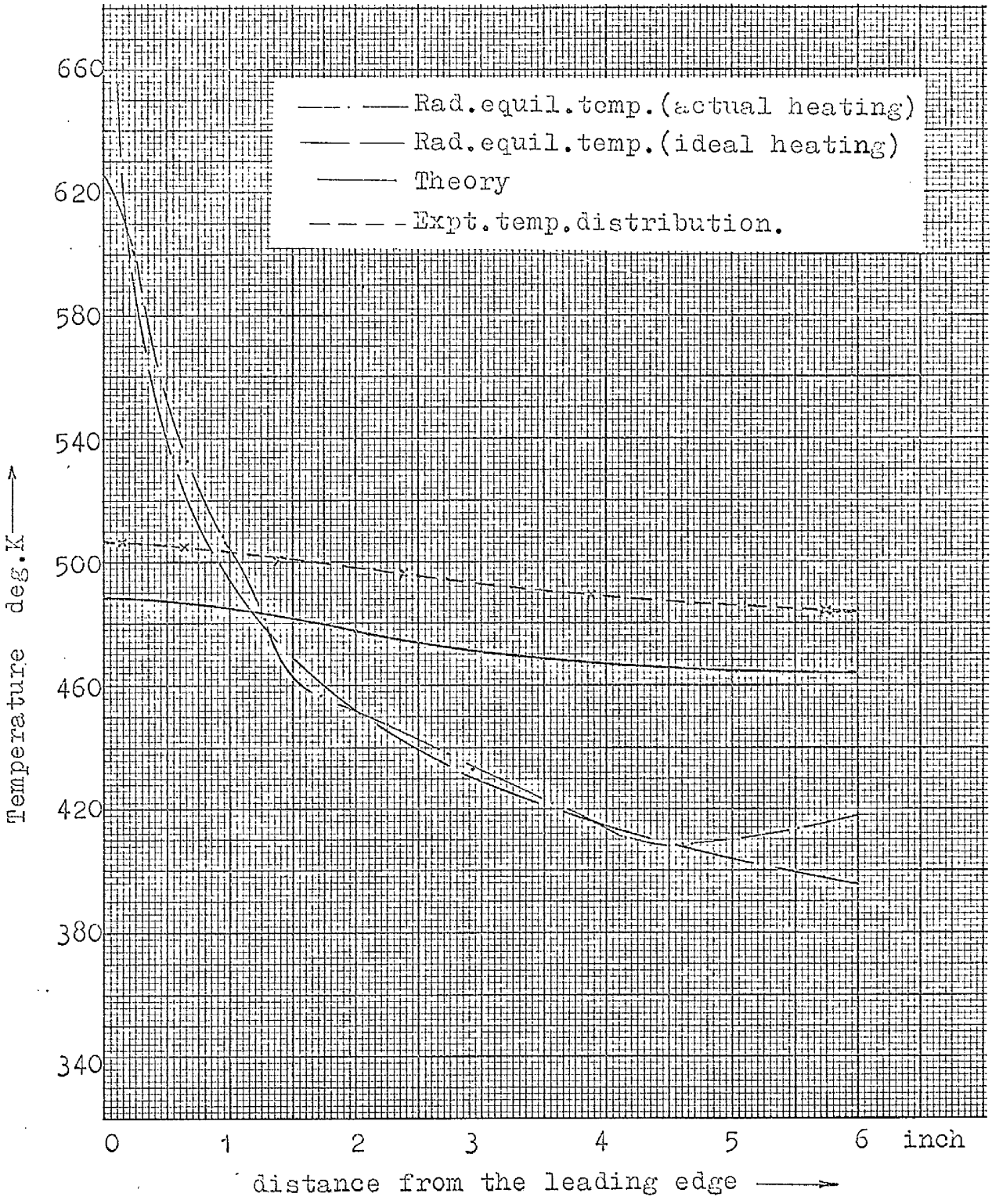

FIG.7.2.4. Temperature distribution in a stainless steel model, t=0.5 inch, Q=46.30ft.lb/ft$^{3/2}$/sec.

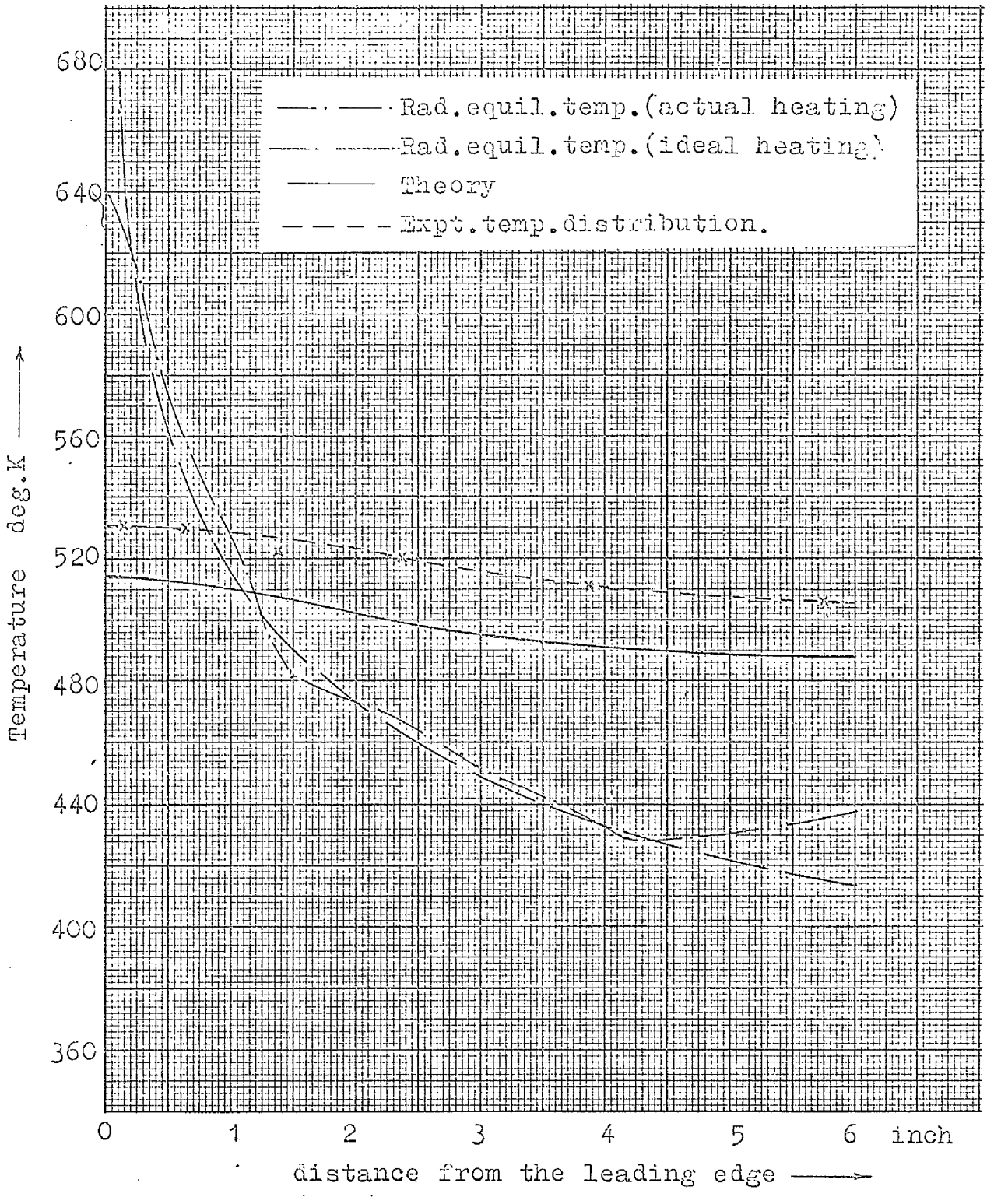

FIG.7.2.5. Temperature distribution in a stainless steel model, t=0.5 inch, Q=55.45ft.lb/ft$^{3/2}$/sec.

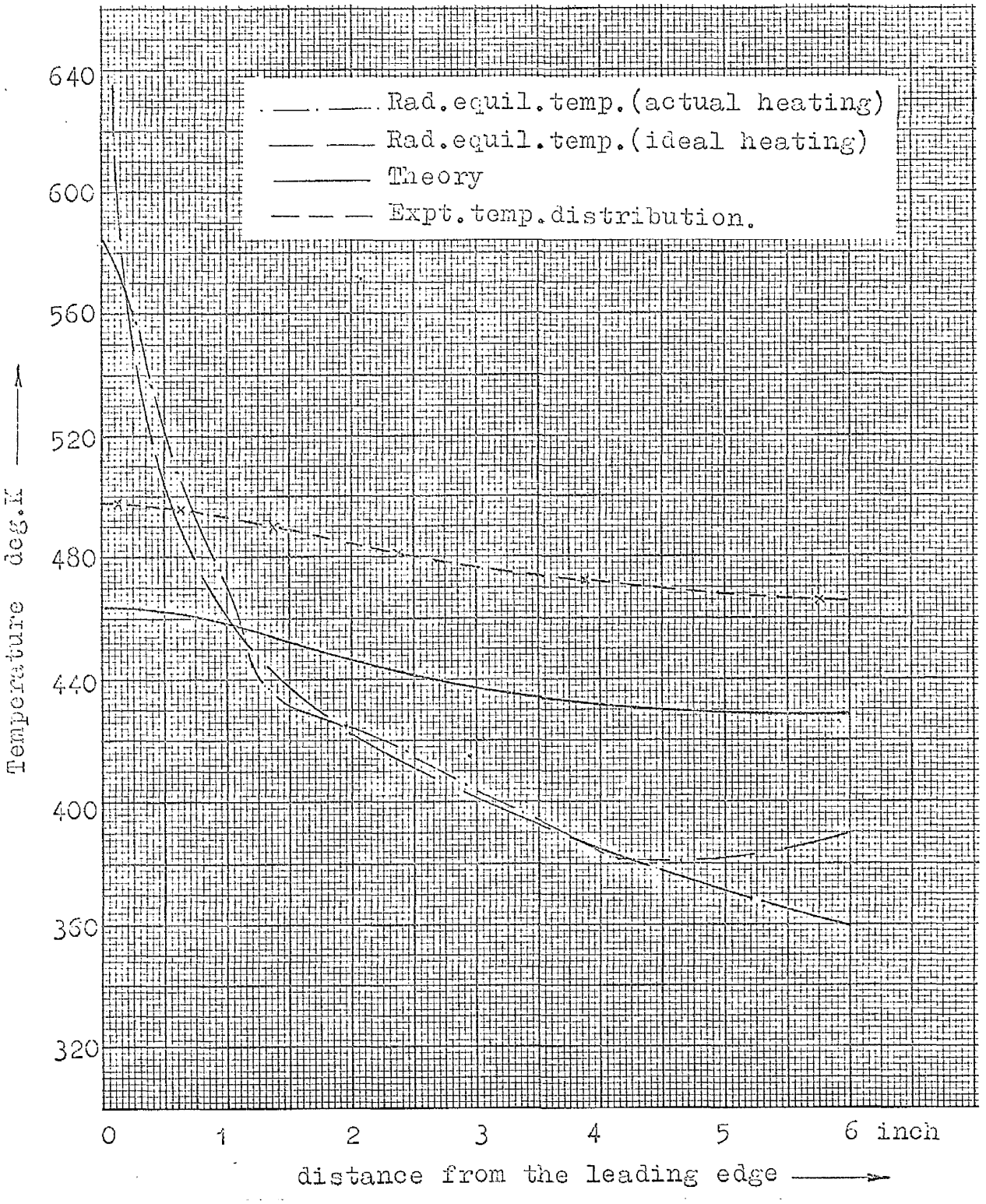

FIG.7.2.6. Temperature distribution in a stainless steel model, t=0.24 inch, Q=35.25ft.lb/ft$^{3/2}$/sec.

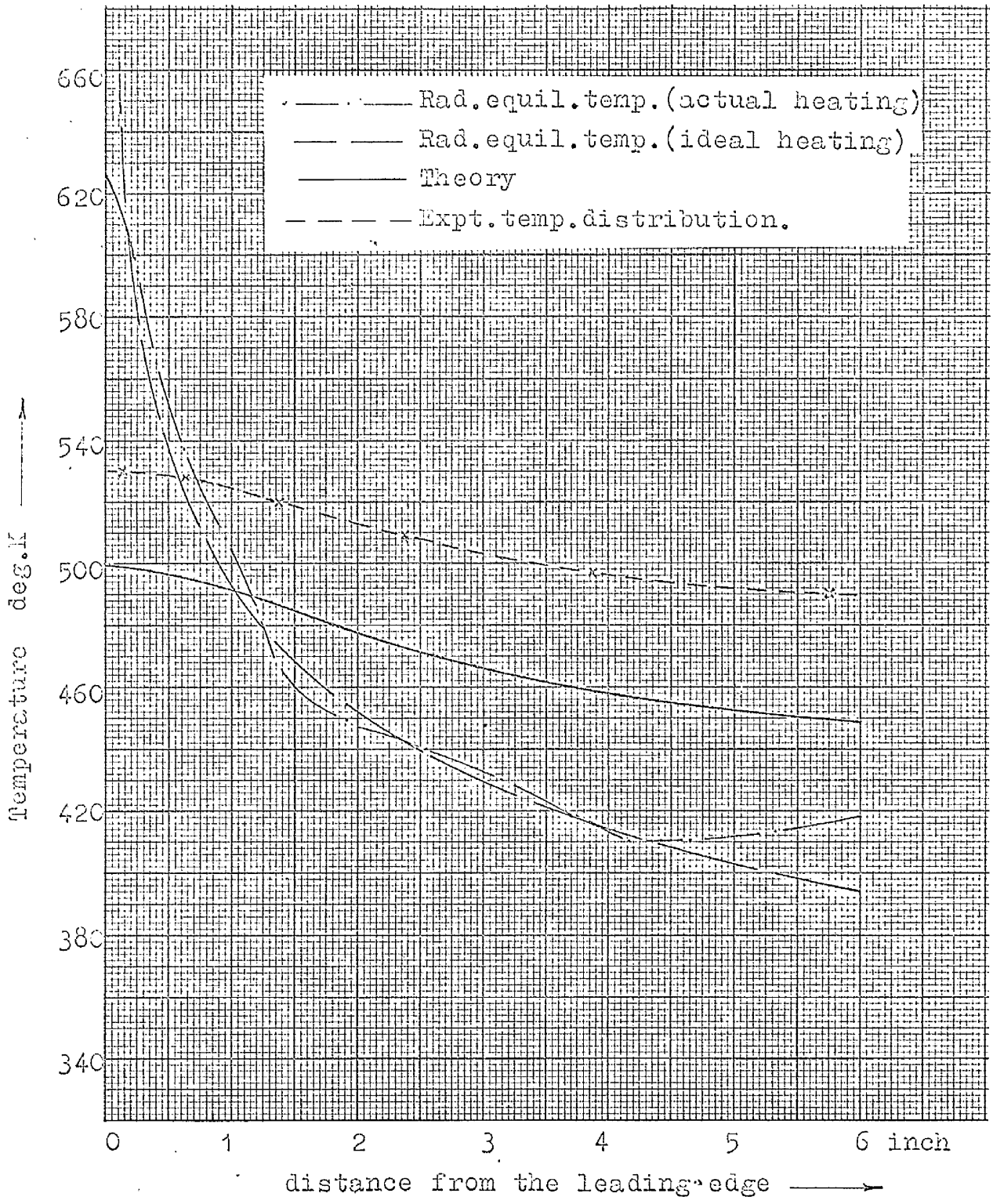

FIG.7.2.7.Temperature distribution in a stainless steel model, t=0.24 inch, Q=46.30ft.lb/ft$^{3/2}$/sec.

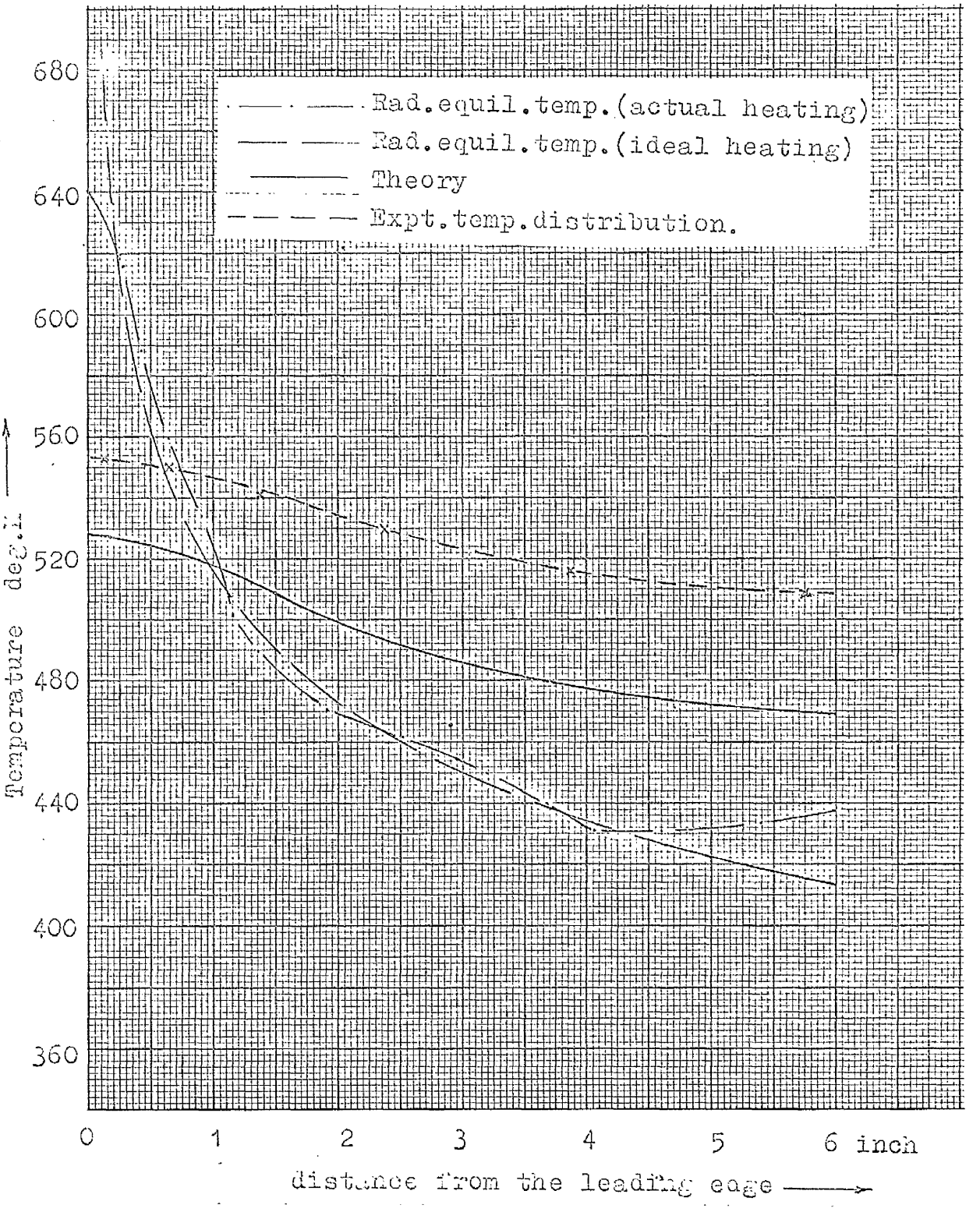

FIG.7.2.8. Temperature distribution in a stainless steel model, t=0.24 inch, Q=55.45ft.lb/ft$^{3/2}$/sec.

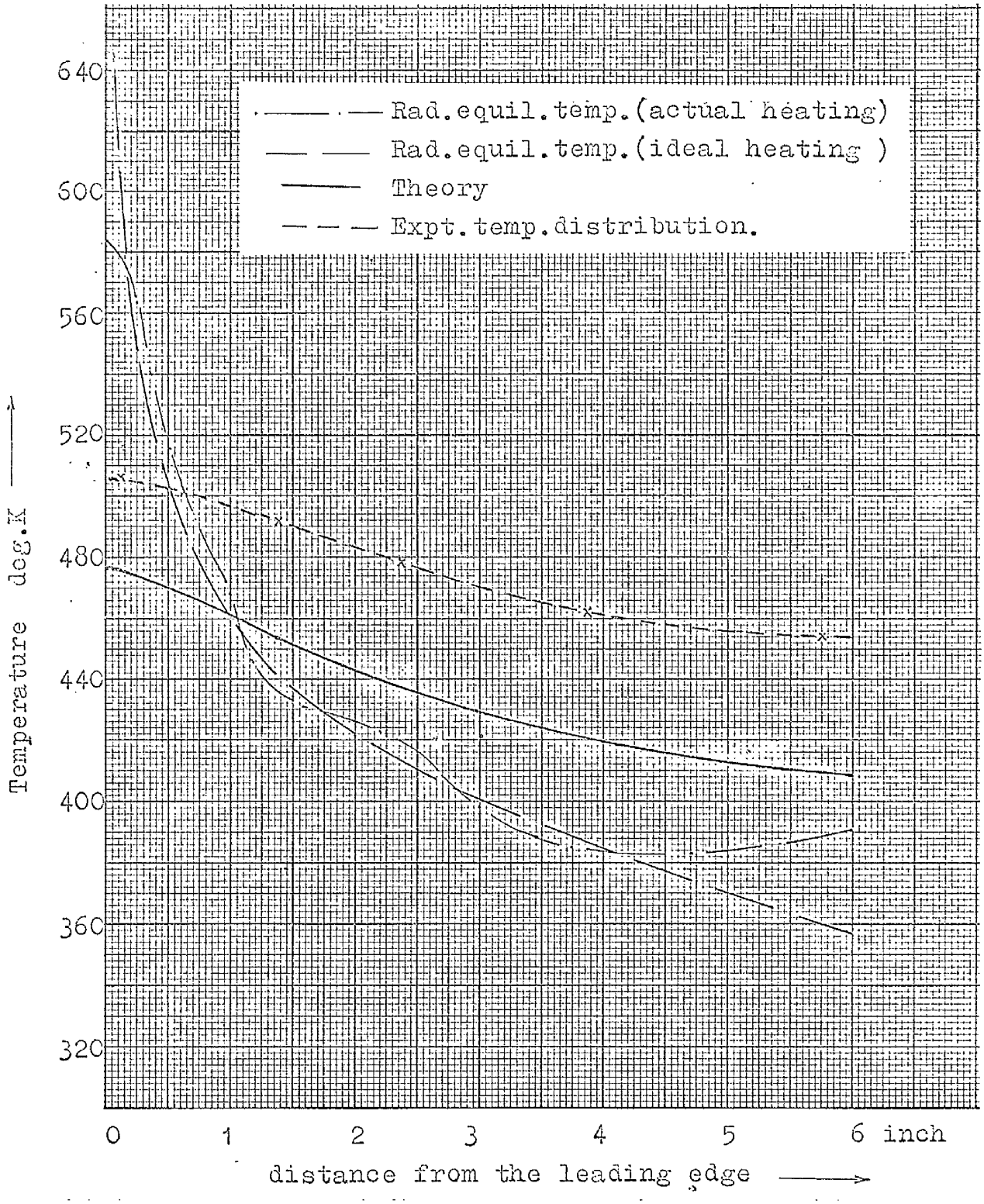

FIG. 7.2.9. Temperature distribution in a stainless steel model, t = 0.125 inch, Q=34.72ft.lb/ft$^{3/2}$/sec.

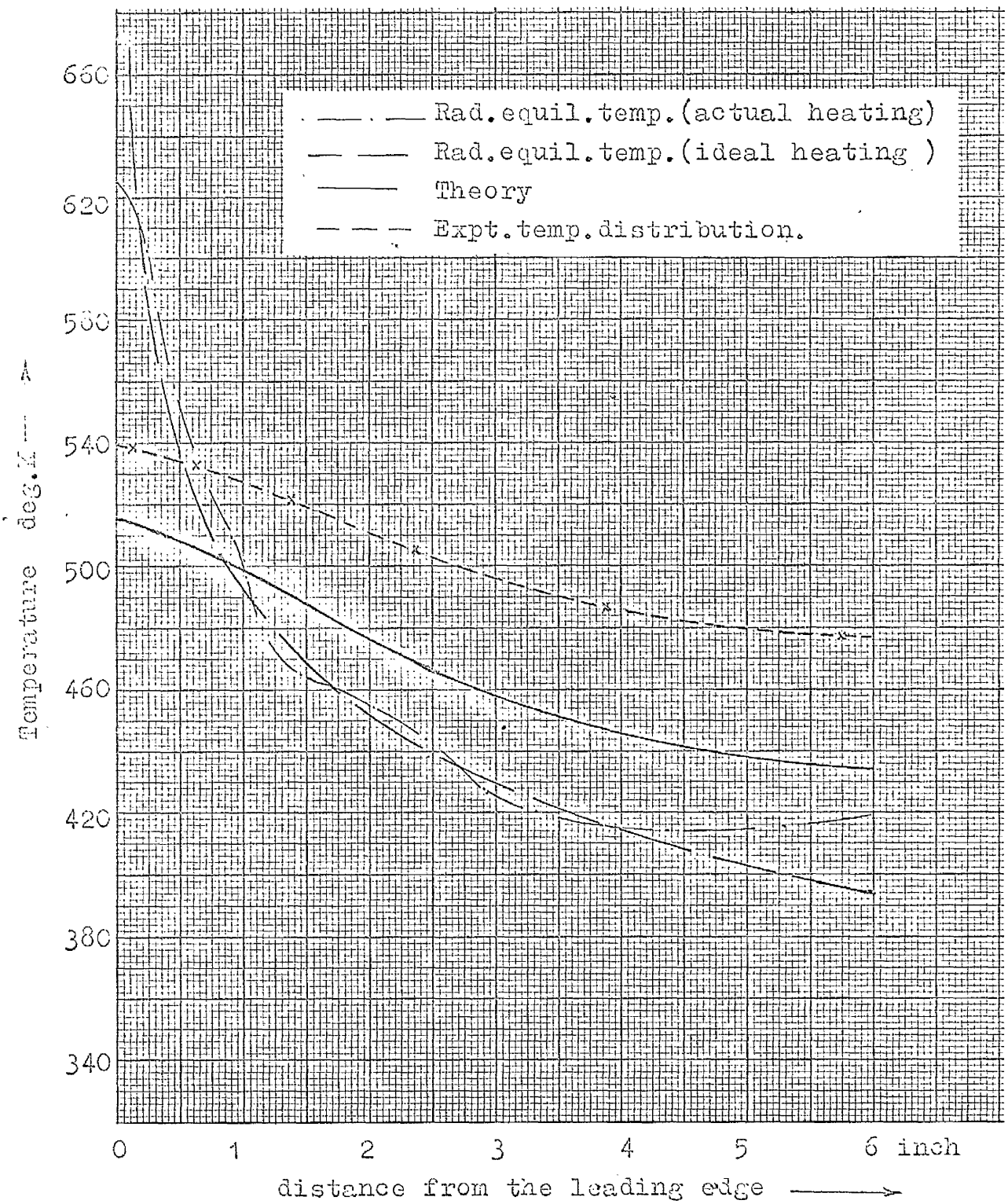

FIG. 7.2.10. Temperature distribution in a stainless steel model, t = 0.125 inch, Q = 44.8ft.lb/ft$^{3/2}$/sec.

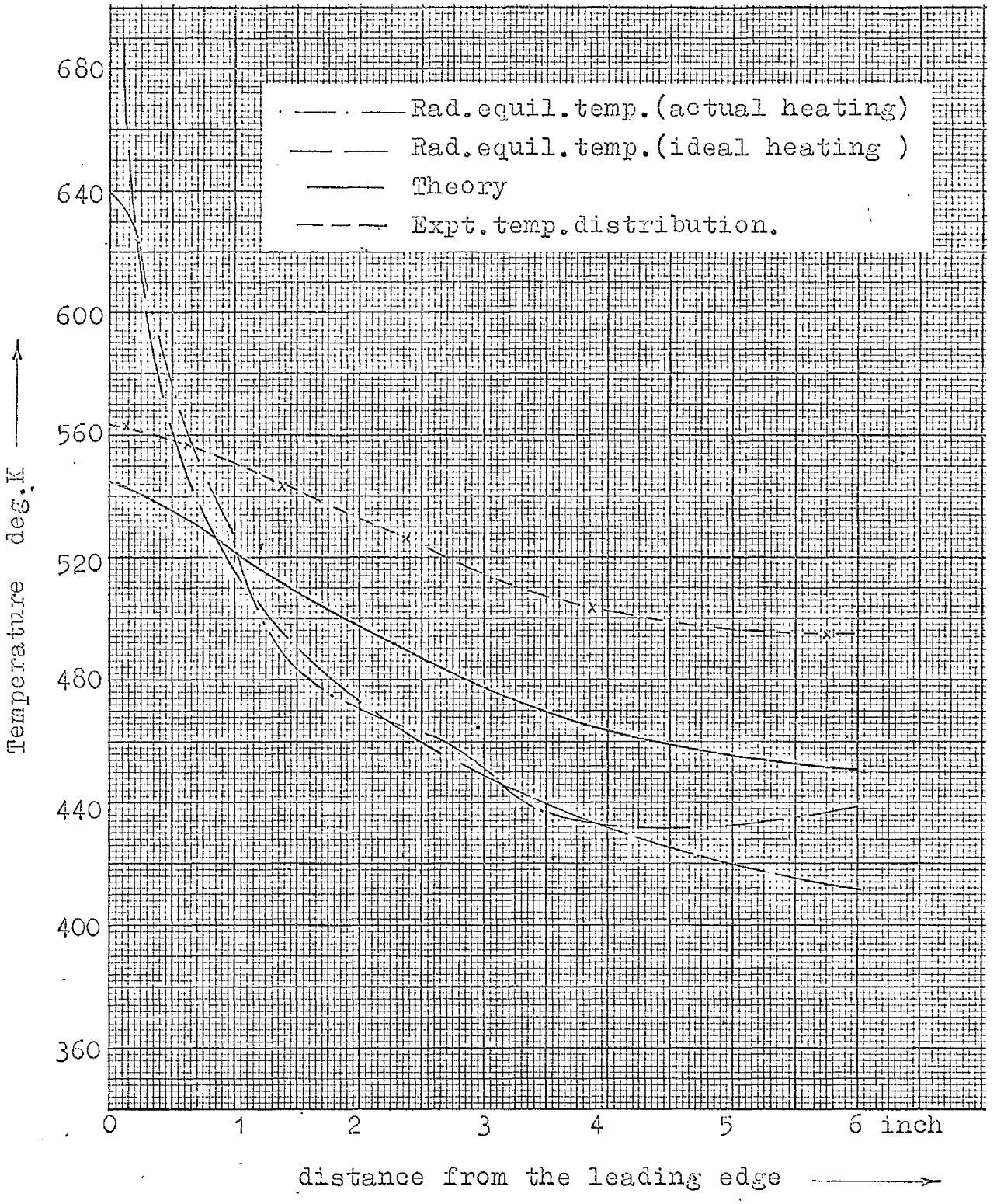

FIG. 7.2.11. Temperature distribution in a stainless steel model, t =0.125 inch, Q = 54 ft.lb/ft$^{3/2}$/sec.

7.3 CERAMIC MODEL

7.3.1 Preparation of the Model:- Due to inherent difficulties of distortion and shrinkage in manufacturing a ceramic body, affecting the accuracy of the shape and size of the model, a single piece of 12 inch x 6 inch x $\frac{1}{2}$ inch model could not be obtained from the ceramic manufacturing concerns. The bigger the size of the ceramic body cast, more is the chance of the presence of blow holes and also of inhomogenity of the structure. To overcome these difficulties, two pieces of Frequentite ceramic blocks 6 inch x 6 inch x 0.45 inch were obtained from Messrs. Steatite Products Ltd., one of which was later sawed into two equal pieces of 3 inch x 6 inch x 0.45 inch. (6 inch x 6 inch piece of Frequentite is the largest they can produce). In the test, these two pieces were arranged; one on either side of the 6 inch x 6 inch x 0.45 inch piece, thus making 12 inches, the required total width of the model.

Two rows of $\frac{1}{8}$ and $\frac{3}{8}$ inch deep holes and of the same sizes and locations as for the $\frac{1}{2}$ inch thick stainless steel model (section 7.2.1) were drilled through one surface of the ceramic model for inserting thermocouples. The other surface was painted with a paste of lampblack and fibrefrax cement to increase the emissivity of the surface, as the ceramics, in general, do not have high emissivity, which was desirable to absorb the maximum radiant heat.

Thermocouples were fixed in the ceramic model in the same way as described in section 7.2.2 for the $\frac{1}{2}$ inch thick stainless steel model. The same Eureka and Vacrome wires of 0.004 inch diameter were used for the thermocouples.

7.3.2 Model support and Insulation of the Bottom Surface:- Since the ceramic model did not consist of only one piece of 12 inch x 6 inch x 0.45 inch, it could not be supported on the head of four ceramic pointed rods at the four corners as was done in case of stainless steel models (section 7.2.3). In

this case, all the three ceramic pieces rested on two quartz tubes of 5/16 inch diameter, which were fixed to the aluminium adjusting screws (vide section 7.2.3). These aluminium screws were supported on the bed of the bed of the model support tray. Thus instead of point contacts, there were line contacts in case of the ceramic models. But with the poor thermal conductivity of quartz (K = 1.5 to 2 ft.lb/ft/sec/^{o}K), heat loss from the model through contact would be expected to be negligibly small.

Aluminium foil below the model was arranged in the same way as in the case of the stainless steel model (vide section 7.2.3) to reflect the radiant heat back to the model.

7.3.3 Tests and Results:- Using a new reflector whose calibration is given in table 6.2.2, tests on the ceramic model were carried on in a high vacuum of about 10^{-5} torr for the three different rates of heating of 800; 1000 and 1200 watts of the heating element. Test results are given in table 7.3.1.

Sully and Waterhouse[43] gave a value of about 0.95 for the emissivity of lampblack. But, in the present case, a lower value of =0.80 was taken on the assumption that mixing the lampblack with fibrefrax cement might have affected the emissivity to a certain extent. The value of Q obtained on the basis of radiometer reading was thus multiplied by 0.80 to obtain an effective value of Q, which is given in table 7.3.2. A thermal conductivity of 0.65 ft.lb/ft/sec/^{o}K, quoted by Messrs. Steatite and Porcelain Products Ltd. was used in the calculation of the theoretical temperature of figure 7.4.4. Its variation with the temperature was not known, but for the temperature range of 250 to 300^{o}C an increase of about 15% was assumed in the theoretical calculation of temperatures given in table 7.3.2. Values of temperatures, calculated according to the theory, are also given in the same table 7.3.2. Temperature distributions on the model, experimental as well as theoretical and for comparison, the radiation equilibrium temperature, are plotted in figures 7.3.1 to 7.3.3 for the different values of Q obtained from the different rates of heating.

TABLE 7.3.1.

Test Values of Temperature in a $\frac{1}{2}$ inch thick ceramic model

Distance from the leading edge	Depth of thermo-couple hole	Heating = 800 Watts Radiometer value of Q = 46.82 ft. lb./ ft $^{3/2}$/ sec.	Heating = 1000 Watts Radiometer value of Q = 50 ft. lb./ft $^{3/2}$/ sec.	Heating = 1200 Watts Radiometer value of Q = 75.10 ft. lb./ ft $^{3/2}$/ sec.
$\frac{1}{8}$	$\frac{1}{8}$	482.24	513.57	528.50
	$\frac{3}{8}$	487.06	520.60	537.71
$\frac{3}{8}$	$\frac{1}{8}$	482.79	514.43	531.12
	$\frac{3}{8}$	485.66	517.86	535.55
$1\frac{3}{8}$	$\frac{1}{8}$	474.10	503.35	519.21
	$\frac{3}{8}$	474.88	504.2	520.94
$2\frac{3}{8}$	$\frac{1}{8}$	-	-	-
	$\frac{3}{8}$	457.54	482.57	501.20
$3\frac{7}{8}$	$\frac{1}{8}$	440.9	466.02	479.16
	$\frac{3}{8}$	441.41	466.38	479.86
$5\frac{3}{4}$	$\frac{1}{8}$	-	-	-
	$\frac{3}{8}$	430.0	453.26	465.84

TABLE 7.3.2.

Theoretical Values of Temperature in a $\frac{1}{2}$ inch thick ceramic model

Distance from the leading Point	Heating = 800 Watts Effective Value of Q = 37.45 ft. lb./ ft $^{3/2}$/ sec.	Heating = 1000 Watts Effective Value of Q = 51.6 ft.lb./ ft $^{3/2}$/ sec.	Heating = 1200 Watts Effective Value of Q = 60.0 ft. lb. / ft $^{3/2}$/ sec.
inch	degrees K	degreesK	degrees K
0	488.25	533.0	559.0
$\frac{1}{8}$	487.50	531.5	557.3
$\frac{3}{8}$	481.2	520.0	541.2
$1\frac{3}{8}$	459.4	495.2	510.10
$2\frac{3}{8}$	435.3	468.8	481.75
$3\frac{7}{8}$	412.80	440.3	455.4
$5\frac{3}{4}$	400.0	426.1	440.4
6	398.8	435.5	440.0

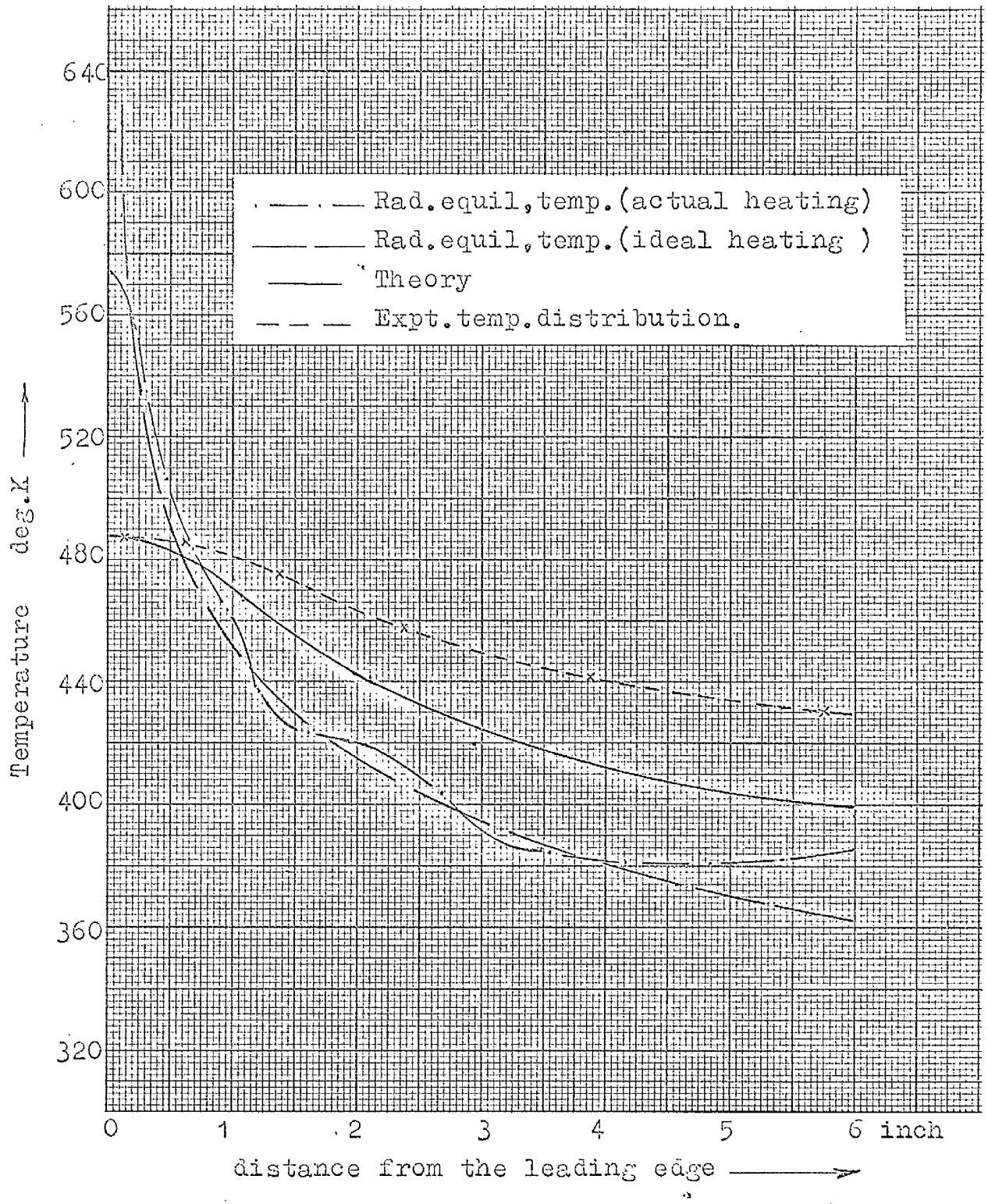

FIG. 7.3.1. Temperature distribution in the ceramic model, t = 0.45 inch, Q = 37.45ft.lb/ft$^{3/2}$/sec.

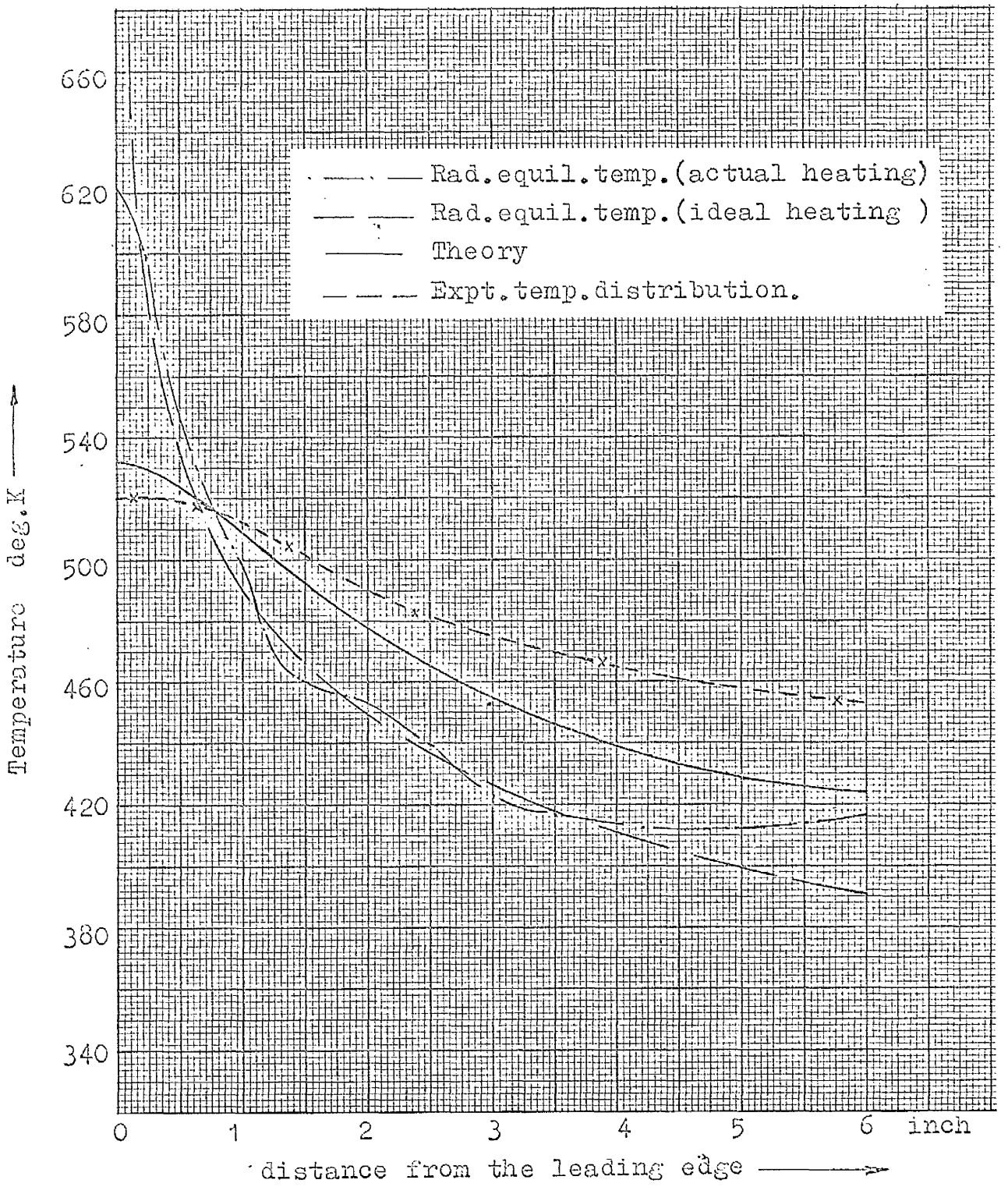

FIG. 7.3.2. Temperature distribution in the ceramic model, t = 0.45 inch, Q = 51.6ft.lb/$ft^{3/2}$/sec.

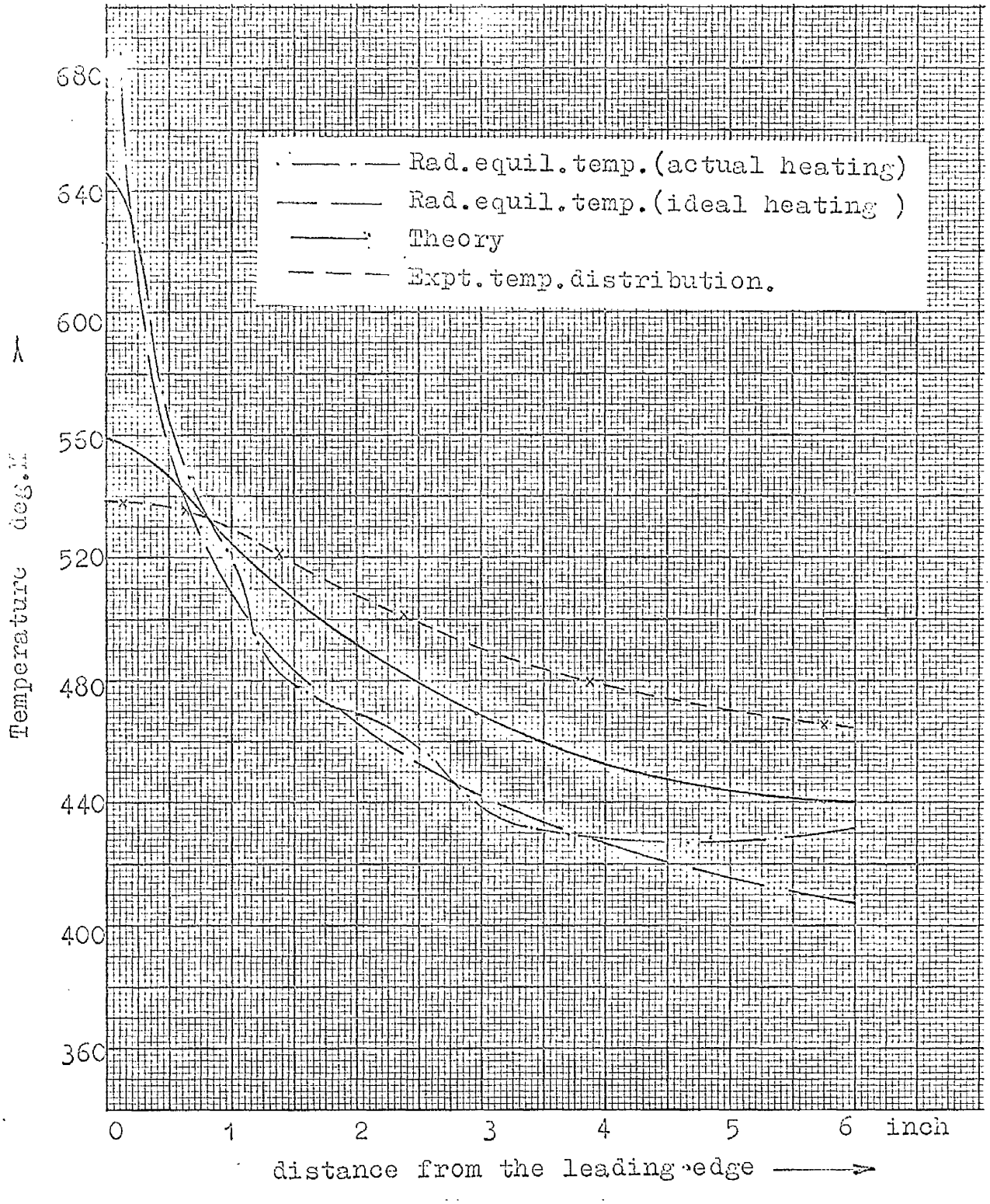

FIG. 7.3.3. Temperature distribution in the ceramic model, t = 0.45 inch, Q = 60 ft.lb/ft$^{3/2}$/sec.

7.4. Temperature Distribution in the Conducting Skin Models for the Different Values of Q, K and E.

In sections 7.2 and 7.3, quoted values of E and K and the measured values of Q measured by the radiometer have been used to calculated the theoretical temperature distribution in the models. But there are reasons to believe that the models' own values of E and K might not be exactly the same as the average quoted ones. For instance the emissivity of the surface will depend on the degree of roughness, temperature of oxidation, depth of the oxide film formed on the surface, etc. Besides, the emissivity may also vary with the temperature of the models.

Similarly, the variation of K with the temperature is well known. For the stainless steel, its values of 3.57 at 20°C and 4.51 ft. lb/ft/ sec/°K at 700°C only were known and hence exact nature of the variation could not be determined. For, Frequentite ceramic average value of K of 0.65 ft. lb/ ft/ sec / °K only was known and its variation with the temperature could not be available.

Certain errors can also be expected in the measurement of Q by the radiometer as well as in the subsequent calculation of the effective value of Q by using a quoted value of E for the top surface of the model. The calibration of the radiometer itself is liable to certain variation with use, due to the deposition of the evaporated particles from the heating element on the different parts of the radiometer. Secondly, taking the measurement of the heat intensity at one point by the radiometer and then transferring this reading with the help of calibration curve of the reflector, is liable to induce some errors. Thirdly, when

calculating the effective value of Q, a quoted value of E (assumed value in case of ceramic model) is used, which might have certain errors.

Under these circumstances, it appears desirable to see, how the theoretical temperature distribution, calculated with the help of certain reasonably appropriate assumed values of Q, K and E compare with the experimental ones. With this view, figures 7.4.1 and 7.4.4 are drawn.

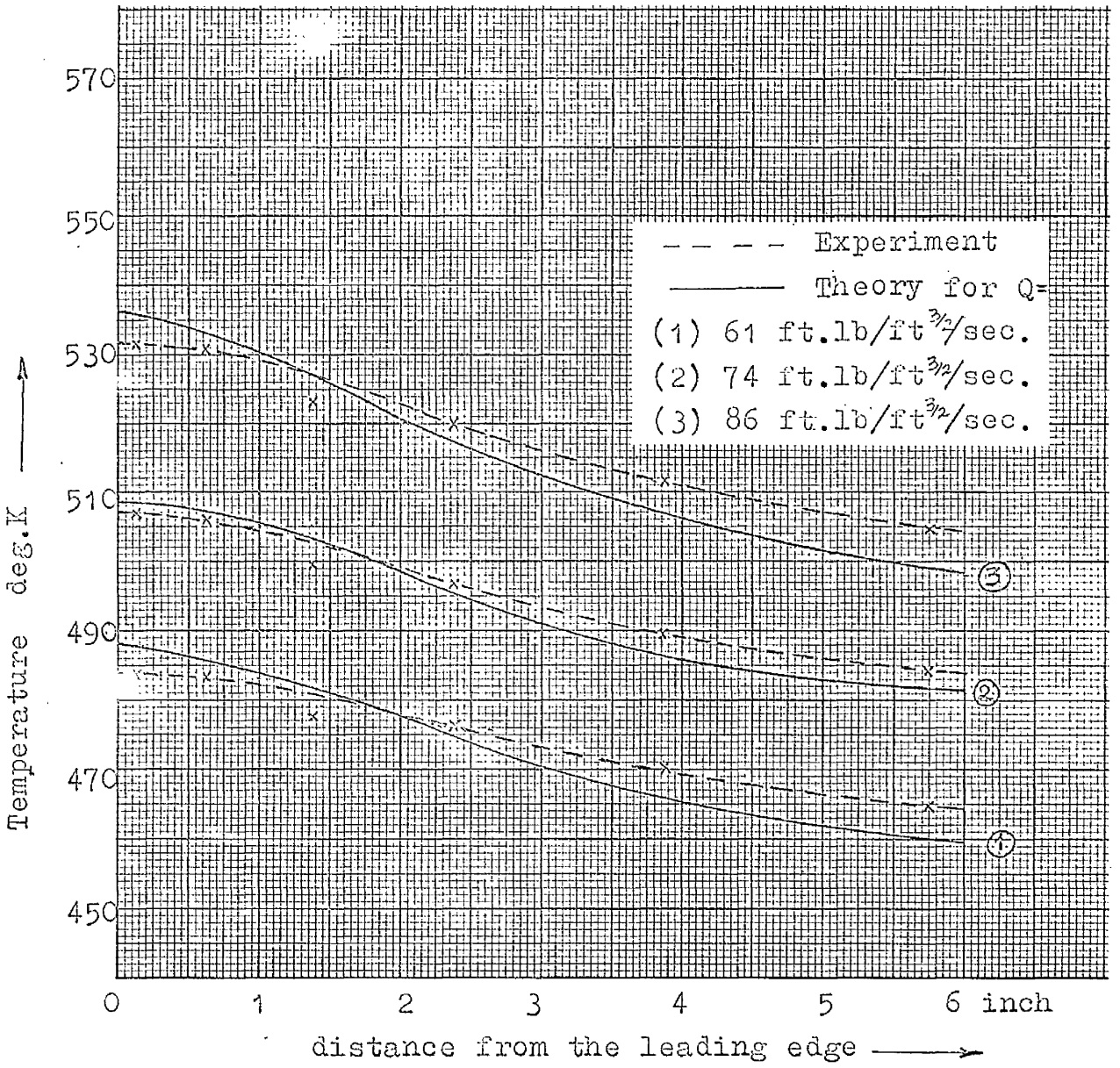

FIG.7.4.1. Temperature distribution in the half inch thick stainless steel model for $\varepsilon = 0.8$ and different values of Q

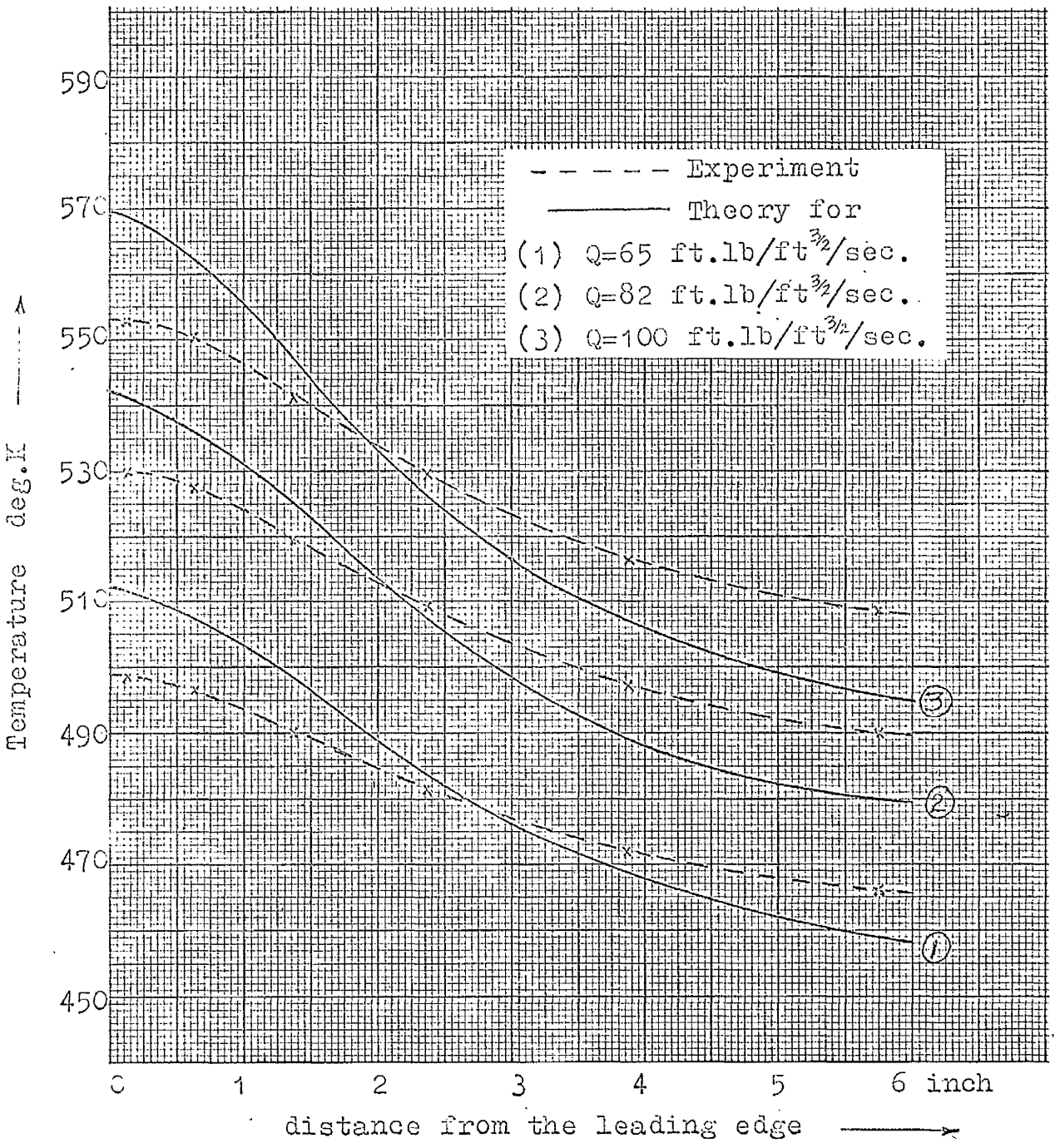

FIG.7.4.2. Temperature distribution in the quarter inch thick stainless steel model for $\varepsilon = 0.8$ and different values of Q

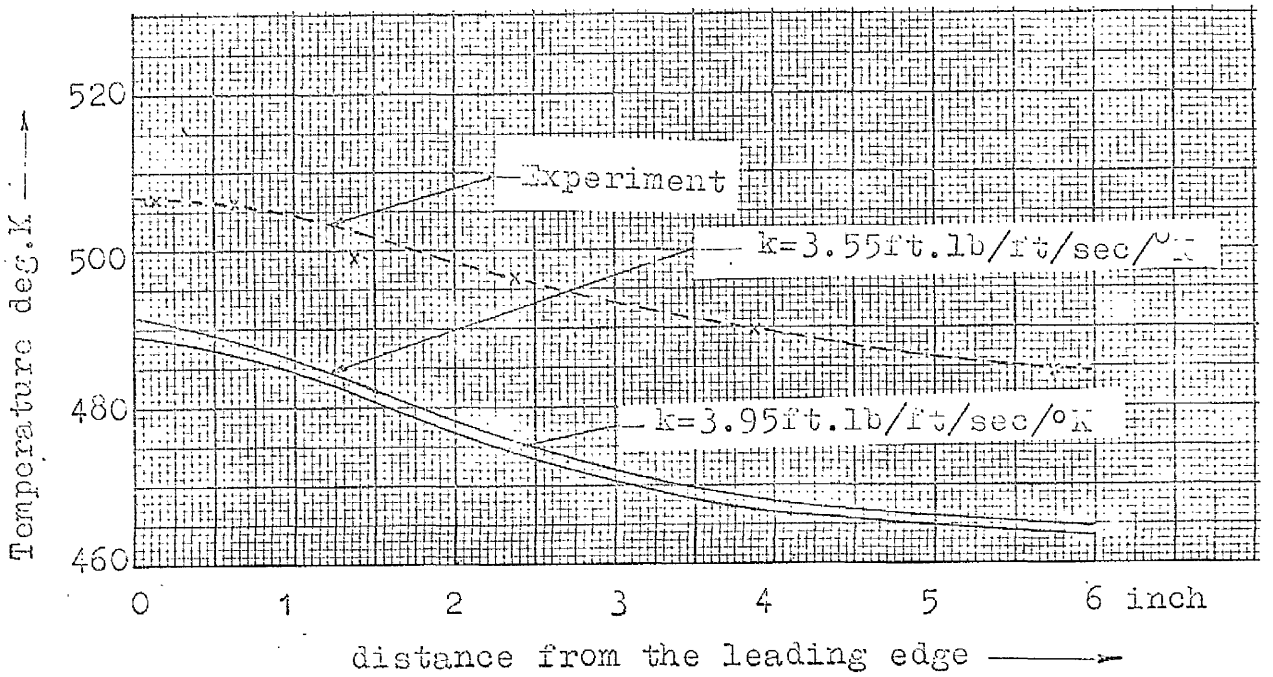

Stainless steel, t=0.50 inch, Q=46.3ft.lb/ft$^{3/2}$/sec.

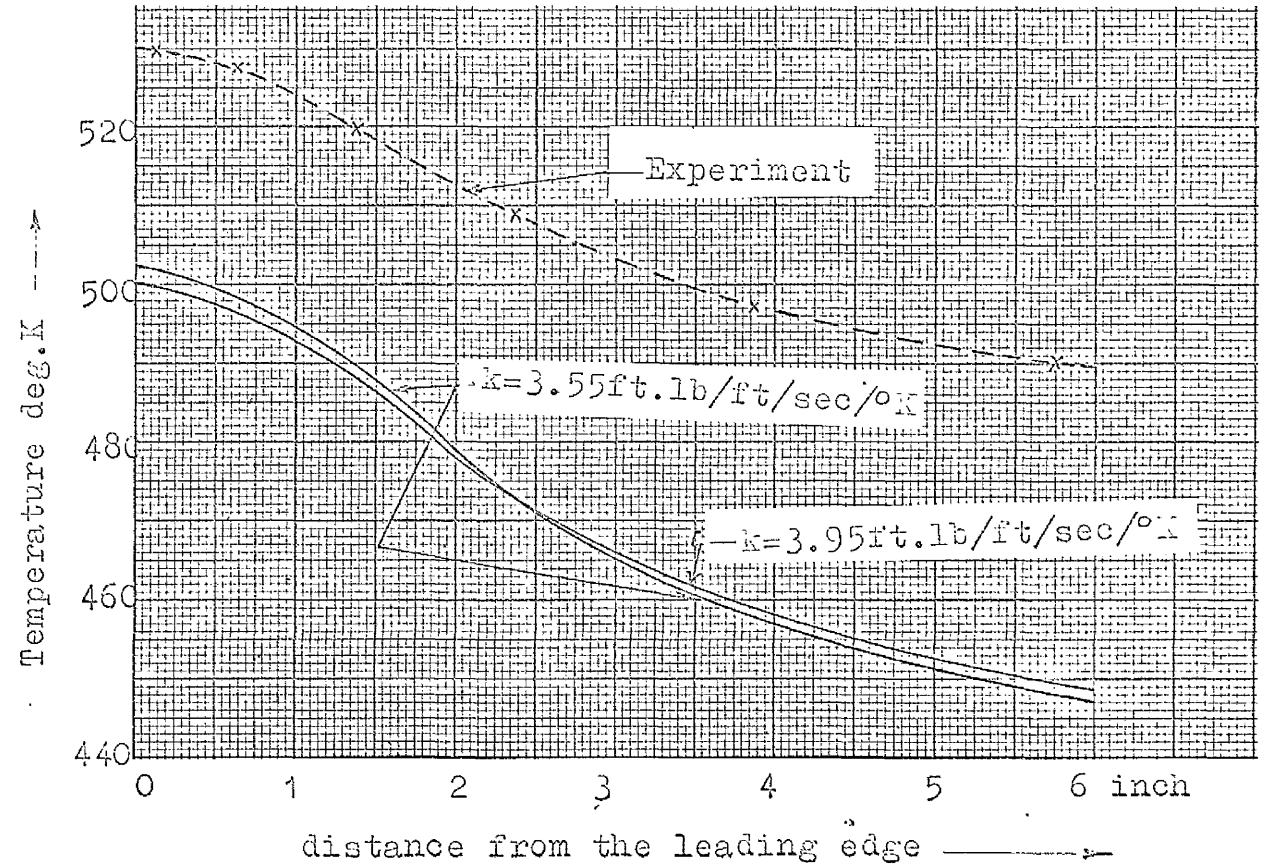

Stainless steel ,t=0.24 inch, Q=46.3ft.lb/ft$^{3/2}$/sec.

FIG.7.4.3. Temperature distribution in stainless models for different values of heat conductivity.

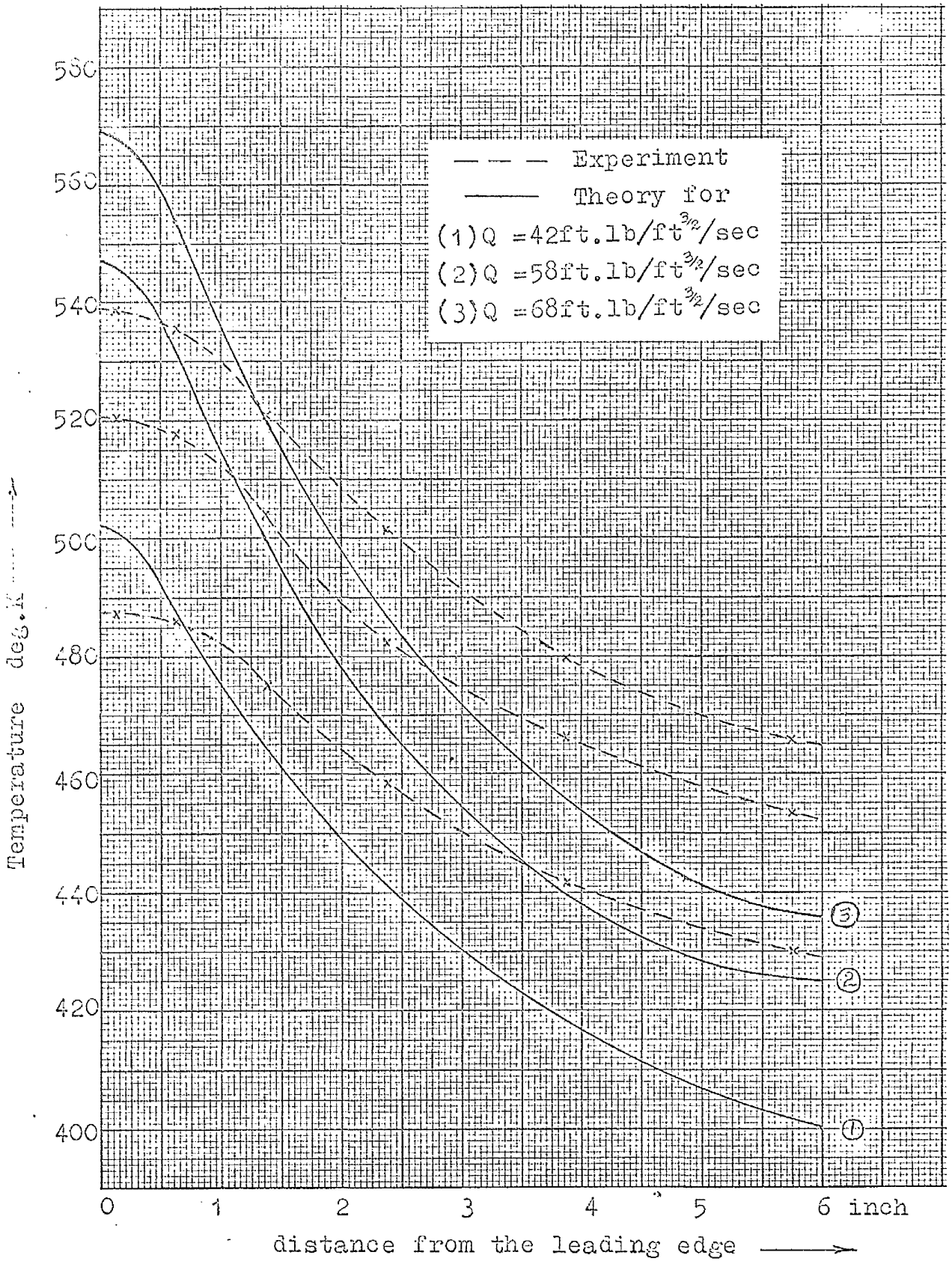

FIG. 7.4.4. Temperature distribution in the ceramic model for $\varepsilon = 0.9, k = 0.65$ ft.lb/ft/sec/°C and different values of Q.

CHAPTER VIII

DISCUSSION OF THE RESULTS AND CONCLUSION

8.1 Observations:- By providing a heating similar to the aerodynamic heating at hypersonic speeds, tests were performed on the conducting skin models of stainless steel and ceramic of different thicknesses (chapter VII) to study the temperature distribution and find the validity of the one-dimensional heat conduction theory, described in sections 2.2 and 2.3. Experimental as well as theoretical predictions of temperature distribution in the models have been plotted in figures of chapter VII. By neglecting the heat conduction through the body and by balancing the aerodynamic heat input with the radiant heat output, the radiation equilibrium temperatures have been calculated and plotted in the same figures. From these results the following observations can be made:-

1. The nature of the curve of temperature distribution in the conducting skin, predicted by the theory of section 2.3 is in excellent agreement with that of the experiment, in the aerodynamic heating range of the tests.

2. The radiation equilibrium temperature at the nose region is much higher than both the experimental and theoretical predictions. On the other hand, everywhere more than about an inch away from the nose, the radiation equilibrium temperatures are lower. This clearly shows that a significant amount of heat is conducted away by the skin from the nose region to the down stream part of the hypersonic body.

3. In none of the tests, the theoretical and the test values of temperatures agree absolutely.

4. Subject to the accuracy of the measured values of Q and the quoted values of and for the stainless steel models,

(a) figures drawn in section 7.2 show that the test values of temperatures are higher than the theoretical predictions on the average about 3 to 5 per cent in the nose region and 5 to 7 per cent near the rear-end.

(b) The difference between the theoretical and the test value of temperatures is least at the leading edge and it goes on increasing towards the rear-end; and

(c) Higher the rates of heating, less is the difference between the theoretical and the test values of temperatures.

5. There is a small temperature gradient observed across the thickness of the conducting skin. In the case of the $\frac{1}{8}$ inch thick stainless steel model, the gradient is about 1 to 1.5°C per inch for Q = 35.25 to 55.45 ft.lb/ft. /Sec. In the case of the ceramic model, the gradient is a bit higher, 2 to 4°C per inch for the similar range of values of Q. However, this is very small compared to the longitudinal temperature gradient in the model.

6. Theory in section 2.2 predicts that the reference temperature in a conducting skin measured in the basic unit of C should be inversely proportional to the thirteenth root of the thickness. This gives a value of 1.054 for the ratio of the nose temperatures in the $\frac{1}{4}$ inch thick stainless steel model (section 7.2) to that in the $\frac{1}{8}$ inch thick (section 7.2). But the test values of temperatures give ratios of 1.019, 1.0246 and 1.025 for the heating rates of 800, 1000 and 1200 watts of the heating element respectively. This shows that higher the rates of heating, better is the agreement between the experimental values and the theoretical predictions.

7. Within the range of the fineness ratios of the stainless steel models tested, i.e. 12 to 48, comparison of the test results with the theoretical predictions does not show any effect of the fineness ratio on the results.

8. Equation (2.3-7) predicts that the nose temperature in a uniform thickness conducting skin varies as $Q^{4/3}$. In the case of half inch thick stainless steel model, this gives values of 1.087 and 1.057 for the ratios of nose temperatures at the heating rates of 1000 and 800 watts, and 1200 and 1000 watts of the filament respectively. The corresponding values from the test results are 1.0465 and 1.0496. This again shows that the higher rates of heating support better the theoretical predictions of temperature in the conducting skin.

9. In the case of the ceramic model, the experimental temperature in the nose region is lower than the theoretical temperature, but away from the nose region it is higher (vide figures 7.3.1 to 7.3.3). This condition remained similar even after the theoretical temperatures were calculated with slightly higher values of Q and ε (figure 7.4.4).

10. Theoretical temperature distribution in stainless steel models calculated with assumed higher values of Q and ε (figures 7.4.1 and 7.4.2) still shows that there is a good amount of agreement in the nature of the theoretical prediction of temperature distribution and the experimental one. The experimental temperature distribution curve shows that slightly higher amount of heat is conducted away from the nose region than predicted by the theory. However, this does not have much importance because the theoretical temperature distribution is based on assumed values of Q and ε.

11. Figure 7.4.3. was drawn to find the effects of a slight variation in the thermal conductivity of the conducting skin on the nature of the theoretical temperature distribution. But this figure shows that the nature of the temperature distribution curve remains the same for all practical purposes for a small variation of conductivity of the skin.

8.2 Discussions of the Results

In spite of the experimental values of temperatures being higher than the theoretical ones, (for measured values of $\dot{Q}$) for which reasons are discussed below, a good agreement in the nature of their curves, indicates how well the theory predicts the actual temperature distribution in a hypersonic body. This clearly demonstrates that heat conductivity of a material may not be important in the downstream region of a hypersonic body, but it is an important factor in reducing the nose temperature to a considerable lower value. Besides, it will not allow a steep temperature gradient to exist in the nose region, as in case of the generally assumed radiation equilibrium temperature distribution.

There are certain reasons for the theoretical prediction of temperatures to appear lower than the experimental ones. First of all, in the theory (section 2.2), the ambient heat gain by the conducting skin has been neglected. Of course, this is fully justified, because it is negligible in comparison to the aerodynamic heating at high Mach numbers of flight. But under the conditions of the present experiments, the contribution due to ambient heating is not negligible. If this is taken into account, the heat balance equation (2.2.1) becomes

$$\frac{d}{dx}\left\{ Kt(x)\,\frac{dT}{dx} \right\} = \varepsilon\sigma T^4 - \varepsilon\sigma Ta^4 - \frac{Q}{x_{\frac{1}{2}}} \qquad \ldots(8.2.1\text{a})$$

where Ta is the ambient temperature.

The non-dimensional form of this equation, for a uniform thickness skin can be expressed as

$$\frac{d^2\phi}{d\xi^2} = \phi^4 - \phi a^4 - \xi^{-\frac{1}{2}} \qquad \text{- - - - 8.2.1}$$

Following Nonweiler's method (section 2.3) it can be solved on a computer by assigning different values of ϕa. But one should remember that for each value of ϕo, there would be several values of ϕa and hence a family of solutions would be obtained for any value of ϕo.

However, a rough estimate of the effects of the ambient heating on the temperature of the model can be made approximately by numerically solving the equations (2.3.1a) and (8.2.1) at a suitable value of ξ and then comparing the results. For a heating element power of 1200 to 800 watts, this shows that ambient heating increases the nose temperature in the model at least by 1 to 2 percent, whereas the corresponding test values of temperatures in the stainless steel models are about 3 to 5 percent higher than the theoretical predictions.

The consideration of the ambient heating explains also the least difference between the experimental and the theoretical values of temperatures at the leading edge; where due to the radiant heating from the heating element being maximum, the proportional contribution due to the ambient heating is least. The same is true if the rate of heating is higher.

Secondly, there is some chance of the actual heating rates on the model being higher than the one measured by the radiometer. This is because during the calibration of the reflector by the radiometer, the radiant heat from the heating element is, more or less entirely, absorbed

when they are incident on the base plate or on the walls of the chamber. But with the model in position, it radiates out its own heat. Also the portion of the heat from the heating element, which is incident on the model is reflected back because its emissivity is not unity. A certain percentage of these heats would be reflected a number of times on the surface of the reflector and some of them would eventually come back to the model again. Of course, when the reflector was designed it was taken into account that the reflector did not make a solid angle at any point on the model of more than 10 per cent of 2π, so that if the reflector reflects back to that point 10 per cent of the radiation received by it from that point, only 1 per cent will actually come back to that point on the model. However, the determination of the exact amount of this radiation coming back to that point on the model is very complicated and could not be estimated exactly.

A little difference in the theoretical and experimental values of temperatures can also be ascribed to the instrumental errors, such as in the calibration of the radiometer and in the further measurement of the heat intensity, etc., the reasons for which have already been discussed in section 7.4. Similarly values of ε and K, taken from other sources, may not be taken as absolutely correct. A small error in them, will also induce certain error in the calculation of the theoretical temperatures.

A very definite conclusion can not be derived from a small temperature gradient measured across the thickness of the $\frac{1}{8}$ inch thick stainless steel and ceramic models. This is because always there is a likelihood of a small quantity of heat being lost from the lower surface of the model due to radiation. Of course, the aluminium foil arranged

below the lower surface of the model would reflect the radiant heat back to the model, but still it will absorb a part of that. This argument also explains the existence of a greater temperature gradient observed in the ceramic model than that in the stainless steel. The lower surface of the stainless steel model was highly polished and hence the radiation of heat was much less than that from the ceramic model due to the latter having a higher emissivity of the lower surface.

8.3 Conclusions and Suggestions for the Further Work:- From the tests performed on the conducting skin models of stainless steel and ceramic (sections 7.2 to 7.5) it is quite obvious that the thermal conductivity of material is an important medium for transporting the heat from the nose region to downstream part of the body subjected to aerodynamic heating. The general practice of predicting the temperature of a hypersonic body by neglecting the conduction of heat through its skin is completely unfounded; especially in the leading edge region. The conducting skin leading edge temperature is much lower than the predicted radiation equilibrium temperature of a non-conducting skin.

In spite of a little discrepancy in the values of the test and theoretical temperatures, the test results establish, beyond doubt, the validity of the theory described in sections 2.2 and 2.3, within the ranges of values of Q, K and ε of the tests. However, it is important to find the compatibility of the theory at higher rates of heating. Tests at higher level of heating will have the advantage of having proportionately less effect of the background radiation on the temperature of the model and thus will enable the test to compare its value with the theoretical

predictions more precisely.

In order to increase the heating on the model, a future work on this problem should attempt both to find means to eliminate the waste of available radiant heat, beyond the hot end of the model and also to increase the heating power of the filament. In order to increase the heat output of the filament, further work on the line adopted in section 5.5 can be pursued. The fibrefrax cement does not work above 1260°C and hence a suitable cement to provide a firm bonding of the lampblack above 1260°C would be needed. Since even the high purity nickel is not suitable for application in a high vacuum above 1100°C, one of the refractory metals such as molybdenum, tungsten etc. has to be tried. In selecting the metal, one having the thermal expansion nearer to that of the lampblack will enable the lampblack to adhere to it better. With nickel, it was possible to oxidise the wire to increase the adherence of lampblack on its surface, but this will not be possible with any of the refractory metals, because oxides of none of them adhere to the base metal beyond 1200°C. However, if a suitable cement is found, oxidising of the metal wire might not be necessary.

Means to reduce the slow evaporation and burning out of the lampblack at the high temperatures of 1100°C and above has to be found out. This is a menace as it reduces the life of the filament as well as it tarnishes the highly polished surface of the reflector. Diffusion of air molecules, outgassing of the vacuum chamber, models, reflector and other equipment inside the chamber, provide enough oxygen molecules for the gradual burning of the lampblack. Use of some suitable 'getters', having high affinity for the oxygen molecules, is expected to reduce the burning of the lampblack.

In view of the excellent agreement in the nature of the test temperature distribution in the uniform thickness conducting skin and Nonweiler's theoretical prediction, it will be interesting to investigate further the temperature distribution in conducting skins of different geometry, theoretical solutions for which are available in Nonweiler's work.[22]

APPENDIX - A

THE REFLECTOR PROFILE USING A FINITE SIZE OF HEATING ELEMENT

Let two rays of radiation CR and DR issuing from the heating element of radius r_h at O be incident at R on the reflector AEB and after having undergone reflection at R, let them strike at P and P_1 respectively, the plane of irradiation at a distance OX = a_o (fig. A -1)

Further, if PR and P_1R make angles ω and ω_1 with XO (extended if necessary) then, a geometrical analysis yields the following relations :-

$$\angle ORN = -\tan^{-1}\left(\frac{dr}{rd\theta}\right)$$

where RN is normal at R and θ is the angle subtended with OX by the radius r of the reflector,

$$\delta = \angle ORN - \angle DRN = \omega - \omega_1'$$

$$= \tan^{-1}\left(\frac{\sin\psi}{\frac{r}{r_h} - \cos\psi}\right) \qquad \ldots (A - 1)$$

$$\omega = \theta - \pi - 2\tan^{-1}\frac{dr}{rd\theta}$$

$$= \text{limit of } \psi = \cos^{-1}\frac{r_h}{r}$$

$$\tan\omega_1 = \frac{x_1 - r\sin\theta}{a_o - r\cos\theta}$$

$$\tan\omega = \frac{x - r\sin\theta}{a_o - r\cos\theta}$$

$$= \tan\left(\theta - \pi - 2\tan^{-1}\frac{x - r\sin\theta}{a_o - r\cos\theta}\right)$$

$$\text{or, } \frac{dr}{rd\theta} = \tan\left(\frac{\theta - \pi}{2} = \frac{1}{2}\tan^{-1}\frac{x_o + L_1S^2 - r\sin\theta}{a_o - r\cos\theta}\right)$$

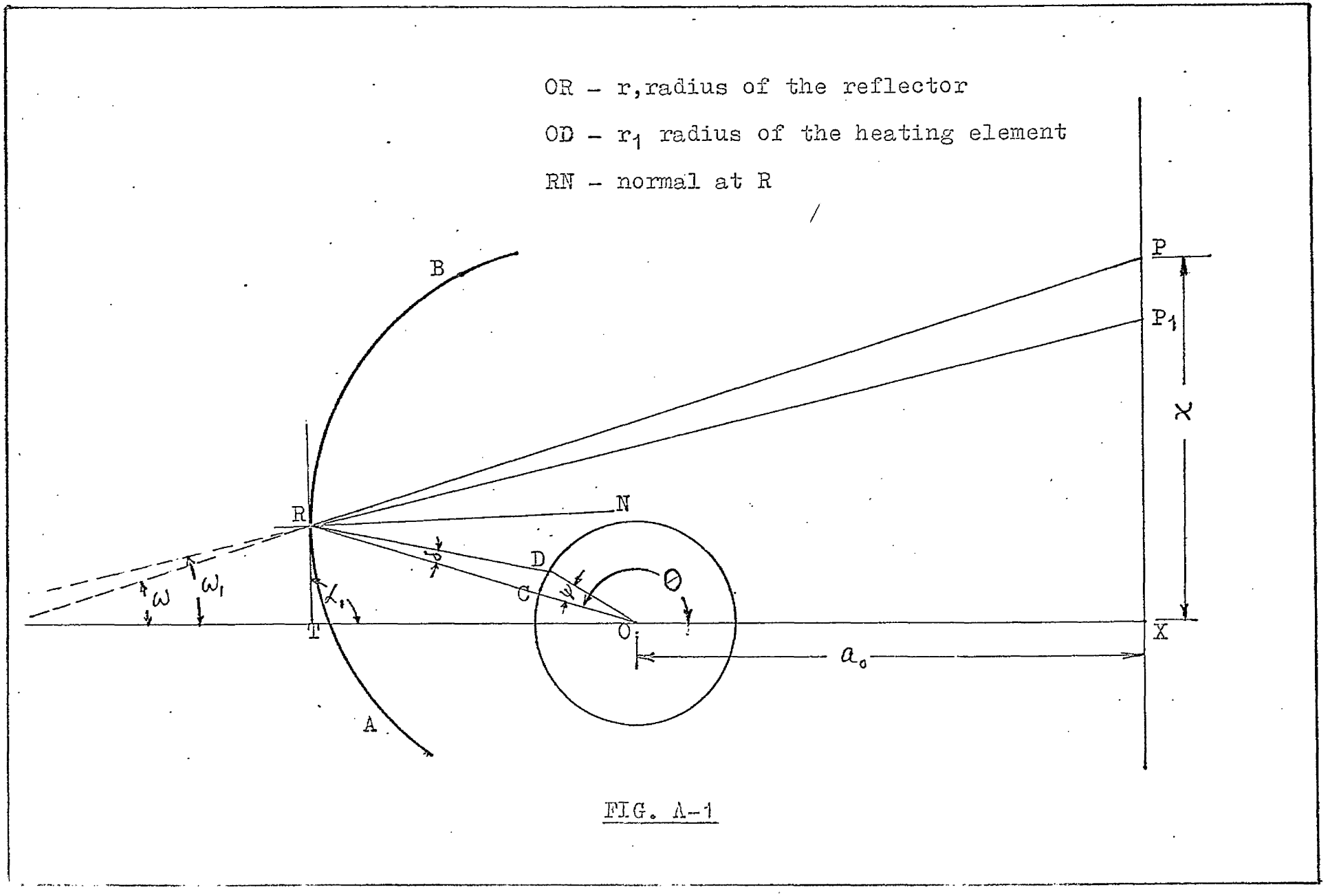
OR – r, radius of the reflector
OD – r_1 radius of the heating element
RN – normal at R
B
P
P_1
χ
R
N
D
C
O
ω
ω_1
χ_1
T
O
X
a_0
A

FIG. A-1

where,

$L_1 = \left(\frac{Q'}{2Q}\right)^2$ as defined by equation(4.2.4)

$S = \left(\frac{X - X_o}{L_1}\right)^{\frac{1}{2}}$ as defined by equation (4.2.11)

and Q' = heat intensity of a point source

The total amount of heat radiation emitted over the surface from ψ_o to $-\psi_o$ of the heating element can be expressed from

$$\frac{2\psi_o Q'}{2\pi} = \frac{\psi_o Q'}{\pi}$$

Using Lambert's Cosine law, the intensity of this heat experienced at a point R on the reflector, can be given as,

$$\frac{\psi_o Q'}{\pi} \text{Cos}\ (\psi + \partial\ )$$

If the heat emitted from the surface of the heating element over an arc $d\omega_1$ falls over dx_1 about P_1 on the plane of irradiation, then the radiation intensity per unit area on the plane of irradiation can be expressed as,

$$\frac{Q'\psi_o}{\pi} \int_{-\psi_o}^{\psi} \text{Cos}\ (\psi + \partial)\ \frac{d\omega}{dx_1}\, d\psi$$

$$= \frac{Q'\psi_o}{\pi} \int_{-\psi_o}^{\psi} \text{Cos}\ (\psi + \partial\ ) \frac{\text{Cos}\ \omega_1}{DR * RP_1}\, d\psi \qquad \ldots(\Lambda - 2)$$

since,

$\frac{d\omega_1}{dx_1} = \frac{\text{Cos}\ \omega_1}{DR + RP_1}$ where $d\omega_1$ is the subtending angle of the arc $dx_1 \text{Cos}\ \omega_1$.

Λ^S in chapter IV, the direct radiation from

the heating element on the plane of irradiation is

$$\frac{Q'_{\circ}\, a_{\circ}}{a_{\circ}^2 + x^2} = \frac{Q' \cdot a_{\circ}}{(L_1 S^2 + x_{\circ})^2 + a_{\circ}^2} \qquad \ldots(A-3)$$

Adding (A-2) and (A-3) and equating the sum to the aerodynamic heating (eqn.4.2.2.) the expression becomes,

$$\frac{Q'\psi_{\circ}}{\pi} \int_{-\psi_{\circ}}^{\psi_{\circ}} \mathrm{Cos}\,(\psi + \partial)\, \frac{\mathrm{Cos}\,\omega_1}{DR + RP_1}\, d\psi + \frac{Q' \cdot a_{\circ}}{a_{\circ}^2 + (L_1 S^2 + x_{\circ})^2}$$

$$= \frac{Q}{(x - x_{\circ})^{\frac{1}{2}}}$$

or,

$$\frac{\psi_{\circ}}{\pi} \int_{-\psi_{\circ}}^{\psi} \mathrm{Cos}\,(\psi + \partial)\, \frac{\mathrm{Cos}\,\omega_1}{DR + RP_1}\, d\psi + \frac{a_{\circ}}{a_{\circ}^2 + (L_1 S^2 + x_{\circ})^2}$$

$$= \frac{1}{2L_1 S} \qquad \ldots(A-4)$$

The integration term of equation (A-4) can be further expanded as follows.-
From equation (A-1),

$$\mathrm{Cos}\,(\psi + \partial) = \frac{\frac{r}{r_h}\mathrm{Cos}\psi - 1}{\left\{\left(\frac{r}{r_h} - \mathrm{Cos}\psi\right)^2 + \mathrm{Sin}^2\psi\right\}^{\frac{1}{2}}}$$

$$\mathrm{Cos}\,\omega_1 = \mathrm{Cos}\,(\omega - \partial)$$

$$= \frac{\mathrm{Cos}\,\omega\left(\frac{r}{r_h} - \mathrm{Cos}\,\psi\right) + \mathrm{Sin}\omega\,\mathrm{Sin}\,\psi}{\left\{\left(\frac{r}{r_h} - \mathrm{Cos}\,\psi\right)^2 + \mathrm{Sin}^2\psi\right\}^{\frac{1}{2}}}$$

$$DR + RP_1 = \frac{r_h \mathrm{Sin}\,\psi}{\mathrm{Sin}\partial} + \frac{a - r\mathrm{Cos}\,\theta}{\mathrm{Cos}\,\omega_1}$$

$$= \frac{r_h \mathrm{Cos}\,\omega_1 \left\{\left(\frac{r}{r_h} - \mathrm{Cos}\psi\right)^2 + \mathrm{Sin}^2\psi\right\}^{\frac{1}{2}} + (a_{\circ} - r\,\mathrm{Cos}\,\theta)}{\mathrm{Cos}\,\omega_1}$$

$$\text{or,}\quad \frac{\text{Cos}\ \omega_1}{DR + RP_1} = \frac{\text{Cos}^2\omega_1}{r_h \text{Cos}\ \omega_1 \left\{\left(\frac{r}{r_h} - \text{Cos}\,\psi\right)^2 + \text{Sin}^2\psi\right\}^{\frac{1}{2}} + (a_o - r\text{Cos}\theta)}$$

$$= \frac{\left\{\text{Cos}\ \omega\left(\frac{r}{r_h} - \text{Cos}\psi\right) + \text{Sin}\omega \cdot \text{Sin}\,\psi\right\}^2}{\left\{\left(\frac{r}{r_h} - \text{Cos}\psi\right)^2 + \text{Sin}^2\psi\right\}\left[r_h \text{Cos}\ \omega\left(\frac{r}{r_h} - \text{Cos}\psi\right) + r_h \text{Sin}\ \omega\ \text{Sin}\,\psi + (a_o - r\text{Cos}\theta)\right]}$$

The integration term ,therefore, can be written as,

$$\frac{\psi_o}{\pi}\int_{-\psi_o}^{\psi_o} \frac{\left(\frac{r}{r_h}\text{Cos}\psi - 1\right)\left[\text{Cos}\ \omega\left(\frac{r}{r_h} - \text{Cos}\psi\right) + \text{Sin}\ \omega\ \text{Sin}\psi\right]^2 \quad d\psi}{\left\{\left(\frac{r}{r_h} - \text{Cos}\,\psi\right)^2 + \text{Sin}^2\psi\right\}^{3/2}\left[r_h \text{Cos}\ \omega\left(\frac{r}{r_h} - \text{Cos}\psi\right) + r_h \text{Sin}\ \omega \cdot \text{Sin}\psi + a_o - r\ \text{Cos}\ \theta\right]}$$

...(A - 5)

The integration of (A-5) is complicated and has to be done numerically. By differetiating with respect to r and taking m increments over the angle ψ_o , equation (A-5) becomes,

$$\sum_{n=-m}^{n=m}\left[\frac{m\Psi}{\pi}\right] \frac{\left(\frac{r}{r_h}\text{Cos}\ n\Psi - 1\right)\left\{\text{Cos}\omega\left(\frac{r}{r_h} - \text{Cos}\ n\Psi\right) + \text{Sin}\ \omega\ \text{Sin}\ n\Psi\right\}^2 \quad \frac{d\Psi}{dr}}{\left\{\left(\frac{r}{r_h} - \text{Cos}\ n\Psi\right)^2 + \text{Sin}^2 n\Psi\right\}^{3/2}\left\{r_h \text{Cos}\ \omega\left(\frac{r}{r_h} - \text{Cos}\ n\Psi\right) + r_h \text{Sin}\ \omega\ \text{Sin}\ n\Psi + (a_o - r\ \text{Cos}\ \theta)\right\}}$$

...(A-6)

where,

$$\Psi = \frac{\psi_o}{m}$$

$$\frac{d\Psi}{dr} = \frac{1}{m}\frac{\left(\frac{r_h}{r^2}\right)}{\left\{1 - \left(\frac{r_h}{r}\right)^2\right\}^{\frac{1}{2}}}$$

Equation (A -6) can be written as ,

$$\frac{\psi_0}{\pi}\left[\cos^2\omega . F_1 + \sin 2\omega . F_2 + \sin^2\omega . F_3\right] \qquad \ldots(\text{A-7})$$

where,

$$F_1 = \sum_{n=-m}^{n=m} \frac{\left(\frac{r}{r_h}\cos n\psi - 1\right)\left(\frac{r}{r_h} - \cos n\psi\right)^2 \cdot \frac{1}{m}\cdot\frac{r_h}{r^2}\sqrt{\left\{1 - \left(\frac{r_h}{r}\right)^2\right\}}}{\left[\left(\frac{r}{r_h} - \cos n\right)^2 + \sin^2 n\psi\right]^{3/2}\left[r_h\cos\omega\left(\frac{r}{r_h} - \cos n\psi\right) + r_h \sin\omega \sin n\psi + \left(a_0 + r\cos\theta\right)\right]}$$

$$F_2 = \sum_{n=-m}^{n=m} \frac{\left(\frac{r}{r_h}\cos n\psi - 1\right)\left[\frac{r}{r_h} - \cos n\psi\right]\sin n\psi \cdot \frac{1}{m}\cdot\frac{r_h}{r^2}\sqrt{\left\{1 - \left(\frac{r_h}{r}\right)^2\right\}}}{\left[\left(\frac{r}{r_h} - \cos n\psi\right)^2 + \sin^2 n\psi\right]^{3/2}\left[r_h\cos\omega\left(\frac{r}{r_h} - \cos n\psi\right) + r_h\sin\omega \sin n\psi + \left(a_0 - r\cos\theta\right)\right]}$$

$$F_3 = \sum_{n=-m}^{n=m} \frac{\left(\frac{r}{r_h}\cos n\psi - 1\right)\sin^2 n\psi \cdot \frac{1}{m}\left(\frac{r_h}{r^2}\right)\sqrt{\left\{1 - \left(\frac{r_h}{r}\right)^2\right\}}}{\left[\left(\frac{r}{r_h} - \cos n\psi\right)^2 + \sin^2 n\psi\right]^{3/2}\left[r_h\cos\omega\left(\frac{r}{r_h} - \cos n\psi\right) + r_h\sin\omega \sin n\psi + \left(a_0 - r\cos\theta\right)\right]}$$

F_2 is negligible. Since $\sin^2 n\psi$ is very small compared to the term

$$\left(\frac{r}{r_h} - \cos n\psi\right)^2$$

and $F_3 << F_1$, equation (A-7) can be simplified to

$$\sum_{n=-m}^{n=m} \frac{\cos^2\omega\left(\frac{r}{r_h}\cos n\psi - 1\right)\frac{1}{m}\left(\frac{r}{r^2}\right)\sqrt{\left\{1 - \left(\frac{r_h}{r}\right)^2\right\}}}{\left(\frac{r}{r_h} - \cos n\psi\right)\left[r_h\cos\omega\left(\frac{r}{r_h} - \cos n\psi\right) + \left(a_0 + r\cos\theta\right)\right]}$$

In the integral form it can be written as

$$\int_{-\psi_o}^{\psi_o} \frac{\left(\frac{r}{r_h}\cos\psi - 1\right)\cos^2\omega \; d\psi}{\left(\frac{r}{r_h} - \cos\psi\right)\left[r_h\cos\omega\left(\frac{r}{r_h} - \cos\psi\right) + (a_o + r\cos\theta)\right]} \qquad \ldots(A-8)$$

In the denominator of this equation, the term $r_h \cos\omega \cdot \cos\psi << a_o$ and v can be dropped to simplify it further. Hence

$$\int_{-\psi_o}^{\psi_o} \frac{\left(\frac{r}{r_h}\cos\psi - 1\right)\cos^2\omega \; d\psi}{\left(\frac{r}{r_h} - \cos\psi\right)(r\cos\omega + a_o - r\cos\theta)}$$

$$= \frac{\psi_o}{\pi} \frac{\cos^2\omega\left[\pi\sqrt{\left(\frac{r}{r_h}\right)^2 - 1} - 2\frac{r}{r_h}\cos^{-1}\left(\frac{r_h}{r}\right)\right]}{(r\cos\omega + a_o - r\cos\theta)} \qquad \ldots(A-9)$$

With (A-9), equation (A-4) becomes

$$\frac{\psi_o}{\pi} \frac{\cos^2\omega\left[\pi\sqrt{\left(\frac{r}{r_h}\right)^2 - 1} - 2\frac{r}{r_h}\cos^{-1}\frac{r_h}{r}\right]}{(r\cos\omega + a_o - r\cos\theta)}$$

$$= 2\frac{1}{L_1 S} - \frac{a}{a^2 + (L_1 S^2 + x)^2} \qquad \ldots(A-10)$$

With equations (4.2.10)and (4.2.11) , equation (A-10) forms the basis for calculation of the reflector profile on the Deuce Computer.

APPENDIX - B

DETERMINATION OF HEAT INTENSITY ON A PLANE IRRADIATED BY A REFLECTOR

In figure (B - 1), any point R_1 on the reflector receives a beam of heat radiation bounded by rays O_1R_1 and O_2R_1 from the heating element of radius r_h at O and reflects it to the plane of irradiation XP at a distance a_o from O. The bounding rays O_1R_1 and O_2R_1 of the beam fall at P_1 and P_2 respectively. Similarly point R_2 on the reflector receives another beam of heat radiation bounded by rays O_3R_2 and O_4R_2 from the heating element and reflects it to the region P_1P_3 of the irradiated plane. Thus it can be appreciated that due to the presence of reflector profile from R_1 to R_2 any point P_1 on the plane of irradiation is able to receive as reflected rays some portion of the heat rays radiated from the region O_1 to O_4 of the heating element. Similarly other points on the plane of irradiation will receive reflected rays due to the presence of the other portion of the reflector profile.

Let an infinitesimally small region δx about the point P_1 receives as reflected radiation the amount of energy emitted by the heat source at O over the arc between $(\theta_2 - \theta_1)$, then the total reflected heat energy received by δx would be

$$\frac{Q'}{2\pi}\left(\theta_2 - \theta_1\right)$$

where, Q' is the heat intensity of the heat source per unit length.

If the same region δx about P_1 receives the heat radiation reflected by some other portion of the reflector

$OO_1 = r_h$ the radius of the heating element,
OR_1 = instn. radius r_1 of the reflector ARB,
R_1N is the normal to the reflector at R_1,
R_1S is parallel to OX,
angle $XOR_1 = \theta_1$
angle $XOR_2 = \theta_2$

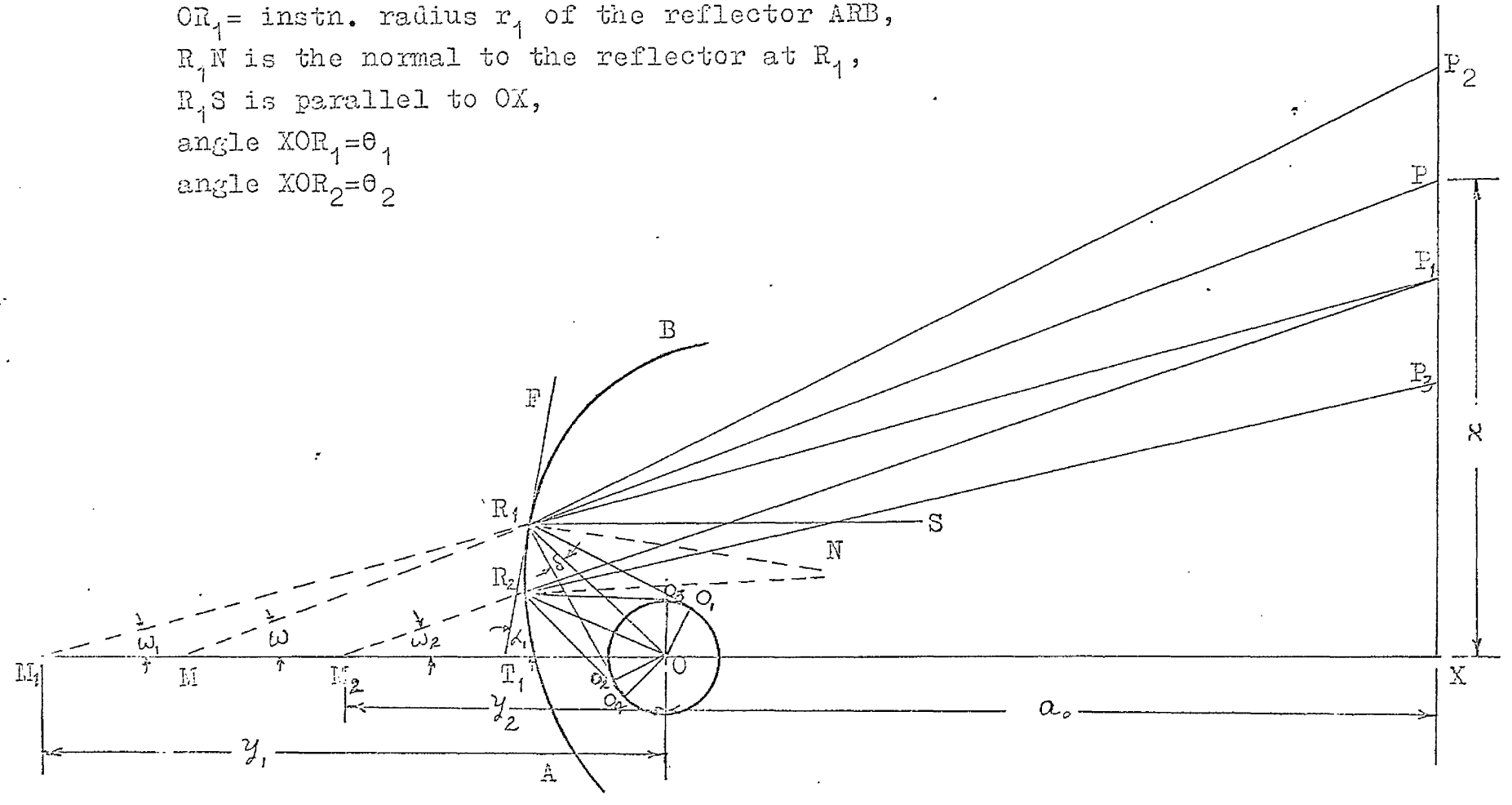

FIG. B--1

energy received from that should be added to that from $(\theta_2-\theta_1)$. Thus,

$$\frac{Q'}{2\pi}\sum(\theta_2-\theta_1) \qquad \ldots (B-1)$$

represents the reflected heat energy received by δx about P_1.

The direct radiation received by δx about P_1 would be,

$$\frac{Q'}{2\pi}\,\frac{\delta x}{(a_o^2+x^2)^{\frac{1}{2}}}\cdot\frac{a_o}{(a_o^2+x^2)^{\frac{1}{2}}} \qquad \ldots (B-2).$$

where,

$$\frac{a_o}{(a_o^2+x^2)^{\frac{1}{2}}} = \cos P_1\hat{O}X.$$

Thus, the total heat received by δx about P_1 is

$$\frac{Q'}{2\pi}\left\{\sum(\theta_2-\theta_1)+\frac{a_o\,\delta x}{(a_o^2+x^2)}\right\}$$

The intensity per unit area at P_1 willbe ,therefore,

$$\frac{Q'}{2\pi}\left\{\frac{\sum(\theta_2-\theta_1)}{\delta x}+\frac{a_o}{a_o^2+x^2}\right\} \qquad \ldots (B-3).$$

The accuracy of the finding of the heat intensity at any point P_1 will depend on the magnitude of δx assumed. The larger value will increase the relative importance of the direct radiation term, whereas the smaller δx will assess more precisely the heat intensity due to the reflected rays.

Inn the reflector of the type being designed with $r_o < a_o$, $r_h \ll r_o$ and so on , the direct radiation term is not comparable to the reflected radiation term. For example, in the multi-curve reflector of table 4.8.1, at the cold end of the plane of irradiation the proportional contribution of the direct radiation is about $0.05\frac{Q'}{2\pi}$, whereas the reflected radiation is about $0.5\,\frac{Q'}{2\pi}$. This is based on δx equal to

0.8 inch. Thus it shows that the direct radiation term on the cold end side of the plane of irradiation is small but not negligible , though , the procedure of testing a reflector becomes much easier by neglecting the part due to the direct radiation. Besides, inthe numerical example considered here , the value of 0.8 inch taken for δx is too large. The smaller value of δx will show that the proportional contribution of the direct radiation term is much less. Therefore, for the sake of simplifying the work on the computer for evolving a most suitable profile of a multi-curve reflector and testing othersn , the direct radiation term was neglected.

To find θ_1 and θ_2

let, the reflected rays R_1P_1 and R_2P_1 make angles ω_1 and ω_2 with XO (extended , if necessary).

$\angle R_1T_1O = \alpha_1$ the slope of reflector at R_1 ,

$\angle O\ R_1O_1 = \delta_1 = \angle O\ R_1O_2$

and R_1S is drawn parallel to OX .

Then , from $\triangle O\ R_1O_1$,

$$\delta_1 = \tan^{-1} \frac{r_h}{(r_1^2 - r_h^2)^{\frac{1}{2}}} \qquad \ldots (B-4).$$

also,

$$P_1R_1S = \alpha_1 - (\theta_1 - \alpha_1 + \delta_1)$$
$$= (2\alpha_1 - \theta_1 - \delta_1) = \omega_1 \qquad \ldots (B-5)$$

Here,

$$T_1R_1O_1 = \theta_1 - \alpha_1 + (\theta_1 - \ldots),$$

and from the laws of spectral reflection,

$$\angle T_1R_1O_1 = \angle F\ R_1P_1 = (\theta_1 - \alpha_1 + \delta_1),$$

From $\triangle R_1 M_1 O$

$$y_1 = M_1O = r_1 \frac{\text{Sin}\{\theta_1 - (2\alpha_1 - \theta_1 - \delta_1)\}}{\text{Sin}(2\alpha_1 - \theta_1 - \delta_1)}$$

$$= r_1 \frac{\text{Sin}(2\theta_1 - 2\alpha_1 + \delta_1)}{\text{Sin}(2\alpha_1 - \theta_1 - \delta_1)} \qquad \ldots(B-6)$$

Therefore, from equations (B-4) to (B-6),

$$X P_1 = x_1 = (a_o + y_1) \tan(2\alpha_1 - \theta_1 - \delta_1)$$

$$= \left\{ a_o + r_1 \frac{\text{Sin}\left[2\theta_1 - 2\alpha_1 + \tan^{-1}\frac{r_h}{(r_1^2 - r_h^2)^{\frac{1}{2}}}\right]}{\text{Sin}\left[2\alpha_1 - \theta_1 - \tan^{-1}\frac{r_h}{(r_1^2 - r_h^2)^{\frac{1}{2}}}\right]} \right\} \tan\left[2\alpha_1 - \theta_1 - \tan^{-1}\frac{r_h}{(r_1^2 - r_h^2)^{\frac{1}{2}}}\right]$$

$\ldots$ (B - 7).

where,

the slope, $\alpha_1 = \theta_1 - \frac{\pi}{2} - \tan^{-1}\left(\frac{1}{r_1}\frac{dr}{d\theta}\right)$ $\ldots.(B-8)$

Similarly, using the same law of spectral reflection and a little trigonometrical analysis, it can be shown that

$$\omega_2 = (2\alpha_2 - \theta_2 - \delta_2)$$

where α_2 is the new slope of the reflector at R_2 and,

$$\delta_2 = \angle O_4 R_2 O = \angle O R_2 O_3 = \tan^{-1}\frac{r_h}{(r_2^2 - r_h^2)^{\frac{1}{2}}}$$

From $\triangle M_2 R_2 O$, therefore,

$$M_2O = y_2 = r_2 \frac{\text{Sin}(2\theta_2 - 2\alpha_2 - \delta_2)}{\text{Sin}(2\alpha_2 - \theta_2 + \delta_2)}$$

Therefore,

$$XP_1 = x_1 = \left\{ a_o + r_2 \frac{\sin\left[2\theta_2 - 2\alpha_2 - \tan^{-1}\frac{r_h}{(r_2^2 - r_h^2)^{\frac{1}{2}}}\right]}{\sin\left[2\alpha_2 - \theta_2 + \tan^{-1}\frac{r_h}{(r_2^2 - r_h^2)^{\frac{1}{2}}}\right]} \right\} \tan\left[2\alpha_2 - \theta_2 + \tan^{-1}\frac{r_h}{(r_2^2 - r_h^2)^{\frac{1}{2}}}\right]$$

... (B -9).

where, the new slope,

$$\alpha_2 = \theta_2 - \frac{\pi}{2} - \tan^{-1}\left(\frac{1}{r_2}\frac{dr}{d\theta}\right) \qquad \text{... (B - 10)}$$

The other bounding ray of the beam from the heating element corresponding to $\theta = \theta_1$ will strike at P_2 given by

$$XP_2 = x_2 = \left\{ a_o + r_1 \frac{\sin\left[2\theta_1 - 2\alpha_1 - \tan^{-1}\frac{r_h}{(r_1^2 - r_h^2)^{\frac{1}{2}}}\right]}{\sin\left[2\alpha_1 - \theta_1 + \tan^{-1}\frac{r_h}{(r_1^2 - r_h^2)^{\frac{1}{2}}}\right]} \right\} \tan\left[2\alpha_1 - \theta_1 + \tan^{-1}\frac{r_h}{(r_1^2 - r_h^2)^{\frac{1}{2}}}\right]$$

... (B - 11).

From the design of the reflector, values of a_o , r α and r_h will be known and hence by solving equations (B-7) and (B-9), the values of θ_1 and θ_2 can be found out for any position of P_1 on the plane of irradiation . For the same point , the direct radiation ,

$$\frac{Q'}{2\pi}\left(\frac{a_o}{a_o^2 + x^2}\right)$$

can be calculated out . Thus a graph of

$$\frac{Q'}{2\pi}\left\{\sum\left(\frac{\theta_2 - \theta_1}{\delta x}\right) + \frac{a_o}{(a_o^2 + x^2)}\right\}$$

plotted against values of x will represent the heat distribution curve given by the reflector.

APPENDIX - C

SENSITIVITY OF REFLECTOR TO MANUFACTURING ERROR

The manufacturing errors in the reflector may be in both positive and negative and are most likely to be randomly distributed in two dimensions over the surface of the profile. This will have the effect of producing a wavy surface and the profile will no longer remain as smooth as designed.

In constructing the reflector (chapter 4.2), there will probably be errors in marking the co-ordinates r and θ and also in subsequent machining. In other words, at any angle θ, the radius r of the profile may have either positive or negative errors. Should the errors be either positive only or negative only , they will not produce as serious effects as when they are almost alternatively positive and negative, which is most likely to be the case. In order to examine the magnitude of their effects on the points of incidence of the reflected rays, the following equations are derived.

Let an error δr in r_2 at $(\theta+\delta\theta)$ cause the slope of the reflector profile at θ to change from α_1 to α_1' (fig. C-1). For small value of $\delta\theta$,the arc AR of the true reflector profile and CR of the reflector profile produced due to manufacturing error AC $(=\delta r)$ in r_2 may be taken as straight lines.

If RX_1 is drawn parallel to OX ,it can be easily shown that

$$\angle ARO = \theta - \alpha_1'$$

Hence, from $\triangle ORC$

$$\tan \alpha_1' = \frac{(r_2+\delta r)\,\mathrm{Sin}\,(\theta+\delta\theta) - r\,\mathrm{Sin}\,\theta}{(r_2+\delta r)\,\mathrm{Cos}\,(\theta+\delta\theta) - r\,\mathrm{Cos}\,\theta}$$

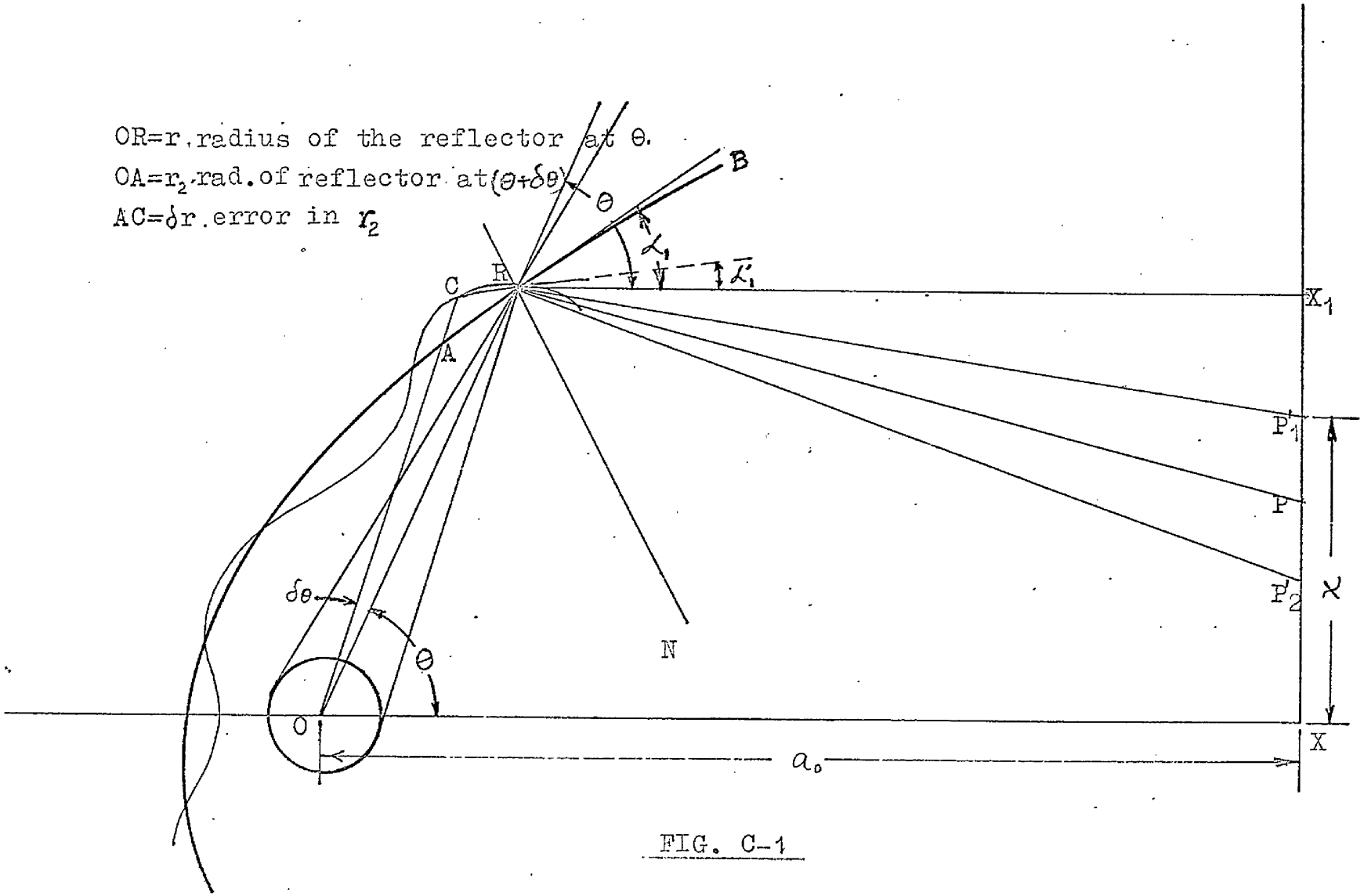
OR=r, radius of the reflector at θ.
OA=r₂ rad. of reflector at (θ+δθ)
AC=δr. error in r₂
B
θ
α₁
α
C
R
A
X₁
P₁
P
P₂
δθ
θ
N
O
a₀
X

FIG. C-1

$$\text{or, } \alpha_1' = \tan^{-1}\left\{\frac{(r_2+\delta r)\sin(\theta+\delta\theta) - r\sin\theta}{(r_2+\delta r)\cos(\theta+\delta\theta) - r\cos\theta}\right\} \qquad \ldots(C-1)$$

Following a similar procedure, it is found that a negative value of δr produces a new slope at R given by -

$$\alpha_1' = \tan^{-1}\left\{\frac{(r_2-\delta r)\sin(\theta+\delta\theta) - r\sin\theta}{(r_2-\delta r)\cos(\theta+\delta\theta) - r\cos\theta}\right\} \qquad \ldots(C-2)$$

Replacing α_1' in equations (B-7) and (B-11) by α_1' obtained from either equation (C-1) or (C-2) according as δr is positive or negative, the new points of incidence of the bounding rays of the reflected beam of radiation; P_1' and P_2' can be obtained as

$$x_1' = XP_1' = \left\{a_0 + r\frac{\sin\left[2\theta-2+\tan^{-1}\frac{r_h}{(r^2-r_h^2)^{\frac{1}{2}}}\right]}{\sin\left[2-\theta-\tan^{-1}\frac{r_h}{(r^2-r_h^2)^{\frac{1}{2}}}\right]}\right\}\tan\left[2\alpha_1'-\theta-\tan^{-1}\frac{r_h}{(r^2-r_h^2)^{\frac{1}{2}}}\right] \qquad \ldots(C-3)$$

and,

$$x_2' = XP_2' = \left\{a_0 + r\frac{\sin\left[2\theta-2-\tan^{-1}\frac{r_h}{(r^2-r_h^2)^{\frac{1}{2}}}\right]}{\sin\left[2-\theta+\tan^{-1}\frac{r_h}{(r^2-r_h^2)^{\frac{1}{2}}}\right]}\right\}\tan\left[2\alpha_1'-\theta-\tan^{-1}\frac{r_h}{(r^2-r_h^2)^{\frac{1}{2}}}\right] \qquad \ldots(C-4)$$

x_1 and x_2 can be calculated, as before, using equations (B-7) and (B-11) and thus the displacements of the points of incidence on the plane of irradiation of the bounding rays of the beam reflected at R can be determined by calculating $(x_1'-x_1)$ and $(x_2'-x_2)$.

A few examples calculated for the final reflector, using these equations indicate that at $\theta = 45°$ and for an

error of $\delta r = 0.001$ inch , at an interval of $\delta\theta = 1^{\circ}$, the displacements of the points of incidence of the reflected rays is of the order of 0.10 inch. However, it is important to remember that the effect is most severe at $\theta = 45^{\circ}$, where the profile slope is least.

BIBLIOGRAPHY

1. Eckert,E.R.G. — Research during the last decades on forced convection heat transfer. Proceedings of the 1961-62 International conferenc A S M E .

2 Johnson,H.A. , and Rubesin,M.W. — Aerodynamic heating and convective heat transfer-- Summary of literature survey. Transaction of ASME,July,1949,pp 447-456.

3 Nonweiler,T — The two-dimensional laminar boundary layer at at hypersonic speeds. C.of Aero. Report 67. 1953.

4. Monaghan,R.J, — Formulae and approximations for aerodynamic heating rates in high speed flight. A.R.C.Tech.Report C.P. no. 360 , 1957.

5. Nonweiler,T. — AerodynamicTheating at high speeds. Jr.Br.Inter.Soc. Vol.10,4,1951,pp 160-176.

6. Kaye,J. — Survey of friction coefficients , recovery factors and heat transfer coefficients for supersonic flow. J.Aero.Sci. 21(2),1954 , pp 117-129.

7. Oguchi,H — The blunt leading edge problem in hypersonic flow. AIAA jour.Vol.2, 1963,pp 361-368.

8. Lees,L — Laminar heat transfer over blunt-nosed bodies at hypersonic flight speeds. Jet Prop. April, 1956, pp 259-269 and 274.

9. Fay,J.A. Riddel,F.R. and Kemp,N.H. — Stagnation point heat transfer in dissociated air flow. Jet Prop. ,27, 1957, pp 672-674.

10. Fay, J.A. and Riddel, F.R. — Theory of stagnation point heat transfer in dissociated air. J. Aero. Sci. 25, 1958 pp 73-85 and 121.

11. Eckert, E and Weise, W. — The temperature of the unheated bodies in a high speed gas. stream. NACA T M 10009 1941.

12. Brainerd, J.G. and Emmons, H.W. — Effects of variable viscosity on boundary layer with a discussion of drag measurements. J.App.Mech.Trans. ASME 64, 1942, pp A-105.

13. Chapman, R. and Rubesin, M.W. — Temperature and velocity profiles in the compressible laminar boundary with arbitrary distribution of surface temperatures. J.Aero.Sci. 16, 1949, pp 547-565.

14. Karman, Th.Von. and Tsien, H. — Boundary layer in compressible fluids. J.Aero.Sci. 5, 1938, pp. 227-232.

15. Probstein, R.F. — Methods of calculating the equilibrium laminar heat transfer rate at hypersonic flight speeds. Jet Prop. 26, 1956, pp. 497-499.

16. Kemp, N.H. Rose, P.H. and Detra, R.W. — Laminar heat transfer around blunt bodies in dissociated air. J.Aero.Space Sci. 26, 1959, pp.421-430.

17. Rose, P.H. and Stark, W.I, — Stagnation point heat transfer measurements in dissociated air. J.Aero.Sci. 25, 1958.

18. Wood, G.P. — Calculation of rate of thermal dissociation of air behind normal shock waves at Mach number of 10, 12, and 14. NACA TN 3634, 1956.

19. Nonweiler , T. Conduction of heat within a structure subjected to kinetic heating.
C.of Aero. Report 48, 1956.

20. Nonweiler,T. Skin temperature and heat transfer over wedge wings at extreme speeds.
C.of aero. Report 105. 1956.

21. Nonweiler,T. Surface condition of the heat transferred from a boundary layer.
C.of Aero. Report 59, 1952.

22. Nonweiler , T. One-dimensional theory of surface heat conduction in a body under aerodynamic heating.
(to be published)

23. Wong, H.H.Y. Radiating Power of oxidised nickel .
Brit.J.Appl.Physics, Sept, 1966.

24. Kohl, W.H. Materials and techniques for electron tubes.
Chapman and Hall ltd., London, 1960.

25. Semchyshen, M. and Hardwood,J.J. Refractory metals and alloys.
Interscience Publishers, New York, 1961.

26. Kieffer,R and Benesovsky. Metallic heating elements materials for high temperature furnaces.
Metallurgia, 58, 1958, pp. 119-124.

27. Jakob, M. Heat Transfer,
Vol. I , Chapman and Hall Ltd., 1959.

28. Schnieder,P. Thermionic Emmission of thoriated tungsten.
J. Chem. Phy. , 28 , 1958, pp. 675-682.

29. ... .. Degussit oxide ceramics: Properties and applications of oxide ceramic tubes and capilaries

30. Sell,G.H.et al. Physical metallurgy of tungsten and tungsten base alloys. Westing house lamp div.WARD TR 60-37,Pt II,1961.

31. Johnson,P.D. Behaviour of refractory oxides and metals alone and in combination in vacuo at hightemperatures. J.Am.Ceram. Soc. 33, 1950, pp. 168-171.

32. ..... Handbook of Chemistry and Physics. The Chemical Rubber Co. Scintific Publishing,1963

33. Hall,R.W. Sikora,P.F. and Ault, G.M. Mechanical properties of refractory metals and and alloys above 2000° F. A.I.M.E. Refractory metals conference,Detroit, May, 1960.

34. Johnson, and Marshall Vapour Bressure of nickel and nickel oxide. J.Amm Chem. Soc. 62, 1940, pp. 1382-1390.

35. Dushman,S. Scientific foundations of vacuum technique. John Wiley and Sons. Inc. New York, 1961.

36. Burgess,G.K. and Foote,P.D. The emissitty of metals and oxides : Nickel oxide in range of 600 to 1300° C . Bul. Bureau of Standards Vol. II, 1914, pp. 41- 64.

37. Moll, W.J.H. A thermopile for measuring radiation. Proc.Phy.Soc. A35, 1922-3, pp .257-260.

38. Houghton,J.T. A new radiometer. J.sci. Inst. 31, 1954, pp. 184- 187.

39. Ward, W.H. Two portable thermistor radiometers. J.Sci, Inst. 34, 1957.

40. Adhav,R.S. and Kemp, J.G. Infra-red radiometers. J. Sci. Inst. 40, 1963, pp.26-27.

41. Gardon , R. An instrument for the direct measurement of intense thermal radiation. Rev. Sci. Inst. 24 , 1953 , pp. 366-370.

42. Simms , D.L. Pickard , R.W. and Hinklay , P.L. Modified Moll thermocouples for measuring thermal radiation of high intensity. J. Sci. Inst. 39 , 1962, pp. 204-207.

43. Sully, A.H. and Waterhouse, R.B. Some measurements of the total emissivity of metals and pure refractory oxides and the variation of emissivity with temperature. BRIT. J. App. Phy. 3, (1952)